Extended Soft-core Baryon-Baryon Interactions [1]

Th.A. Rijken[a,b,*], Y. Yamamoto[b], M.M. Nagels[c]

[a] *Institute for Mathematics Astrophysics and Particle Physics Radboud University Nijmegen the Netherlands*
[b] *Nishina Center for Accelerator-Based Science Institute for Physical and Chemical Research (RIKEN) Wako Saitama 351-0198 Japan*
[c] *Institute for Mathematics Astrophysics and Particle Physics Radboud University Nijmegen the Netherlands*

Abstract

Background The Nijmegen extended-soft-core (ESC) models treat in a unified way, using broken flavor SU(3) symmetry, the low- and intermediate-energy interactions of nucleon-nucleon (NN), hyperon-nucleon (YN), and hyperon-hyperon/nucleon (YY/ΞN) systems with strangeness S=0,-1,-2,-3,-4 respectively. The potentials consist of local and non-local potentials due to (i) One-boson exchanges (OBE), which are the members of nonets of pseudoscalar-, vector-, scalar-, and axial-vector mesons, (ii) Two pseudoscalar exchange (TPS), (iii) Meson-Pair-exchange (MPE) and (iv) Diffractive exchanges. Both the OBE- and Pair-vertices are regulated by Gaussian form factors producing potentials with a soft behavior near the origin. Broken SU(3) symmetry serves to connect the NN, YN and YY channels. In particular, the meson-baryon coupling constants are calculated via SU(3) using the coupling constants of the NN-analysis as input. The assignment of the cut-off masses for the BBM-vertices is dependent on the SU(3)-classification of the exchanged mesons for OBE, and a similar scheme for MPE.

Purpose The NN,YN,YY results presented are those from ESC16, which is the latest version of the ESC-potential model for Baryon-baryon (BB) scattering. The two body BB-potentials are also applied to the hyperonic many-body systems. Next to the standard ingredients of the ESC-models, in the ESC16 version a contribution of the short range repulsion due to the quark Pauli-principle in the BB-channels has been included systematically for the first time.

Methods In this review the (new) derivation of the potentials is based on the formulation of relativistic quantum field theory (RQFT) as developed by Kadyshevsky. Here, in contrast to the usual Feynman formulation, the particles in the Kadyshevsky graphs remain on-mass-shell also in the intermediate states. This implies that Gaussian form factors, a characteristic of the soft-core models, are well-defined and can be handled easily in the Kadyshevsky formalism. Furthermore, pair-suppression can be handled phenomenological by introducing factors at the vertices without conflict with relativistic invariance.
Major novel ingredients with respect to the former versions ESC04-ESC08 is the inclusion of (i) short-range Odderon-potentials corresponding to the odd numbers of gluon-exchanges next to the Pomeron-potentials representing the even number of gluon-exchanges, (ii) short range repulsion in all NN, YN and YY channels due to Pauli-forbidden six-quark cluster $(0s)^6$-configurations. Further new elements are (a) the extension of the $J^{PC} = 1^{++}$ axial-vector meson coupling, (b) the inclusion of the $J^{PC} = 1^{+-}$ axial-vector mesons, and (iii) a completion of the $1/M$-corrections for the meson-pair-exchange (MPE) potentials, and (c) the treatment of the scalar $\kappa(861)$ meson within the Gell-Mann-Okubo (GMO) meson-mixing scheme, and as a broad meson, like the $\rho(760)$ and $\epsilon(620)$. In contrast to ESC04, in ESC16 a medium strong flavor-symmetry-breaking (FSB) of the coupling constants is not considered. The charge-symmetry-breaking (CSB) in the Λp and Λn channels, which is an SU(2) isospin breaking, is included in the OBE-, TPS-, and MPE-potentials. In addition to the old set of 35 YN-data and 3 $\Sigma^+ p$ cross sections from the KEK-experiment E289, 11 elastic and inelastic Λp and 3 elastic $\Sigma^- p$ cross sections at higher energy are included in the YN database. For the ESC16-model, a simultaneous fit has been performed to the combined NN and YN scattering data, supplied with constraints on the YN and YY interaction due to information from the G-matrix calculations of hypernuclei.

[1] Published: Progress in Nuclear and Particle Physics **149** (2026) 104243

Results 1. NN,YN (S=0,-1): The fitting of NN dominates the determination of the couplings and the cut-off masses. Only a few parameters are strongly influenced by the YN-data, and by the constraints for the YY-interactions following from G-matrix analyses of hypernuclei and hyperonic matter. Like in the ESC04-model, the ESC16 octet and singlet coupling constants and F/(F+D) ratios of the model are conform to the predictions of the quark-antiquark pair-creation (QPC) model with dominance of the $^3P_0$-mechanism. This is not only for the OBE-couplings but also for the MPE-couplings and F/(F+D) ratios. In a simultaneous fit of all the selected NN and YN data the obtained result is $\chi^2/NN_{data} = 1.10$ and $\chi^2/YN_{data} = 1.04$. In particular, it was possible to fit the precise experimental datum $r_R = 0.468 \pm 0.010$ for the inelastic $\Sigma^- p$ capture ratio at rest very well.
2. YN,YY(S=-2): Various properties of the S=-2 potentials are illustrated by giving results for scattering lengths, bound states, phase parameters, and total cross sections. The well-depth U_Ξ is calculated and ΞN G-matrix interactions are derived and applied to Ξ^--capture reactions. Combined with three-body forces derived from the ESC meson-pair vertices and the Fujita-Miyazawa interaction, yields good baryon well-depths. The ESC16 S=-2 potentials, with kinematical broken SU(3)-symmetry, *i.e.* couplings are SU(3)-symmetric and physical masses for mesons and baryons, provide a basis for realistic calculations in nuclear and hypernuclear physics. For a successful description of the well-depths U_N, U_Λ, U_Σ, and U_Ξ and hypernuclear S=-2 reactions phenomenological additions are needed.
3. YY(S=-3,-4): For these channels, no experimental scattering data exist, apart from the BB-correlations measured at CERN. Also, there is no information from hypernuclei or hyperonic matter. The predictions of the ESC16 model for low-energy parameters and phase shifts for the $S = -3, -4$ BB channels are calculated. No $\Xi\Xi, \Xi\Lambda, \Xi\Sigma$ bound states are predicted by the ESC16 model.
4. Neutron-star: The extension of the ESC-interactions to nucleon-quark and quark-quark channels has been used to study mixed nuclear-quark matter and gives a satisfactory description of the mass M_{NS} and radius R_{NS} of the heavy neutron stars.

Conclusions The ESC approach leads to an excellent description of the NN- and YN-data, and for the scarce YY-data. The added innovations, as well as the treatment of kinematically broken SU(3) make it possible to keep the meson coupling parameters and the $F/(F + D)$-ratios of the model in accordance with the predictions of the $^3P_0$-dominated quark-antiquark pair creation (QPC) model. Therefore, the obtained OBE-couplings and the $F/(F + D)$-ratio's can be well understood in the context of the QPC-model.
The information about estimates of (i) the Λ- and Σ-nuclear well-depth, and (ii) the $\Lambda\Lambda$ hypernuclei played an important role in the form of using constraints. in particular, the experimental indications for the $\Lambda\Lambda$-attraction and the Σ-nuclear well-depth were directive.
Besides the good results for the fit to the NN and YN scattering data, which to a large extent defines the model, the information of hypernuclear systems, using the G-matrix method, is also rather important in establishing the complete ESC-model. Different versions of the model give somewhat different results for hypernuclei. The reported G-matrix calculations are performed for YN (ΛN and ΣN) in nuclear matter and also for some hypernuclei. The obtained well depths (U_Λ, U_Σ, U_Ξ) reveal distinct features of the ESC-model. The inclusion of a quark core Pauli-repulsion can make the Σ-nucleus interaction less attractive, as seems to be required by the available experimental evidence. Furthermore, the ESC16 model gives a small spin-orbit splittings in Λ-hypernuclei, which is also indicated by experiment.

For a detailed description of the hypernuclear S=-2 reactions and the well-depths U_N, U_Λ, U_Σ, and U_Ξ phenomenological "corrections" have been added. These are (i) SU(3)-symmetric short-range Gaussian contact interactions, and (ii) extra three-body forces from meson-pairs (PS-SC, PS-VC, SC-SC, SC-VC, VC-VC, etc.).

Keywords: Soft-core Baryon-Baryon interactions SU(3) symmetry Baryon-Quark mixed-matter Neutron-stars

*Corresponding author
Email address: t.rijken@science.ru.nl (Th.A. Rijken)

Contents

[2] FORTRAN code ESC16/NNPOTESC16, Open-access website, NN-Online: *http://nn-online.org*.

[3] "Adiabatic" approximation: an effective potential between the interacting particles is calculated, neglecting during the exchange of the mesons the motion of the baryons, *i.e.* baryon energy differences are put to zero, see Ref. [26].

1. Introduction

This review of the Extended-soft-core (ESC) baryon-baryon (BB) model [1, 2, 3, 4, 5, 6, 7, 8] on the low and intermediate energy interaction presents the comparison of the theory and scattering data, and its applications to nuclei and hyper-nuclei. Recently, the ESC model has been extended to baryon-quark (BQ) and quark-quark (QQ) interactions, utilizing the connection with the BB-interactions in the constituent quark model (CQM) [9]. The BB-, BQ-, and QQ-interactions have been applied in the Bruckner-Hartree-Fock (BHF) framework to mixed quark-baryon matter calculations for (heavy) neutron stars [10, 11, 12].
The baryons (B) are the ground-state $J^P = \frac{1}{2}^+$ SU(3)-octet members: p,n,Λ, $\Sigma^{0,\pm}$, $\Xi^{0,-}$, characterized by the isospin (I) and strangeness (S). The focus is on the ESC16 model, which is the most recent and complete model published. For the earlier models ESC04 and ESC08, see the review [13].
In the first part a new and complete relativistic derivation of the ESC-model potentials is given within the context of the Kadyshevsky RQFT [14, 15, 16, 17], henceforth denoted as KFT. In the Kadyshevsky formulation of field theory, in contrast to the Feynman formulation, the particles stay on the mass-shell in the intermediate states. The consequence of this is that there is no four-momentum conservation at the vertices. Besides non-conservation of energy, as happens in the Lippmann-Schwinger equation for the intermediate states, there is also non-conservation of the three-momentum, in general. Formally, four-momentum conservation is restored by introducing quasi-particles carrying only four-momentum. The motive for taking the KFT formulation of RQFT as the starting point is that for nucleon-nucleon one has composite particles and not elementary ones. Therefore, a relativistic formulation of a theory using phenomenological (Gaussian) form factors, and the possibility to suppress the transition between positive and negative energy states is feasible in this approach, by introducing phenomenological factors at the vertices, without conflicting relativistic invariance [18].
The derivation of two-meson-exchange (TME) starts from the relativistic two-body equation [19, 20, 21], where the interaction kernel is given by the two-nucleon-irreducible Kadyshevsky graphs. In this paper, the KFT alternative in

the RQFT formulation is used. The relativistic Kadyshevsky two-body equation is analogous to the Bethe-Salpeter equation (BSE) [21], and leads in the center-of-mass system to the Kadyshevsky quasi-potential equation. This is a three-dimensional integral equation similar to the "relativistic" Lippmann-Schwinger [22] and Thompson [23] equation.
In this review, the TPS-exchange potentials are derived using the KFT formulation of RQFT. In momentum space, the connection is established with OBE-exchange, TME-, and MPE-exchange of the ESC-model as derived and applied in [2, 3, 5, 6, 7, 8]. These are originally derived using the Klein-Macke formalism [24, 25, 26]. It is shown that the "adiabatic" and "non-adiabatic" potentials [26], used in the ESC-models, correspond to the interactions from the Kadyshevsky theory.
The Kadyshevsky graphs calculated are the parallel and crossed fourth-order TPS-graphs, as well as the meson pair-exchange (MPE) graphs. In carrying through the analytic derivation of the formulas, a generalization is given of the techniques used in Refs. [26, 29, 30], deriving formulas for the amplitudes where the three-momenta of the two mesons are separated using integral representations. The procedures, indicated above, are first carried out for point-like vertices. Then, the results are generalized for the presence of the Gaussian form factors.
It has to be noted that, in particular the TME and MPE potentials are represented in ESC16 by the (long range) PS-PS potentials only, leaving out contributions with vector, scalar, axial-vector mesons and resonances $\Delta_{33}(1236)$, etc. Adding *e.g.* the complete two-meson exchange potentials would make the fitting much more time-consuming and did not improve the NN- and YN-fit really. The extra TME potentials with vector, scalar, and axial-vector mesons are of a much shorter range than the PS-PS potentials. However, to describe the Ξ correlations in the baryon production experiments at CERN [31] and at RHIC [32], next to the ESC16-model an ESC16$^{(\star)}$-model has been introduced. Here, a phenomenological short-range SU(3)-symmetric attractive contact interaction is added, as a substitute for the missing potentials mentioned above. The fit to the data with ESC16$^{(\star)}$ is qualitatively the same as for ESC16, improving the Ξ correlations and also the Ξ-well depth.

This review consists of two parts:
In part A, the derivation of the ESC-model is reviewed, and the results for the fit to the NN- and YN-data, , the coupling constants, nucleon-nucleon (NN) phase shifts, hyperon-nucleon (YN) and hyperon-hyperon (YY) low-energy parameters, and cross sections. This applies to NN-channels, as well as to YN- and YY-channels with S=-1, -2, -3, and -4.
In part B, the application to mixed nuclear-quark and neutron-star matter is reviewed. Here, the most recent model and results are presented, which show a satisfactory description of the $M_{NS} = 2.1 M_{\odot}$ recently observed heavy neutron star. Due to the repulsive multi-pomeron three-, four-body-, and diquark-exchange repulsion, there is no "hyperon-puzzle".
The content of the sections and appendices is as follows: In section 2 the BB-channels and the first elastic and inelastic thresholds are given. In section 3 and 4 BB-scattering, interactions, and potentials are described using the flavor SU(3)-symmetry formalism. Moreover, the meson-baryon interaction Hamiltonians are given. In section 5 the two-body relativistic Kadyshevsky quasi-equation is derived and its connection with the three-dimensional Thompson and Lippmann-Schwinger equations. In section 6 the partial wave expansion (PWA) for the Kadyshevsky and Lippmann-Schwinger amplitudes are given. In section 7 the Kadyshevsky formulation of the One-Boson-Exchange (OBE) is worked out, and in section 8 this is done for the fourth-order Kadyshevsky graphs. In section 9 two-pseudo-scalar potentials are reviewed in detail for positive-energy intermediate states, and in section 10 similarly for one- and two-pair exchange.
In sections 11 and 12 the nucleon-nucleon (NN) fit of the data and coupling parameters are described. In sections 13 the hyperon-nucleon (YN) results are shown. In section 14 the G-matrix analysis results are described for $\Lambda N, \Sigma N$ and Λ-hypernuclei. In section 15 the hyperon-nucleon (YN) and hyperon-hyperon (YY) channels with strangeness $S = -2$ are reviewed. In particular, the extension of ESC16 to the ESC16$^{(\star)}$ model is described in some detail. In section 16 the hyperon-hyperon (YY) results are given for channels with strangeness $S = -3, -4$.
In section 17 and section 18 the topics neutron-stars (NS), hadronic matter, and mixed nuclear-quark matter are reviewed. Also, a report of the most recent calculations for the heavy neutron-star $M_{NS} \approx 2.1 M_{\odot}$.
In section 19 the general physics background for the ESC-model as embedded in the standard model (SM). Finally, in section 20 the paper is closed with a summary of the important topics, a short overview of the baryon-baryon models in the literature, and future prospects.

In Appendix A the Kadyshevsky rules in momentum-space are given. In Appendix B are shown the 24 orientations of the fermion momenta in the Kadyshevsky graphs for the planar and crossed box graphs. In Appendix C the fourth-order Kadyshevsky graphs with positive energy intermediate fermions in the intermediate states are given. In Appendix D for the fourth-order graphs, the relations between the Kadyshevsky and Klein-Macke potentials, and the adiabatic approximations are given explicitly. The Klein-Macke formalism has been used originally in the ESC-models.) In Appendix E similarly for the one- and two-pair graphs. In Appendix F for completeness, the reduction of the vertices with Dirac-spinors to those for Pauli-spinors is given. In Appendix G ESC16 configuration-space OBE-potentials are given in detail. In Appendix H results from the quark-pair-creation (QPC) model for the coupling constants are given. In Appendix K the topic is a general detailed treatment of the exchange-forces. In particular, attention is given to the treatment of identical particles. In Appendix L the diquark-exchange quark-nucleon interaction is reported, which plays an important role in the mixed nuclear-quark matter model for heavy neutron stars. Finally, in Appendix M a table of acronyms and abbreviations is given.

2. BB-channels and Thresholds

The baryon-baryon channels, with baryons having spin and parity $J^P = \frac{1}{2}^+$, and strangeness $S = 0, -1, -2$, are described as

$$B_a(p_a, s_a) + B_b(p_b, s_b) \to B'_a(p'_a, s'_a) + B'_b(p'_b, s'_b), \tag{2.1}$$

where B and B' denote the baryons, $p_x, s_x (x = a, b)$ denote the momenta and helicities in the initial state. Similarly, B'_a and B'_b, and $p'_y, s'_y (y = a, b)$ for the final state.
Like in Refs. [5, 6] and Refs. [33, 34, 35], for the BB-channels B_a and B'_a are referred to as particles 1 and 3, and to B_b and B'_b as particles 2 and 4. For the kinematics and the definition of the amplitudes, see [3] of this series. Similar material can be found in Refs. [34, 36].

Table 1: Two-baryon channels on the particle basis.

S= 0	:	I= 1, 0
q= +2,+1,0	:	$(pp \to pp), (pn \to pn), (nn \to nn)$.
S=–1	:	I= 3/2, 1/2
q=+2	:	$\Sigma^+ p \to \Sigma^+ p$,
q=+1	:	$(\Lambda p, \Sigma^0 p, \Sigma^+ n) \to (\Lambda p, \Sigma^0 p, \Sigma^+ n)$,
q= 0	:	$(\Lambda n, \Sigma^- p, \Sigma^0 n) \to (\Lambda n, \Sigma^- p, \Sigma^0 n)$,
q=–1	:	$(\Sigma^- n \to \Sigma^- n$.
S=–2	:	I= 2,1,0
q=+2	:	$\Sigma^+\Sigma^+ \to \Sigma^+\Sigma^+$,
q=+1	:	$(\Xi^0 p, \Sigma^+\Lambda, \Sigma^0\Sigma^+) \to (\Xi^0 p, \Sigma^+\Lambda, \Sigma^0\Sigma^+)$,
q= 0	:	$(\Lambda\Lambda, \Xi^0 n, \Xi^- p, \Sigma^0\Lambda, \Sigma^0\Sigma^0, \Sigma^-\Sigma^+) \to (\Lambda\Lambda, \Xi^0 n, \Xi^- p, \Sigma^0\Lambda, \Sigma^0\Sigma^0, \Sigma^-\Sigma^+)$,
q=–1	:	$(\Xi^- n, \Sigma^-\Lambda, \Sigma^-\Sigma^0) \to (\Xi^- n, \Sigma^-\Lambda, \Sigma^-\Sigma^0)$,
q=–2	:	$\Sigma^-\Sigma^- \to \Sigma^-\Sigma^-$.
S=–3	:	I= 3/2, 1/2
q=+1	:	$\Sigma^+\Xi^0 \to \Sigma^+\Xi^0$,
q= 0	:	$(\Lambda\Xi^0, \Sigma^0\Xi^0) \to (\Lambda\Xi^0, \Sigma^0\Xi^0)$,
q=–1	:	$(\Lambda\Xi^-, \Sigma^0\Xi^-, \Sigma^-\Xi^0) \to (\Lambda\Xi^-, \Sigma^0\Xi^-, \Sigma^-\Xi^0)$,
q=–2	:	$(\Sigma^-\Xi^- \to \Sigma^-\Xi^-)$.
S=–4	:	I= 1, 0
q= 0, –1, –2	:	$(\Xi^0\Xi^0 \to \Xi^0\Xi^0), (\Xi^0\Xi^- \to \Xi^0\Xi^-), (\Xi^-\Xi^- \to \Xi^-\Xi^-)$.

In Table 1 the BB-channels are listed according to the strangeness S, electric charge q, and isospin I [4] For further orientation, the thresholds of the (S=0,1,2) BB-channels are drawn in Fig. 1. The low and intermediate interactions can be defined roughly as the interactions in the energy region below the threshold for resonance production and somewhat above the pion production threshold. The following can be noted:

(i) In NN-scattering the first inelastic two-particle are the $N\Delta(1236)$ channel for $I = 1$ with a threshold energy of about 300 MeV in the center-of-mass (CM) system, and the NN'(1470) channel for $I = 0$ with a threshold energy of about 530 MeV in the CM-system. These inelastic two-particle channels in NN scattering have a rather high threshold. The $NN\pi$-threshold is 140 MeV, but the coupling to $NN\pi$ is rather weak.

(ii) The first inelastic two-particle threshold in the ΛN-channel is the ΣN-threshold, which appears at 80 MeV in the CM-system. Therefore, a realistic description of the low-energy ΛN interaction must take into account these coupled ΛN and ΣN channels. The next BB-thresholds occur at the opening of the $NY_1^*(1385)$, $\Lambda\Delta(1236)$, $NY_0^*(1405)$, and $\Sigma\Delta(1236)$ channels. These are all high up and therefore are not taken into account in the Nijmegen BB-models.

(iii) For the Y=0 channels the thresholds of the different $B(1/2^+)B(1/2^+)$ and $B(1/2^+)B(3/2^+)$ channels are rather spread out in energy. The choice of channels to take into account is less clear.

In Fig. 1 for the S=-2 YN,YY channels the beam momenta p_{Lab} at the thresholds are shown in MeV/c. Here, the beam particles are Λ, Ξ, Σ. Similarly, in Fig. 2 and Fig. 3 the threshold momenta for the YY-channels with S=-2 and S=-3,-4, respectively.

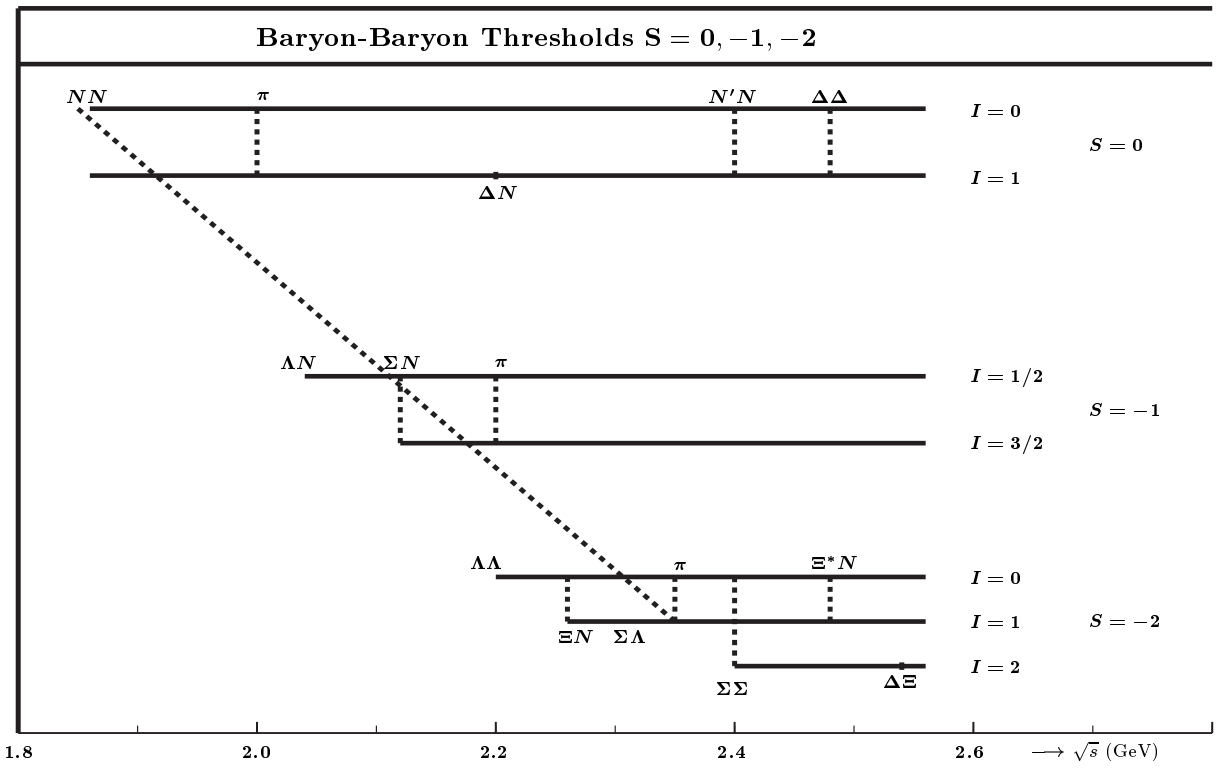

Figure 1: Thresholds in NN- and YN-channels for strangeness S=0,-1,-2. $\sqrt{s}$ is the total energy in the CM-system.

[4]The isospin is denoted by I. In some sections the nuclear physics notation T is used for the isospin.

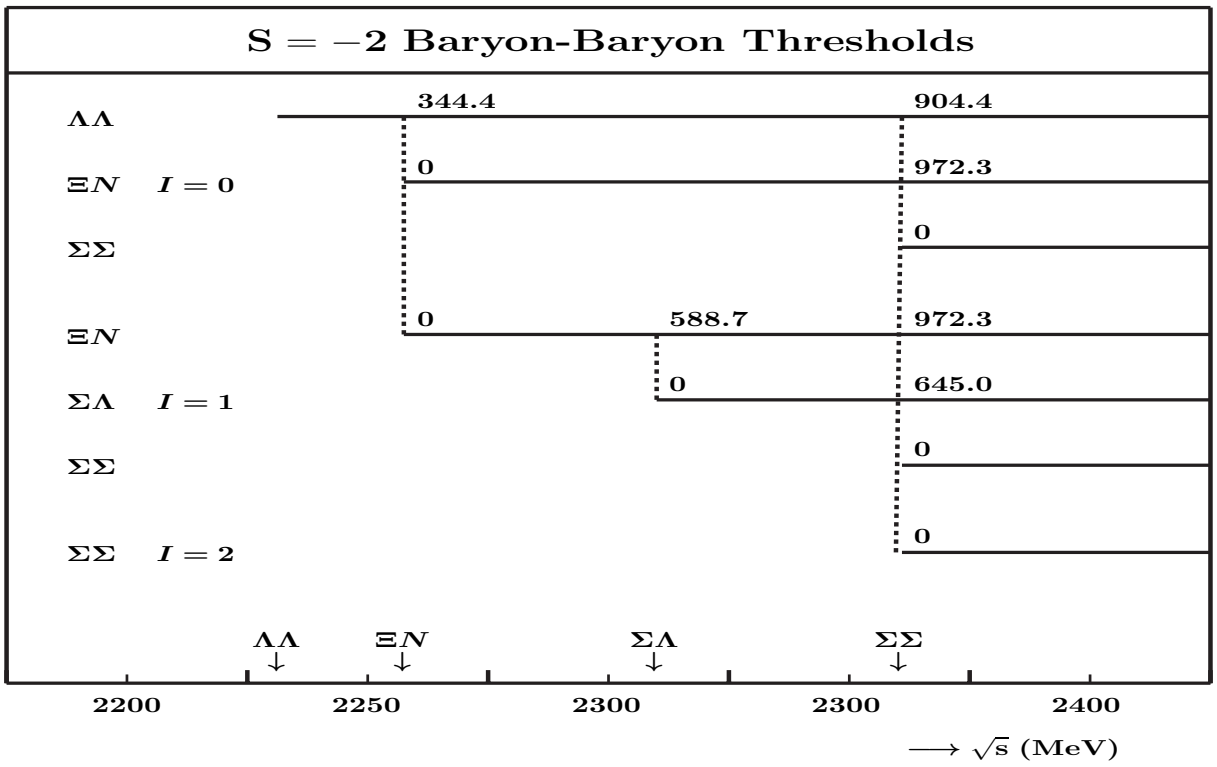

Figure 2: Thresholds in YN- and YY-channels for S=-2. $\sqrt{s}$ is the total energy in the CM-system. p_Λ, p_Σ, and p_Ξ are the CM-momenta in MeV/c.

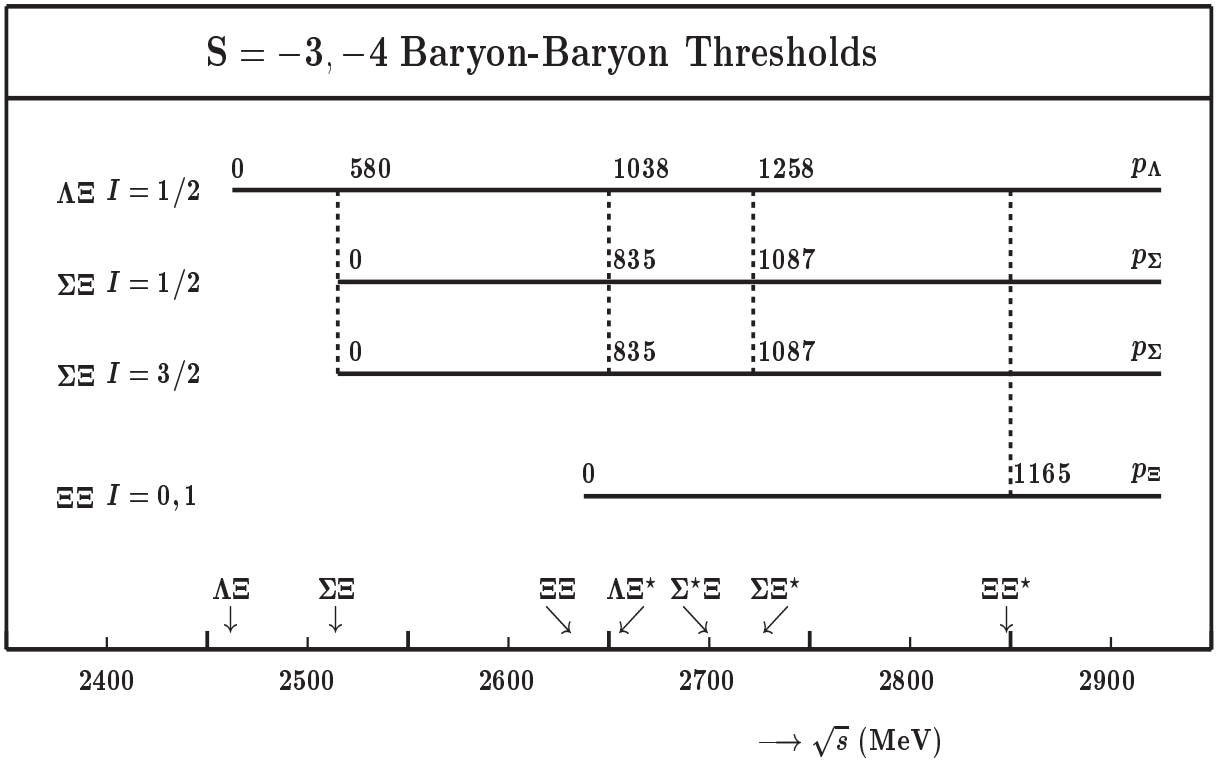

Figure 3: Thresholds in YY-channels for S=-3,-4 $\sqrt{s}$ is the total energy in the CM-system

3. Baryon-Baryon Scattering and SU(3) symmetry

3.1. Baryon-Baryon states and SU(3)-irreps

The baryons considered in this review are the members of the $J^P = \frac{1}{2}^+$ baryon octet $\{8\}$. Then, BB-scattering occurs in the SU(3)-basis in the $\{8\} \otimes \{8\}$ channels. Expanding in the irreducible SU(3) representations (irreps), see [37], one has

$$\{8\} \otimes \{8\} = \{27\} \oplus \{10\} \oplus \{10\}^* \oplus \{8_s\} \oplus \{8_a\} \oplus \{1\}. \tag{3.1}$$

The irreps on the r.h.s. in (3.1) are called the SU(3) eigenchannels, since in the case of exact SU(3) symmetry there will be no transitions between these channels. The inelastic two-particle channels to which these could be coupled with the lowest thresholds are the $[8] \otimes \{10\}$ and $\{8\} \otimes \{1\}$ channels. In terms of eigenchannels, one has [37]

$$\{8\} \otimes \{10\} = \{35\} \oplus \{27\} \oplus \{10\} \oplus \{8\}, \ \{8\} \otimes \{1\} = \{8\}, \tag{3.2}$$

which means that resonances in the channels $\{27\}, \{10\}$, or $\{8\}$ could be produced by strong forces in these inelastic channels.

Table 2: SU(3) content of the different BB-channels. S is the total strangeness and I is the isospin. The upper half refers to the space-spin symmetric states ${}^3S_1, {}^1P_1, {}^3D, \ldots$, while the lower half refers to the space-spin anti-symmetric states ${}^1S_0, {}^3P, {}^1D_2, \ldots$

Space-spin symmetric				Space-spin anti-symmetric			
S	I	Channels	SU(3)-irreps	S	I	Channels	SU(3)-irreps
0	0	NN	$\{10^*\}$	0	1	NN	$\{27\}$
–1	1/2	$\Lambda N, \Sigma N$	$\{10^*\}, \{8\}_a$	–1	1/2	$\Lambda N, \Sigma N$	$\{27\}, \{8\}_s$
	3/2	ΣN	$\{10\}$		3/2	ΣN	$\{27\}$
–2	0	ΞN	$\{8\}_a$	–2	0	$\Lambda\Lambda, \Xi N, \Sigma\Sigma$	
	1	$\Xi N, \Sigma\Sigma$	$\{10\}, \{10^*\}, \{8\}_a$		1	$\Xi N, \Sigma\Lambda$	$\{27\}, \{8\}_s$
		$\Sigma\Lambda$	$\{10\}, \{10^*\}$		2	$\Sigma\Sigma$	$\{27\}$
–3	1/2	$\Xi\Lambda, \Xi\Sigma$	$\{10\}, \{8\}_a$	–3	1/2	$\Xi\Lambda, \Xi\Sigma$	$\{27\}, \{8\}_s$
	3/2	$\Xi\Sigma$	$\{10^*\}$		3/2	$\Xi\Sigma$	$\{27\}$
–4	0	$\Xi\Xi$	$\{10\}$	–4	1	$\Xi\Xi$	$\{27\}$

The baryons are fermions and the total wave functions of the $\{8\} \otimes \{8\}$-states are anti-symmetric. In Table 2 the SU(3) content of the BB-states is listed both for the space-spin symmetric and anti-symmetric partial waves.
As is well known SU(3) is not an exact symmetry. Sources of SU(3)-breaking are (i) kinematic breaking by using the physical masses of the baryons, (ii) dynamically breaking by using physical masses and mixing [37] in the meson-exchange potentials, and (iii) taking into account the Coulomb interactions between charged baryons.

In the Nijmegen work on baryon-baryon interactions, flavor SU(3)-symmetry of the interactions is the most important working hypothesis. The other important dynamical symmetry is chiral-symmetry (CS). In the ESC model the non-linear realization has been chosen [38, 39]. In the non-linear realization of chiral-symmetry, for the couplings of the scalar-, vector-, axial-vector mesons, and pair-interactions SU(3) symmetry is sufficient [39, 40]. As the peudoscalar mesons are concerned, one-pion and two-pion exchange has been included in ESC.

3.2. Interaction Hamiltonian, Baryon-octet presentation and SU(2)-isospin States

The SU(3)-invariant interaction Hamiltonian for the baryon-baryon (BB) pseudoscalar (P) meson interaction reads [37]

$$\mathcal{H}_I \quad = \quad g_{P,8}\sqrt{2}\Big\{\alpha_P\left[\bar{B}BP\right]_F + (1-\alpha_P)\left[\bar{B}BP\right]_D\Big\} + g_{P,1}\left[\bar{B}BP\right]_S . \tag{3.3}$$

Here, the baryons are the members of the $J^P = \frac{1}{2}^+$ baryon octet, which are represented by the traceless Gell-Mann matrices $B(8) = \sum_{i=1}^{8} B_i\lambda_i/\sqrt{2}$. Explicitly,

$$B(8) = \begin{pmatrix} \frac{\Sigma^0}{\sqrt{2}} + \frac{\Lambda}{\sqrt{6}} & \Sigma^+ & p \\ \Sigma^- & -\frac{\Sigma^0}{\sqrt{2}} + \frac{\Lambda}{\sqrt{6}} & n \\ -\Xi^- & \Xi^0 & -\frac{2\Lambda}{\sqrt{6}} \end{pmatrix}. \tag{3.4}$$

Similar to (3.4) the nonets M(9) for the pseudoscalar, vector, scalar, and axial-vector mesons can be represented by (i) the traceless matrices $M(8) = \sum_{i=1}^{8} M_i\lambda_i/\sqrt{2}$, and (ii) the unitary singlet mesons M(0) are included via the definition

$$M^\alpha_\beta(9) = M^\alpha_\beta(8) + \delta^\alpha_\beta M(0)/\sqrt{3}. \tag{3.5}$$

For the assignment of the meson fields M_i and the Gell-Mann matrices λ_i see [37]. Taking the pseudoscalar mesons with $J^P = 0^-$ as a specific example, the nonet is written as $P(9) = P(8) + P(0)$ where the singlet matrix $P(0)$ has $\eta_0/\sqrt{3}$ on the diagonal, and the octet matrix $P(8)$ is given explicitly by

$$P(8) = \begin{pmatrix} \frac{\pi^0}{\sqrt{2}} + \frac{\eta_8}{\sqrt{6}} & \pi^+ & K^+ \\ \pi^- & -\frac{\pi^0}{\sqrt{2}} + \frac{\eta_8}{\sqrt{6}} & K^0 \\ K^- & \overline{K^0} & -\frac{2\eta_8}{\sqrt{6}} \end{pmatrix}. \tag{3.6}$$

Here, η_8 and η_0 are the 'bare' SU(3) octet and singlet states, respectively, and the physical $\eta(448), \eta'(958)$ are mixtures of the bare ones.
Similarly the interaction with the vector $J^{PC} = 1^{--}$, scalar $J^{PC} = 0^{++}$, axial-vectors $J^{PC} = 1^{++}$ and $J^{PC} = 1^{+-}$ mesons. The $SU(3)$ octet and singlet mesons, denoted by the subscript 8 respectively 1 are, in terms of the physical ones and the mixing angles θ, defined as follows:

$$J^{PC} = 0^{-+} \quad : \quad \eta_1 = \cos\theta_{PS}\eta' - \sin\theta_{PS}\eta, \quad \eta_8 = \sin\theta_{PS}\eta' + \cos\theta_{PS}\eta, \tag{3.7a}$$
$$J^{PC} = 1^{--} \quad : \quad \phi_1 = \cos\theta_V\omega - \sin\theta_V\phi, \quad \phi_8 = \sin\theta_V\omega + \cos\theta_V\phi, \tag{3.7b}$$
$$J^{PC} = 0^{++} \quad : \quad \epsilon_1 = \cos\theta_S f_0 - \sin\theta_S f_0', \quad \epsilon_8 = \sin\theta_S f_0 + \cos\theta_S f_0', \tag{3.7c}$$
$$J^{PC} = 1^{++} \quad : \quad A_1 = \cos\theta_A f_1 - \sin\theta_A f_1', \quad A_8 = \sin\theta_A f_1 + \cos\theta_A f_1', \tag{3.7d}$$
$$J^{PC} = 1^{+-} \quad : \quad B_1 = \cos\theta_B h_1 - \sin\theta_B h_1', \quad B_8 = \sin\theta_B h_1 + \cos\theta_B h_1'. \tag{3.7e}$$

Here, η', η are the physical pseudo-scalar mesons $\eta(957), \eta(548), \phi, \omega$ are the physical vector mesons $\phi(1019), \omega(783)$, and f_0, f_0' are the physical scalar mesons $\epsilon(620), S^*(993)$. For the axial mesons the physical mesons are $f_1(1420), f_1'(1285)$, and $h_1(1380), h_1'(1170)$. For the actually used masses in the ESC16 models, see Table 9.

Using the isodoublets,

$$N = \begin{pmatrix} p \\ n \end{pmatrix}, \quad \Xi = \begin{pmatrix} \Xi^0 \\ \Xi^- \end{pmatrix}, \quad K = \begin{pmatrix} K^+ \\ K^0 \end{pmatrix}, \quad K_c = \begin{pmatrix} \overline{K^0} \\ -K^- \end{pmatrix}, \tag{3.8}$$

the SU(3) invariant interaction Hamiltonian for pseudoscalar mesons, omitting the Lorentz structure, reads given by the interaction Hamiltonian [37]

$$\begin{aligned} \mathcal{H}_I^{\rm oct} = \; & g_{NN\pi}(\overline{N}\boldsymbol{\tau}N)\cdot\boldsymbol{\pi} - ig_{\Sigma\Sigma\pi}(\overline{\boldsymbol{\Sigma}}\times\boldsymbol{\Sigma})\cdot\boldsymbol{\pi} + g_{\Lambda\Sigma\pi}(\overline{\Lambda}\boldsymbol{\Sigma} + \overline{\boldsymbol{\Sigma}}\Lambda)\cdot\boldsymbol{\pi} + g_{\Xi\Xi\pi}(\overline{\Xi}\boldsymbol{\tau}\Xi)\cdot\boldsymbol{\pi} + \\ & g_{\Lambda NK}\left[(\overline{N}K)\Lambda + \overline{\Lambda}(\overline{K}N)\right] + g_{\Xi\Lambda K}\left[(\overline{\Xi}K_c)\Lambda + \overline{\Lambda}(\overline{K_c}\Xi)\right] + \\ & g_{\Sigma NK}\left[\overline{\boldsymbol{\Sigma}}\cdot(\overline{K}\boldsymbol{\tau}N) + (\overline{N}\boldsymbol{\tau}K)\cdot\boldsymbol{\Sigma}\right] + g_{\Xi\Sigma K}\left[\overline{\boldsymbol{\Sigma}}\cdot(\overline{K_c}\boldsymbol{\tau}\Xi) + (\overline{\Xi}\boldsymbol{\tau}K_c)\cdot\boldsymbol{\Sigma}\right] + \\ & g_{NN\eta_8}(\overline{N}N)\eta_8 + g_{\Lambda\Lambda\eta_8}(\overline{\Lambda}\Lambda)\eta_8 + g_{\Sigma\Sigma\eta_8}(\overline{\boldsymbol{\Sigma}}\cdot\boldsymbol{\Sigma})\eta_8 + g_{\Xi\Xi\eta_8}(\overline{\Xi}\Xi)\eta_8 + \\ & g_{NN\eta_0}(\overline{N}N)\eta_0 + g_{\Lambda\Lambda\eta_0}(\overline{\Lambda}\Lambda)\eta_0 + g_{\Sigma\Sigma\eta_0}(\overline{\boldsymbol{\Sigma}}\cdot\boldsymbol{\Sigma})\eta_0 + g_{\Xi\Xi\eta_0}(\overline{\Xi}\Xi)\eta_0. \end{aligned} \tag{3.9}$$

For the other mesons the octet matrix is obtained by the following substitutions: (i) vector mesons $\pi \to \rho, \eta_8 \to \phi_8$, $K \to K^*$, (ii) scalar $\pi \to a_0, \eta_8 \to \varepsilon_8, K \to \kappa$, (iii) axial(A) ($\pi \to a_1, \eta_8 \to A_8, K \to K_{1A}$, (iv) axial(B) $\pi \to b_1$, $\eta_8 \to B_8, K \to K_{1B}$. Similarly $\mathcal{H}_I^{singlet}$ for the SU(3)-singlet mesons.

All coupling constants for the physical mesons can be expressed in terms of three SU(3) parameters: (i) singlet and octet couplings (f_1, f_8) respectively, and (ii) the F/(F+D)-ratio α_P. For details, in particular the explicit formula for the couplings as a function of the F/(F+D)-ratio, see *e.g.* Refs. [35, 37]. The same applies to the nonets of the vector, scalar, and axial-vector mesons. Meson-mixing [41] is an important ingredient to describe the meson spectra and is included in the models. The pomeron and odderon are treated as SU(3)-singlets.

3.3. MPE-interactions and SU(3)-symmetry

In the ESC work, only the one-pair graphs are included, *i.e.* only pair-exchange potentials linear in the pair-coupling constants. The argument for neglecting the two-pair graph is to avoid some 'double-counting'. For example, the $\pi\pi$-pair exchange is (partly) taken into account by the broad ρ- and ϵ-exchange. Viewing the pair-vertex as containing heavy-meson exchange means that the contributions from $\rho(750)$ and $\epsilon = f_0(620)$ to the two-pair graphs is already accounted for by our treatment of the broad ρ and ϵ OBE-potential. For a more complete discussion of the physics behind MPE, see Refs. [1, 29, 30]. The MPE-potentials for nucleon-nucleon have been given in Refs. [29, 30]. The generalization to baryon-baryon is similar to that for the TPS-potentials. This means that threshold differences between the initial, intermediate, and final states are neglected. This because, although in principle possible, it complicates the computation of the potentials considerably. For a proper appreciation of the physics, it is useful to scale the phenomenological meson-pair baryon-baryon interaction Hamiltonian's different from the originally used scalings [29, 30]. Below, $\sigma, \mathbf{a}_0, \mathbf{A}_1, \ldots$ are short-hands for respectively the nucleon densities $\bar\psi\psi$, $\bar\psi\boldsymbol{\tau}\psi$, $\bar\psi\gamma_5\gamma_\mu\boldsymbol{\tau}\psi, \ldots$.

The $SU(3)$-invariant pair-interaction Hamiltonian's is [3]: 1. $SU(3)$-singlet couplings $S^\alpha_\beta = \delta^\alpha_\beta\sigma/\sqrt{3}$:

$$\mathcal{H}_{S_1PP} = \frac{g_{S_1PP}}{\sqrt{3}}\left\{\boldsymbol{\pi}\cdot\boldsymbol{\pi} + 2K^\dagger K + \eta_8\eta_8\right\}\cdot\sigma \tag{3.10}$$

2. $SU(3)$-octet symmetric couplings I, $S^\alpha_\beta = (S_8)^\alpha_\beta \Rightarrow (1/4)Tr\{S[P,P]_+\}$:

$$\begin{aligned}\mathcal{H}_{S_8PP} &= \frac{g_{S_8PP}}{\sqrt{6}}\Big[(\mathbf{a}_0\cdot\boldsymbol{\pi})\eta_8 + \frac{\sqrt{3}}{2}\mathbf{a}_0\cdot(K^\dagger\boldsymbol{\tau}K) + \frac{\sqrt{3}}{2}\left\{(K_0^\dagger\boldsymbol{\tau}K)\cdot\boldsymbol{\pi} + h.c.\right\}\\ &- \frac{1}{2}\left\{(K_0^\dagger K)\eta_8 + h.c.\right\} + \frac{1}{2}f_0\left(\boldsymbol{\pi}\cdot\boldsymbol{\pi} - K^\dagger K - \eta_8\eta_8\right)\Big].\end{aligned} \tag{3.11}$$

3. $SU(3)$-octet symmetric couplings II, $S^\alpha_\beta = (B_8)^\alpha_\beta \Rightarrow (1/4)Tr\{B^\mu[V_\mu, P]_+\}$:

$$\begin{aligned}\mathcal{H}_{B_8VP} &= \frac{g_{B_8VP}}{\sqrt{6}}\Big\{\frac{1}{2}\left[\left(\mathbf{B}_1^\mu\cdot\boldsymbol{\rho}_\mu\right)\eta_8 + \left(\mathbf{B}_1^\mu\cdot\boldsymbol{\pi}_\mu\right)\phi_8\right] + \frac{\sqrt{3}}{4}\left[\mathbf{B}_1\cdot(K^{*\dagger}\boldsymbol{\tau}K) + h.c.\right]\\ &+ \frac{\sqrt{3}}{4}\left[(K_1^\dagger\boldsymbol{\tau}K^*)\cdot\boldsymbol{\pi} + (K_1^\dagger\boldsymbol{\tau}K)\cdot\boldsymbol{\rho} + h.c.\right] - \frac{1}{4}\left[(K_1^\dagger\cdot K^*)\eta_8 + (K_1^\dagger\cdot K)\phi_8 + h.c.\right]\\ &+ \frac{1}{2}H^0\left[\boldsymbol{\rho}\cdot\boldsymbol{\pi} - \frac{1}{2}\left(K^{*\dagger}\cdot K + h.c.\right) - \phi_8\eta_8\right]\Big\}.\end{aligned} \tag{3.12}$$

4. $SU(3)$-octet a-symmetric couplings III, $A^\alpha_\beta = (V_8)^\alpha_\beta \Rightarrow (-i/\sqrt{2})Tr\{V^\mu[P, \partial_\mu P]_-\}$:

$$\begin{aligned}\mathcal{H}_{V_8PP} &= g_{A_8PP}\Big\{\frac{1}{2}\boldsymbol{\rho}_\mu\cdot\boldsymbol{\pi}\times\overleftrightarrow{\partial^\mu}\boldsymbol{\pi} + \frac{i}{2}\boldsymbol{\rho}_\mu\cdot(K^\dagger\boldsymbol{\tau}\overleftrightarrow{\partial^\mu}K) + \frac{i}{2}\left(K^{*\dagger}_\mu\boldsymbol{\tau}(K\overleftrightarrow{\partial^\mu}\boldsymbol{\pi}) - h.c.\right)\\ &+ i\frac{\sqrt{3}}{2}\left(K^{*\dagger}_\mu\cdot(K\cdot\overleftrightarrow{\partial^\mu}\eta_8) - h.c.\right) + \frac{i}{2}\sqrt{3}\phi_\mu(K^\dagger\overleftrightarrow{\partial^\mu}K)\Big\}.\end{aligned} \tag{3.13}$$

5. $SU(3)$-octet a-symmetric couplings IV, $A^\alpha_\beta = (A_8)^\alpha_\beta \Rightarrow (-i/\sqrt{2})Tr\{A^\mu[P, V_\mu]_-\}$:

$$\begin{aligned}\mathcal{H}_{A_8VP} &= g_{A_8VP}\Big\{ \mathbf{A}_1\cdot\boldsymbol{\pi}\times\boldsymbol{\rho} + \frac{i}{2}\mathbf{A}_1\cdot\Big[(K^\dagger\boldsymbol{\tau}K^*) - (K^{*\dagger}\boldsymbol{\tau}K)\Big] \\ &- \frac{i}{2}\Big(\Big[(K^\dagger\boldsymbol{\tau}K_A)\cdot\boldsymbol{\rho} + (K_A^\dagger\boldsymbol{\tau}K^*)\cdot\boldsymbol{\pi}\Big] - h.c.\Big) - i\frac{\sqrt{3}}{2}\Big(\Big[(K^\dagger\cdot K_A)\phi_8 + (K_A^\dagger\cdot K^*)\eta_8\Big] - h.c.\Big) \\ &+ \frac{i}{2}\sqrt{3}f_1\Big[K^\dagger\cdot K^* - K^{*\dagger}\cdot K\Big]\Big\}. \end{aligned} \tag{3.14}$$

The relation with the pair-couplings of [2, 3] is $g_{S_1PP}/\sqrt{3} = g_{(\pi\pi)_0}/m_\pi$, $g_{A_8VP} = g_{(\pi\rho)_1}/m_\pi$ etc.

3.4. Potentials on the Isospin-basis

1. Y=2, S=0 channels: the NN-channels are pp, np, and nn, with the isospins I=0,1.
2. Y=1, S=-1 channels: On the physical particle basis, there are four charge channels:

$$\begin{aligned} q = +2: &\quad \Sigma^+p \to \Sigma^+p, \\ q = +1: &\quad (\Lambda p, \Sigma^+n, \Sigma^0p) \to (\Lambda p, \Sigma^+n, \Sigma^0p), \\ q = \ 0: &\quad (\Lambda n, \Sigma^0n, \Sigma^-p) \to (\Lambda n, \Sigma^0n, \Sigma^-p), \\ q = -1: &\quad \Sigma^-n \to \Sigma^-n. \end{aligned} \tag{3.15}$$

Like in Refs. [34, 35], the potentials are calculated on the isospin basis. For $S = -1$ hyperon-nucleon systems there are only two isospin channels: (i) $I = \frac{1}{2}:\ (\Lambda N, \Sigma N \to \Lambda N, \Sigma N)$, and (ii) $I = \frac{3}{2}:\ \Sigma N \to \Sigma N$. Obviously, the potential on the particle basis for the $q = 2$ and $q = -1$ channels are given by the $I = \frac{3}{2}$ ΣN potential on the isospin basis. For $q = 1$ and $q = 0$, the potentials are related to the potentials on the isospin basis by an isospin rotation. Using a notationlisting only the hyperons [$V_{\Lambda\Sigma^+} = (\Lambda p|V|\Sigma^+n)$, etc.], for $q = 1$

$$V(q=1) = \begin{pmatrix} V_{\Lambda\Lambda} & \sqrt{\frac{2}{3}}V_{\Lambda\Sigma} & -\sqrt{\frac{1}{3}}V_{\Lambda\Sigma} \\ \sqrt{\frac{2}{3}}V_{\Sigma\Lambda} & \frac{2}{3}V_{\Sigma\Sigma}(\frac{1}{2}) + \frac{1}{3}V_{\Sigma\Sigma}(\frac{3}{2}) & \frac{\sqrt{2}}{3}\Big[V_{\Sigma\Sigma}(\frac{3}{2}) - V_{\Sigma\Sigma}(\frac{1}{2})\Big] \\ -\sqrt{\frac{1}{3}}V_{\Sigma\Lambda} & \frac{\sqrt{2}}{3}\Big[V_{\Sigma\Sigma}(\frac{3}{2}) - V_{\Sigma\Sigma}(\frac{1}{2})\Big] & \frac{1}{3}V_{\Sigma\Sigma}(\frac{1}{2}) + \frac{2}{3}V_{\Sigma\Sigma}(\frac{3}{2}) \end{pmatrix}, \tag{3.16}$$

while for $q = 0$

$$V(q=0) = \begin{pmatrix} V_{\Lambda\Lambda} & \sqrt{\frac{1}{3}}V_{\Lambda\Sigma} & -\sqrt{\frac{2}{3}}V_{\Lambda\Sigma} \\ \sqrt{\frac{1}{3}}V_{\Sigma\Lambda} & \frac{1}{3}V_{\Sigma\Sigma}(\frac{1}{2}) + \frac{2}{3}V_{\Sigma\Sigma}(\frac{3}{2}) & \frac{\sqrt{2}}{3}\Big[V_{\Sigma\Sigma}(\frac{3}{2}) - V_{\Sigma\Sigma}(\frac{1}{2})\Big] \\ -\sqrt{\frac{2}{3}}V_{\Sigma\Lambda} & \frac{\sqrt{2}}{3}\Big[V_{\Sigma\Sigma}(\frac{3}{2}) - V_{\Sigma\Sigma}(\frac{1}{2})\Big] & \frac{2}{3}V_{\Sigma\Sigma}(\frac{1}{2}) + \frac{1}{3}V_{\Sigma\Sigma}(\frac{3}{2}) \end{pmatrix}. \tag{3.17}$$

3. Y=0, S=-2 channels: The I=2 state is $|\Sigma\Sigma\rangle$, and the three I=1 states are $|\Lambda\Sigma\rangle, |\Sigma\Sigma\rangle$, and $|N\Xi(0)\rangle$. The four I=0 states are $|\Lambda\Lambda\rangle, |\Sigma\Sigma\rangle, |\Xi N(0)\rangle$, and $|N\Xi(0)\rangle$. Choosing the same ordering, the potential written as a 3×3-matrix reads

$$V(q=0) = \begin{pmatrix} (\Lambda\Lambda|V|\Lambda\Lambda) & (\Lambda\Lambda|V|\Xi N) & (\Lambda\Lambda|V|N\Xi) \\ (\Xi N|V|\Lambda\Lambda) & (\Xi N|V|\Xi N) & (\Xi N|V|N\Xi) \\ (N\Xi|V|\Lambda\Lambda) & (N\Xi|V|\Xi N) & (N\Xi|V|N\Xi) \end{pmatrix}. \tag{3.18}$$

With a similar notation for the T-matrix, the Lippmann-Schwinger equation can be written compactly as a 3×3-matrix equation:

$$T = V + V\,G\,T\ ,\ \text{with}\ G_{ij} = G_i\,\delta_{ij}\ . \tag{3.19}$$

Next, a transformation to states is made, which are either symmetric or anti-symmetric for particle interchange. Then, see Appendix K Eqn. (K.7), one can separate them in the Lippmann-Schwinger equation. This is achieved by the transformation of the T-matrix and the V-matrix to the new base states

$$\begin{pmatrix} \Lambda\Lambda \\ \Xi N \\ N\Xi \end{pmatrix} \Rightarrow \begin{pmatrix} \Lambda\Lambda \\ (\Xi N + N\Xi)/\sqrt{2} \\ (\Xi N - N\Xi)/\sqrt{2} \end{pmatrix}. \tag{3.20}$$

The details are worked out in Appendix K. This in particular for the case of a mixture of non-identical and identical YN-states. The results for the isospin factors for the S=-2 channels are given in Table 3.

Table 3: Meson-exchange isospin factors for the YN and YY elastic and inelastic channels with strangeness S=-2 and isospin I. P_f is the flavor-exchange operator. The $I = 2$ occurs only in the $S = -2$ $\Sigma\Sigma$ channels, where the isospin factors are given by $(\Sigma\Sigma|\eta, \eta', \pi|\Sigma\Sigma) = \frac{1}{2}(1 + P_f)$.

$S = -2$	$I = 0$	$I = 1$
$(\Lambda\Lambda\|\eta, \eta'\|\Lambda\Lambda)$	$\frac{1}{2}(1 + P_f)$	—
$(\Xi N\|\eta, \eta'\|\Xi N)$	$\frac{1}{2}(1 + P_f)$	1
$(\Sigma\Sigma\|\eta, \eta'\|\Sigma\Sigma)$	$\frac{1}{2}(1 + P_f)$	$\frac{1}{2}(1 - P_f)$
$(\Sigma\Lambda\|\eta, \eta'\|\Sigma\Lambda)$	—	1
$(\Xi N\|\pi\|\Xi N)$	-3	1
$(\Sigma\Sigma\|\pi\|\Sigma\Sigma)$	$-(1 + P_f)$	$-\frac{1}{2}(1 - P_f)$
$(\Lambda\Lambda\|\pi\|\Sigma\Sigma)$	$-\frac{1}{2}\sqrt{3}(1 + P_f)$	—
$(\Sigma\Lambda\|\pi\|\Lambda\Sigma)$	—	P_f
$(\Sigma\Sigma\|\pi\|\Sigma\Lambda)$	—	$(1 - P_f)$
$(\Lambda\Lambda\|K\|\Xi N)$	$1 + P_f$	—
$(\Sigma\Sigma\|K\|\Xi N)$	$\sqrt{3}(1 + P_f)$	$\sqrt{2}(1 - P_f)$
$(\Xi N\|K\|\Sigma\Lambda)$	—	$\sqrt{2}; -P_f\sqrt{2}$

4. Y=-1,-2, S=-3,-4 channels: In Table 4 the relation between the potentials on the isospin-basis is given, see (3.16)-(3.17), and the SU(3)-irreps. Here $V_{\Xi\Xi} = V_{\Xi\Xi,\Xi\Xi}$, $V_{\Lambda\Lambda} = V_{\Lambda\Xi,\Lambda\Xi}$ etc.
Obviously, the potentials on the particle basis for the $Y = -2$ channels are given by the $I = 0, 1$ $\Xi\Xi$-potential

Table 4: SU(3)-contents of the various potentials on the isospin basis.

Space-spin anti-symmetric states ${}^1S_0,\ {}^3P,\ {}^1D_2, ...$		
$\Xi\Xi \to \Xi\Xi$	$Y = -2, I = 1$	$V_{\Xi\Xi}(I = 1) = V_{27}$
$\Lambda\Xi \to \Lambda\Xi$		$V_{\Lambda\Lambda}\left(I = \frac{1}{2}\right) = (9V_{27} + V_{8_s})/10$
$\Lambda\Xi \to \Sigma\Xi$	$Y = -1, I = \frac{1}{2}$	$V_{\Sigma\Lambda}\left(I = \frac{1}{2}\right) = (-3V_{27} + 3V_{8_s})/10$
$\Sigma\Xi \to \Sigma\Xi$		$V_{\Sigma\Sigma}\left(I = \frac{1}{2}\right) = (V_{27} + 9V_{8_s})/10$
$\Sigma\Xi \to \Sigma\Xi$	$Y = -1, I = \frac{3}{2}$	$V_{\Sigma\Sigma}\left(I = \frac{3}{2}\right) = V_{27}$
Space-spin symmetric states ${}^3S_1,\ {}^1P_1,\ {}^3D, ...$		
$\Xi\Xi \to \Xi\Xi$	$Y = -2, I = 0$	$V_{\Xi\Xi}(I = 0) = V_{10}$
$\Lambda\Xi \to \Lambda\Xi$		$V_{\Lambda\Lambda}\left(I = \frac{1}{2}\right) = (V_{10} + V_{8_a})/2$
$\Lambda\Xi \to \Sigma\Xi$	$Y = -1, I = \frac{1}{2}$	$V_{\Sigma\Lambda}\left(I = \frac{1}{2}\right) = (V_{10} - V_{8_a})/2$
$\Sigma\Xi \to \Sigma\Xi$		$V_{\Sigma\Sigma}\left(I = \frac{1}{2}\right) = (V_{10} + V_{8_a})/2$
$\Sigma\Xi \to \Sigma\Xi$	$Y = -1, I = \frac{3}{2}$	$V_{\Sigma\Sigma}\left(I = \frac{3}{2}\right) = V_{10^\star}$

on the isospin basis. For $Y = -1$ channels the potentials are related to the potentials on the isospin basis by an

isospin rotation. Ordering the channels in the $q = 0$ sector according to increasing rest mass $(\Lambda\Xi^0, \Sigma^0\Xi^0, \Sigma^+\Xi^-)$ one obtains in channel space the potential matrix , $V_{ab}(I) \equiv V_{a,\Xi;b,\Xi}(I)$, with $a, b \equiv \Lambda, \Sigma$,

$$V(q=0, Y=-1) = \begin{pmatrix} V_{\Lambda\Lambda}(\frac{1}{2}) & -\sqrt{\frac{1}{3}}V_{\Lambda\Sigma} & \sqrt{\frac{2}{3}}V_{\Lambda\Sigma} \\ -\sqrt{\frac{1}{3}}V_{\Lambda\Sigma} & \frac{1}{3}\left[V_{\Sigma\Sigma}(\frac{1}{2}) + 2V_{\Sigma\Sigma}(\frac{3}{2})\right] & \frac{\sqrt{2}}{3}\left[-V_{\Sigma\Sigma}(\frac{1}{2}) + V_{\Sigma\Sigma}(\frac{3}{2})\right] \\ \sqrt{\frac{2}{3}}V_{\Lambda\Sigma} & \frac{\sqrt{2}}{3}\left[-V_{\Sigma\Sigma}(\frac{1}{2}) + V_{\Sigma\Sigma}(\frac{3}{2})\right] & \frac{1}{3}\left[2V_{\Sigma\Sigma}(\frac{1}{2}) + V_{\Sigma\Sigma}(\frac{3}{2})\right] \end{pmatrix}, \tag{3.21}$$

and for $q = -1$ the ordering is $(\Lambda\Xi^-, \Sigma^-\Xi^0, \Sigma^0\Xi^-)$, and the potential matrix reads

$$V(q=-1, Y=-1) = \begin{pmatrix} V_{\Lambda\Lambda}(\frac{1}{2}) & -\sqrt{\frac{2}{3}}V_{\Lambda\Sigma} & \sqrt{\frac{1}{3}}V_{\Lambda\Sigma} \\ -\sqrt{\frac{2}{3}}V_{\Lambda\Sigma} & \frac{1}{3}\left[2V_{\Sigma\Sigma}(\frac{1}{2}) + V_{\Sigma\Sigma}(\frac{3}{2})\right] & \frac{\sqrt{2}}{3}\left[-V_{\Sigma\Sigma}(\frac{1}{2}) + V_{\Sigma\Sigma}(\frac{3}{2})\right] \\ \sqrt{\frac{1}{3}}V_{\Lambda\Sigma} & \frac{\sqrt{2}}{3}\left[-V_{\Sigma\Sigma}(\frac{1}{2}) + V_{\Sigma\Sigma}(\frac{3}{2})\right] & \frac{1}{3}\left[V_{\Sigma\Sigma}(\frac{1}{2}) + 2V_{\Sigma\Sigma}(\frac{3}{2})\right] \end{pmatrix}. \tag{3.22}$$

In Appendix C, Table 2 and Table 4 the relation between the potentials on the isospin-basis is given, see Eqn's (3.16)-(3.17), and the SU(3)-irreps.

Given the interaction Hamiltonian (3.9) and a theoretical scheme for deriving the potential representing a particular Feynman graph, it is now straightforward to derive the one-meson-exchange baryon-baryon potentials. Following the approach in Refs. [23, 26, 29, 30], expressions for the potentials in momentum space, as well as configuration space potentials can be derived. Since the nucleons have strangeness $S = 0$, the hyperons $S = -1$, and the cascades $S = -2$, the possible baryon-baryon interaction channels can be classified according to their total strangeness, ranging from $S = 0$ for NN to $S = -4$ for $\Xi\Xi$. Apart from the wealth of accurate NN scattering data for the total strangeness $S = 0$ sector, there are only a few, and not very accurate, YN scattering data for the $S = -1$ sector, while there are no data at all for the $S < -1$ sectors [5].

Therefore, at this stage it is not worthwhile yet to explicitly account for the small mass differences between the specific charge states of the baryons and mesons; i.e., average masses are used, isospin is a good quantum number, and the potentials are calculated on the isospin basis. The possible channels on the isospin basis are given in (3.16).

However, the Lippmann-Schwinger or Schrödinger equation is solved for the physical particle channels, and so scattering observables are calculated using the proper physical baryon masses. The possible channels on the physical particle basis can be classified according to the total charge Q; these are given in (3.15). The corresponding potentials are obtained from the potential on the isospin basis by making the appropriate isospin rotations. The matrix elements of the isospin rotation matrices are nothing else but the Clebsch-Gordan coefficients for the two baryon isospins making up the total isospin. (Note that this is the reason why the potential on the particle basis, obtained from applying an isospin rotation to the potential on the isospin basis, will have the correct sign for any coupling constant on a vertex which involves a Σ^+.)

In order to construct the potentials on the isospin basis, the matrix elements of the various OBE exchanges between particular isospin states are needed. Using the iso-multiplets (3.6) and the Hamiltonian (3.9) the isospin-factors can be calculated. For the NN and YN(S=-1) the isospin factors are standard, and well known. For YY(S=-2) these factors are more subtle, which is due to the occurrence of coupled channels with a mix of identical and non-identical two-hyperon states. This is treated in Appendix K. The results are given in Table 3, with the pseudoscalar mesons as a specific example. The entries in this table contain the flavor-exchange operator P_f, which is $+1$ for a flavor symmetric and -1 for a flavor anti-symmetric two-baryon state. Since two-baryon states are totally antisymmetric, one has $P_f = -P_x P_\sigma$. Therefore, the exchange operator P_f has the value $P_f = +1$ for even-L singlet and odd-L triplet partial waves, and $P_f = -1$ for odd-L singlet and even-L triplet partial waves. To understand Table 3 fully, in Appendix K a general treatment of exchange forces is given, which also shows how to deal with the case where the initial/final state involves identical particles and the final/initial state does not.

Secondly, the TME and the MPE exchanges have to be evaluated. The method used is the same as for hyperon-nucleon, and is described in Ref. [3], Sec. IID.

[5] Recent data on the $S \leq -1$ channels are mentioned in the Summary, section 20.

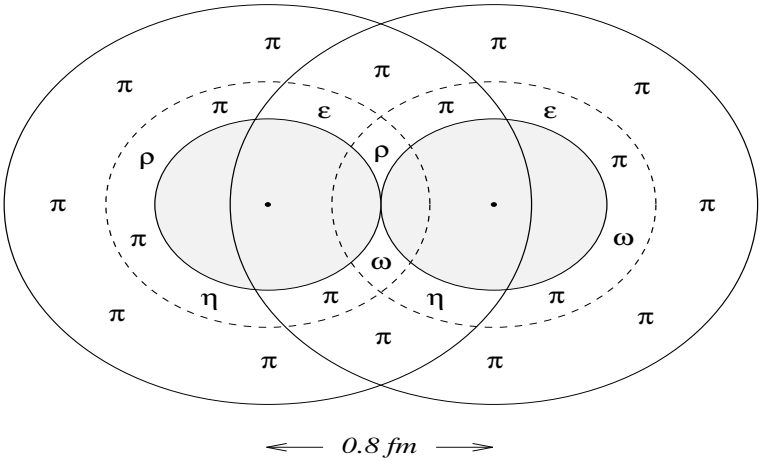

Figure 4: Composition two baryon-system: quark-cores and meson-clouds. Distance d=0.8 fm.

4. Interactions and Potentials ESC-model

In Fig. 4 an intuitive picture of the two-baryon system is drawn, with the quark cores at the centers and the (virtual) meson clouds. Virtual quark-antiquark pair creation (QPC) in the cores, leads to meson coupling and exchange. This picture suggests pionic exchanges dominating at long distances and vector-, scalar-, axial-, etc. meson-exchanges at shorter distances, corresponding to the interactions employed in the ESC-model.
The potentials of the ESC-model are generated by (i) One-Boson-Exchange (OBE), (ii) uncorrelated Two-Meson-Exchange (TME), (iii) Meson-Pair-Exchange (MPE), (iv) Diffractive/Multi-gluon Exchange, (v) Quark-Core Effects (QCE).

The OBE part of the dynamical contents of the ESC16 model is determined by the following meson-exchanges:

1. $J^{PC} = 0^{--}$: The pseudoscalar-meson nonet $\pi,\ \eta,\ \eta',\ K$ with the $\eta - \eta'$ mixing angle $\theta_P = -11.4^0$ [42], close to the Gell-Mann-Okubo (GMO) quadratic mass formula [41].
2. $J^{PC} = 1^{--}$: The vector-meson nonet $\rho,\ \phi,\ K^\star,\ \omega$ with the $\phi - \omega$ mixing angle $\theta_V = 39.1^0$ [42] This follows from the quadratic GMO mass-formula, and is close to ideal mixing.
3. $J^{PC} = 1^{++}$: The axial-vector-meson nonet $a_1, f_1,\ K_{1A}, f_1'$ with the $f_1 - f_1'$ mixing angle $\theta_A = 50.0^0$ [43].
4. $J^{PC} = 0^{++}$: The scalar-meson nonet $a_0(962) = \delta, f_0(993) = S^\star, \kappa(861), f_0(620) = \varepsilon$ [44]. The scalar $S^\star - \varepsilon$ mixing angle $\theta_S = 44.0^0$ is fitted and deviates from the ideal mixing angle $\theta_S = 35.26^0$. The $\kappa(861)$ mass is determined via GMO.
5. $J^{PC} = 1^{+-}$: The axial-vector-meson nonet $b_1, h_1,\ K_{1B}, h_1'$ with the $h_1 - h_1'$ ideal mixing angle $\theta_B = 35.26^0$. (Furthermore $K_{1,A}$ and $K_{1,B}$ are completely mixed.)

The soft-core approach of the OBE was originally given for NN in [33], and for YN in [34]. With respect to these OBE-interactions, the ESC-models contain the modification of the form factor by introducing a zero for the mesons being P-wave quark-antiquark states in the CQM: the scalar- and axial-vector-mesons. Such a zero is natural in the $^3P_0$-quark-pair-creation (QPC) [45, 46] model for the coupling of the mesonic quark-antiquark ($Q\bar{Q}$) system to baryons. A consequence of such a zero is that a bound state in Λp-scattering is less likely to occur.

(ii) The configuration space soft-core uncorrelated two-meson exchange for NN has been derived in [26, 29]. Similarly to ESC04, also in ESC16 these potentials are used for PS-PS exchange with a complete SU(3)-symmetric treatment in NN, YN, and YY. For example, included is double K-exchange in NN-scattering. Since this includes two-pion exchange (TPE), the long-range part of the potentials is represented. Here it is tacitly assumed that other TME potentials, like PS-VC, PS-SC, etc., are either small due to cancellations, or can be described adequately by using effective couplings in the OBE-potentials. When these effective couplings do not deviate from experimentally determined couplings, it may be assumed that the corrections from these other SU(3)

meson-nonets in the TME potentials are small. This is our working hypothesis for the TME-potentials. From the point of view of SU(3), since OBE contains only {8}- and {1}-exchange, TME can not be represented completely in terms of OBE. This, because there also occur the {27}, {10}, and {10^*} irreps of SU(3). Therefore, the predictions made by the ESC-models could be sensitive to this incompleteness of TME in the ESC-models. At present, the BB-data and the hypernuclear-data do not give information at this point.

(iii) Meson-pair exchanges (MPE) have been introduced in [1] for NN and described in detail in [30]. The two-meson-baryon-baryon vertices are the low-energy approximations of (a) the heavy-meson and their two-meson decays, and (b) baryon-resonance contributions $\Delta_{33}(1236)$, etc [30, 43].

(iv) Diffractive contributions to the soft-core potential have been introduced from the beginning, cf. [33]. The pomeron is thought of being related to an even number of gluon-exchanges. In ESC16 also the odderon-potential is introduced, which is related to an odd number of gluon exchanges.

(a) $J^{PC} = 0^{++}$: The 'diffractive' contribution from the pomeron (P), which is a unitary singlet. These interactions give a repulsive contribution to the potentials in all channels of a Gaussian type.

(b) $J^{PC} = 1^{--}$: The 'diffractive' contribution from the odderon (O). The origin of the odderon is assumed to be purely the exchange of the color-singlets with an odd number of gluons. Similarly to the pomeron, the odderon-potential is taken to be an SU(3) singlet and of the Gaussian form.

As an explanation of the repulsive character of the pomeron-potential, the following: The J^{PC} is identical to that for the scalar mesons. Naively, one would expect an attractive central potential. However, considering the two-gluon model for the pomeron [47, 48], the two-gluon parallel and crossed graph contributions to the BB-interaction can be shown to cancel adiabatically. The remaining non-adiabatic contribution is repulsive [49].

(v) Quark-Core-Effects in the soft-core model can supply extra repulsion, which may be required in some BB-channels. Baryon-baryon studies with the soft-core OBE and ESC models thus far show that it is difficult to achieve a strong enough repulsive short-range interactions in (i) the $\Sigma^+ p(I = 3/2, {}^3S_1)$- and (ii) the $\Sigma N(I = 1/2, {}^1S_0)$-channel. The short-range repulsion in baryon-baryon may in principle come from: (a) meson- and multi-gluon-exchange [2, 3], and/or (b) the occurrence of forbidden six-quark SU(6)-states by the Pauli-principle [50, 51, 52]. In view of the mentioned difficulties, a phenomenological method has been developed for the ESC models, which enables us to incorporate this quark-structural effect. This is an important new ingredient of the here presented ESC16 model. This structural effect is described phenomenologicallyl by Gaussian repulsions, similar to the pomeron. In the ESC16 model, the strength of this repulsion is taken proportional to the weights of the SU(6)-forbidden [51]-configuration in the various BB-channels. This is in contrast to ESC08a,b [53, 13] where the quark-core effect is only included in the BB-channels with a dominant occurrence of the [51]-configuration.

4.1. The meson-baryon interaction Hamiltonian densities

The local interaction Hamiltonian densities for the baryon-meson couplings are

a) Pseudo-vector-meson exchange ($J^{PC} = 0^{-+}$):

$$\mathcal{H}_{PV} = \frac{f_{pv}}{m_{\pi^+}} [\bar{\psi}\gamma_\mu\gamma_5\psi]\partial^\mu\phi_P. \tag{4.1}$$

The pseudoscalar coupling coupling constant is $g_{ps} = (2M/m_{\pi^+})\, f_p$, where M is the baryon mass.

The relation between the PV interaction Lagrangian and the Hamiltonian involves a non-covariant "contact" term

$$\mathcal{H}_I \quad = \quad (f/m_\pi)\bar{\psi}\gamma_5\gamma_\mu\psi \cdot \partial^\mu\phi + (f/m_\pi)^2(\psi^*\gamma_5\psi)^2.$$

This contact term gives no contribution to the Green functions or the potentials, since in the Wick-expansion it is compensated by the non-covariant piece in the contraction $\langle 0|T(\partial_\mu\phi(x)\partial_\nu\phi(y))|0\rangle$, see [26, 27, 28]. Similarly for derivatives in other meson-exchange interactions.

b) Vector-meson exchange ($J^{PC} = 1^{--}$):

$$\mathcal{H}_V = g_V[\bar{\psi}\gamma_\mu\psi]\partial^\mu\phi_V^\mu + \frac{f_V}{4\mathcal{M}}[\bar{\psi}\sigma_{\mu\nu}\psi]\left(\partial^\mu\phi_V^\nu - \partial^\nu\phi_V^\mu\right), \tag{4.2}$$

where $\sigma_{\mu\nu} = i[\gamma_\mu, \gamma_\nu]/2$, and the scaling (proton) mass $\mathcal{M}$.

c) Axial-vector-meson exchange ($J^{PC} = 1^{++}$), 1^{st} kind):

$$\mathcal{H}_A = g_A[\bar{\psi}\gamma_\mu\gamma_5\psi]\partial^\mu\phi_A^\mu + \frac{if_A}{\mathcal{M}}[\bar{\psi}\gamma_5\psi]\partial^\mu\phi_A^\mu. \tag{4.3}$$

For the treatment of this density in momentum-space, see Ref. [4].

d) Axial-vector-meson exchange (($J^{PC} = 1^{+-}$), 2^{nd} kind):

$$\mathcal{H}_B = \frac{if_B}{\mathcal{M}}[\bar{\psi}\sigma_{\mu\nu}\psi]\partial^\nu\phi_B^\mu. \tag{4.4}$$

e) Scalar-meson exchange ($J^{PC} = 0^{++}$):

$$\mathcal{H}_S = g_S[\bar{\psi}\psi\phi_S]. \tag{4.5}$$

f) Pomeron exchange ($J^{PC} = 0^{++}$): The vertices for this "diffractive"-exchange have the same Lorentz structure as those for scalar-exchange. The origin of this coupling can be related to an even-number of gluon-exchange.

g) Odderon-meson exchange ($J^{PC} = 1^{--}$):

$$\mathcal{H}_O = g_O[\bar{\psi}\gamma_\mu\psi]\partial^\mu\phi_O^\mu + \frac{f_O}{4\mathcal{M}}[\bar{\psi}\sigma_{\mu\nu}\psi]\left(\partial^\mu\phi_O^\nu - \partial^\nu\phi_O^\mu\right), \tag{4.6}$$

which can be related to an odd-number of gluon-exchange. Since the gluons are flavorless, the Pomeron- and Odderon-exchange are treated as SU(3) singlets. For further details, see Ref. [4].

With the form factors $F(\mathbf{x}' - \mathbf{x})$, the interaction density becomes modified

$$H_I(\mathbf{x}) = \int d^3x'\, F(\mathbf{x}' - \mathbf{x})\mathcal{H}_I(\mathbf{x}'). \tag{4.7}$$

The form of the potentials in momentum space is the same as for point interactions, except that the coupling constants are multiplied by the Fourier transform $F(\mathbf{k}^2)$ of the form factor, where $\mathbf{k}$ is the momentum transfer at the MBB-vertex. For space-like momentum transfers a Gaussian parameterization of the form factors is used in all mesonic vertices, *i.e.* $F(\mathbf{k}^2) \approx \exp(-\mathbf{k}^2/\Lambda^2)$. *In the description of the ESC-model in this paper, the Gaussian form factors are always understood, but omitted from the formulas.* An exception are the basic configuration space functions ϕ_C^0 etc. in Appendix G.3.

4.2. Non-local Potentials, SU(3)-breaking, and Coulomb

As is well known, the non-local potentials are inherent to a relativistic theory, and occur in the central, spin-spin, tensor, spin-orbit, etc. potentials. In the ESC-models, included are the non-local contributions to the central/spin-spin potentials for scalar, vector, axial, and diffractive exchanges, as in the soft-core OBE-models [33, 34]. In addition, for all BB-channels, included are the pseudoscalar-type of potentials, which occur from pseudoscalar-, axial A- and B-mesons, the non-local spin-spin and tensor contributions [54]. This, because it turned out that the non-local pion-exchange spin-spin and tensor force are rather important for achieving a very good fit to the NN-data. The different sources of SU(3)-breaking are discussed in [6].

As in all Nijmegen models, the Coulomb interaction is included exactly, for which the multichannel Schrödinger equation is solved on the physical particle basis. The nuclear potentials are calculated on the isospin basis. This means that only the so-called 'medium strong' SU(3)-breaking and the charge symmetry breaking (CSB) are included in the potentials.

5. Two-Body Integral Equations in Momentum Space

Consider the baryon-baryon reaction

$$B_a(p_a, s_a) + B_b(p_b, s_b) \to B'_a(p'_a, s'_a) + B'_b(p'_b, s'_b), \tag{5.1}$$

with on the energy-shell $p_a + p_b = p_{a'} + p_{b'}$, and in the center-of-mass system (CM-system) the momenta $\mathbf{p}$ and $\mathbf{p}'$ for the initial and final state, respectively. On the mass-shell, one has $p_a^0 = E_a(\mathbf{p}) = \sqrt{\mathbf{p}^2 + M_a^2}$ and $p_b^0 = E_b(\mathbf{p}) = \sqrt{\mathbf{p}^2 + M_b^2}$ and similarly for b and b' The transition M-matrix is related to the S-matrix via [6]

$$\langle f|S|i\rangle = \langle f|i\rangle - i(2\pi)^4\delta^4(P_f - P_i)\langle f|M|i\rangle. \tag{5.2}$$

The two-particle states are normalized in the following way

$$\langle \mathbf{p}'_1, \mathbf{p}'_2|\mathbf{p}_1, \mathbf{p}_2\rangle \quad = \quad (2\pi)^3 2E(\mathbf{p}_1)\delta^3(\mathbf{p}'_1 - \mathbf{p}_1)\,(2\pi)^3 2E(\mathbf{p}_2)\delta^3(\mathbf{p}'_2 - \mathbf{p}_2). \tag{5.3}$$

Below, a three-dimensional equation is derived in the context of the Kadyshevsky field theory (KFT).

5.1. Relativistic Kadyshevsky Two-Body Equation

Introducing, as usual, the total and relative four-momentum for the initial and final state

$$\begin{array}{lll} P = p_a + p_b & , & P' = p'_a + p'_b\,, \\ p = \frac{1}{2}(p_a - p_b) & , & p' = \frac{1}{2}(p'_a - p'_b)\,, \end{array} \tag{5.4}$$

with the following notations $P_0 \equiv W$ and $P'_0 \equiv W'$. In the Kadyshevsky approach to relativistic scattering, four-momenta spurions are introduced, making formally four-momentum conservation at the vertices. These are described by quasi-particle states $|\kappa\rangle$, normalized by $\langle\kappa'|\kappa\rangle = \delta(\kappa' - \kappa)$. Then the four-momentum of such a spurion state is κn^μ, where n^μ is time-like with $n^0 > 0$ and $n^2 = 1$. So, considered is the process in (3.4) with non-conservation of the four-momentum, *i.e.* off-momentum-shell. This off-shellness is given by

$$p_a + p_b + \kappa n = p'_a + p'_b + \kappa' n \tag{5.5}$$

Therefore, in the Kadyshevsky formalism generalized amplitudes $M_{\kappa',\kappa}$ and interaction kernels $I_{\kappa',\kappa}$ are introduced, see Fig. 5 In the Kadyshevsky formulation, the particles are on-mass-shell in the Green-functions. The on-mass-shell propagator $S^{(\pm)}(p)$ of a spin-0 particle can be written as

$$S^{(\pm)}(p) = \delta_\pm(p^2 - M^2) = \frac{1}{2E(\mathbf{p})}\delta\left(p_0 \mp E(\mathbf{p})\right), \tag{5.6}$$

with $\delta_\pm(p^2 - M^2) \equiv \theta(\pm p^0)\delta(p^2 - M^2)$. The propagator $G_0(\kappa)$ for the quasi-particles is given by [15]

$$G_0(\kappa) = (1/2\pi)\left[1/(\kappa - i\epsilon)\right]. \tag{5.7}$$

In the Kadyshevsky-formalism the rules for the computation of the off-shell S-matrix, denoted by R, corresponding to the analogs of the Feynman graphs are given [15, 16]. The usual M-matrix is introduced as

$$\begin{array}{lll} R_{\kappa',\kappa}(p'_a, p'_b; p_a, p_b) & = & \delta(\kappa' - \kappa)\delta(p'_a - p_a)\delta(p'_b - p_b) - (2\pi)^4 i\delta^4(\kappa' n + p'_a + p'_b - p_a - p_b - \kappa n)\cdot \\ & & \times M_{\kappa',\kappa}(p'_a, p'_b; p_a, p_b)\,. \end{array} \tag{5.8}$$

Notice that the S-matrix is given by $R_{0,0}$ [15]. One has

$$\delta(\kappa' - \kappa)\delta(p'_a - p_a)\delta(p'_b - p_b) = \delta(P' + \kappa' n - P - \kappa n)\delta(p'_a - p_a)\delta(p'_b - p_b)\,, \tag{5.9}$$

[6] The conventions of Ref. [55] for the metric etc., are used in this paper. This, except for the sign of the M-matrix.

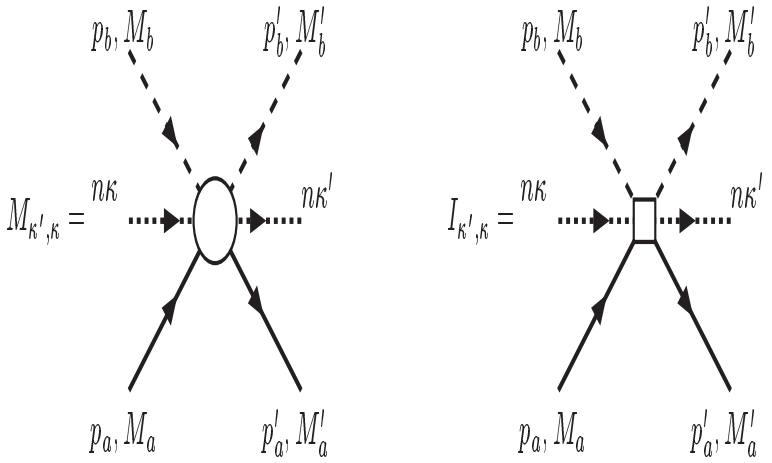

Figure 5: *M- and I-matrix.*

showing the overall 4-momentum conservation for the R-matrix, including the momentum spurions. The $M_{\kappa',\kappa}$-amplitude and the $I_{\kappa',\kappa}$-interaction, depicted in Fig. 5, satisfy the integral equation

$$\begin{aligned} M_{\kappa',\kappa}(p'_a, p'_b; p_a, p_b) &= I_{\kappa',\kappa}(p'_a, p'_b; p_a, p_b) + \int d^4p''_a \int d^4p''_b \int d\kappa'' I_{\kappa'\kappa''}(p'_a, p'_b; p''_a, p''_b) \cdot \\ &\quad \times G_{\kappa''}(p''_a, p''_b) M_{\kappa'',\kappa}(p''_a, p''_b; p_a, p_b) \cdot \delta(p''_a + p''_b + \kappa'' n - p_a - p_b - \kappa n), \end{aligned} \tag{5.10}$$

which is shown graphically in Fig. 6 Here, the propagation of the two nucleons and of the quasi-particle is described by

$$G_\kappa(p_a, p_b)_{\alpha',\beta';\alpha,\beta} = -(2\pi)^{-2}\delta(p_a^2 - M_a^2)\delta(p_b^2 - M_b^2) \cdot G_0(\kappa)\,. \tag{5.11}$$

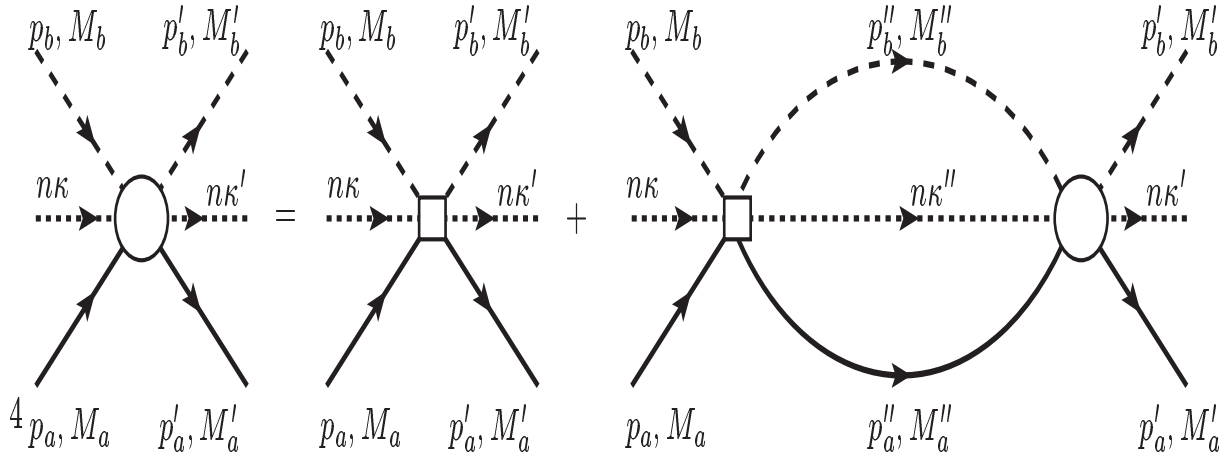

Figure 6: *Kadyshevsky Integral Equation*

5.2. Kadyshevsky Quasi-Potential Equation

The Kadyshevsky analog (5.10) of the Bethe-Salpeter equation, is written in the form

$$M_{\kappa',\kappa}(p'_a,p'_b;p_a,p_b) = I_{\kappa',\kappa}(p'_a,p'_b;p_a,p_b) + \int d^4p''_a \int d^4p''_b \int d\kappa'' \cdot$$
$$\times I_{\kappa',\kappa''}(p'_a,p'_b;p''_a,p''_b) G_{\kappa''}(p''_a,p''_b) M_{\kappa'',\kappa}(p''_a,p''_b;p_a,p_b) \cdot$$
$$\times \delta(p''_a + p''_b + \kappa'' n - p_a - p_b - \kappa n) \; . \tag{5.12}$$

In the CM-frame, one has

$$P = (W,\mathbf{0}) \;\; , \;\; p = (0,\mathbf{p}) \;\; ; P' = (W',\mathbf{0}) \;\; , \;\; p' = (0,\mathbf{p}') \; . \tag{5.13}$$

Following [15, 17], it is assumed that the unit vector n^μ, which defines the time axis, is collinear to $P = p_a + p_b$ and hence also to $P' = p'_a + p'_b$. Then [7]

$$n^\mu = \frac{p_a^\mu + p_b^\mu}{\sqrt{(p_a+p_b)^2}} = \frac{p_a'^\mu + p_b'^\mu}{\sqrt{(p'_a+p'_b)^2}} \xrightarrow{CM} (1,\mathbf{0}). \tag{5.14}$$

In the CM-variables, equation (5.12), for the (+, +)-components only, reads

$$M_{\kappa',\kappa}(p',W';p,W) = I_{\kappa',\kappa}(p',W';p,W) + \int dW'' \int d^4p'' \int d\kappa'' \cdot$$
$$\times I_{\kappa',\kappa''}(p',W';p'',W'') G_{\kappa''}(p'',W'') M_{\kappa''}(p'',W'';p,W) \cdot$$
$$\times \delta\left[W'' - W + (\kappa'' - \kappa) n_0\right] \; . \tag{5.15}$$

In the CM-frame, the two-nucleon propagator (5.11) becomes

$$G_\kappa(W'',p'') \;\; = \;\; -(2\pi)^{-2} \delta\left(\frac{1}{2}W'' + p''_0 - E''_a\right) \delta\left(\frac{1}{2}W'' - p''_0 - E''_b\right) G_0(\kappa'') \; . \tag{5.16}$$

Now, the integrations over W'', p''_0, and κ'' can be carried through in (5.15) giving

$$M_{\kappa',\kappa}(\mathbf{p}',W';\mathbf{p},W) = I_{\kappa',\kappa}(\mathbf{p}',W';\mathbf{p},W) + \int \frac{d^3p''}{(2\pi)^3} \cdot$$
$$\times I_{\kappa',\kappa''}(\mathbf{p}',W';\mathbf{p}'',W'') \left(\frac{M_a M_b}{E''_a E''_b}\right) \frac{1}{\sqrt{s''} - \left(\sqrt{s}+\kappa\right) - i\epsilon} M_{\kappa'',\kappa}(\mathbf{p}'',W'';\mathbf{p},W) \; , \tag{5.17}$$

with the constraints

$$W \;\; = \;\; \sqrt{s} \;\; , \;\; W' = \sqrt{s'} = \sqrt{s} + \kappa - \kappa' \; , \; W'' = \sqrt{s''} = E''_a + E''_b \; . \tag{5.18}$$

Notice that the left-half-off-shell M-matrix satisfies an integral equation of the type

$$M_{\kappa',0} = I_{\kappa',0} + \int I_{\kappa',\kappa''} \; G_{\kappa''} \; M_{\kappa'',0}$$

where the κ's are all fixed in terms of the momenta of the particles, since

$$\kappa' = \sqrt{s} - \sqrt{s'} \;\; , \;\; \kappa'' = \sqrt{s} - \sqrt{s''}.$$

Defining the T-matrix etc. in terms of the left-half-off-shell M-matrix , and the quasi-potential K in terms of the left and right off-shell interaction kernel I, by

$$T(\mathbf{p}',\mathbf{p}) \;\; = \;\; M_{\kappa',\kappa=0}(\mathbf{p}',W';\mathbf{p},W) \; , \; K(\mathbf{p}',\mathbf{p}) = I_{\kappa',\kappa=0}(\mathbf{p}',W';\mathbf{p},W) \; , \tag{5.19}$$

[7] Notice that with this choice for n^μ, the four-velocity of the system is conserved even off the energy-shell.

one has, instead of (5.17),

$$T(\mathbf{p}',\mathbf{p}) \;=\; K(\mathbf{p}',\mathbf{p}) + \int \frac{d^3p''}{(2\pi)^3}\, K(\mathbf{p}',\mathbf{p}'') \left(\frac{M_a M_b}{E''_a E''_b}\right) \frac{1}{\sqrt{s''}-\sqrt{s}}\, T(\mathbf{p}'',\mathbf{p})\,, \tag{5.20}$$

which is the so-called "quasi-potential equation", see *e.g.* equations (II.26) and (II.27) in Ref. [56]. Notice, that for $\kappa = 0$, one has $\kappa' = \sqrt{s} - \sqrt{s'}$, and so κ' is fixed by $p = |\mathbf{p}|$ and $p' = |\mathbf{p}'|$.

For equal masses, *i.e.* $M_a = M_b = M$, one has

$$E''_a \;=\; E''_b = E(\mathbf{p}''),\; s = 4E^2(\mathbf{p}) = 4(p^2+M^2),\; s'' = 4E^2(\mathbf{p}'') = 4(p''^2+M^2). \tag{5.21}$$

Then, (5.20) goes over into the equation

$$T(\mathbf{p}',\mathbf{p}) \;=\; K(\mathbf{p}',\mathbf{p}) + \frac{1}{(2\pi)^3}\int \frac{d^3p''}{2E(\mathbf{p}'')}\, K(\mathbf{p}',\mathbf{p}'')\, \frac{M^2}{E(\mathbf{p}'')\left[E(\mathbf{p}'')-E(\mathbf{p})-i\epsilon\right]}\, T(\mathbf{p}'',\mathbf{p}), \tag{5.22}$$

which is the quasi-potential Kadyshevsky equation, see [16] equation (6.33).

5.3. Thompson and Lippmann-Schwinger Equations

The Thompson equation is obtained from (5.22) by the transformation

$$\mathcal{T}(\mathbf{p}',\mathbf{p}) = N(\mathbf{p}')\, T(\mathbf{p}',\mathbf{p})\, N(\mathbf{p})\,,\; \mathcal{V}(\mathbf{p}',\mathbf{p}) = N(\mathbf{p}')\, K(\mathbf{p}',\mathbf{p})\, N(\mathbf{p}), \tag{5.23}$$

with $N(\mathbf{p}) = M/(\sqrt{2}E(\mathbf{p}))$. The non-relativistic Lippmann-Schwinger equation is obtained by using in the Green function and the potential, the non-relativistic approximation $E(\mathbf{p}) \approx M + \mathbf{p}^2/2M$, giving

$$\mathcal{T}(\mathbf{p}',\mathbf{p}) \;=\; \mathcal{V}(\mathbf{p}',\mathbf{p}) + \frac{1}{(2\pi)^3}\int \frac{d^3p''}{2E(\mathbf{p}'')}\, \mathcal{V}(\mathbf{p}',\mathbf{p}'')\, \frac{M}{(\mathbf{p}''^2-\mathbf{p}^2-i\epsilon)}\, \mathcal{T}(\mathbf{p}'',\mathbf{p}). \tag{5.24}$$

For the details of the formalism of spin 1/2-1/2 scattering, using the expansion in Pauli-invariants, see the papers on the ESC-model, *e.g.* [2, 3].

6. Partial Wave Expansion Kadyshevsky Equation

The partial wave expansion for spin-1/2 spin-1/2 has been discussed in e.g. [57, 58]. For the 'derivative' $T_{\beta,\alpha}$ amplitudes [58], the partial wave expansion are as simple as for spinless particle scattering

$$T_{\beta,\alpha}(\mathbf{p}',\mathbf{p}) = \sum_{J=0}^{\infty}(2J+1)\, T^J_{\beta,\alpha}(p',p)\, P_J(\cos\theta). \tag{6.1}$$

The partial wave expansion for the corresponding Kadyshevsky equation is

$$T^J_{\beta,\alpha}(p',p) \;=\; K^J_{\beta,\alpha}(p',p) + \frac{1}{16\pi^3}\int \frac{p''^2 dp''}{E(\mathbf{p}'')}\, K^J_{\beta,\alpha}(p',p'')\, \frac{M^2}{E(\mathbf{p}'')\,(E(\mathbf{p}'')-E(\mathbf{p})-i\epsilon)}\, T^J_{\beta,\alpha}(p'',p). \tag{6.2}$$

The connection with the helicity amplitudes is [58]

$$T^J_{++,++} = \tfrac{1}{2}\left[T^J_{0,0}+T^J_{1,1}\right] \quad , \quad T^J_{++,--} = \tfrac{1}{2}\left[-T^J_{0,0}+T^J_{1,1}\right],$$

$$T^J_{+-,+-} = \tfrac{1}{2}J(J+1)\left[-T^J_{2,2}-T^J_{3,3}\right] \quad , \quad T^J_{+-,-+} = \tfrac{1}{2}J(J+1)\left[+T^J_{2,2}-T^J_{3,3}\right],$$

$$T^J_{++,+-} = \tfrac{1}{2}\sqrt{J(J+1)}\left[+T^J_{0,2}-T^J_{1,3}\right] \quad , \quad T^J_{++,-+} = \tfrac{1}{2}\sqrt{J(J+1)}\left[-T^J_{0,2}-T^J_{1,3}\right],$$

$$T^J_{+-,++} = \tfrac{1}{2}\sqrt{J(J+1)}\left[-T^J_{2,0}+T^J_{3,1}\right] \quad , \quad T^J_{-+,++} = \tfrac{1}{2}\sqrt{J(J+1)}\left[T^J_{2,0}+T^J_{3,1}\right].$$

For the helicity amplitudes, one has [58]

$$T^J_{\lambda'_a\lambda'_b;\lambda_a\lambda_b}(p',p) = K^J_{\lambda'_a\lambda'_b;\lambda_a\lambda_b}(p',p) + \frac{1}{16\pi^3}\int \frac{p''^2 dp''}{E(\mathbf{p}'')}\, K^J_{\lambda'_a\lambda'_b;\lambda''_a\lambda''_b}(p',p'')\cdot \times \frac{M^2}{E(\mathbf{p}'')\,(E(\mathbf{p}'')-E(\mathbf{p})-i\epsilon)}\, T^J_{\lambda''_a\lambda''_b;\lambda_a\lambda_b}(p'',p). \tag{6.3}$$

The physical properties of the partial waves $T^J_{\beta,\alpha}$ is exhibited by the relation with the parity-conserving partial wave amplitudes

$$f^{J,\eta}_{\lambda'\lambda} = T^J_{\lambda_c,\lambda_d;\lambda_a\lambda_b} - \eta\, T^J_{\lambda_c,\lambda_d;-\lambda_a-\lambda_b},\ \ \eta=\pm \tag{6.4}$$

which is

$$\begin{bmatrix} f^{J-}_{00} & f^{J-}_{01} \\ f^{J-}_{10} & f^{J-}_{11} \end{bmatrix} = \begin{bmatrix} T^J_{0,0} & +\sqrt{J(J+1)}\,T^J_{0,2} \\ -\sqrt{J(J+1)}\,T^J_{2,0} & -J(J+1)\,T^J_{2,2} \end{bmatrix}, \tag{6.5a}$$

$$\begin{bmatrix} f^{J+}_{00} & f^{J+}_{01} \\ f^{J+}_{10} & f^{J+}_{11} \end{bmatrix} = \begin{bmatrix} T^J_{1,1} & -\sqrt{J(J+1)}\,T^J_{1,3} \\ +\sqrt{J(J+1)}\,T^J_{3,1} & -J(J+1)\,T^J_{3,3} \end{bmatrix}. \tag{6.5b}$$

From (6.5a) one sees that $T^J_{0,0}, T^J_{2,0}, T^J_{0,2}$ and $T^J_{2,2}$ correspond to the spin singlet and triplet-uncoupled transitions ${}^1J_J \Leftrightarrow {}^1J_J, {}^1J_J \Leftrightarrow {}^3J_J, {}^3J_J \Leftrightarrow {}^1J_J$, and ${}^3J_J \Leftrightarrow {}^3J_J$. The partial waves $T^J_{1,1}, T^J_{3,3}, T^J_{3,1}$ and $T^J_{1,3}$ correspond to the spin triplet coupled transitions. Denoting by $f^{J+}_{L'L}(f,i)$ the amplitudes for the ${}^3J_{L'} \Leftrightarrow {}^3J_L$, the explicit connection is [57]

$$f^{J+}_{L'L}(f,i) = \sum_{k,k'} X^\dagger_{L',k'}\, f^{J+}_{k'k}(f,i) X_{k,L} \tag{6.6}$$

with

$$\begin{pmatrix} X_{1,J-1} & X_{1,J+1} \\ X_{2,J-1} & X_{2,J+1} \end{pmatrix} = \frac{1}{\sqrt{2J+1}} \begin{pmatrix} \sqrt{J} & -\sqrt{J+1} \\ \sqrt{J+1} & \sqrt{J} \end{pmatrix} \tag{6.7}$$

On the energy shell one has, due to time-reversal invariance, that $T^J_{2,0} = -T^J_{0,2}$ and $T^J_{3,1} = -T^J_{1,3}$, and so $f^J_{01} = f^J_{10}$. In the equal mass case $T^J_{0,2} = T^J_{2,0} = 0$, and the coupling between the singlet and triplet-uncoupled states vanishes.

---

7. General One-Boson-Exchange

The two Kadyshevsky OBE graphs are shown in Fig. 7. The meson-nucleon-nucleon vertices are given by the matrix elements of the interaction Hamiltonian densities. Defining the vertex functions $\Gamma_{i,\alpha}$ (i=S,PS,V,A), by

$$[\bar u(p')\Gamma_{i,\alpha}(p',p)\,u(p)]\cdot\epsilon^\alpha_i = \langle p'|\mathcal{H}_I(0)|p\rangle, \tag{7.1}$$

where ϵ^α_i is the meson polarization vector, defined as $\epsilon_S = \epsilon_P = \epsilon_D = 1$, $\epsilon_V = \rho^\alpha_V$, $\epsilon_A = \rho^\alpha_A$, and $\epsilon_B = \rho^\alpha_B$. The interaction Hamiltonians are given in e.g. [2, 13], leading to the vertex functions

$$\Gamma_S(p',p) = g_S,\ \ \Gamma_D(p',p) = g_D,\ \ \Gamma_{PV}(p',p) = \frac{if_{pv}}{m_{\pi^+}}\gamma\cdot(p'-p)\gamma_5, \tag{7.2a}$$

$$\Gamma_{V,\mu}(p',p) = g_V\gamma_\mu - \frac{if_V}{2\mathcal{M}}\sigma_{\mu\nu}(p'-p)^\nu = G_V\gamma_\mu + \frac{f_V}{2\mathcal{M}}(p'+p)^\mu, \tag{7.2b}$$

$$\Gamma_{A,\mu}(p',p) = g_A\gamma_\mu\gamma_5 - \frac{f_A}{\mathcal{M}}(p'-p)_\mu\gamma_5,\ \ \Gamma_{B,\mu}(p',p) = -\frac{f_B}{\mathcal{M}}(p'-p)^\nu\sigma_{\mu\nu}. \tag{7.2c}$$

Here, $G_V = g_V + f_V$. The Pomeron and Odderon vertices are similar to those for the scalar- and vector-mesons, respectively.

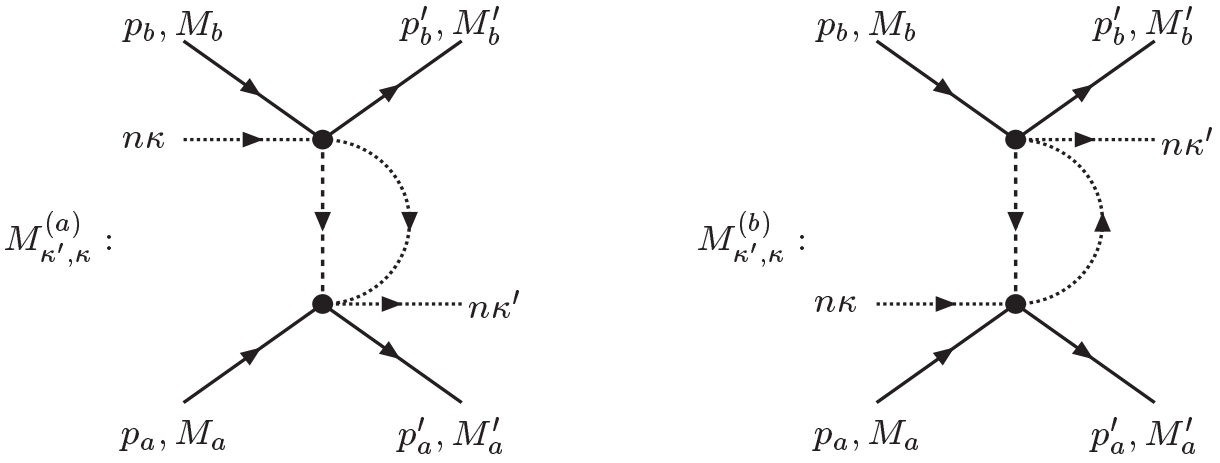

Figure 7: *Kadyshevsky-graphs One-Boson-Exchange. On the left graph (a) and on the right graph (b). The dashed arrow meson lines leave at vertex 2 and end at vertex 1.*

7.1. OBE Kadyshevsky matrix elements

From the Kadyshevsky rules given in Appendix A one has for graph (a)

$$(2\pi)^4\delta^4\left(p'_a+p'_b+\kappa' n-p_a-p_b-\kappa n\right)\; M^{(a)}_{\kappa',\kappa}=-\left[\bar{u}_{a'}(\mathbf{p}'_a)\Gamma_{i,\alpha}u_a(\mathbf{p}_a)\right]P^{\alpha,\beta}(k_a)\cdot$$
$$\times\left[\bar{u}_{b'}(\mathbf{p}'_b)\Gamma_{i,\beta}u_b(\mathbf{p}_b)\right]\frac{1}{2\pi}\int_{-\infty}^{+\infty}\frac{d\kappa_1}{\kappa_1-i\epsilon}\int\frac{d^4k_a}{(2\pi)^3}\cdot(2\pi)^4\delta^4\left(k_a+p_a+\kappa n-p'_a-\kappa_1 n\right)\cdot$$
$$\times(2\pi)^4\delta^4\left(k_a+p'_b+\kappa' n-p_b-\kappa_1 n\right)\cdot\Delta^{(+)}(k_a), \tag{7.3}$$

where the meson momentum k_a leaves vertex 2 and enters vertex 1, and $\Delta^{(+)}(k_a)=\delta_+(k_a^2-m_i^2)$, with m_i the mass of the meson. The projection operator $P^{\alpha,\beta}(k)$ is defined as

$$\begin{aligned}P_i^{\alpha,\beta} &= 1 \text{ for } i=S,P,D,\\ P_{V,A}^{\alpha,\beta} &= -g^{\alpha\beta}+k^\alpha k^\beta/m_{V,A}^2.\end{aligned} \tag{7.4}$$

The product of the two $\delta^4(k_a+\dots)$-functions can be rewritten as

$$\delta^4(p'_a+p'_b+\kappa' n-p_a-p_b-\kappa n)\cdot\delta^4(k_a-\Delta+\frac{1}{2}(\kappa'+\kappa)n-\kappa_1 n), \tag{7.5}$$

with

$$\Delta=\left(p'_a-p_a-p'_b+p_b\right)/2\;\;,\;\;t=\Delta^2. \tag{7.6}$$

Carrying out the d^4k_a-integration, one gets

$$\begin{aligned}M^{(a)}_{\kappa',\kappa} &= -\left[\bar{u}_{a'}(\mathbf{p}'_a)\Gamma_{i,\alpha}u_a(\mathbf{p}_a)\right]P^{\alpha,\beta}(k_a)\left[\bar{u}_{b'}(\mathbf{p}'_b)\Gamma_{i,\beta}u_b(\mathbf{p}_b)\right]\cdot\int_{-\infty}^{+\infty}\frac{d\kappa_1}{\kappa_1-i\epsilon}\cdot\\ &\quad\times\Delta^{(+)}\left(\frac{1}{2}(p'_a-p_a-p'_b+p_b)-\frac{1}{2}(\kappa'+\kappa)n+\kappa_1 n\right).\end{aligned} \tag{7.7}$$

Similarly, for graph (b), one defines k_b as the meson momentum that leaves vertex 1 and enters into vertex 2. One finds that $k_b=k_a(-\Delta)$, and one obtains

$$\begin{aligned}M^{(b)}_{\kappa',\kappa} &= -\left[\bar{u}_{a'}(\mathbf{p}'_a)\Gamma_{i,\alpha}u_a(\mathbf{p}_a)\right]P^{\alpha,\beta}(k_a)\left[\bar{u}_{b'}(\mathbf{p}'_b)\Gamma_{i,\beta}u_b(\mathbf{p}_b)\right]\cdot\int_{-\infty}^{+\infty}\frac{d\kappa_1}{\kappa_1-i\epsilon}\cdot\\ &\quad\times\Delta^{(+)}\left(-\frac{1}{2}(p'_a-p_a-p'_b+p_b)-\frac{1}{2}(\kappa'+\kappa)n+\kappa_1 n\right).\end{aligned} \tag{7.8}$$

So, addition gives

$$M_{\kappa',\kappa} = M^{(a)}_{\kappa',\kappa} + M^{(b)}_{\kappa',\kappa} \quad = \quad -\left[\bar{u}_{a'}(\mathbf{p}'_a)\Gamma_{i,\alpha}u_a(\mathbf{p}_a)\right] P^{\alpha,\beta}(k_a)\left[\bar{u}_{b'}(\mathbf{p}'_b)\Gamma_{i,\beta}u_b(\mathbf{p}_b)\right]\cdot\int_{-\infty}^{+\infty}\frac{d\kappa_1}{\kappa_1 - i\epsilon}\cdot$$
$$\times\left\{\Delta^{(+)}\left(\frac{1}{2}(p'_a - p_a - p'_b + p_b) - \frac{1}{2}(\kappa' + \kappa)n + \kappa_1 n\right)\right.$$
$$\left.+\Delta^{(+)}\left(-\frac{1}{2}(p'_a - p_a - p'_b + p_b) - \frac{1}{2}(\kappa' + \kappa)n + \kappa_1 n\right)\right\}. \tag{7.9}$$

The zero's in the argument as function of κ_1 for $\Delta^{(+)}$ are given by

$$(a) \quad : \quad \kappa_1^{(\pm)} = \left[\frac{1}{2}(\kappa' + \kappa) - (\Delta\cdot n) \pm \left\{m_i^2 - \Delta^2 + (\Delta\cdot n)^2\right\}^{1/2}\right],$$
$$(b) \quad : \quad \kappa_1^{(\pm)} = \left[\frac{1}{2}(\kappa' + \kappa) + (\Delta\cdot n) \pm \left\{m_i^2 - \Delta^2 + (\Delta\cdot n)^2\right\}^{1/2}\right]. \tag{7.10}$$

Now, $\Delta^{(+)}(k) = \theta(k^0)\delta(k^2 - m_i^2) = (1/2\omega)\delta(k^0 - \omega)$, where $\omega = \sqrt{\mathbf{k}^2 + m_i^2}$. Therefore, it is important to check the sign of $k^0(\kappa^{(\pm)})$. One has

$$(a) \quad : \quad k_a(\pm) = +\Delta - (\Delta\cdot n)\, n \pm A_t\, n\,,$$
$$(b) \quad : \quad k_b(\pm) = -\Delta + (\Delta\cdot n)\, n \pm A_t\, n, \tag{7.11}$$

with

$$A_t = \sqrt{m_i^2 - \Delta^2 + (\Delta\cdot n)^2}. \tag{7.12}$$

Then, the κ_1-integration is simple, using for both (a) and (b) that

$$\delta_+\left[(\kappa_1 - \kappa_1^{(+)})(\kappa_1 - \kappa_1^{(-)})\right] = \left|\left[\kappa_1^{(+)} - \kappa_1^{(-)}\right]\right|^{-1}\ \delta\left(\kappa_1 - \kappa_1^{(+)}\right), \tag{7.13}$$

and one finds easily that

$$M_{\kappa',\kappa} \quad = \quad M^{(a)}_{\kappa',\kappa} + M^{(b)}_{\kappa',\kappa} = -\left[\bar{u}_{a'}(\mathbf{p}'_a)\Gamma_{i,\alpha}u_a(\mathbf{p}_a)\right] P^{\alpha,\beta}(k_a)\left[\bar{u}_{b'}(\mathbf{p}'_b)\Gamma_{i,\beta}u_b(\mathbf{p}_b)\right]\cdot$$
$$\times\frac{1}{2A}\left\{\frac{1}{\frac{1}{2}(\kappa' + \kappa) - \Delta\cdot n + A_t - i\epsilon} + \frac{1}{\frac{1}{2}(\kappa' + \kappa) + \Delta\cdot n + A_t - i\epsilon}\right\}. \tag{7.14}$$

Using now that

$$n^\mu = \frac{p_a^\mu + p_b^\mu}{\sqrt{(p_a + p_b)^2}} = \frac{p_a'^\mu + p_b'^\mu}{\sqrt{(p'_a + p'_b)^2}} \xrightarrow{CM} (1, \mathbf{0}), \tag{7.15}$$

it follows that

$$\Delta^2 \quad = \quad \frac{1}{4}\left\{\left[(E' - E) - (\mathcal{E}' - \mathcal{E})\right]^2 - 4\mathbf{k}^2\right\}\,,$$
$$\Delta_E \quad \equiv \quad \Delta\cdot n = \frac{1}{2}\left[(E' - E) - (\mathcal{E}' - \mathcal{E})\right], \tag{7.16}$$

where $\mathbf{k} = \mathbf{p}' - \mathbf{p}$, and $E' = E_{a'}, E = E_a$ and $\mathcal{E}' = E_{b'}, \mathcal{E} = E_b$. Using (7.16) one gets for A_t the familiar and simple expression

$$A_t = \sqrt{\mathbf{k}^2 + m_i^2} \equiv \omega(\mathbf{k}). \tag{7.17}$$

The expression for M becomes

$$\begin{aligned} M_{\kappa',\kappa} &= -\left[\bar{u}_{a'}(\mathbf{p}'_a)\Gamma_{i,\alpha}u_a(\mathbf{p}_a)\right]P^{\alpha,\beta}(k_a)\left[\bar{u}_{b'}(\mathbf{p}'_b)\Gamma_{i,\beta}u_b(\mathbf{p}_b)\right]\cdot \\ &\quad\times\frac{1}{2\omega(\mathbf{k})}\left\{\frac{1}{\frac{1}{2}(\kappa'+\kappa)-\Delta_E+\omega(\mathbf{k})-i\epsilon}+\frac{1}{\frac{1}{2}(\kappa'+\kappa)+\Delta_E+\omega(\mathbf{k})-i\epsilon}\right\}. \end{aligned} \tag{7.18}$$

Using the separation of variables formula for $1/(\omega+a)$, given in Ref. [26], one obtains

$$\begin{aligned} M_{\kappa',\kappa} &= -\left[\bar{u}_{a'}(\mathbf{p}'_a)\Gamma_{i,\alpha}u_a(\mathbf{p}_a)\right]P^{\alpha,\beta}(k_a)\left[\bar{u}_{b'}(\mathbf{p}'_b)\Gamma_{i,\beta}u_b(\mathbf{p}_b)\right]\cdot \\ &\quad\times\frac{a}{\pi}\int_0^\infty\frac{d\lambda}{(\omega^2+\lambda^2)}\frac{\lambda^2+a^2-b^2}{(\lambda^2+(a-b)^2)(\lambda^2+(a+b)^2)} \\ &\equiv -\left[\bar{u}_{a'}(\mathbf{p}'_a)\Gamma_{i,\alpha}u_a(\mathbf{p}_a)\right]P^{\alpha,\beta}(k_a)\left[\bar{u}_{b'}(\mathbf{p}'_b)\Gamma_{i,\beta}u_b(\mathbf{p}_b)\right]\cdot\Delta(\omega;a,b), \end{aligned} \tag{7.19}$$

where $a=\frac{1}{2}(\kappa'+\kappa),\ b=\Delta_E$, and

$$\Delta(\omega;a,b) = \frac{a}{\pi}\int_0^\infty\frac{d\lambda}{(\omega^2+\lambda^2)}\frac{\lambda^2+a^2-b^2}{(\lambda^2+(a-b)^2)(\lambda^2+(a+b)^2)} \tag{7.20}$$

This expression has the big advantage that the partial wave expansion can be made readily. The CM-angle dependence $z=\cos\theta$ is given by

$$\omega^2+\lambda^2=2p'p\,[x-z]\,,\ x=\frac{1}{2p'p}\left(p'^2+p^2+\mu^2+\lambda^2\right). \tag{7.21}$$

7.2. Off-shell Interaction Kernel

In the integral equation for the left-half-shell $M_{\kappa',0}$-amplitude the left- and right-off-shell matrix elements of the interaction kernel $I_{\kappa',\kappa''}$ are needed. The lowest order contribution from scalar exchange is given by (7.17)

$$\begin{aligned} I_{\kappa',\kappa''} &= -\left[\bar{u}_{a'}(\mathbf{p}'_a)\Gamma_{i,\alpha}u_a(\mathbf{p}_a)\right]P^{\alpha,\beta}(k_a)\left[\bar{u}_{b'}(\mathbf{p}'_b)\Gamma_{i,\beta}u_b(\mathbf{p}_b)\right]\cdot \\ &\quad\times\frac{1}{2\omega(\mathbf{k})}\left\{\frac{1}{\frac{1}{2}(\kappa'+\kappa'')-\Delta_E+\omega(\mathbf{k})-i\epsilon}+\frac{1}{\frac{1}{2}(\kappa'+\kappa'')+\Delta_E+\omega(\mathbf{k})-i\epsilon}\right\}. \end{aligned} \tag{7.22}$$

Because the energy, including the quasi-particle, in the initial state is $\sqrt{s}$, the energy in the intermediate state is $\sqrt{s''}+\kappa''$, and the energy in the final state is $\sqrt{s'}+\kappa'$ The conditions on κ and κ'' from energy conservation are

$$\kappa''=\sqrt{s}-\sqrt{s''}\ ,\ \kappa'=\sqrt{s}-\sqrt{s'}. \tag{7.23}$$

which implies that all κ's are fixed in terms of the particle external and intermediate energies. This gives that

$$\begin{aligned} a_- &\equiv \frac{1}{2}(\kappa'+\kappa'')-\Delta_E=(E-E')+(\mathcal{E}-\mathcal{E}'')\,, \\ a_+ &\equiv \frac{1}{2}(\kappa'+\kappa'')+\Delta_E=(E-E'')+(\mathcal{E}-\mathcal{E}'). \end{aligned} \tag{7.24}$$

Since there is, in principle, no upper-bound on the off-shell final and intermediate energies, the expression (7.19) develops singularities, which should be taken care of by the $i\epsilon$-prescription.
In the CM-system $\mathbf{p}=-\mathbf{q}$ and $\mathbf{p}'=-\mathbf{q}'$, and

$$\Delta_E \approx \frac{M'-M}{4MM'}(p'^2-p^2)=\frac{M'-M}{2MM'}(\mathbf{q}\cdot\mathbf{k})\approx 0. \tag{7.25}$$

Hence, the simplest and very good approximation is to ignore the energy-differences (and mass-differences), i.e. non-relativistic approximation. Then one gets

$$I^{(NR)}_{0,0}(P';P) = -\left[\bar{u}_{a'}(\mathbf{p}'_a)\Gamma_{i,\alpha}u_a(\mathbf{p}_a)\right]P^{\alpha,\beta}(k_a)\left[\bar{u}_{b'}(\mathbf{p}'_b)\Gamma_{i,\beta}u_b(\mathbf{p}_b)\right]/\omega^2(\mathbf{k}). \tag{7.26}$$

For baryon-baryon scattering, in the ESC models thus far, the mass differences at the vertices are neglected. Then, $\Delta_E = 0$ and

$$a \equiv a_+ = a_- = \sqrt{s} - \frac{1}{2}\left(\sqrt{s'} + \sqrt{s''}\right). \tag{7.27}$$

Hence, from (7.19) one finds for the interaction kernel

$$K(\sqrt{s};\mathbf{p}',\mathbf{p}'') \equiv I_{\kappa',\kappa''}(P';P) = -\left[\bar{u}_{a'}(\mathbf{p}'_a)\Gamma_{i,\alpha}u_a(\mathbf{p}_a)\right] P^{\alpha,\beta}(k_a)\left[\bar{u}_{b'}(\mathbf{p}'_b)\Gamma_{i,\beta}u_b(\mathbf{p}_b)\right]\frac{1}{\omega(\mathbf{k})\,(\omega(\mathbf{k})+a-i\epsilon)}. \tag{7.28}$$

Notice that with our choice of n^μ-vector, the spinor factors will lead to the same expression in terms of the three-momenta as in the usual case. Furthermore, these OBE-potentials correspond to those from the so-called old-fashion-perturbation (OPT) graphs in Fig. 8, see [29, 30], and which for $a = 0$ become the standard Yukawa potentials: $K(\sqrt{s};\mathbf{p}',\mathbf{p}'') \to I^{(NR)}_{0,0}(P';P)$. In the configuration space ESC model calculations the NR form is used. *In momentum space calculations, it is simple to use the full relativistic form.*
For the diffractive exchanges, pomeron and odderon, being "contact interactions", there are no propagators and the Kadyshevsky and Feynman matrix elements are identical.

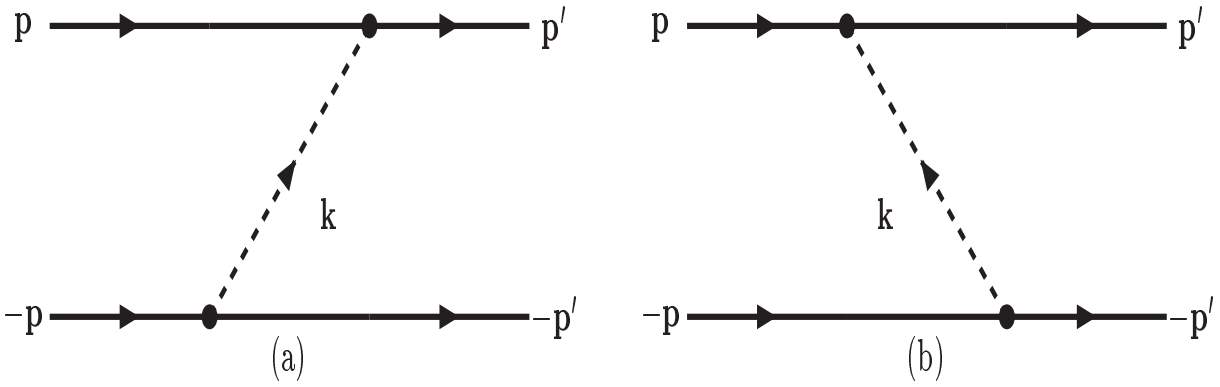

Figure 8: One-boson-exchange CM momentum-space OPT graphs: The dashed lines with momentum **k** refer to the bosons: pseudo-scalar, vector, axial-vector, or scalar mesons.

---

8. General Fourth-order Kadyshevky graphs

The fourth-order Kadyshevsky graphs, with positive energy intermediate state baryons, are shown in the figures of Appendix C.1 for the parallel graphs, and in Appendix C.2 for the crossed graphs. In this work only graphs with positive energy baryons in the intermediate states are included. M denotes the average $(M_{B_1} + M_{B_2})/2$.
In the CM, choosing n^μ as in (5.14) $n^\mu = (1,\mathbf{0})$, i.e. the quasi-particles carry no three-momentum, and

$$\mathbf{p}_a \;=\; -\mathbf{p}_b = \mathbf{p}\;,\;\; \mathbf{p}'_a = -\mathbf{p}'_b = \mathbf{p}'. \tag{8.1}$$

The integration over the zero-components can be done using the δ_+-functions, which means that

$$\begin{aligned} p_{a,0} = E_a(\mathbf{p}) \quad &, \quad p_{b,0} = E_b(\mathbf{p}) \\ p'_{a,0} = E_a(\mathbf{p}') \quad &, \quad p'_{b,0} = E_b(\mathbf{p}')\,. \end{aligned} \tag{8.2}$$

Also, the three-momenta of the intermediate state are now fixed in terms of the external momenta and the two meson momenta $\mathbf{k}_{1,2}$. For example, in graphs (a), (a'), (b), the relation is

$$\mathbf{q} \equiv \mathbf{q}_a = -\mathbf{q}_b = \mathbf{p} - \mathbf{k}_1 = \mathbf{p}' + \mathbf{k}_2, \tag{8.3}$$

and always $\mathbf{q}_a = -\mathbf{q}_b \equiv \mathbf{q}$. For the other graphs (b'), (c), and (c'), it is a little different, because the direction of the meson four-momenta is otherwise, see figures in Appendix C.1-Appendix C.2. The direction of the three-momenta can always be chosen to be the same.

For the planar and crossed fourth-order Kadyshevsky graphs, the matrix elements can be written in the general form [8]

$$M^{(//,a)}_{\sigma;\kappa',\kappa}\left(p'_a,p'_b;p_a,p_b\right) = +(2\pi)^3\int d^3q\int\frac{d^3k_1}{(2\pi)^3 2\omega_1}\int\frac{d^3k_2}{(2\pi)^3 2\omega_2}\,N^{(\sigma)}_{//}(\mathbf{p}',\mathbf{p};\mathbf{q})\cdot$$

$$\times\delta^{(3)}(\mathbf{k}_1-\mathbf{p}+\mathbf{q})\,\delta^{(3)}(\mathbf{k}_2+\mathbf{p}'-\mathbf{q})\,D^{(//,a)}_{\sigma;\kappa',\kappa}(\omega_1,\omega_2), \tag{8.4a}$$

$$M^{(X,a)}_{\sigma;\kappa',\kappa}\left(p'_a,p'_b;p_a,p_b\right) = +(2\pi)^3\int d^3q\int\frac{d^3k_1}{(2\pi)^3 2\omega_1}\int\frac{d^3k_2}{(2\pi)^3 2\omega_2}\,N^{(\sigma)}_{X}(\mathbf{p}',\mathbf{p};\mathbf{q})\cdot$$

$$\times\delta^{(3)}(\mathbf{k}_1-\mathbf{p}_a+\mathbf{q}_a)\,\delta^{(3)}(\mathbf{k}_2+\mathbf{p}'_a+\mathbf{q}_a)\,D^{(X,a)}_{\sigma;\kappa',\kappa}(\omega_1,\omega_2), \tag{8.4b}$$

where the numerators $N^{(\sigma)}_{//}(p',p;q)$ and $N^{(\sigma)}_{X}(p',p;q)$ contains the vertex factors and the fermion Dirac-operator. They depend on $\sigma = ++,+-,-+,--$ referring to a nucleon (+) and antinucleon (-) in the intermediate state.
The expressions for the fourth-order Kadyshevsky graphs are given in Appendix C.1-Appendix C.2, where the denominators $D^{//,X}_{\sigma;\kappa',\kappa}$ are given for $\sigma = [++,+-,--]$.
Since the spinor-numerator factors for all parallel, respectively crossed, graphs can be made to be the same, the fourth-order kernels $K(\mathbf{p}',\mathbf{p})$ have the denominators

$$D^{(//)}_{\sigma;\kappa',\kappa}(\omega_1,\omega_2) = \sum_{\alpha=a,a',b,b',c,c'} D^{(//,\alpha)}_{\sigma;\kappa',\kappa}(\omega_1,\omega_2), \tag{8.5}$$

$$D^{(X)}_{\sigma;\kappa',\kappa}(\omega_1,\omega_2) = \sum_{\alpha=a,a',b,b',c,c'} D^{(X,\alpha)}_{\sigma;\kappa',\kappa}(\omega_1,\omega_2), \tag{8.6}$$

The application of two-meson-exchange $K(\sqrt{s};\mathbf{p}',\mathbf{p})$ kernel in the ESC models is in configuration space. Henceforth, only the on-energy-shell matrix elements are considered, i.e. $\kappa = \kappa' = 0$.
Furthermore, in the ESC- model application to low and intermediate energy NN the restriction $\sigma = [++]$ has been imposed, since the $\sigma = [+-,-+,--]$ are suppressed by factors $1/M_N$ from the denominators. In Fig. 9, the three-momenta of the Kadyshevsky graph for the evaluation of the integrals in Eqns (8.4) are shown.

9. Two-Pseudoscalar-Exchange Potentials

The formalism below is very similar to that used in [26, 29, 30]. This because for $\kappa' = \kappa = 0$, i.e. on-energy-shell potentials, the expressions of the energy denominators $D_{\sigma;0,0}$ are identical to those obtained in the Klein-Macke formalism. In Appendix C.1-Appendix C.2 the two-meson exchange Kadyshevsky graphs are evaluated. On-energy-shell, the results are identical to those obtained from the old-fashioned perturbation theory (OPT) BW-graphs [59] and TMO-graphs [60], see e.g. Refs. [26, 29] Figures 1 and 2. [9]
To be specific, here the $\pi\pi$-exchange potential for nucleon-nucleon (NN) is derived. The results can readily be generalized to baryon-baryon channels. In ESC-models the potentials are evaluated up to order $1/M^2$. Although the expansion of Eq. (8.4) takes care of the normalization factors $N^{\sigma}_{//,X}$ of the nucleon Dirac-spinors of the initial and final nucleons, one still has to include the expansion of the normalization factors of the nucleon Dirac-spinors in the

[8] In (8.4) the arguments in the $\delta^{(3)}$-functions can have a different sign for the meson momenta. Since the rest of the integrand via the ω-variables depends on the squares of the three-momenta, by a simple sign change in the relevant meson momenta, the arguments can be made as in (8.4). *Then, the performance of the d^3q-integral leads to identical expressions for the numerators $N_G(\mathbf{p}',\mathbf{p};\mathbf{q})$ for $G = //$ and $G = X$, i.e. the parallel and crossed graphs respectively.*

[9] In Ref. [29], besides the potentials for PS-PS, also those for pseudoscalar-vector and pseudoscalar-scalar are given. These have not been used in the ESC16-model calculations

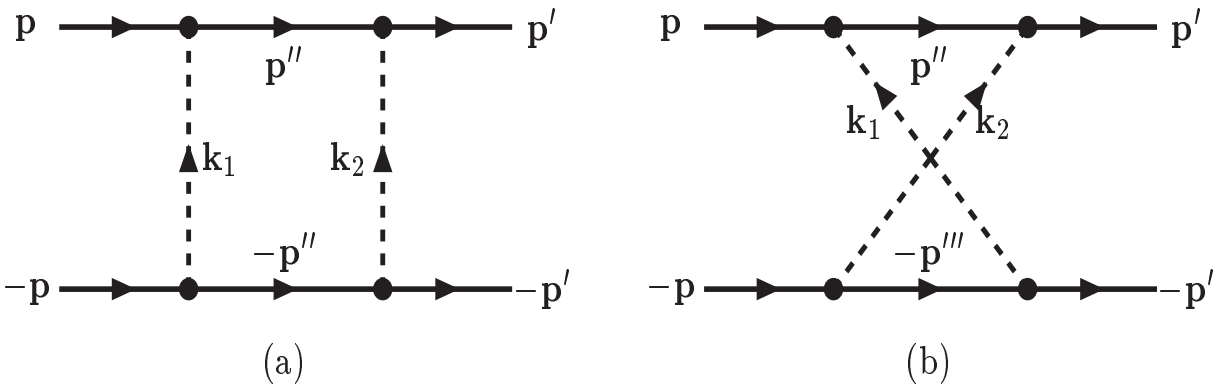

Figure 9: *CM-three-momenta graphs $\sigma = [++]$. The solid lines denote baryons. The dashed lines refer to the pseudoscalar mesons, $\mathbf{k}_1$ and $\mathbf{k}_2$. The intermediate state momenta are $\mathbf{p}'' = \mathbf{p} + \mathbf{k}_1 = \mathbf{p}' - \mathbf{k}_2$ and $\mathbf{p}''' = \mathbf{p} + \mathbf{k}_2 = \mathbf{p}' - \mathbf{k}_1$.*

intermediate two-nucleon state, which also contributes a factor of order $1/M^2$. Furthermore, there are non-adiabatic terms from the expansion of the energy denominators in $D^{\sigma}_{//,X}$.
In the following, $(\mathbf{k}_1, \omega_1)$ refers to the π meson 1 and $(\mathbf{k}_2, \omega_2)$ refers to the π meson 2. Using the vertex operators as given in table 5, the planar (BW+TMO) and crossed (BW) graphs Fig. 9 give [10]

$$V^{(\sigma)}_{\pi\pi}(i) \;=\; C^{(i)}_{NN}(I)\left(\frac{f_{NN\pi}}{m_\pi}\right)^4 \int\!\!\int \frac{d^3k_1 d^3k_2}{(2\pi)^6}\, e^{i(\mathbf{k}_1+\mathbf{k}_2)\cdot\mathbf{r}}\, F_\pi(\mathbf{k}_1^2) F_\pi(\mathbf{k}_2^2)\, O^i_{PS}(\sigma)\, D^{(\sigma)}_i(\omega_1,\omega_2). \tag{9.1a}$$

Here $i = //, X$ for the planar and crossed graphs respectively. The isospin coefficients for $\pi\pi$ are $C^{(//)}_{NN}(I) = 3 - \boldsymbol{\tau}_1\cdot\boldsymbol{\tau}_2$ and $C^{(X)}_{NN}(I) = 3 + \boldsymbol{\tau}_1\cdot\boldsymbol{\tau}_2$. For $\pi\eta$, the isospin coefficients are $C^{(//)}_{NN}(I) = C^{(X)}_{NN}(I) = C^{(1,0)}_{NN}(I) = \boldsymbol{\tau}_1\cdot\boldsymbol{\tau}_2$, and $f^4_{NN\pi} \to f^2_{NN\pi} f^2_{NN\eta}$. The momentum operators $O^{(//,X)}_{PS}(\sigma)$ are displayed in Table 5.

Table 5: Momentum operators $O^{(i)}(\mathbf{k}_1, \mathbf{k}_2)$ for the planar (//) and crossed (X) π-meson-exchange graphs. The subscript PS refers to the π-pseudoscalar operators.

σ		$O^{(i)}(\mathbf{k}_1, \mathbf{k}_2)$
(++)	$O^{(//)}_{PS}$	$+[2(\mathbf{k}_1\cdot\mathbf{k}_2)^2 - 2\boldsymbol{\sigma}_1\cdot(\mathbf{k}_1\times\mathbf{k}_2)\boldsymbol{\sigma}_2\cdot(\mathbf{k}_1\times\mathbf{k}_2)]$
(++)	$O^{(X)}_{PS}$	$+[2(\mathbf{k}_1\cdot\mathbf{k}_2)^2 + 2\boldsymbol{\sigma}_1\cdot(\mathbf{k}_1\times\mathbf{k}_2)\boldsymbol{\sigma}_2\cdot(\mathbf{k}_1\times\mathbf{k}_2)]$
(+-)	$O^{(//)}_{PS}$	$-[2(\mathbf{k}_1\cdot\mathbf{k}_2) - i(\boldsymbol{\sigma}_1 + \boldsymbol{\sigma}_2)\cdot(\mathbf{k}_1\times\mathbf{k}_2)]$
(+-)	$O^{(X)}_{PS}$	$-[2(\mathbf{k}_1\cdot\mathbf{k}_2) + i(\boldsymbol{\sigma}_1 + \boldsymbol{\sigma}_2)\cdot(\mathbf{k}_1\times\mathbf{k}_2)]$

9.1. Nucleon-nucleon in the intermediate states: $\sigma = [++]$

As shown in Appendix D, the adiabatic and non-adiabatic denominators from the relativistic Kadyshevsky denominator expressions are identical to those derived in [26, 29]. Therefore, for completeness, listed here are the PS-PS exchange potentials from these references. Graph (a) in Fig. 9 generates the parallel BW and TMO graphs described in [26, 29], and graph (b) in Fig.9 generates the crossed BW graphs.

[10] For the sign compare with formulas in [26], and see footnote in Appendix A.

The parallel BW graphs and their "mirror" graphs give

$$V^{BW}_{\pi\pi}(//) = +C^{(//)}_{NN}(I)\left(\frac{f_{NN\pi}}{m_\pi}\right)^4 \int\int \frac{d^3k_1 d^3k_2}{(2\pi)^6}\, e^{i(\mathbf{k}_1+\mathbf{k}_2)\cdot\mathbf{r}}\, F_\pi(\mathbf{k}_1^2)F_\pi(\mathbf{k}_2^2)\, D^{BW}_{//}(\omega_1,\omega_2)\cdot$$
$$\times \left[(\mathbf{k}_1\cdot\mathbf{k}_2)^2 - [\boldsymbol{\sigma}_1\cdot(\mathbf{k}_1\times\mathbf{k}_2)][\boldsymbol{\sigma}_2\cdot(\mathbf{k}_1\times\mathbf{k}_2)]\right] \tag{9.2}$$

The crossed BW graphs and their "mirror" graphs give

$$V^{BW}_{\pi\pi}(X) = +C^{(//)}_{NN}(I)\left(\frac{f_{NN\pi}}{m_\pi}\right)^4 \int\int \frac{d^3k_1 d^3k_2}{(2\pi)^6}\, e^{i(\mathbf{k}_1+\mathbf{k}_2)\cdot\mathbf{r}}\, F_\pi(\mathbf{k}_1^2)F_\pi(\mathbf{k}_2^2)\, D^{BW}_{//}(\omega_1,\omega_2)\cdot$$
$$\times \left[(\mathbf{k}_1\cdot\mathbf{k}_2)^2 + [\boldsymbol{\sigma}_1\cdot(\mathbf{k}_1\times\mathbf{k}_2)][\boldsymbol{\sigma}_2\cdot(\mathbf{k}_1\times\mathbf{k}_2)]\right] \tag{9.3}$$

The adiabatic energy denominators $D_i(\omega_1,\omega_2)$, and the non-adiabatic ones $D_i^{(1)}(\omega_1,\omega_2)$ are given in Table 6.

Table 6: Planar and crossed graph energy denominators: (i) adiabatic $D_i(\omega_1,\omega_2)$, and (ii) non-adiabatic $D_i^{(1)}$.

$$D_{//}(\omega_1,\omega_2) = +\frac{1}{2\omega_1^2\omega_2^2}\left[\frac{1}{\omega_1}+\frac{1}{\omega_2}-\frac{1}{(\omega_1+\omega_2)}\right] \quad , \quad D^{(1)}_{//}(\omega_1,\omega_2) = +\frac{1}{2\omega_1^2\omega_2^2}\left[\frac{1}{\omega_1^2}+\frac{1}{\omega_2^2}\right]$$
$$D_X(\omega_1,\omega_2) = -\frac{1}{2\omega_1^2\omega_2^2}\left[\frac{1}{\omega_1}+\frac{1}{\omega_2}-\frac{1}{(\omega_1+\omega_2)}\right] \quad , \quad D^{(1)}_X(\omega_1,\omega_2) = -\frac{1}{\omega_1^2\omega_2^2}\left[\frac{1}{\omega_1^2}+\frac{1}{\omega_2^2}\right].$$

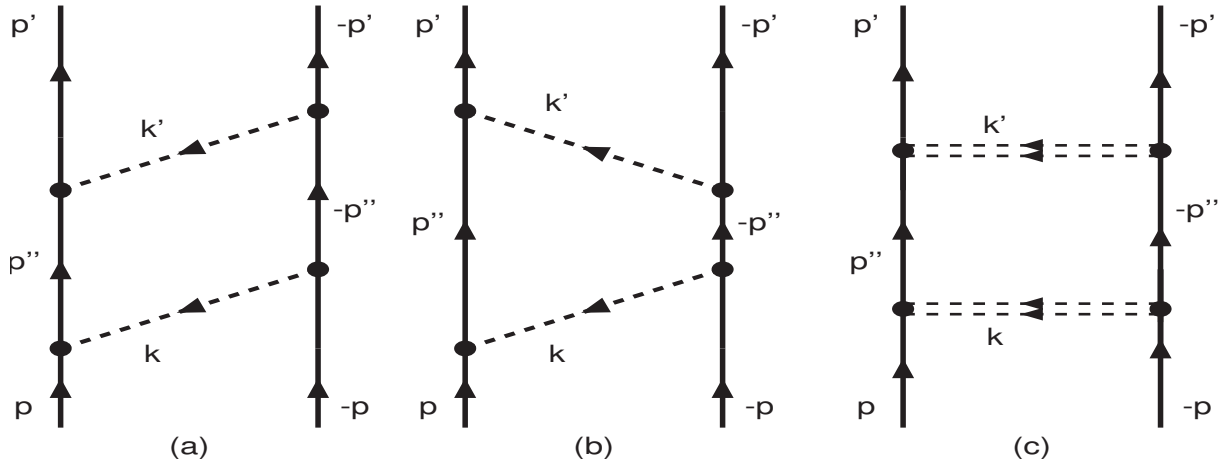

Figure 10: Planar-box time-ordered TMO two-meson-exchange graphs (a), (b), and OPE-iterated potential-graph (c). The double lines in (c) denote the instantenuous exchanges To (a) and (b) the "mirror" graphs have to be added. For non-identical mesons, the graphs with interchanged mesons have to be added.

9.2. TMO and OPE-iterated Pion-exchange Potential

The fourth-order potential $V^{(4)}$ consists of two parts. The first part is given by the fourth-order planar and crossed BW graphs, shown in Figs. 11(a) and 10, respectively, and their "mirror" counterparts. The second part occurs, because the two different time orderings are not distinguished in the one-boson-exchange graphs. Hence, solving the scattering equation does not generate the time-ordered TMO graphs of Figs. 10(a) and 10(b), nor their "mirror"

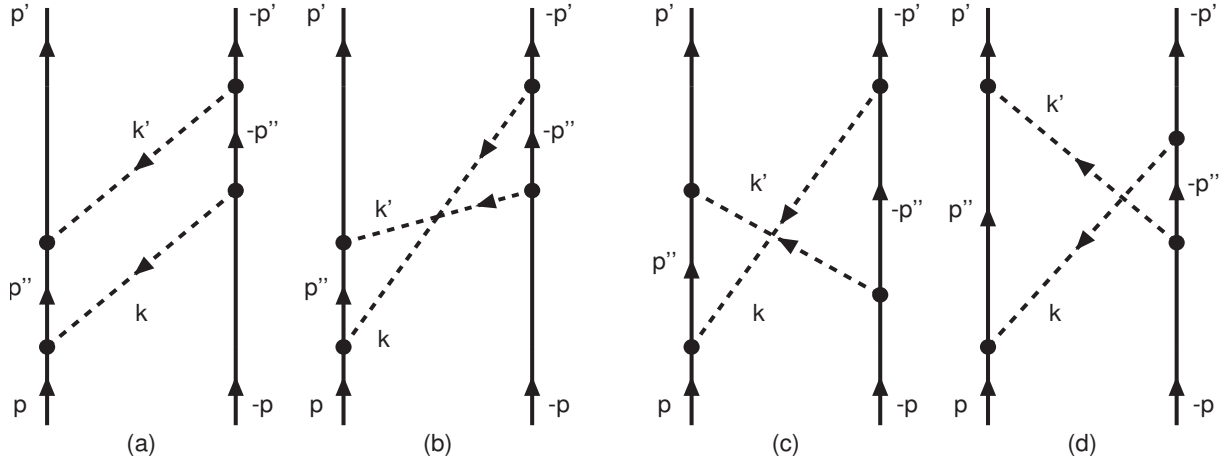

Figure 11: BW two-meson-exchange OPT graphs: (a) planar and (b)–(d) crossed box. The dashed lines with momenta $\mathbf{k}$ and $\mathbf{k}'$ refer to pions, for example. To these one has to add the "mirror" graphs, and the graphs where the two meson lines are interchanged.

counterparts. These TMO graphs are included explicitly, by subtracting the once-iterated one-meson contribution, see [26, 29], $V^{(4)}_{\rm Born} = V^{(2)} g_{++}\, V^{(2)}$, with $V^{(2)} = K^{(2)}$, and so the fourth-order TMO-potential reads $V^{(4)}_{TMO} = K^{(4)}_{TMO} - V^{(2)} g_{++}\, V^{(2)}$, where g_{++} is the Green function for the Lippmann-Schwinger equation, as given by [26],

$$g_{++}(\mathbf{p}; W) = \frac{1}{(2\pi)^3}\, \Lambda^a_+(\mathbf{p})\Lambda^b_+(-\mathbf{p})\, \frac{M}{\mathbf{p}_i^2 - \mathbf{p}^2 + i\epsilon}\,. \tag{9.4}$$

This subtraction has already been accounted for the $D_{//}$ in Table 6.
The contribution from TMO-graphs (a) and (b) in Fig. (10)

$$\begin{aligned} V^{(TMO)}_{\parallel} &= -\frac{(3 - 2\boldsymbol{\tau}_1\cdot\boldsymbol{\tau}_2)}{(2\pi)^6}\left(\frac{f}{m_\pi}\right)^4 \int\int d^3k_1 d^3k_2\; F(\mathbf{k}_1^2)F(\mathbf{k}_2^2)\, \frac{e^{i(\mathbf{k}_1+\mathbf{k}_2)\cdot\mathbf{r}}}{\omega(\mathbf{k}_1)\omega(\mathbf{k}_2)}\cdot \\ &\times\quad (a - i\,\mathbf{b}\cdot\boldsymbol{\sigma}_1)(a - i\,\mathbf{b}\cdot\boldsymbol{\sigma}_2)[E_{\mathbf{p}} + E_{\mathbf{p}-\mathbf{k}_1} - W + \omega(\mathbf{k}_1)]^{-1}\cdot \\ &\times\quad [2E_{\mathbf{p}-\mathbf{k}_1} - W]^{-1}[E_{\mathbf{p}'} + E_{\mathbf{p}-\mathbf{k}_1} - W + \omega(\mathbf{k}_2)]^{-1}\,, \end{aligned} \tag{9.5}$$

where the approximation $W = 2E_{\mathbf{p}}$ is made.
To avoid double counting when solving the Schrödinger equation, one subtracts from (9.5) the once iterated OPE shown in panel (c) of Fig. 10

$$\begin{aligned} T^{(4)}_{Born} &= -\frac{(3 - 2\boldsymbol{\tau}_1\cdot\boldsymbol{\tau}_2)}{(2\pi)^6}\left(\frac{f}{m_\pi}\right)^4 \int\int d^3k_1 d^3k_2\; F(\mathbf{k}_1^2)F(\mathbf{k}_2^2)\, \frac{e^{i(\mathbf{k}_1+\mathbf{k}_2)\cdot\mathbf{r}}}{\omega^2(\mathbf{k}_1)\omega^2(\mathbf{k}_2)}\cdot \\ &\times\quad (a - i\mathbf{b}\cdot\boldsymbol{\sigma}_1)(a - i\mathbf{b}\cdot\boldsymbol{\sigma}_2)[2E_{\mathbf{p}-\mathbf{k}_1} - W]^{-1}. \end{aligned} \tag{9.6}$$

The remaining difference

$$V_{TMO} \equiv V^{(TMO)}_{\parallel} - T^{(4)}_{Born} \tag{9.7}$$

is referred to as the TMO-potential. This contribution to the potential is neglected in the BW-potential, but is part of the TMO-potential [60]. Since all corrections are taken up to order $1/M^2$ in the potentials into account, which come from the recoil-corrections in the denominators from the intermediate states, it is clear that this contribution should be included. Notice that the adiabatic contributions vanish. This is obvious for the contribution from the leading terms in

all vertices. However, also for the $1/M$-contributions from the vertices cancel [26]. The non-adiabatic contributions give nonzero potentials in first order in $1/M$, and are given below.
(i) *Non-adiabatic contributions,* $1/M$*-terms*:
Expanding the energies in the intermediate states to order $1/M$, one finds

$$V^{(1)}_{TMO}(r) = (3-2\boldsymbol{\tau}_1\cdot\boldsymbol{\tau}_2)\left(\frac{f}{m_\pi}\right)^4 (2\pi)^{-6}\int\int d^3k_1 d^3k_2\,\frac{e^{i(\mathbf{k}_1+\mathbf{k}_2)\cdot\mathbf{r}}}{\omega^3(\mathbf{k}_1)\omega^2(\mathbf{k}_2)}\cdot$$

$$\times\quad F(\mathbf{k}_1^2)F(\mathbf{k}_2^2)\Big[a^2-(\mathbf{b}\cdot\boldsymbol{\sigma}_1)(\mathbf{b}\cdot\boldsymbol{\sigma}_2)\Big]\,. \tag{9.8}$$

(ii) *Non-adiabatic contributions,* $(1/M)^2$*-terms*:
Expanding the energies in the intermediate states to order $(1/M)^2$, one finds

$$V^{(2)}_{TMO}(r) = \frac{(3-2\boldsymbol{\tau}_1\cdot\boldsymbol{\tau}_2)}{(2\pi)^6}\left(\frac{1}{4M}\right)\left(\frac{f}{m_\pi}\right)^4\int\int d^3k_1 d^3k_2\,e^{i(\mathbf{k}_1+\mathbf{k}_2)\cdot\mathbf{r}}$$

$$\times\quad F(\mathbf{k}_1^2)F(\mathbf{k}_2^2)\Big[a^2-(\mathbf{b}\cdot\boldsymbol{\sigma}_1)(\mathbf{b}\cdot\boldsymbol{\sigma}_2)\Big]\cdot(\mathbf{k}_1\cdot\mathbf{k}_2)\cdot$$

$$\times\quad\left\{\frac{1}{\omega^4(\mathbf{k}_1)\omega^2(\mathbf{k}_2)}+\frac{1}{\omega^2(\mathbf{k}_1)\omega^4(\mathbf{k}_2)}+\frac{1}{\omega^3(\mathbf{k}_1)\omega^3(\mathbf{k}_2)}\right\}\,. \tag{9.9}$$

Notice here the well-known cancellation between the non-adiabatic contribution from the BW-graphs and the third term in the curly brackets of (9.9), see [26]. For the explicit form of these potentials, see Refs. [26, 29].

10. One-pair and Two-pair Exchange Potentials

For the 1-pair and 2-pair momentum-space graphs in Fig. 12 the contribution to the matrix elements can be written in the general form

$$M^{(1-pair)}_{\sigma;\kappa',\kappa}\left(p'_a,p'_b;p_a,p_b\right) = +(2\pi)^3\int d^3q\int\frac{d^3k_1}{(2\pi)^3 2\omega_1}\int\frac{d^3k_2}{(2\pi)^3 2\omega_2}\,N^{(\sigma)}_{1-pair}(\mathbf{p}',\mathbf{p};\mathbf{q})\cdot$$

$$\times\delta^{(3)}(\mathbf{p}'+\mathbf{k}_1+k_2-\mathbf{p})\,\delta^{(3)}(\mathbf{p}''-\mathbf{p}'+\mathbf{k}_1)\,\delta^{(3)}(\mathbf{p}''-\mathbf{k}_2-\mathbf{q})\,D^{(1-pair)}_{\sigma;\kappa',\kappa}(\omega_1,\omega_2), \tag{10.1a}$$

$$M^{(2-pair)}_{\kappa',\kappa}\left(p'_a,p'_b;p_a,p_b\right) = +(2\pi)^3\int\frac{d^3k_1}{(2\pi)^3 2\omega_1}\int\frac{d^3k_2}{(2\pi)^3 2\omega_2}\,N_{2-pair}(\mathbf{p}',\mathbf{p})\cdot$$

$$\times\delta^{(3)}(\mathbf{p}'+\mathbf{k}_1+\mathbf{k}_2-\mathbf{p})D^{(2-pair)}_{\kappa',\kappa}(\omega_1,\omega_2), \tag{10.1b}$$

where the numerators $N^{(\sigma)}_{1-pair}$ and N_{2-pair} contain the vertex factors etc. The expressions for the 1-pair and 2-pair Kadyshevsky graphs are given in section Appendix E, Eqns. E.4 and (E.8), together with the denominators.
The corresponding time-ordered (OPT) pair graphs are shown in Fig. 13, which have been evaluated with Gaussian form factors in Ref. [30]. The adiabatic energy denominators corresponding to the graphs in Fig. 13 are are given in Table 7. The non-adiabatic energy denominators corresponding to the graphs in Fig. 13 are are given in Table 8. As shown in Appendix E, the adiabatic and non-adiabatic denominators from the relativistic Kadyshevsky denominator expressions are identical to those derived in [30]. For a more complete explanation and derivation, see Ref. [30].

11. ESC16-model: Fitting NN⊕YN⊕YY-data

In the simultaneous χ^2-fit of the NN-, YN-, and YY-data a *single set of parameters* was used, which means the same parameters for all BB-channels. The input NN-data are the same as in Ref. [2], and the reader is refered to this

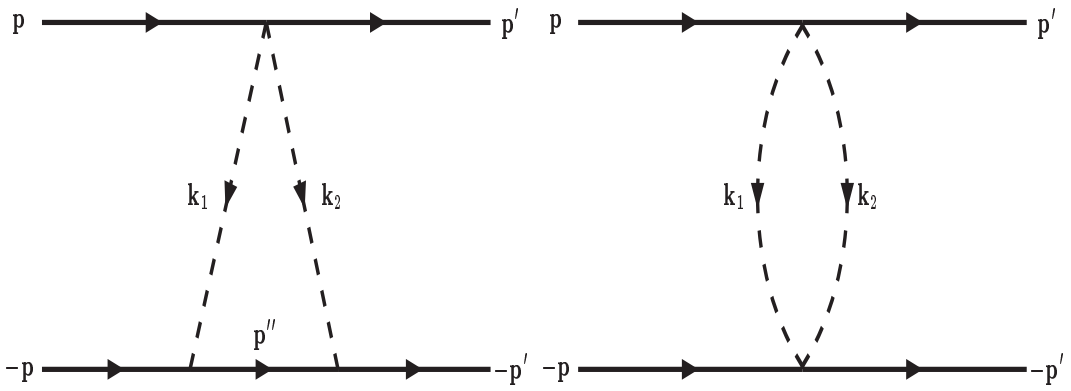

Figure 12: *One- and Two-pair Feynman graphs.*

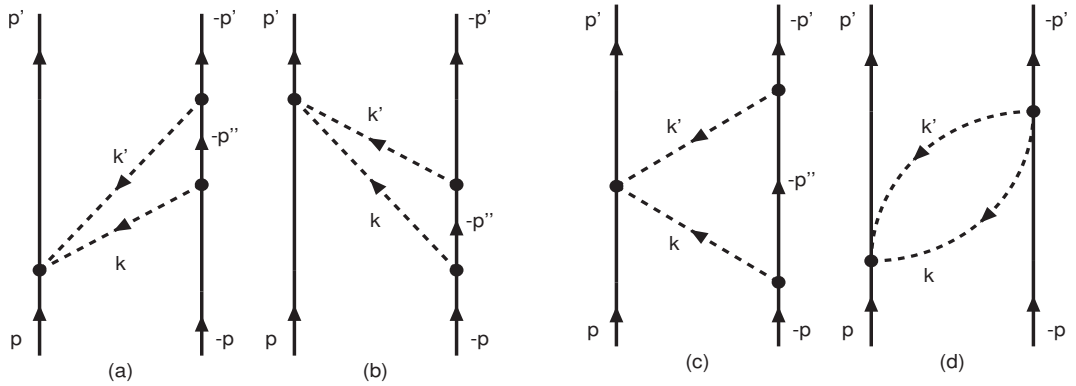

Figure 13: One- and Two-pair exchange time-ordered (OPT) graphs. To these are added the "mirror" graphs, and the graphs where the meson lines are interchanged.

Table 7: Adiabatic energy denominators 1-pair and 2-pair graphs.

$$D_a^{(1)}(\omega_1,\omega_2) = \frac{1}{2\omega_1\omega_2}\,\frac{1}{\omega_2(\omega_1+\omega_2)} \quad , \quad D_b^{(1)}(\omega_1,\omega_2) = \frac{1}{2\omega_1^2\omega_2^2},$$
$$D_c^{(1)}(\omega_1,\omega_2) = \frac{1}{2\omega_1\omega_2}\,\frac{1}{\omega_1(\omega_1+\omega_2)} \quad , \quad D^{(2)}(\omega_1,\omega_2) = -\frac{1}{2\omega_1\omega_2}\,\frac{1}{(\omega_1+\omega_2)}.$$

Table 8: Adiabatic energy denominators 1-pair and 2-pair graphs.

$$D_a^{(na)}(\omega_1,\omega_2) = \frac{1}{2\omega_1\omega_2}\,\frac{1}{\omega_2^2(\omega_1+\omega_2)} \quad , \quad D_b^{(na)}(\omega_1,\omega_2) = \frac{1}{2\omega_1\omega_2}\left(\frac{1}{\omega_1^2\omega_2}+\frac{1}{\omega_1\omega_2^2}\right),$$
$$D_c^{(na)}(\omega_1,\omega_2) = \frac{1}{2\omega_1\omega_2}\,\frac{1}{\omega_1^2(\omega_1+\omega_2)}.$$

paper for a description of the employed phase shift analysis [61, 62, 63]. Note that in addition to the NN-phases, including their correlations, in the ESC16-model also the NN-low energy parameters and the deuteron binding energy is fitted. The YN-data are those used in Ref. [3] with the addition of higher energy data, see Ref. [6]. Of course, it is to be expected that the accurate and very numerous NN-data essentially fix most of the parameters. Only some of the parameters, for example, certain $F/(F+D)$-ratios, are quite influenced by the YN-data. In the fitting procedure, the following constraints are applied: (i) A strong restriction imposed on YN-models is the absence of S=-1 bound states. (ii) During the fitting process, sometimes constraints are imposed in the form of 'pseudo-data' for some YN scattering lengths. These constraints are based on experiences with Nijmegen YN-models in the past or on imposing constraints from the G-matrix results. In some cases, it is necessary to add some extra weight of the YN-scattering data w.r.t. the NN-data in the fitting process. (iii) After obtaining a solution for the scattering data, the corresponding model is tested by checking the corresponding G-matrix results for the well-depths for $U_\Sigma > 0$ and $U_\Xi < 0$, and sufficient s-wave spin splitting in the U_Λ. If not satisfactory, the scattering data, are refitted etc. This iterative process implements the constraints from the G-matrix well-depths results, and plays a vital role in obtaining the final results of the combined fit. (For the G-matrix approach to hyperon-nucleus systems, see e.g. Ref. [64].) The fitting process is discussed more elaborately in Ref. [6].

The χ^2 is a very shallow function of the quark-core parameter, which influences only the YN- and YY-channels. Accordingly, solutions have been obtained using different assumptions about the quark-core-effects, all with a strength of about 25% of the total diffractive contribution. In previous work [13], models ESC08a and ESC08a", the solutions were obtained by assuming quark-core effects only for the channels where the [51]-component is dominant: $\Sigma^+p(^3S_1, I=3/2), \Sigma N(^1S_0, I=1/2)$, and $\Xi N(^1S_0, I=1)$. The solution ESC16 is obtained by application of the quark-core effects according to equation (8.4) in [13], see Ref. [6] for a full description of the Pauli-blocking scheme.

Like in the NN-fit, described in Ref. [2], also in the simultaneous χ^2-fit of the NN- and YN-data, it appeared again that the OBE-couplings could be constrained successfully by the 'naive' predictions of the QPC-model [45, 46]. Although these predictions, see section Appendix H, are 'bare' ones; it is tried to keep during the searches many OBE-couplings in the neighborhood of the QPC-values. Also, it appeared that one can either fix the $F/(F+D)$ ratios to those as suggested by the QPC-model, or apply the same restraining strategy as for the OBE-couplings.

11.1. Fitted BB-parameters

The treatment of the broad mesons ρ and ϵ is similar to that in the OBE-models [33, 34]. For the ρ-meson, the same parameters are used as in these references. However, for the $\epsilon = f_0(620)$ in this work the mass $m_\epsilon = 620$ MeV and width $\Gamma_\epsilon = 464$ MeV. Using the the Bryan-Gersten "dipole" parameters [65] for the two-pole approximation one gets: $m_1 = 455.15919$ MeV, $m_2 = 1158.56219$ MeV, and $\beta_1 = 0.28193, \beta_2 = 0.71807$. Other meson masses are given in Table 9. The sensitivity for the values of the cut-off masses of the η and η' is very weak. Therefore, the {1}-cut-off mass for the pseudoscalar nonet is set equal to that for the {8}. Likewise, for the two nonets of the axial-vector mesons, see table 9. Furthermore, a rather shallow dependence on the value of α_P in the range 0.33-0.40 was found. Therefore, it is fixed at the Cabibbo-theory value 0.365.

Summarizing, the parameters for baryon-baryon (BB) are (i) NN Meson-couplings: $f_{NN\pi}, f_{NN\eta'}$, $g_{NN\rho}, g_{NN\omega}$, $f_{NN\rho}, f_{NN\omega}$, $g_{NNa_0}, g_{NN\epsilon}$, g_{NNa_1}, f_{NNa_1}, $g_{NNf_1'}$, $f_{NNf_1'}$, f_{NNb_1}, $f_{NNh_1'}$, (ii) $F/(F+D)$-ratios: α_V^m, α_A, (iii) NN Pair couplings: $g_{NN(\pi\pi)_1}, f_{NN(\pi\pi)_1}$, $g_{NN(\pi\rho)_1}$, $g_{NN\pi\omega}, g_{NN\pi\eta}, g_{NN\pi\epsilon}$, (iv) Diffractive couplings and mass parameters g_{NNP}, g_{NNO}, f_{NNO}, m_P, m_O, (v) Meson cut-off masses: $\Lambda_8^P = \Lambda_1^P = \Lambda_8^B = \Lambda_1^B$, Λ_8^V, Λ_1^V, Λ_8^S, Λ_1^S, and $\Lambda_8^A = \Lambda_1^A$.

The pair coupling $g_{NN(\pi\pi)_0}$ was kept fixed at zero. Note that in the interaction Hamiltonians of the pair-couplings (3.10)-(3.14) the partial derivatives are scaled by m_π, and there is a scaling mass M_N.

The ESC-model described here is fully consistent with SU(3)-symmetry using a straightforward extension of the NN-model to YN and YY. This is the case for the OBE- and TPS-potentials, as well as for the Pair-potentials. For example $g_{(\pi\rho)_1} = g_{A_8VP}$, and besides $(\pi\rho)$-pairs one sees also that $KK^*(I=1)$- and $KK^*(I=0)$-pairs contribute to the NN potentials. All $F/(F+D)$ ratios are taken as fixed with heavy-meson saturation in mind. The approximation was made to neglect the baryon mass differences in the TPS-potentials. (This because, not yet worked out have been the formulas for the inclusion of these mass differences, which is straightforward in principle.)

11.2. Coupling Constants, $F/(F+D)$ Ratios, and Mixing Angles

In Table 9 the ESC16 meson masses are given, and the fitted couplings and cut-off parameters. Note that the axial-vector couplings for the B-mesons are scaled with m_{B_1}. The mixing for the pseudo-scalar, vector, and scalar

mesons, as well as the handling of the diffractive potentials, has been described elsewhere, see e.g. Refs. [34, 35]. The mixing scheme of the axial-vector mesons is completely similar to that for the vector mesons, except for the mixing angle. In [6] the SU(3) singlet and octet couplings are listed, and also the $F/(F+D)$-ratios and mixing angles. Also, the Pauli-blocking effect parameter a_{PB}, described in [13], section 8, for ESC16 is given. As mentioned above, searched are for solutions where all OBE-couplings are compatible with the QPC-predictions. This time, the QPC-model contains a mixture of the $^3P_0$ and $^3S_1$ mechanism, whereas in Ref. [2] only the $^3P_0$-mechanism was considered. For the pair-couplings all $F/(F+D)$-ratios were fixed to the predictions of the QPC-model.

Table 9: Meson couplings and parameters employed in the ESC16-potentials. Coupling constants are at $\mathbf{k}^2 = 0$. An asterisk denotes that the coupling constant is constrained via SU(3). The masses and Λ's are given in MeV. Notation $f_0 = \varepsilon(620)$, $f_0' = S^*(993)$.

meson	mass	$g/\sqrt{4\pi}$	$f/\sqrt{4\pi}$	Λ
π	138.04		0.2684	1030.96
η	547.45		0.1368*	,,
η'	957.75		0.3181	,,
ρ	768.10	0.5793	3.7791	680.79
ϕ	1019.41	–1.2384*	2.8878*	,,
ω	781.95	3.1149	–0.5710	734.21
a_1	1270.00	–0.8172	–1.6521	1034.13
f_1	1420.00	0.5147	4.4754	,,
f_1'	1285.00	–0.7596	–4.4179	,,
b_1	1235.00		–2.2598	1030.96
h_1	1380.00		–0.0830*	,,
h_1'	1170.00		–1.2386	,,
a_0	962.00	0.5393		830.42
f_0'	993.00	–1.5766*		,,
f_0	620.00	2.9773		1220.28
Pomeron	212.06	2.7191		
Odderon	268.81	4.1637	–3.8859	

One notices that all the BBM α's have values rather close to those expected from the QPC-model. In the ESC16 solution $\alpha_A \approx 0.383$, which is close to $\alpha_A \sim 0.4$. As in previous works, e.g. Ref. [33, 34], $\alpha_V^e = 1$ is kept fixed. Above, it is remarked that the axial-nonet parameters may be sensitive to whether or not the heavy pseudoscalar nonet with the $\pi(1300)$ are included.

Table 10: Pair-meson coupling constants employed in the ESC16 MPE-potentials. Coupling constants are at $\mathbf{k}^2 = 0$. The F/(F+D) ratios are QPC-predictions, except that $\alpha_{(\pi\omega)} = \alpha_P$, which is very close to QPC.

J^{PC}	SU(3)-irrep	$(\alpha\beta)$	$g/4\pi$	$F/(F+D)$
0^{++}	$\{1\}$	$g(\pi\pi)_0$	—	—
0^{++}	,,	$g(\sigma\sigma)$	—	—
0^{++}	$\{8\}_s$	$g(\pi\eta)$	-0.6894	1.000
1^{--}	$\{8\}_a$	$g(\pi\pi)_1$	0.2519	1.000
		$f(\pi\pi)_1$	–1.7762	0.400
1^{++}	,,	$g(\pi\rho)_1$	5.7017	0.400
1^{++}	,,	$g(\pi\sigma)$	–0.3899	0.400
1^{++}	,,	$g(\pi P)$	—	—
1^{+-}	$\{8\}_s$	$g(\pi\omega)$	–0.3287	0.365

In Table 10 listed are the fitted Pair-couplings for the MPE-potentials. Only one-pair graphs are included, in order to avoid double counting, see Ref. [2]. The $F/(F+D)$-ratios are all fixed, assuming heavy-boson domination of the pair-vertices. The ratios are taken from the QPC-model for $Q\bar{Q}$-systems with the same quantum numbers as the dominating boson. For example, the α-parameter for the axial $(\pi\rho)_1$-pair could be fixed at the quark-model prediction 0.40, see Table 10. The *BB*-Pair couplings are calculated, assuming unbroken SU(3)-symmetry, from the NN-Pair coupling and the $F/(F+D)$-ratio using SU(3). Unlike in Refs. [29, 30], here, the pair couplings are not fixed using a theoretical model, *e.g.* based on heavy-meson saturation and chiral-symmetry. So, in addition to the 14 parameters used in Refs. [29, 30], one has 6 pair-coupling fit parameters. In Table 10 the fitted pair-couplings are given. Note that the $(\pi\pi)_0$-coupling gets a non-zero contribution from the $\{8_s\}$-pairs, giving $g_{(\pi\pi)_0} = -0.688/2 \approx -0.34$, which is opposite in sign compared to the result in [29, 30]. The $f_{(\pi\pi)_1}$-pair coupling has opposite sign as compared to Refs. [29, 30]. In a model with a more complex and realistic meson-dynamics [43], this coupling is predicted as found in the present ESC-fit. The $(\pi\rho)_1$-coupling is large as expected from A_1-saturation, see Refs. [29, 30].

In Table 9 the NN OBE-coupling constants and the Gaussian cut-offs Λ are shown. The used $\alpha =: F/(F+D)$ ratios for the OBE-couplings are: pseudoscalar mesons $\alpha_P = 0.365$, vector mesons $\alpha_V^e = 1.0, \alpha_V^m = 0.4655$, scalar-mesons $\alpha_S = 1.0$, axial mesons $\alpha_A = 0.3830$ and $\alpha_B = 0.4$. In Table 11 the BBM-couplings are are displayed for the ESC16 model.

In Table 10 the MPE-coupling constants are shown. The used $\alpha =: F/(F+D)$ ratios for the MPE-couplings are: $(\pi\eta)$ pairs $\alpha(\{8_s\}) = 1.0$, $(\pi\pi)_1$ pairs $\alpha_V^e(\{8\}_a) = 1.0, \alpha_V^m(\{8\}_a) = 0.400$, and the $(\pi\rho)_1$ pairs $\alpha_A(\{8\}_a) = 0.400$. The $(\pi\omega)$ pairs $\alpha(\{8_s\})$ has been set equal to $\alpha_P = 0.365$.

Table 11: Coupling constants for model ESC16, divided by $\sqrt{4\pi}$. *M* refers to the meson. The coupling constants are listed in the order pseudoscalar, vector (g and f), axial vector A (g and f), scalar, axial vector B, and diffractive.

	M	NNM	$\Sigma\Sigma M$	$\Sigma\Lambda M$	$\Xi\Xi M$	M	ΛNM	$\Lambda\Xi M$	ΣNM	$\Sigma\Xi M$
f	π	0.2684	0.1959	0.1968	–0.0725	K	–0.2681	0.0713	0.0725	–0.2684
g	ρ	0.5793	1.1586	0.0000	0.5793	K^*	–1.0034	1.0034	–0.5793	–0.5793
f		3.7791	3.5185	2.3323	–0.2606		–4.2132	1.8810	0.2606	–3.7791
g	a_1	–0.8172	–0.6260	–0.5822	0.1912	K_{1A}	0.8333	–0.2511	–0.1912	0.8172
f		–1.6521	–1.2656	–1.1770	0.3865		1.6846	–0.5076	–0.3865	1.6521
g	a_0	0.5393	1.0786	0.0000	0.5393	κ	–0.9341	0.9341	–0.5393	–0.5393
f	b_1	–2.2598	–1.8078	–1.5656	0.4520	K_{1B}	2.3484	–0.7828	–0.4520	2.2598
	M	NNM	$\Lambda\Lambda M$	$\Sigma\Sigma M$	$\Xi\Xi M$	M	NNM	$\Lambda\Lambda M$	$\Sigma\Sigma M$	$\Xi\Xi M$
f	η	0.1368	–0.1259	0.2599	–0.1958	η'	0.3181	0.3711	0.2933	0.3852
g	ω	3.1148	2.4820	2.4820	1.8492	ϕ	–1.2384	–2.0171	–2.0171	–2.7958
f		–0.5710	–3.2282	–0.2863	–4.4144		2.8878	–0.3819	3.2380	–1.8416
g	f_1'	–0.7596	–0.1213	–1.0133	0.0710	f_1	0.5147	1.0503	0.3019	1.2117
f		–4.4179	–3.1274	–4.9303	–2.7386		4.4754	5.5582	4.0450	5.8844
g	ε	2.9773	2.3284	2.3284	1.6795	f_0	–1.5766	–2.2485	–2.2485	–2.9205
f	h_1'	–1.2386	0.1171	–1.6905	0.5690	h_1	–0.0830	1.8346	–0.7222	2.4738
g	P	2.7191	2.7191	2.7191	2.7191					
g	O	4.1637	4.1637	4.1637	4.1637					
f		–3.8859	–3.8859	–3.8859	–3.8859					

12. ESC16-model *NN*-Results

12.1. Nucleon-nucleon Fit, Low-energy and Phase Parameters

In this section the *NN* results of [5] are reviewed. For a more detailed discussion on the NN-fitting, see Ref. [2]. Here, the fit is to the 1993 Nijmegen representation of the χ^2-hypersurface of the NN scattering data below $T_{lab} = 350$ MeV [61, 62], and also the low-energy parameters are fitted for pp, np and nn. In this simultaneous fit of NN and YNi

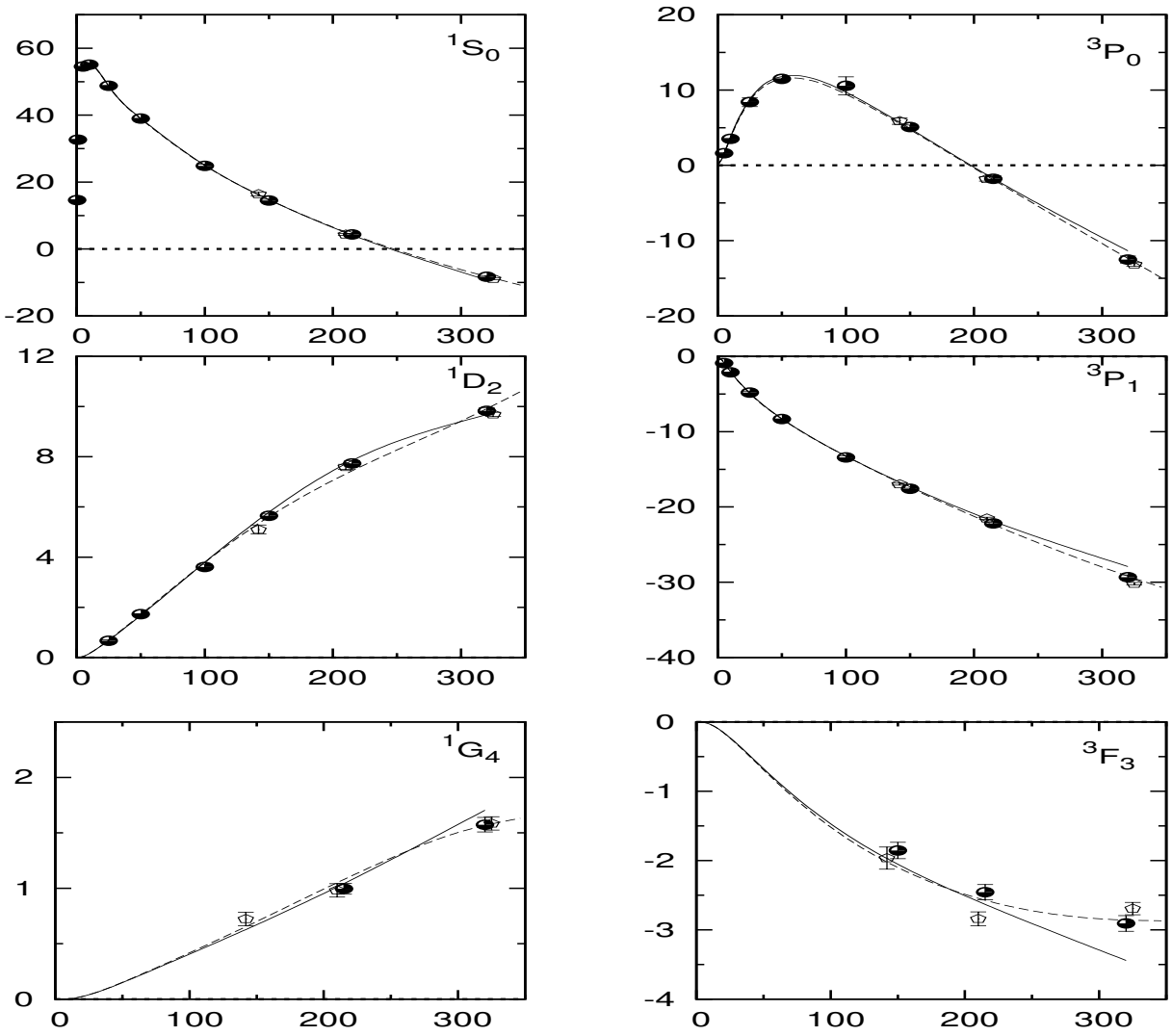

Figure 14: Solid line: proton-proton I=1 phase shifts in degrees vs. T_{lab} in MeV for the ESC16-model. The dashed line: the m.e. phases of the Nijmegen93 PW-analysis [61]. The black dots: the s.e. phases of the Nijmegen93 PW-analysis. The diamonds: Bugg s.e. [66].

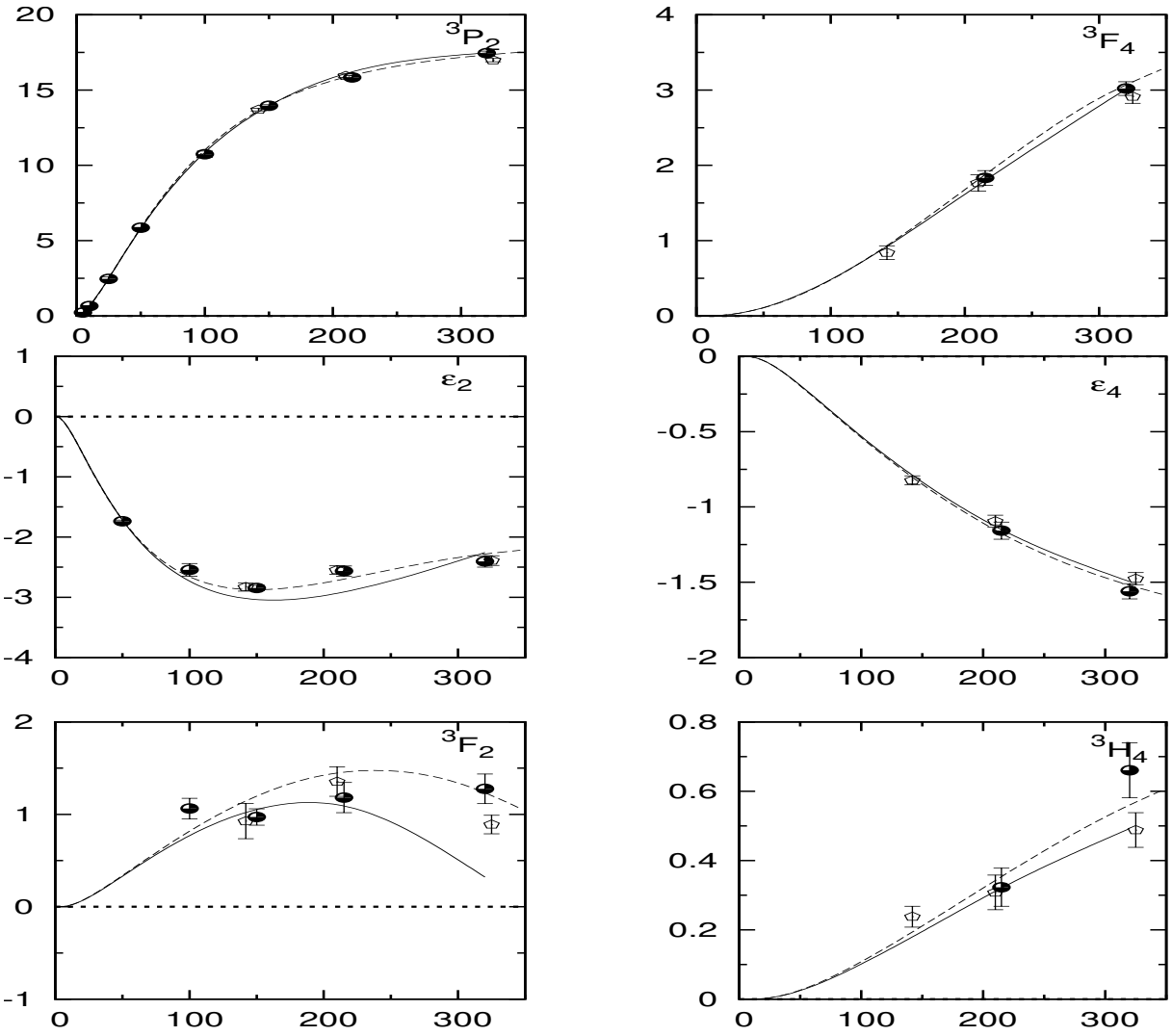

Figure 15: Solid line: proton-proton I=1 phase shifts in degrees vs. T_{lab} in MeV for the ESC16-model. The dashed line: the m.e. phases of the Nijmegen93 PW-analysis [61]. The black dots: the s.e. phases of the Nijmegen93 PW-analysis. The diamonds: Bugg s.e. [66].

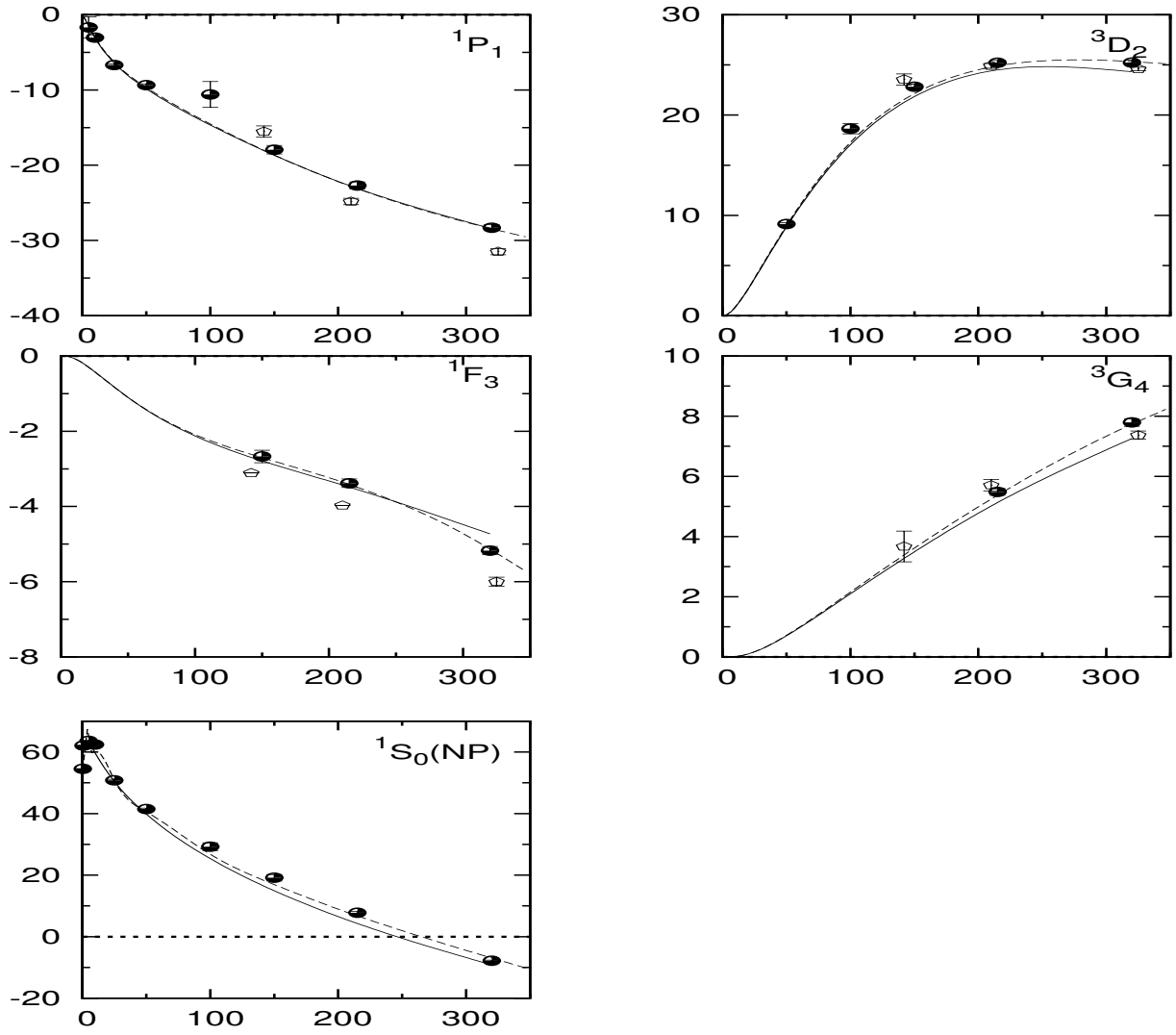

Figure 16: Solid line: neutron-proton I=0, and the I=1 $^1S_0(NP)$ phase shifts in degrees vs. T_{lab} in MeV for the ESC16-model. The dashed line: the m.e. phases of the Nijmegen93 PW-analysis [61]. The black dots: the s.e. phases of the Nijmegen93 PW-analysis. The diamonds: Bugg s.e. [66].

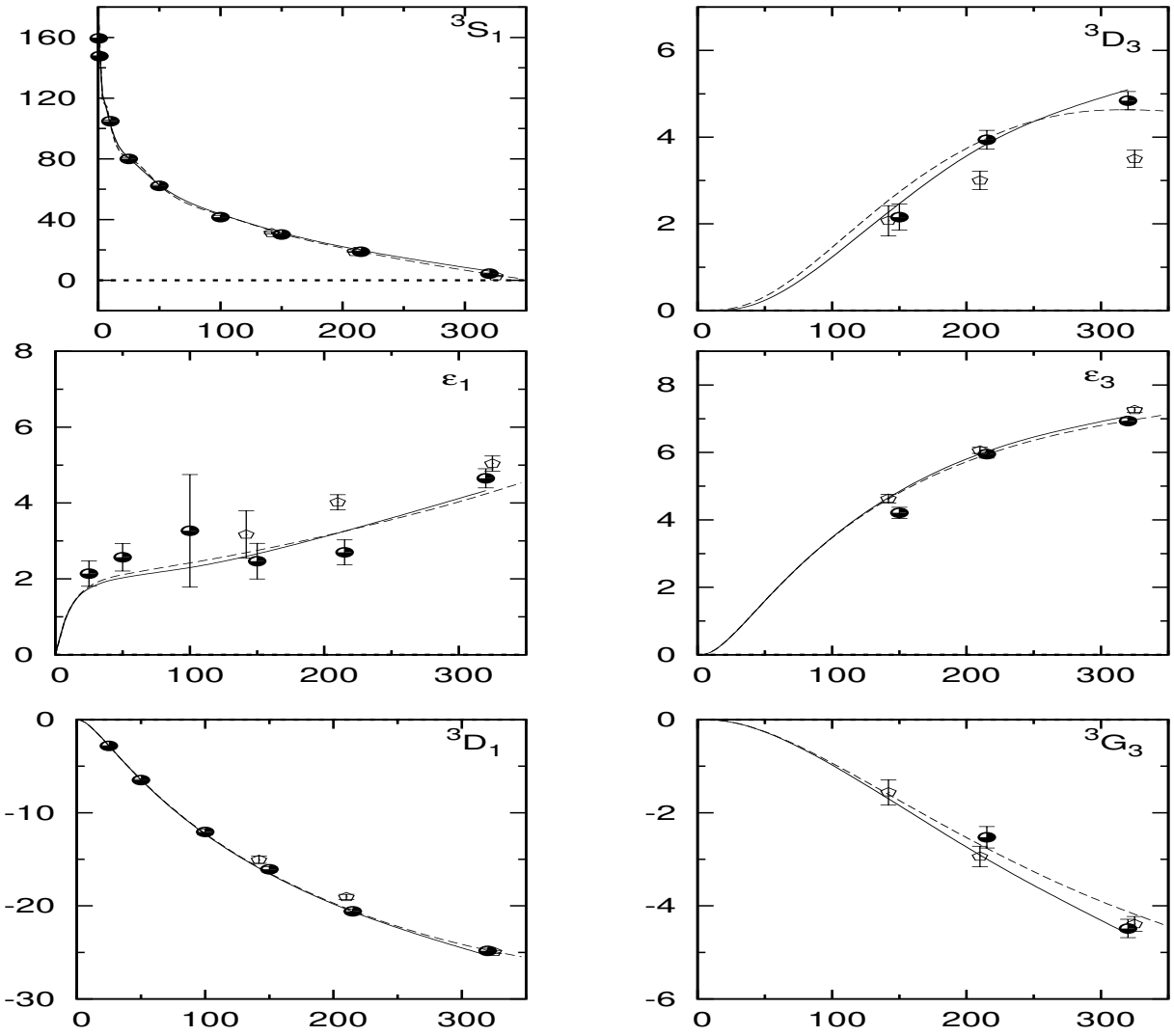

Figure 17: Solid line: neutron-proton I=0 phase shifts in degrees vs. T_{lab} in MeV for the ESC16-model. The dashed line: the m.e. phases of the Nijmegen93 PW-analysis [61]. The black dots: the s.e. phases of the Nijmegen93 PW-analysis. The diamonds: Bugg s.e. [66].

data, with the ESC16 model for the NN phase shifts a $\chi^2/Ndata = 1.10$ was obtained. For a comparison with Ref. [2], and for the use of this model for the description of NN, see Table 12 for the nuclear-bar phases for pp in case $I = 1$, and for np in the case of $^1S_0(I = 1)$ and the $I = 0$-phases. Here, $\Delta\chi^2$ denotes the accrescence in χ^2 of the ESC-model w.r.t. the phase shift analysis [61, 62].

The deuteron has been included in the fitting procedure, as well as the low-energy parameters. The fitted binding energy $E_B = 2.224636$ MeV, which is very close to $E_B(experiment) = 2.224644$ MeV. The charge-symmetry breaking is described phenomenologically by having next to $g_{\rho nn}$ free couplings for $g_{\rho np}$, and $g_{\rho pp}$. This phenomenological treatment is successful for the various NN-channels, especially for the $np(^1S_0, I = 1)$-phases, which were included in the NN-fit.

Table 12: ESC16 nuclear-bar pp and np phases in degrees.

$T_{\rm lab}$	0.38	1	5	10	25	50	100	150	215	320
$^1S_0(np)$	54.57	62.02	63.47	59.72	50.48	39.82	25.45	15.11	4.65	–8.34
$^1S_0$	14.62	32.62	54.75	55.16	48.67	38.97	25.06	14.85	4.44	–8.53
$^3S_1$	159.39	147.77	118.25	102.72	80.81	63.03	43.62	31.27	19.58	5.83
ϵ_1	0.03	0.11	0.68	1.17	1.82	2.15	2.50	2.94	3.64	4.93
$^3P_0$	0.02	0.14	1.61	3.81	8.81	11.80	9.68	4.83	–1.86	–11.73
$^3P_1$	–0.01	–0.08	–0.89	–2.04	–4.89	–8.29	–13.28	–17.35	–21.87	–27.90
$^1P_1$	–0.05	–0.19	–1.50	–3.07	–6.39	–9.81	–14.65	–18.75	–23.38	–29.44
$^3P_2$	0.00	0.02	0.22	0.67	2.51	5.80	10.90	14.04	16.24	17.07
ϵ_2	–0.00	–0.00	–0.05	–0.20	–0.81	–1.71	–2.71	–2.99	–2.84	–2.18
$^3D_1$	–0.00	–0.01	–0.18	–0.68	–2.83	–6.51	–12.40	–16.69	–20.72	–25.04
$^3D_2$	0.00	0.01	0.22	0.85	3.70	8.93	17.22	22.15	24.99	25.05
$^1D_2$	0.00	0.00	0.04	0.17	0.69	1.70	3.78	5.70	7.64	9.20
$^3D_3$	0.00	0.00	0.00	0.00	0.03	0.24	1.17	2.31	3.61	4.86
ϵ_3	0.00	0.00	0.01	0.08	0.55	1.59	3.46	4.81	5.97	6.99
$^3F_2$	0.00	0.00	0.00	0.01	0.11	0.34	0.80	1.10	1.14	0.39
$^3F_3$	–0.00	–0.00	–0.01	–0.03	–0.23	–0.67	–1.46	–2.06	–2.66	–3.50
$^1F_3$	–0.00	–0.00	–0.01	–0.06	–0.41	–1.10	–2.11	–2.77	–3.46	–4.69
$^3F_4$	0.00	0.00	0.00	0.00	0.02	0.12	0.51	1.04	1.80	3.00
ϵ_4	–0.00	–0.00	–0.00	–0.00	–0.05	–0.19	–0.53	–0.83	–1.13	–1.46
$^3G_3$	–0.00	–0.00	–0.00	–0.00	–0.05	–0.26	–0.93	–1.73	–2.77	–4.17
$^3G_4$	0.00	0.00	0.00	0.01	0.17	0.71	2.11	3.52	5.17	7.28
$^1G_4$	0.00	0.00	0.00	0.00	0.04	0.15	0.41	0.69	1.06	1.70
$^3G_5$	–0.00	–0.00	–0.00	–0.00	–0.01	–0.05	–0.16	–0.25	–0.28	–0.19
ϵ_5	0.00	0.00	0.00	0.00	0.04	0.20	0.70	1.22	1.83	2.62

In the fit of the NN-data, the single-energy (s.e.) phases and χ^2-surface [62] has been used. The details of the χ^2 distributions from the NN-fit are displayed in Table 14. The multi-energy (m.e.) phases of the PW-analysis [61] in Fig. 14-Fig. 17 are the dashed lines in these figures. One notices that the central value of the s.e. phases does not correspond to the m.e. phases in general, illustrating that there has been a certain amount of noise fitting in the s.e. PW-analysis, see e.g. ϵ_1 and $^1P_1$ at $T_{lab} = 100$ MeV. The m.e. PW-analysis reaches $\chi^2/N_{data} = 0.99$, using 39 phenomenological parameters plus normalization parameters. The related phenomenological PW-potentials NijmI, NijmII, and Reid93 [63], with respectively 41, 47, and 50 parameters, turn out all with $\chi^2/Ndata = 1.03$. This should be compared to the ESC-model, which has $\chi^2/N_{data} = 1.10$ using for NN 32 meson-related parameters. These are 14 QPC-constrained meson-nucleon-nucleon couplings, 6 meson-pair-nucleon-nucleon couplings, 6 Gaussian cut-off parameters, 3 diffractive couplings, and 2 diffractive mass parameters. The 3 remaining fitting parameters (2 F/(F+D) ratios and the Pauli blocking fraction) are mainly or totally determined by the YN-fit. From the figures, it is obvious

Table 13: ESC16 Low-energy parameters: S-wave scattering lengths and effective ranges, deuteron binding energy E_B, and electric quadrupole Q_e. Experimental values and references, see [67, 68]. The asterisk denotes that the low-energy parameters were not searched.

	experimental data			ESC16
$a_{pp}(^1S_0)$	–7.828	±	0.008	–7.7718
$r_{pp}(^1S_0)$	2.800	±	0.020	2.7612*
$a_{np}(^1S_0)$	–23.748	±	0.010	–23.7346
$r_{np}(^1S_0)$	2.750	±	0.050	2.6992*
$a_{nn}(^1S_0)$	–18.63	±	0.48	–17.783
$r_{nn}(^1S_0)$	2.860	±	0.15	2.8301*
$a_{np}(^3S_1)$	5.424	±	0.004	5.4396*
$r_{np}(^3S_1)$	1.760	±	0.005	1.7488*
E_B	–2.224644	±	0.000046	–2.224636
Q_e	0.286	±	0.002	0.2727

Table 14: ESC16 χ^2 and χ^2 per datum at the ten energy bins for the Nijmegen93 Partial-Wave-Analysis. N_{data} lists the number of data points within each energy bin. The bottom line gives the results for the total 0 – 350 MeV interval. The χ^2-accrescence for the ESC model is denoted by $\Delta\chi^2$ and $\Delta\hat{\chi}^2$, respectively.

$T_{\rm lab}$	N_{data}	χ^2_0	$\Delta\chi^2$	$\hat{\chi}^2_0$	$\Delta\hat{\chi}^2_0$
0.383	144	137.555	18.7	0.960	0.130
1	68	38.019	57.3	0.560	0.843
5	103	82.226	7.5	0.800	0.073
10	290	257.995	29.8	1.234	0.103
25	352	272.197	32.6	0.773	0.093
50	571	538.522	33.5	0.957	0.059
100	399	382.499	20.9	0.959	0.052
150	676	673.055	82.6	0.996	0.122
215	756	754.525	132.7	0.998	0.176
320	954	945.379	254.1	0.991	0.266
Total	4313	4081.971	669.8	0.948	0.153

that the ESC-model deviates from the m.e. PW-analysis in particular at the highest energy.

In Table 13 the results for the low energy parameters are given. In order to discriminate between the $^1S_0$-wave for pp, np, and nn, some charge independence breaking is introduced by taking $g_{pp\rho} \neq g_{np\rho} \neq g_{nn\rho}$. With this device the difference between the $^1S_0(pp)$ and $^1S_0(np)$ phases has been fitted, and the different scattering lengths and effective ranges as well. Obtained are $g_{np\rho} = 0.5427$, $g_{pp\rho} = 0.5932$, which are not far from $g_{nn\rho} = 0.5793$, see Table 9. The NN low-energy parameters are described very well, see Table 13. Here, except for a_{nn} and r_{nn}, the experimental values are taken from the compilation given in Ref. [67]. For $a_{nn}(^1S_0)$, used in the fitting has been the value from an investigation of the n-p and n-n final state interaction in the $^2H(n, nnp)$ reaction at 13 MeV [68]. The value for $a_{nn}(^1S_0)$ is still somewhat in discussion. Another recent determination [69] obtained e.g. $a_{nn}(^1S_0) = -16.27 \pm 0.40$ fm. The ESC16-model has the value -17.78 fm, which is between these values. Although the values from [67] are not recent, here they still give an adequate presentation since this ESC-model is not a detailed study of the low-energy parameters. For a discussion of the theoretical and experimental situation w.r.t. these low-energy parameters, see [70]. The binding energy of the deuteron is fitted excellently. The electric quadrupole moment result is typical for models without meson-exchange current effects. Further properties of the deuteron in this model are: $P_D = 6.15\%, D/S = 0.025698, N_G^2 = 0.771658$, and $\rho_{-\epsilon,-\epsilon} = 1.725857$.

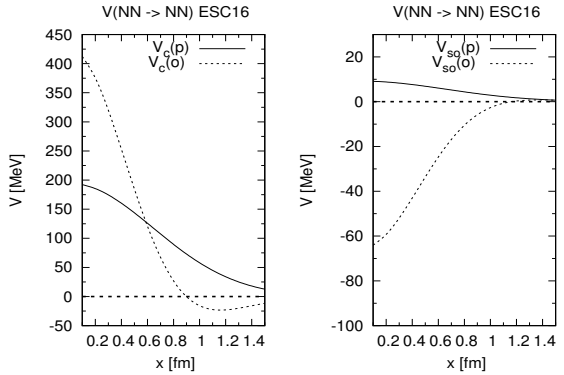

Figure 18: Pomeron(p) and Odderon(o) central- and spin-orbit potentials. The distance is denoted by x in fm.

12.2. Nucleon-Nucleon Potentials [11]

The nucleon-nucleon OBE-, TPS-, and Pair-potentials are qualitatively rather similar in character to the hyperon-nucleon potentials, which are shown in Ref. [3] for the ESC04 model. Therefore, the reader is refered to the cited YN paper for pictures of the potentials. The odderon and the derivative axial-vector coupling, and the non-local pseudoscalar type spin-spin and tensor potentials are added.

The odderon potential is a novel feature of the ESC16 model. In Fig. 18 the central and spin-orbit potentials are shown. The spin-spin, tensor, and quadratic spin-orbit potentials are very small. One notices from this figure that the pomeron potential is like an 'anti-scalar' potential, whereas the odderon is a normal vector-exchange potential. Note the strong cancellation in the spin-orbit, giving a negligible summed contribution. The upshot is a universal central repulsion from the pomeron+odderon. In ESC models, the strength of the pomeron is related to that of the ε. The pomeron curve in Fig. 18 corresponds to a fit with $\varepsilon = f_0(760)$, whereas in this paper $\varepsilon = f_0(620)$. This results in weaker couplings of ε, ω, and pomeron, reducing the strength of the pomeron by $\approx 2/3$.

13. ESC16-model *YN*($S = -1$)-Results

In this section the *YN* results of [6] are reviewed.

[11] FORTRAN code ESC16/NNPOTESC16, Open-access website, NN-Online: *http://nn-online.org*.

13.1. Hyperon-nucleon (S=-1) cross sections, phases, etc.

The used *YN* scattering data from Refs. [71]-[80] in the combined NN and YN fit are shown in Table 15. The NN interactions put very strong constraints on most of the parameters, and so only a limited set of parameters are left, which have some freedom to steer the YN-channels as compared to the NN-channels.

The present study aimed to construct a realistic potential model for baryon-baryon systems with parameters that are optimal theoretically, but at the same time to describe the baryon-baryon scattering data very satisfactorily.

This model can then be used with a great deal of confidence in calculations of hypernuclei and in their predictions for the $S = -2, -3$, and -4 sectors. Especially for the latter application, these models will be the first models for the $S = -2, -3, -4$ sectors to have their foundation in the NN and YN sectors.

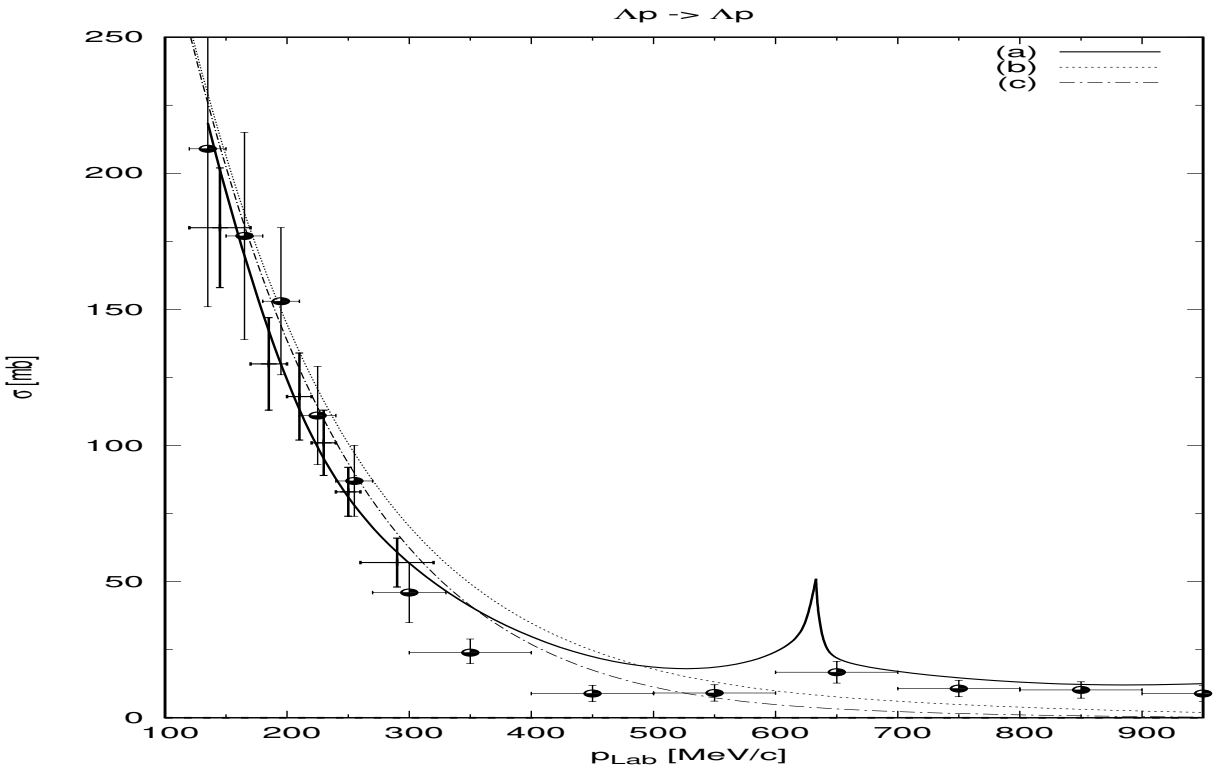

Figure 19: Model fits total cross sections Λp, and Rehovoth-Heidelberg-, Maryland-, and Berkeley-data. (a): ESC16, (b,c): Effective range approximation I without a shape parameter, and II with a shape parameter.

The χ^2 on the 52 *YN* scattering data for the ESC16 model is given in Table 15. The ΛN total cross sections have been calculated with $L \leq 2$, and the ΣN total cross sections with $L \leq 1$. For the definition of the capture ratio at rest, given in the last row of the table, see e.g. [35]. This capture ratio turns out to be rather constant in the momentum range from 100 to 170 MeV/c. Obviously, for very low momenta the cross sections are almost completely dominated by s waves, and so the capture ratio in flight converges to the capture ratio at rest.

The $\Sigma^+ p$ nuclear-bar phase shifts as a function of energy are given in Table 16. Notice that the $^3S_1$-phase shows repulsion.

The ΛN nuclear-bar phase shifts as a function of energy are given in Table 17. In Fig. 19 the Λp total cross sections are shown for ESC16 together with the data. At the ΣN-threshold, the cross section shows a sizeable cusp with a large D-wave nuclear-bar phase-shift $\delta(^3D_1) = 69.10^o$. This signals the fact that in the $\Sigma N(^3S_1, I = 1/2)$-state, there is a strong attraction, with presumably a deuteron-like virtual bound-state on the non-physical sheet. Also, in Fig. 19 are shown the cross sections in the effective range approximation, dashed lines I and II. Line II is including the shape parameter in the effective range expansion. The two-term effective range expansion with the a and r parameters describes the s-wave phases well up to $p_\Lambda \approx 400$ MeV/c.

Table 15: Comparison of the calculated ESC16 and experimental values for the 52 YN-data that were included in the fit. The superscript *RH* and *M* denote, respectively, the Rehovoth-Heidelberg Ref. [71] and Maryland data Ref. [72]. Also included are (i) 3 $\Sigma^+ p$ cross sections at $p_{lab} = 400, 500, 650$ MeV from Ref. [77], (ii) Λp cross sections from Ref. [78]: 7 elastic between $350 \leq p_{lab} \leq 950$, and 4 inelastic with $p_{lab} = 667, 750, 850, 950$ MeV, and (iii) 3 elastic $\Sigma^- p$ cross sections at $p_{lab} = 450, 550, 650$ MeV from Ref. [79]. The laboratory momenta are in MeV/c, and the total cross sections in mb. The total $\chi^2 = 54.2$

$\Lambda p \to \Lambda p$		$\chi^2 = 3.7$	$\Lambda p \to \Lambda p$		$\chi^2 = 4.3$
p_Λ	σ^{RH}_{exp}	σ_{th}	p_Λ	σ^{M}_{exp}	σ_{th}
145	180±22	192.7	135	209.0±58	209.7
185	130±17	134.0	165	177.0±38	160.8
210	118±16	106.4	195	153.0±27	122.3
230	101±12	88.3	225	111.0±18	92.6
250	83± 9	73.3	255	87.0±13	69.9
290	57± 9	50.3	300	46.0±11	45.8
$\Lambda p \to \Lambda p$		$\chi^2 = 3.7$			
350	23.9±5.0	28.6	750	10.7±3.0	8.2
450	8.9±3.0	11.6	850	10.2±3.0	9.4
550	9.1±3.0	7.3	950	8.9±3.0	10.9
650	16.7±4.0	14.3			
$\Lambda p \to \Sigma^0 p$		$\chi^2 = 8.0$			
667	2.8 ±2.0	3.3	850	10.7±3.0	3.8
750	7.5±2.5	3.8	950	5.0±2.0	3.6
$\Sigma^+ p \to \Sigma^+ p$		$\chi^2 = 17.3$	$\Sigma^- p \to \Sigma^- p$		$\chi^2 = 6.3$
p_{Σ^+}	σ_{exp}	σ_{th}	p_{Σ^-}	σ_{exp}	σ_{th}
145	123.0±62	147.3	142.5	152±38	148.8
155	104.0±30	134.3	147.5	146±30	142.4
165	92.0±18	123.0	152.5	142±25	136.2
175	81.0±12	112.8	157.5	164±32	130.5
			162.5	138±19	125.0
			167.5	113±16	119.8
400	93.5±28.1	32.7	450.0	31.7±8.3	25.9
500	32.5±30.4	28.1	550.0	48.3±16.7	17.9
650	64.6±33.0	25.4	650.0	25.0±13.3	13.7
$\Sigma^- p \to \Sigma^0 n$		$\chi^2 = 6.0$	$\Sigma^- p \to \Lambda n$		$\chi^2 = 4.9$
p_{Σ^-}	σ_{exp}	σ_{th}	p_{Σ^-}	σ_{exp}	σ_{th}
110	396±91	205.6	110	174±47	242.3
120	159±43	179.9	120	178±39	207.1
130	157±34	159.3	130	140±28	179.2
140	125±25	142.5	140	164±25	156.6
150	111±19	128.6	150	147±19	138.2
160	115±16	116.9	160	124±14	123.0
$r_R^{exp} = 0.468 \pm 0.010$			$r_R^{th} = 0.467$		$\chi^2 = 0.01$

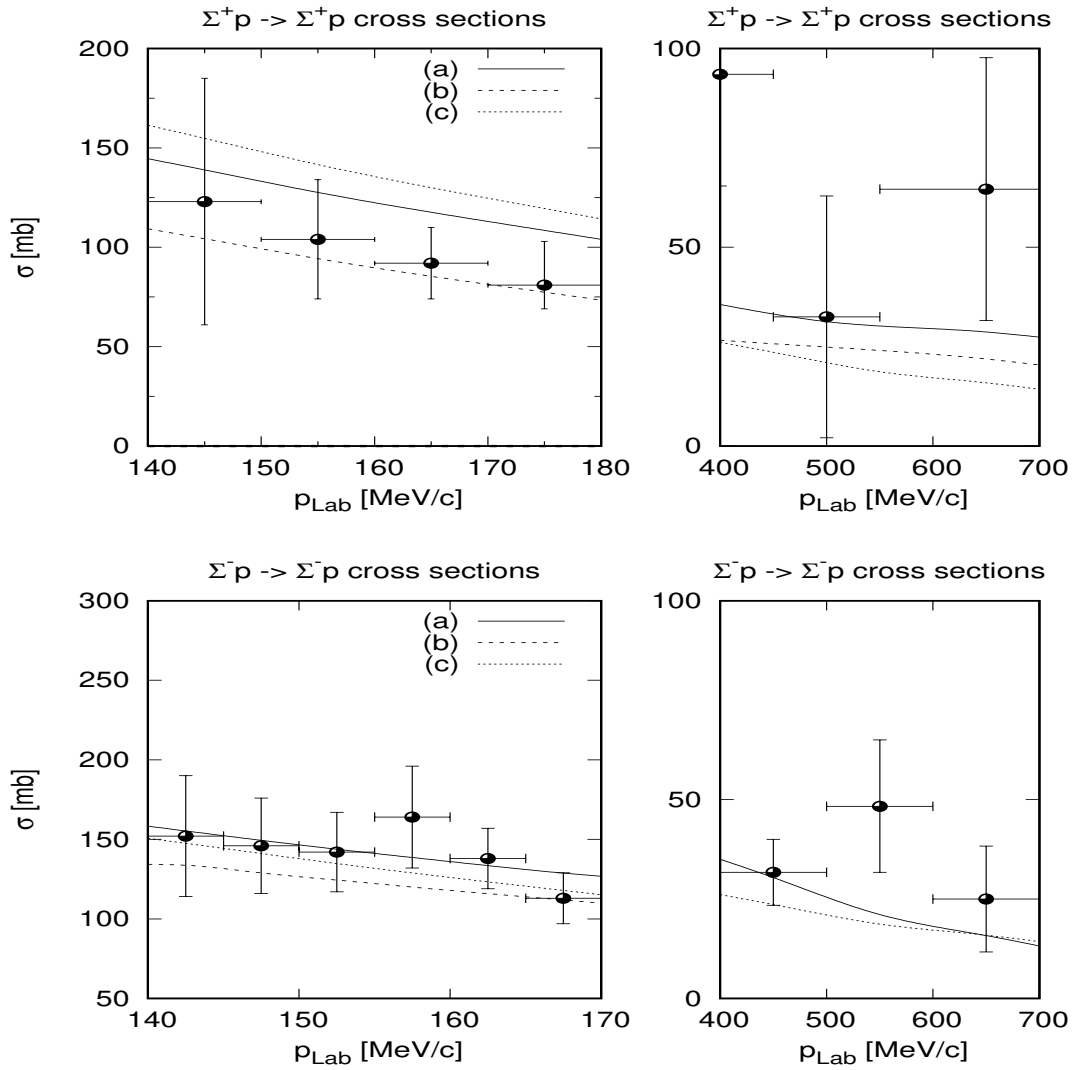

Figure 20: Model fits total elastic cross sections $\Sigma^{\pm}p$ and Rehovoth-Heidelberg-, KEK-data. Left panels (a): ESC16, (b): ESC04d, (c): NSC89, Right panels the same.

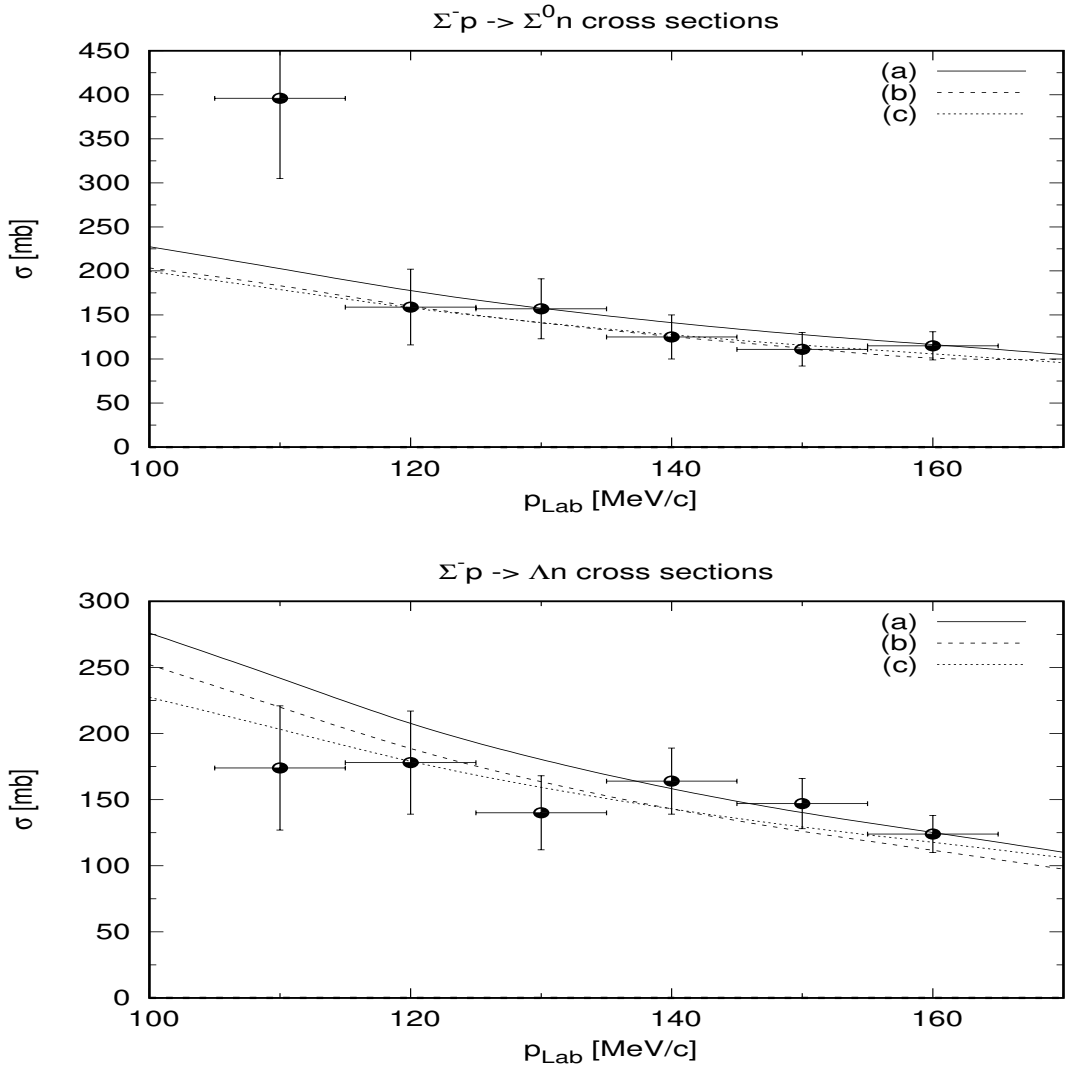

Figure 21: Model fits total inelastic cross sections $\Sigma^- p \to \Sigma^0 n, \Lambda n$ and Rehovoth-Heidelberg-data. (a): ESC16, (b): ESC04d, (c): NSC89.

Table 16: ESC16 nuclear-bar $\Sigma^+ p$ phases in degrees.

p_{Σ^+}	100	200	300	400	500	600	700	800	900	1000
$T_{\rm lab}$	4.2	16.7	37.3	65.5	100.8	142.8	190.7	244.0	302.1	364.5
$^1S_0$	35.10	41.06	35.49	27.54	19.12	10.81	2.80	–4.80	–11.99	–18.76
$^3S_1$	-5.11	–11.11	-16.94	–22.62	-27.89	–32.55	-36.55	–39.99	-43.04	–45.84
ϵ_1	-0.37	–1.81	-3.33	–4.43	–5.04	–5.24	–5.14	–4.86	–4.48	–4.07
$^3P_0$	0.96	4.90	8.42	9.12	7.19	3.59	–0.92	–5.81	–10.81	–15.73
$^1P_1$	0.43	2.33	4.84	7.05	8.33	8.45	7.46	5.55	2.94	–0.17
$^3P_1$	–0.59	–3.00	–6.13	–9.53	–13.15	–16.93	–20.79	–24.64	–28.41	–32.05
$^3P_2$	0.10	0.90	2.58	4.70	6.76	8.50	9.82	10.65	10.95	10.71
ϵ_2	–0.03	–0.37	–1.05	–1.81	–2.44	–2.85	–3.02	–2.98	–2.78	–2.49
$^3D_1$	0.02	0.30	0.84	1.32	1.35	0.69	–0.70	–2.75	–5.29	–8.21
$^1D_2$	0.02	0.31	0.97	2.00	3.38	4.99	6.61	8.01	8.97	9.33
$^3D_2$	–0.03	–0.45	–1.30	–2.35	–3.53	–4.87	–6.42	–8.15	–10.04	–12.04
$^3D_3$	0.00	0.05	0.26	0.66	1.14	1.59	1.93	2.20	2.45	2.70
ϵ_3	-0.00	–0.07	-0.29	–0.63	–1.00	–1.35	–1.64	–1.86	–1.99	–2.04
$^3G_3$	0.00	0.00	0.04	0.12	0.25	0.41	0.57	0.70	0.75	0.67

Table 17: ESC16 nuclear-bar Λp phases in degrees.

p_Λ	100	200	300	400	500	600	633.0
$T_{\rm lab}$	4.5	17.8	39.6	69.5	106.9	151.1	167.3
$^1S_0$	20.21	25.86	23.13	17.24	10.34	3.40	1.43
$^3S_1$	20.25	26.62	24.84	19.99	14.17	8.51	7.46
ϵ_1	0.04	0.16	0.23	0.21	0.29	2.01	9.16
$^3P_0$	0.02	0.08	–0.19	–1.34	–3.54	–6.51	–7.52
$^1P_1$	–0.07	–0.55	–1.78	–3.88	–6.67	–9.80	–10.82
$^3P_1$	0.00	–0.10	–0.60	–1.70	–3.25	–4.67	–4.71
$^3P_2$	0.11	0.70	1.74	2.86	3.73	4.25	4.34
ϵ_2	0.00	–0.00	–0.04	–0.15	–0.31	–0.50	–0.57
$^3D_1$	0.00	0.07	0.48	1.82	5.42	18.93	59.97
$^1D_2$	0.00	0.06	0.37	1.12	2.36	3.96	4.53
$^3D_2$	0.00	0.08	0.42	1.17	2.31	3.68	4.16
$^3D_3$	0.00	0.05	0.27	0.76	1.52	2.41	2.71

Table 18: Comparison Λp and Λn scattering lengths and effective ranges in fm for different Nijmegen models.

	Λp		Λn	
Model	a_s	a_t	a_s	a_t
ESC16	-1.88	-1.86	-1.96	-1.84
NSC97e	-2.10	-1.86	-2.24	-1.83
NSC97f	-2.51	-1.75	-2.68	-1.67
NSC89	-2.73	-1.48	-2.86	-1.24
HC-D	-1.77	-2.06	-2.03	-1.84
Model	r_s	r_t	r_s	r_t
ESC16	3.58	3.37	3.65	3.33
NSC97e	3.19	3.19	3.24	3.14
NSC97f	3.03	3.32	3.07	3.34
NSC89	2.87	3.04	2.91	3.33
HC-D	3.78	3.18	3.66	3.32

In Table 18 the low-energy parameters for Λp and Λn are shown. The singlet and triplet parameters are displayed with the $\Lambda\Sigma^0$-mixing turned on for pseudoscalar-, vector-, scalar-, meson-pairs-, and ps-ps- exchanges. Notice that the effect for the scalar mesons of the $\Lambda\Sigma^0$-mixing is zero because $\alpha_s = 1.0$. It is clear from these tables that the total effect of the $\Lambda\Sigma^0$-mixing is largely given by pseudoscalar and vector exchanges. The differences in the scattering lengths are

$$\Delta a_s = a_s(\Lambda p) - a_s(\Lambda n) = +0.08\ fm, \tag{13.1a}$$

$$\Delta a_t = a_t(\Lambda p) - a_t(\Lambda n) = -0.04\ fm. \tag{13.1b}$$

These differences are comparable to those for the soft-core OBE models [34, 35], and therefore predict a too small binding energy difference in the A=4 hypernuclei, which is $\Delta B_\Lambda(exp) = B_\Lambda({}^4_\Lambda He) - B_\Lambda({}^4_\Lambda H) = (0.29 \pm 0.06)$ MeV. This is in contrast to the HC-model D, which has a much larger Δa_t [81]. It appeared that CSB via meson-mixing, like $\pi^0 - \eta, \rho^0 - \omega$ etc., is small and does not improve the CSB for ESC16, which is understandable in view of the large cancellations. In Ref. [82] it has been shown that by introducing CSB interaction in the contact terms for $\Lambda p \to \Lambda p$ and $\Lambda n \to \Lambda n$, this problem can be solved. Similarly, in the ESC models one could introduce extra CSB in *e.g.* the MPE potentials.

In Table 19 are listed the $\Sigma^+ p$ scattering lengths and effective ranges. Here, (a_s, r_s) are these quantities for $\Sigma^+ p({}^1S_0)$ and (a_t, r_t) for $\Sigma^+ p({}^3S_1)$.

Notice that the difference between a_s in ESC08a$''$ and ESC16. This is mainly a consequence of the inclusion of the non-local tensor force in $\Sigma^+ p$, like in pp. This means that there is still less room for variations in the ${}^3S_1$-wave because of the cross section fit. Because with SU(3) symmetry for the couplings the ${}^1S_0$-wave is strongly constrained by pp, since the ${}^1S_0$-states in NN and $\Sigma^+ p$ are both in the {27}-irrep. Therefore, much extra repulsion in the triplet wave is impossible.

Table 19: $\Sigma^+ p$ scattering lengths and effective ranges in fm.

Model	a_s	a_t	r_s	r_t
ESC16	-4.30	+0.57	3.25	-3.11
ESC08a$''$	-3.85	+0.62	3.40	-2.13
ESC04d	-3.43	+0.217	3.98	-28.94

In Fig. 20 and Fig. 21 the elastic and inelastic cross sections are shown respectively.

13.2. Flavor SU(3)-irrep potentials

In Fig. 22 and 23 the potentials in the SU(3)-irrep base states are displayed. In the upper and lower panels the diagonal and the non-diagonal potentials are shown respectively. Notice that the non-diagonal potentials are considerably smaller than the diagonal ones, which shows the approximate SU(3)-symmetry. The red/solid lines

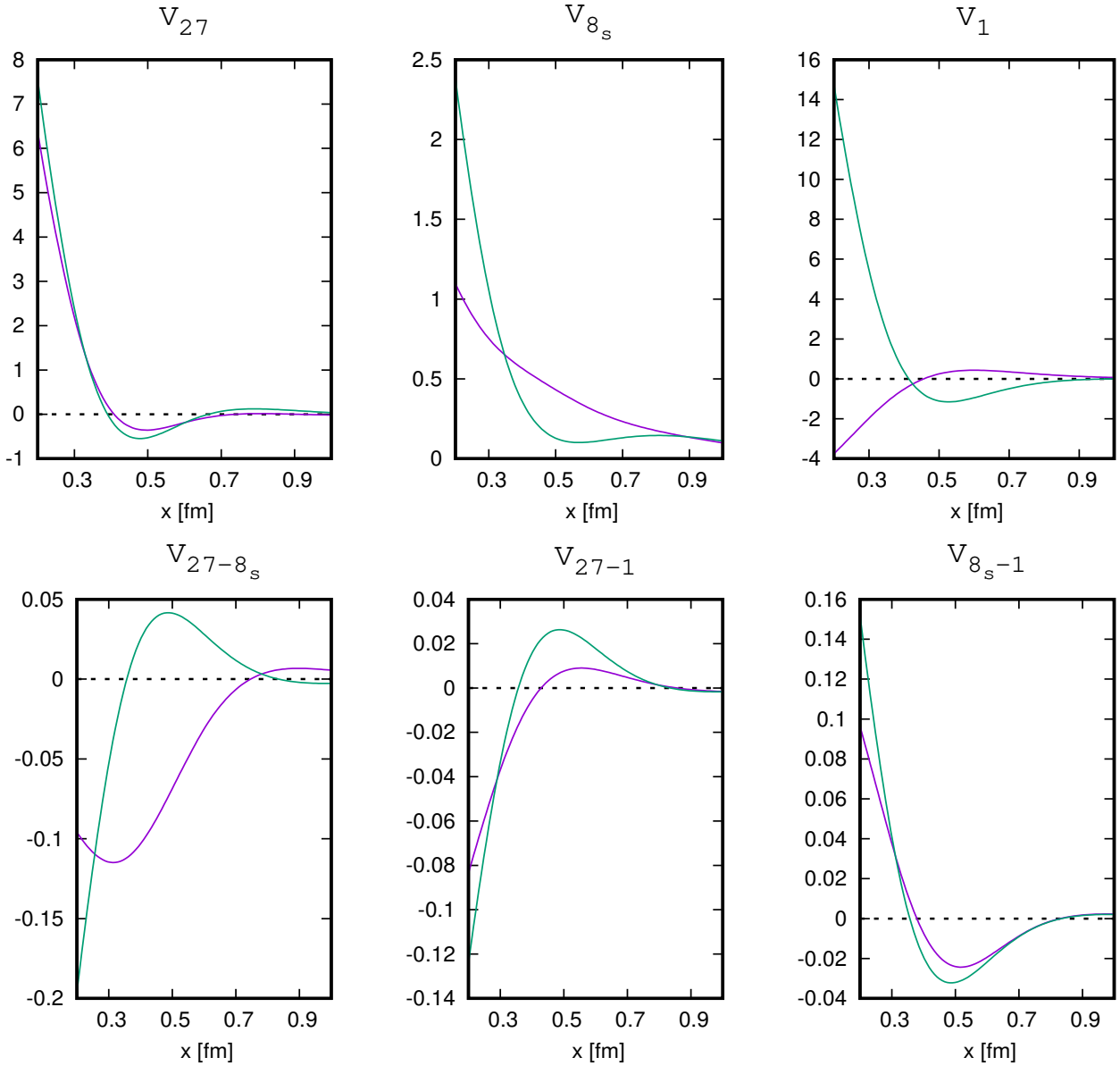

Figure 22: Potentials in the symmetric SU(3)-irrep base. The red and green lines denote potentials with and without SU(3)-symmetry breaking respectively. The units of the vertical axes are [GeV].

show averages of the SU(3)-irrep potentials using the potentials on the particle basis. The green/dashed lines are the irrep potentials in an SU(3) limit, where $M_N = M_\Lambda = M_\Sigma = M_\Xi = 1115.6$ MeV, $m_\pi = m_K = m_\eta = m_{\eta'} = 400$ MeV, $m_\rho = m_{K^*} = m_\omega = m_\phi = 800$ MeV, and $m_{a0} = m_\kappa = m_\sigma = m_{f_0'} = 880$ MeV. These values for the masses are close to the GMO [41] octet and singlet masses 410 and 885 MeV for the pseudoscalar and vector mesons respectively. The cut-off masses for pseudoscalar, vector, and axial-vector have been set equal to the octet ones, i.e. $\Lambda_1^P = \Lambda_8^P$ etc. But,

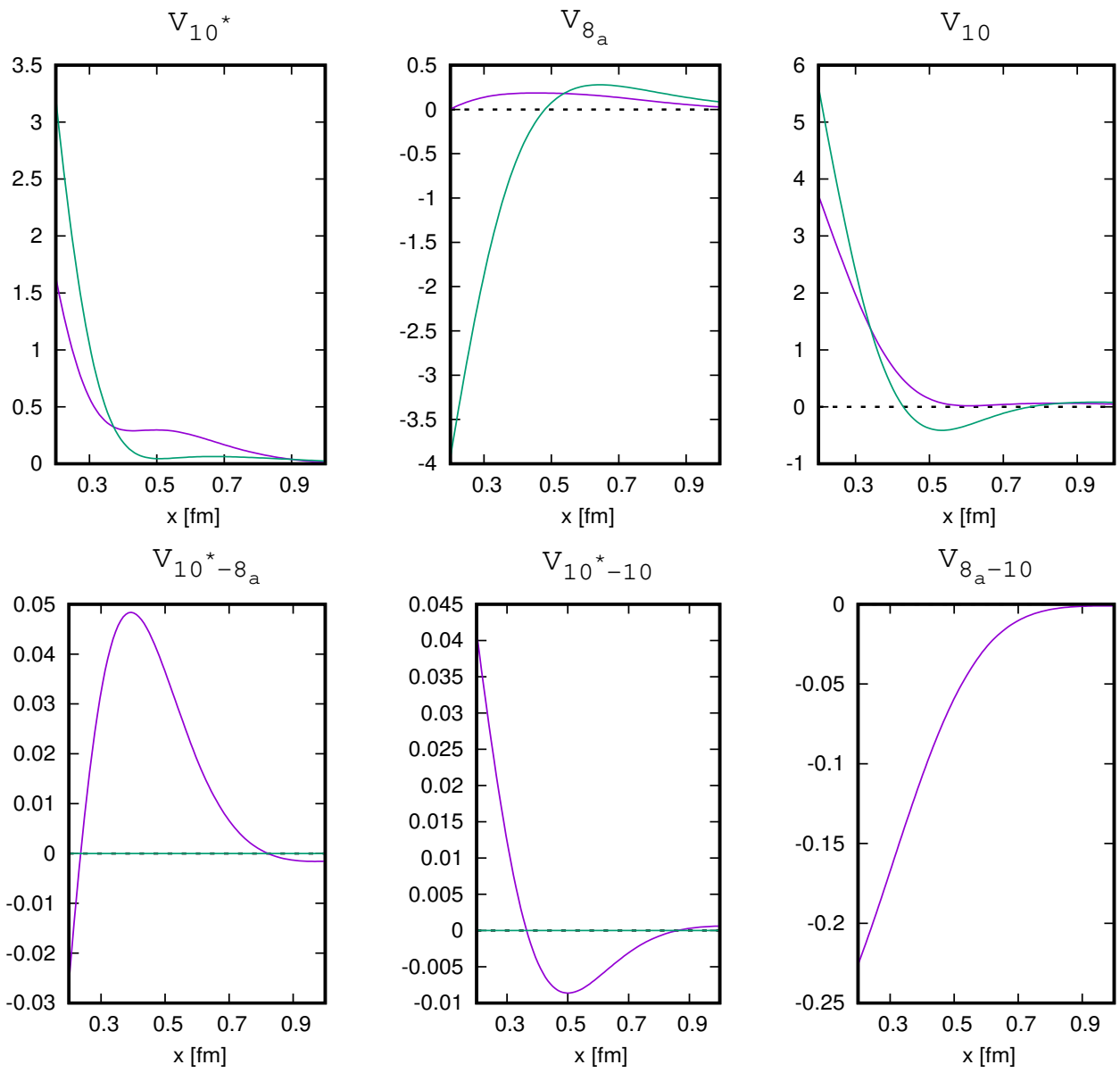

Figure 23: Potentials in the anti-symmetric SU(3)-irrep base. The red and green lines denote potentials with and without SU(3)-symmetry breaking respectively. The units of the vertical axes are [GeV].

for the scalar nonet $\Lambda_8^S = \Lambda_1^S$.
Comparison with the results from LQCD [83] shows qualitatively very similar results. The exception is the SU(3)-singlet {1}-irrep. Here LQCD potential is attractive for $0 < r < \infty$, whereas in ESC16 there is an attractive pocket for $r \leq 0.5$ fm and is repulsive for $r > 0.5$ fm. This shape is due to the behavior of the spin-spin potentials from pseudoscalar and vector exchange, which have zero volume integrals.

14. Analyses with G-matrix interactions

The G-matrix theory gives a good starting point for studies of hyperonic many-body systems on the basis of free-space *YN* interaction models [84, 85] and [64]. Here, the correlations induced by hyperonic coupling interactions such as ΛN-ΣN ones are renormalized into single-channel G-matrices. These G-matrix interactions are considered as effective interactions used in models of hypernuclei. Thus, the hypernuclear phenomena and the underlying *YN* interaction models are linked through the *YN* G-matrix interactions, and the hypernuclear information gives a feedback to the interaction models. Here, the properties of ΛN and ΣN sectors of ESC16 in nuclear medium are studied on the basis of the G-matrix theory.

In Refs. [86, 87, 88, 89] the three-body interaction is added on ESC16, being composed of the multi-pomeron exchange repulsive potential (MPP) and the phenomenological three-baryon attraction (TBA). The effective two-body potential derived from MPP is given as

$$V_{MPP}(r;\rho) = g_P^{(3)}(g_P)^3 \frac{\rho_N}{\mathcal{M}^5} \cdot \frac{1}{4\pi} \frac{4}{\sqrt{\pi}} \left(\frac{m_P}{\sqrt{2}}\right)^3 \exp\left(-\frac{1}{2} m_P^2 r^2\right) , \tag{14.1}$$

where $g_P^{(3)}$ is the triple-pomeron coupling, and the pomeron mass m_P and the two-body pomeron coupling g_P are fitted to the NN-data etc. In a similar way, one can obtain an effective two-body potential with a quartic pomeron coupling $g_P^{(4)}$. TBA also is given by a density-dependent two-body potential

$$V_{TBA}(r;\rho) = V_{TBA}^0 \exp(-(r/2.0)^2)\rho \exp(-\eta\rho)(1 + P_r)/2, \tag{14.2}$$

where $\rho = \rho_N$ and P_x being a space-exchange operator. The values of $g_P^{(3)}$, $g_P^{(4)}$, V_{TBA}^0 and η in *NN* channels are adjusted to reproduce the angular distribution of ^{16}O+^{16}O elastic scattering at $E/A = 70$ MeV with use of the G-matrix folding potential, and values of the saturation density and the energy per nucleon there in nuclear matter [86, 87, 88]. Here, the set ($g_P^{(3)} = 5.25$, $g_P^{(4)} = 87.0$) is adopted, that gives rise to the stiff EoS of neutron matter with a maximum mass $2M_\odot$ for a neutron star [86, 87]. Other sets, like MPa and MPa$^+$ in [88], lead to similar results in the normal density region, differences appear only in the high density region.

MPP works universally in all baryon-baryon channels according to its definition. Assuming here that TBA works also in ΛN channels, the parameters are adjusted to reproduce well energy spectra of Λ hypernuclei. For simplicity, taken is $V_{TBA}^0 = -16.0$ MeV, being more attractive than $V_{TBA}^0 = -8.0$ MeV in *NN* channels, and the same value of $\eta = 4.0$ fm^3. Hereafter, the interaction ESC16+MPP+TBA is denoted as ESC16$^+$.

The channel-coupled G-matrix equation for the baryon pair B_1B_2 in nuclear matter [84], where $B_1B_2 = \Lambda N$ and ΣN reads

$$G_{cc_0} = v_{cc_0} + \sum_{c'} v_{cc'} \frac{Q_{y'}}{\omega - \epsilon_{B_1'} - \epsilon_{B_2'} + \Delta_{yy'}} G_{c'c_0} , \tag{14.3}$$

where c denotes a *YN* relative state (y, T, L, S, J) with $y = (B_1, B_2)$. S and T are spin and isospin quantum numbers, respectively. Then, a two-particle state is represented as $^{2S+1}L_J$. In Eq. (14.3), ω gives the starting energy in the starting channel c_0. $\Delta_{yy'} = M_{B_1} + M_{B_2} - M_{B_1'} - M_{B_2'}$ denotes the mass difference between two-baryon channels. The Pauli operator Q_y acts on intermediate nucleon states in a channel $y = (B_1, B_2) = (\Lambda N, \Sigma N)$. Here, adopted is the continuous (CON) choice for intermediate single particle potentials in the G-matrix equation, where an off-shell potential is taken continuously frpm an on-shell one [90]. The G-matrix equation (14.3) is represented in the coordinate space, whose solutions give G-matrix interactions. The hyperon single particle (s.p.) energy ϵ_Y in nuclear matter is given by

$$\epsilon_Y(k_Y) = \frac{\hbar^2 k_Y^2}{2M_Y} + U_Y(k_Y) , \tag{14.4}$$

where k_Y is the hyperon momentum. The potential energy U_Y is obtained self-consistently in terms of the G-matrix as

$$U_Y(k_Y) = \sum_{|\mathbf{k}_N|} \langle \mathbf{k}_Y \mathbf{k}_N \mid G_{YN}(\omega = \epsilon_Y(k_Y) + \epsilon_N(k_N)) \mid \mathbf{k}_Y \mathbf{k}_N \rangle \tag{14.5}$$

14.1. ΛN G-matrix

Table 20: Values of $U_\Lambda(\rho_0)$ and partial wave contributions in $^{2S+1}L_J$ states from the G-matrix calculations (in MeV). The value specified by D gives the sum of $^{2S+1}D_J$ contributions. Contributions from S-state spin-spin interactions are given by $U_{\sigma\sigma} = (U_\Lambda(^3S_1) - 3U_\Lambda(^1S_0))/12$.

	$^1S_0$	$^3S_1$	$^1P_1$	$^3P_0$	$^3P_1$	$^3P_2$	D	U_Λ	$U_{\sigma\sigma}$
ESC16	−13.3	−30.0	2.3	0.1	1.1	−2.3	−1.6	−43.7	0.83
ESC16$^+$	−12.3	−27.4	2.9	0.3	1.7	−1.2	−1.9	−37.9	0.79

Let us calculate Λ binding energies in nuclear matter. In Table 20 shown are the potential energies $U_\Lambda(\rho_0)$ for a zero-momentum Λ and their partial-wave contributions in $^{2S+1}L_J$ states at normal density ρ_0 (k_F=1.35 fm^{-1}) in the CON choice, where a statistical factor $(2J + 1)$ is included in each contribution in $^{2S+1}L_J$ state. The value of U_Λ for ESC16$^+$ is rather less attractive than that for ESC16, because repulsive contributions of MPP are canceled partially by attractive TBA contribution. Here, the value of V^0_{TBA} is chosen so as to reproduce B_Λ values of observed Λ hypernuclei, as shown in next subsection. The contributions to U_Λ from S-state spin-spin components can be seen qualitatively in values of $U_{\sigma\sigma} = (U_\Lambda(^3S_1) - 3U_\Lambda(^1S_0))/12$. These values of $U_{\sigma\sigma}$ also are given in Table 20. In the same treatment, obtained were $U_{\sigma\sigma}$=1.54 and 0.92 MeV for NSC97f and NSC97e, respectively. Various analyses suggest that the reasonable value of $U_{\sigma\sigma}$ is between these values [64]. The $U_{\sigma\sigma}$ values for ESC16$^+$ seem to be slightly too small compared to this value.

Table 21: Parameters of YNG-ESC16. Continuous choice : $\mathcal{G}(k_F; r) = \sum_{i=1}^{3}(a_i + b_i k_F + c_i k_F^2)\exp[-(r/\beta_i)^2]$

	β_i	0.50	0.90	2.00
^1E	a	−3548	413.2	−1.787
	b	7135	−1087	0.0
	c	−2723	428.5	0.0
^3E	a	−2820	325.1	−1.372
	b	5888	−909.3	0.0
	c	−2434	397.6	0.0
^1O	a	1635	88.84	−.9019
	b	−338.7	45.01	0.0
	c	138.2	−2.532	0.0
^3O	a	2283	−223.6	−1.070
	b	−2359	204.7	0.0
	c	823.6	−45.50	0.0

Table 22: Parameters of the additional interaction in YNG-ESC16$^+$: $\Delta\mathcal{G}(k_F; r) = (a + bk_F + ck_F^2)\exp[-(r/0.9)^2]$

	^1E	^3E	^1O	^3O
a	18.23	16.54	27.78	26.20
b	−45.62	−42.85	−78.02	−75.33
c	27.46	25.80	69.16	70.44

For applications to various hypernuclear problems, it is convenient to construct k_F-dependent effective local potentials $\mathcal{G}(k_F; r)$ simulating the G-matrices in coordinate space, called YNG. Here, the G-matrices are parameterized in a three-range Gaussian form

$$\mathcal{G}(k_F, r) = \sum_{i=1}^{3} (a_i + b_i k_F + c_i k_F^2) \exp[(-r^2/\beta_i^2)]. \tag{14.6}$$

The parameters (a_i, b_i, c_i) are determined so as to simulate the calculated G-matrix for each ${}^{2S+1}L_J$ state. The procedures to fit the parameters are given in Ref. [64]. The obtained parameters for ESC16 are shown in Table 21. For ESC16$^+$, contributions from MPP+TBA are represented by modifying the second-range parts of $\mathcal{G}(k_F, r)$ for ESC16 by $\Delta\mathcal{G}(k_F, r) = (a + bk_F + ck_F^2) \exp[-(r/0.9)^2]$. The parameters for $\Delta\mathcal{G}(k_F, r)$ are given in Table 22. Then, the G-matrix interaction for ESC16$^+$ is given by $\mathcal{G}(k_F, r) + \Delta\mathcal{G}(k_F, r)$.

Here, it is worthwhile to comment about a qualitative feature of $\Delta\mathcal{G}(k_F, r)$. The MPP contributions increase rapidly with matter density: In high (low) density region, they are very large (small), and canceled considerably by TBA at normal-density region. Then, net contributions of MPP+TBA given by $\Delta\mathcal{G}(k_F, r)$ are attractive for smaller values of k_F than 1.35 fm^{-1}.

Table 23: Central coupling parts of G-matrix interactions for ESC16, represented in a Gaussian form $\sum_{i=1}^{3}(a_i + b_i k_F + c_i k_F^2) \exp(-(r/\beta_i)^2)$.

	β_i	0.50	0.90	2.00
	a	5254	−796.7	8.509
ΛN-ΣN ${}^1S_0$	b	–8049	1302	0.0
	c	3126	–497.9	0.0
	a	–365.9	167.5	8.606
ΣN-ΣN ${}^1S_0$	b	881.7	–72.20	0.0
	c	–354.3	60.39	0.0
	a	–2868	393.9	–2.740
ΛN-ΣN ${}^3S_1$	b	4683	–729.1	0.0
	c	–1978	320.5	0.0
	a	773.5	–156.2	–4.313
ΣN-ΣN ${}^3S_1$	b	159.0	–10.37	0.0
	c	–172.2	31.04	0.0

Table 24: Tensor coupling parts of G-matrix interactions for ESC16, represented in a r^2-Gaussian form $\sum_{i=1}^{3}(a_i + b_i k_F + c_i k_F^2) r^2 \exp(-(r/\beta_i)^2)$.

	β_i	0.50	0.90	2.00
	a	−44610	547.5	−.7435
ΛN-ΣN ${}^3S_1$	b	69890	−1018	0.0
	c	−26870	389.0	0.0
	a	−2476	25.46	−.0220
ΛN-ΛN ${}^3S_1$	b	3179	−28.42	0.0
	c	−677.6	−.5974	0.0

The solved G-matrices include not only ΛN-ΛN diagonal parts but also ΛN-ΣN coupling parts, and it is possible to extract such coupling parts to treat ΛN-ΣN mixing problems. The ΛN-ΣN coupling interaction is determined so that its matrix elements in k space simulate the corresponding G-matrix elements and its radial form tend to that of the bare interaction in the outermost region. In Table 23 (Table 24), the parameters of the central (tensor) parts of ΛN-ΣN and

ΣN-ΣN interactions in S states are given in a three-range Gaussian (r^2-Gaussian) form. Here, the k_F dependencies are represented in the same form as the above diagonal parts. These coupling interactions can be used for ΛN-ΣN mixing problems together with the ΛN-ΛN diagonal interactions in the Table 21.

Table 25: Parameters of SLS and ALS G-matrix interactions represented by three-range Gaussian forms $\mathcal{G}(r;k_F) = \sum_i (a_i + b_i k_F + c_i k_F^2) \exp -(r/\beta_i)^2$ in the cases of ESC16.

	β_i	0.40	0.80	1.20
SLS	a	−11820	355.7	−1.541
	b	23600	−810.3	0.0
	c	−9796	325.2	0.0
ALS	a	1809	1.423	.7805
	b	−1547	37.07	0.0
	c	578.0	−15.73	0.0

In terms of the G-matrices $\mathcal{G}^{JS}_{LL'}(r)$ with S=1, the SLS interactions are given by the linear combination $\mathcal{G}_{SLS}(r) = \left(-2\mathcal{G}^{01}_{11} - 3\mathcal{G}^{11}_{11} + 5\mathcal{G}^{21}_{11}\right)(r)/12$. The ALS G-matrix interaction $\mathcal{G}_{ALS}$ between ^{3}P$_1$ and ^{1}P$_1$ states is given so that its matrix elements in k space simulate the corresponding G matrix elements $\langle {}^3P_1 \,|\, G \,|\, {}^1P_1 \rangle$. Because $\langle {}^3P_1 \,|\, G \,|\, {}^1P_1 \rangle$ and $\langle {}^1P_1 \,|\, G \,|\, {}^3P_1 \rangle$ are different from each other, $\mathcal{G}_{ALS}$ is derived from their averaged values. The SLS and ALS G-matrix interactions obtained as a function of k_F are represented in three-range Gaussian forms, the parameters of which are given for ESC16 in Table 25.

In order to compare clearly the SLS and ALS components, it is convenient to derive the strengths of the Λ l-s potentials in hypernuclei. In the same way as in Refs. [35, 3], the expression can be derived with the Scheerbaum approximation [91] as $U^{ls}_\Lambda(r) = K_\Lambda \frac{1}{r}\frac{d\rho}{dr}\mathbf{l}\cdot\mathbf{s}$. The values of K_Λ can be calculated with use of $\mathcal{G}_{SLS}(r)$ and $\mathcal{G}_{ALS}(r)$: The obtained value at $k_F = 1.0$ fm^{-1} is 3.8 MeV fm^5. This value is smaller than those for not only NSC97e/f but also ESC08a/b [64].

14.2. Λ hypernuclei by G-matrix folding potentials

The YNG ΛN G-matrix interaction given by Table 21 is expressed as $\mathcal{G}^S_{(\pm)}(r)$, S and $(\pm)$ denoting spin and party quantum numbers, respectively. A Λ-nucleus potential in a finite system is derived from this ΛN interaction by the expression

$$\begin{aligned} U_\Lambda(\mathbf{r},\mathbf{r}') &= U_{dr} + U_{ex}\,, \\ U_{dr} &= \delta(\mathbf{r}-\mathbf{r}')\int d\mathbf{r}''\rho(\mathbf{r}'')\,V_{dr}(|\mathbf{r}-\mathbf{r}''|;k_F) \\ U_{ex} &= \rho(\mathbf{r},\mathbf{r}')V_{ex}(|\mathbf{r}-\mathbf{r}'|;k_F)\,, \end{aligned} \tag{14.7}$$

$$\begin{pmatrix} V_{dr} \\ V_{ex} \end{pmatrix} = \frac{1}{4}\sum_{S=0,1}(2S+1)[\mathcal{G}^S_{(\pm)} \pm \mathcal{G}^S_{(\mp)}]\,. \tag{14.8}$$

Here, densities $\rho(r)$ and mixed densities $\rho(r,r')$ are obtained from spherical Skyrme-HF wave functions.

An important problem is how to treat k_F values included in G-matrix interactions. Here, the following Averaged-Density Approximation (ADA) is used, where an averaged value $\langle\rho\rangle$ is calculated by $\langle\phi_\Lambda(r)|\rho(r)|\phi_\Lambda(r)\rangle$ for each Λ state $\phi_\Lambda(r)$, and $\langle k_F\rangle$ is obtained by $(1.5\pi^2\langle\rho\rangle)^{1/3}$.

Let us calculate the energy spectra of Λ hypernuclei systematically ($^{13}_\Lambda$C, $^{16}_\Lambda$O, $^{28}_\Lambda$Si, $^{51}_\Lambda$V, $^{89}_\Lambda$Y, $^{139}_\Lambda$La, $^{208}_\Lambda$Pb). In Fig. 24, the calculated values are compared with the experimental values marked by open circles, the horizontal axis being given as $A^{-2/3}$, where solid and dashed curves are for YNG-ESC16$^+$ and YNG-ESC16, respectively. Here, the experimental data are shifted by 0.5 MeV from the values given in Ref. [92], which has been recently proposed according to the improved calibration [93]. The G-matrix interaction for ESC16 is found to give, compared to the

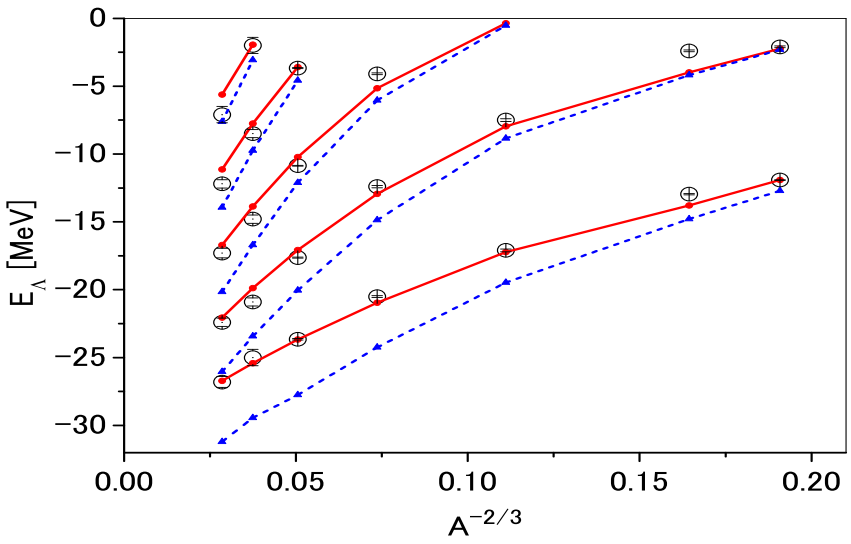

Figure 24: Energy spectra of ${}^{13}_{\Lambda}$C, ${}^{28}_{\Lambda}$Si, ${}^{51}_{\Lambda}$V, ${}^{89}_{\Lambda}$Y, ${}^{139}_{\Lambda}$La and ${}^{208}_{\Lambda}$Pb are given as a function of $A^{-2/3}$, A being mass numbers of core nuclei. Solid (dashed) lines show calculated values by the G-matrix folding model derived from ESC16$^+$ (ESC16). Open circles and error bars denote the experimental values taken from Ref. [92].

experimental values, an over-binding for B_Λ. In ESC16$^+$ values of $V^0_{TBA} = -16.0$ MeV with $\eta = 4.0$ fm^3 are chosen so that the value of $B_\Lambda({}^{89}_{\Lambda}Y)$ is reproduced well and the global fitting of B_Λ values is nicely improved in comparison with that for ESC16.

The difference between ESC16$^+$ and ESC16 is due to the extra terms $\Delta\mathcal{G}(k_F, r)$ originated from MPP+TBA. Especially, MPP plays an essential role to reproduce the nuclear saturation property and the stiffness of the EoS of neutron-star matter [86, 87, 88]. Then, it is very important that ESC16$^+$ gives a better fitting than ESC16: The density-dependent attraction $\Delta\mathcal{G}(k_F, r)$ in low-density region works to reproduce better the energy spectra of heavy systems and B_Λ values of light systems. In high-density region, this extra term is dominated by MPP and leads to the stiff EoS of the hyperon-mixed neutron-star matter [87, 88]. The present result suggests that such an effect of MPP+TBA is based on terrestrial data of B_Λ values.

Finally, note that the Λ s.p. energies in finite systems are not related simply to the $U_\Lambda(\rho_0)$ values given in Table 20. The $U_\Lambda(\rho_0)$ values of -43.7 MeV (-37.9 MeV) for ESC16 (ESC16$^+$) are very attractive compared to the value of -30 MeV, which is the depth U_{WS} of the Λ Woods-Saxon (WS) potential suitable to the data of Λ hypernuclei [94]. However, it is misleading to compare the $U_\Lambda(\rho_0)$ value directly to the U_{WS} one. The Λ-nucleus folding potential depends not only on the strengths of ΛN G-matrices but also on their k_F dependencies.

Table 26: Values of $U_\Sigma(\rho_0)$ at normal density and partial wave contributions in $({}^{2S+1}L_J, T)$ states for ESC16$^+$ (in MeV).

model	T	${}^1S_0$	${}^3S_1$	${}^1P_1$	${}^3P_0$	${}^3P_1$	${}^3P_2$	D	U_Σ
ESC16	1/2	10.2	−24.7	1.9	2.1	−5.3	−0.2	−0.6	
	3/2	−13.1	29.5	−3.5	−2.1	5.3	−2.6	−0.2	−3.3
ESC16$^+$	1/2	10.8	−20.7	2.1	2.2	−5.0	0.2	−0.5	
	3/2	−11.4	33.3	−3.0	−2.0	5.6	−1.8	−0.0	+9.9

14.3. ΣN G-matrix

Here, studied are the Σ binding energies in nuclear matter by solving the ΣN starting channel G-matrix equation. The universal repulsion MPP has to work also in ΣN channels. Then, the problem is how to choose the phenomenological TBA part on the basis of experimental information. The positive values of $U_\Sigma(\rho_0)$ can be compared roughly with the repulsive component of the Σ nuclear potential obtained from analyzing strong-interaction shifts and widths in Σ^- atoms [95]. The size of repulsion is model dependent, giving rise to the estimation of 30 ± 20 MeV. Another experimental information for the repulsive Σ-nucleus potentials are given by the observed (π^-, K^-) spectra [96, 97, 98]. In Ref. [97], they performed the DWIA analysis for the data of ^{28}Si(π^-, K^-) reaction, where some ΣN interaction models were studied. The experimental spectrum was reproduced nicely by the Σ-nucleus potential obtained from G-matrices for the Nijmegen OBE-model F [99] with the local density approximation, where the value of $U_\Sigma(\rho_0)$ was 24 MeV. Considering that the experimentally suggested values of $U_\Sigma(\rho_0)$ are strongly repulsive, taken is $V^0_{TBA} = 0.0$ MeV. ESC16$^+$ in ΣN channels is given by ESC16+MPP without TBA.

In Table 26 are shown the potential energies $U_\Sigma(\rho_0)$ for a zero-momentum Σ and their partial-wave contributions in $(^{2S+1}L_J, T)$ states for ESC16 and ESC16$^+$. It should be noted here that the strongly repulsive contributions in $^3S_1$ $T = 3/2$ and $^1S_0$ $T = 1/2$ states are due to the Pauli-forbidden effects in these states, being taken into account by strengthening the pomeron coupling in the ESC16 modeling.

In the left (right) panel of Fig. 25, U_Σ values (their S-state contributions) are drawn as a function of k_F for ESC16 and ESC16$^+$ by dashed and solid curves, respectively. It is demonstrated that the repulsive U_Σ values are due to $T = 3/2$ $^3S_1$ and $T = 1/2$ $^1S_0$ contributions, and the repulsions are enhanced by the MPP contributions.

The value of U_Σ is sensitive to the Pauli-repulsion parameter a_{PB}. Though $a_{PB} = 0.39$ is taken in ESC16, a larger value of a_{PB} gives rise to a more repulsive value of U_Σ. Taking $a_{PB} = 0.59$, $U_\Sigma(\rho_0)$=7.4 MeV and 20.3 MeV for ESC16 and ESC16$^+$ are obtained, respectively. Such a high value for the Pauli-blocking repulsion gives too high $\Sigma^+ p$ cross sections. In order to obtain strongly repulsive values of U_Σ without over-estimating $\Sigma^+ p$ cross sections, it might be necessary to introduce further many-body repulsions.

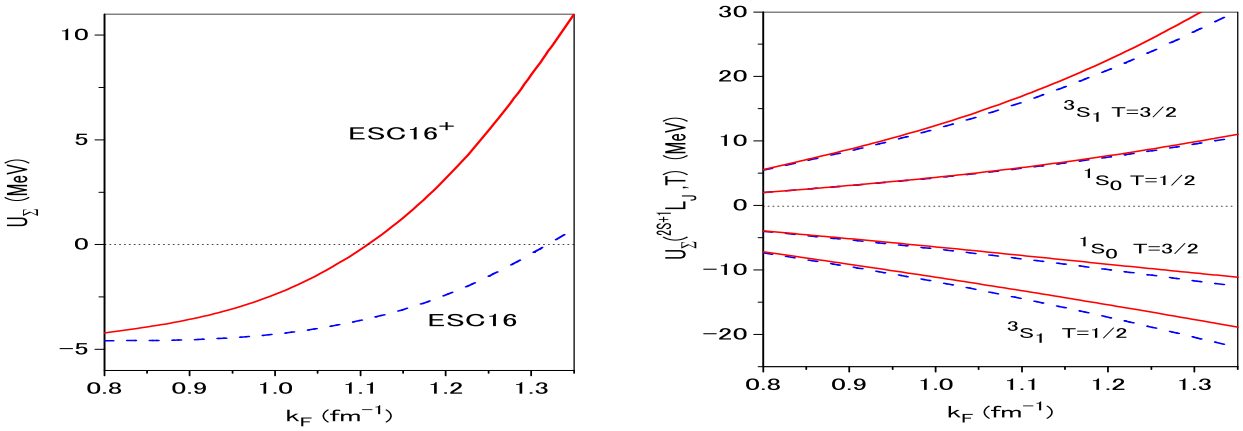

Figure 25: In the left (right) panel, the values of U_Σ (partial-wave contributions) are drawn as a function of k_F by dashed and solid curves for ESC16 and ESC16$^+$, respectively.

15. ESC16-model *YN*($S = -2$)-Results

In this section the results for the S=-2 calculations in [7] are reviewed: the effective-range parameters, the 'deuteron' channel, and the G-matrix calculations. Because of the difficulty for the ESC16-model to give a sufficient attraction for the well-depth U_Ξ, in [7] the extended models ESC16$^{(\star)}(A, B)$, see subsection 15.3, for BB-scattering have been developed. Furthermore, a model with an effective ΞN-interaction for the description of the Ξ-nucleus interaction has been studied. These are reviewed in 15.3 and 15.4, respectively. For the phase shifts, cross sections, and potential figures, see [7].

15.1. Effective-range parameters

The effective-range parameters are given here and elsewhere in this review, because they contain some information on the strength of the interaction since the scattering lengths are roughly proportional to the volume integral of the potentials, see [57]. This is useful for the comparison with other BB-channels. For ESC16 the $I = 0$ $\Lambda\Lambda(^1S_0)$ and $\Xi N(^3S_1)$ low-energy parameters are

$$\begin{aligned} a_{\Lambda\Lambda}(^1S_0) &= -0.439\,[fm]\,, \quad r_{\Lambda\Lambda}(^1S_0) = 9.533\,[fm] \\ a_{\Xi N}(^3S_1) &= -0.269\,[fm]\,, \quad r_{\Xi N}(^3S_1) = -10.250\,[fm]. \end{aligned}$$

For $I = 1$ and ESC16:

$$\begin{aligned} a_{\Xi N}(^1S_0) &= 0.556\,[fm]\,, \quad r_{\Xi N}(^1S_0) = -3.043\,[fm], \\ a_{\Xi N}(^3S_1) &= 0.144\,[fm]\,, \quad r_{\Xi N}(^3S_1) = 41.005\,[fm], \end{aligned}$$

For the $\Sigma\Sigma$ channels:

$$\begin{aligned} a_{\Sigma^0\Sigma^0} &= +0.495\,[fm]\,, \quad r_{\Sigma^0\Sigma^0} = +11.943\,[fm], \\ a_{\Sigma^\pm\Sigma^\pm} &= -0.432\,[fm]\,, \quad r_{\Sigma^\pm\Sigma^\pm} = -594.51\,[fm], \\ a_{\Sigma^\pm\Sigma^\mp} &= +9.983\,[fm]\,, \quad r_{\Sigma^\pm\Sigma^\mp} = -44.578\,[fm]. \end{aligned}$$

We note that the $\Sigma\Sigma(I = 2)$ channels are purely {27}-irrep, like the pp and $\Sigma^+p(^1S_0, I = 3/2)$. This implies that the nuclear interaction is rather attractive and rather close to a bound-state. In contrast to pp and Σ^+p in the channels $\Sigma^\pm\Sigma^\mp$ the Coulomb is attractive. Indeed, there is a Coulomb-assisted bound-state for $\Sigma^\pm\Sigma^\mp$, which by the effective-range formula has a binding energy $E_B = 0.076$ MeV. This does not happen for pp and Σ^+p, where the Coulomb is repulsive.

For the results at the ΞN threshold, and at the $\Lambda\Sigma$ threshold, see [7]. The $\Lambda\Lambda(^1S_0)$ scattering lengths are found to be larger in absolute value than in the NSC97 models [36], indicating a more attractive $\Lambda\Lambda$ interaction.

The old experimental information ${}^{\;6}_{\Lambda\Lambda}$He seemed to indicate a separation energy of $\Delta B_{\Lambda\Lambda} = 4 - 5$ MeV, corresponding to a rather strong attractive $\Lambda\Lambda$ interaction. As a matter of fact, an estimate for the $\Lambda\Lambda$ $^1S_0$ scattering length, based on such a value for $\Delta B_{\Lambda\Lambda}$, gives $a_{\Lambda\Lambda}(^1S_0) \approx -2.0$ fm [100, 101]. However, in recent years the experimental information and interpretation of the ground state levels of ${}^{\;6}_{\Lambda\Lambda}$He, ${}^{10}_{\Lambda\Lambda}$Be, and ${}^{13}_{\Lambda\Lambda}$B [102], has been changed drastically. This because the Nagara-event, identified uniquely as ${}^{\;6}_{\Lambda\Lambda}$He [80], established that the $\Lambda\Lambda$-interaction is weaker ($\Delta B_{\Lambda\Lambda} \approx 0.7$ MeV). Furthermore, in $\Lambda\Lambda$-correlation studies of Heavy-Ion collisions [103] a small inegative $a_{\Lambda\Lambda}(^1S_0)$ is favored.

In NSC97 [35] it was only possible to increase the attraction in the $\Lambda\Lambda$ channel by modifying the scalar-exchange potential. If the scalar mesons are viewed as being mainly $q\bar{q}$ states, one finds that the (attractive) scalar-exchange part of the interaction in the various channels satisfies

$$|V_{\Lambda\Lambda}| < |V_{\Lambda N}| < |V_{NN}|, \tag{15.1}$$

suggesting indeed a rather weak $\Lambda\Lambda$-potential. The NSC97 fits to the *YN* scattering data [35] give values for the scalar-meson mixing angle which seem to point to almost ideal mixing for the scalars as $q\bar{q}$ states. In NSC97 an increased attraction in the $\Lambda\Lambda$ channel would give rise to (experimentally unobserved) deeply bound states in the ΛN channel. On the other hand, in the ESC-models there are in principle more possibilities because of the presence of meson-pair potentials and this problem does not occur.

15.2. No deuteron-like state in $\Xi N(^3S_1 -^3 D_1, I = 1)$

The possible bound-states, using the SU(3) content of the different $S = 0, -1, -2$ channels are discussed in [36]. In ESC16 there is no bound-state with isospin I=1 or I=0 and strangeness S=-2. Apparently, the tensor contribution in the spin triplet-coupled states is not large enough to give a bound state. In ESC08c a deuteron-like bound-state was produced, belonging to the $\{10^*\}$ SU(3)-irrep, which is a ΞN bound state in the $^3S_1$-$^3D_1$ coupled partial wave. In model ESC04d [104], there occurs in the $\{8_a\}$-state a ΞN bound state in the $\Xi N(^3S_1$-$^3D_1, (I = 0)$ partial wave. In the ESC04 models, this occurrence was ascribed to the inclusion of the potentials of the axial-vector-mesons, and the meson pairs. Since the ESC04a-c versions did not show such a bound state it is considered to be accidental.

15.3. ESC16$^{(\star)}$: ESC16 $\oplus$ SU(3)-symmetric Gaussians

The observation of the twin Λ hypernuclei [105, 106] and the KISO event [107] are strong indications that the Ξ-nucleus interaction is not repulsive, but (moderately) attractive. Two events with "twin" Λ hypernuclei (I) [105] and (II) [106] were observed in the KEK E-176 experiment, and an event (III) [107] in the KEK E373 experiment. This is in line with the result of the BNL-E885 experiment [108] giving $U_\Xi \approx -14$ MeV. It appeared that this could not be accomodated by the ESC16-model, which is strongly constrained by the NN and $YN(S = -1)$ data. Moreover, ESC16 fails to describe the $\Xi^- p$-correlations found in the ALICE-experiment at CERN [31]. Therefore, there are indications that the potentials of the ESC-models, although very successful for the NN and YN(S=-1) interactions, are inadequate for the ΞN interaction, showing some "incompleteness". Possible sources of "incompleteness" are *e.g.*: (i) In the two-meson exchange potentials only the PS-PS are included, but not PS-VC, PS-SC, VC-VC, VC-SC etc. (Inclusion of these exchanges was tested for NN and YN(S=-1) giving no improvements.), (ii) The SU(3)-structure of the 33-resonances, like the Fujita-Miyazawa interaction, is not covered completely by the meson-pair exchanges, (iii) Two-pair exchanges are not fully taken into account.

In [7] a new version ESC16$^{(\star)}$ has been introduced by adding to the ESC16 model SU3-symmetric (s-wave) phenomenological two-body forces: gaussian central-, spin-spin-, and tensor-potentials. This in the t- and u-channel [109] SU(3)-irreps $\{\mu'\}$: $\{\underline{27}\}$, $\{\underline{8}_s\}$, $\{8_a\}$, $\{10^*\}$, $\{10\}$. These new potentials, indicated by the subscript X, in the t- and u-channel are denoted as $\widetilde{W}_c$, $\widetilde{W}_\sigma$, and $\widetilde{W}_t$ for respectively the central-, spin-spin-, and tensor-potential, and taken of the form

$$\begin{aligned} \widetilde{W}_{\mu',c}(r) &= C_{\{\mu'\}}\, f_W(r),\ \widetilde{W}_{\mu',\sigma}(r) = S_{\{\mu'\}}\, f_W(r), \\ \widetilde{W}_{\mu',t}(r) &= -(4/3) T_{\{\mu'\}}\, (m_W r)^2 f_W(r), \end{aligned} \tag{15.2}$$

where C, S, T are the t- and u-channel coefficients for the central (C), spin-spin (S) and tensor (T) potentials, and $f_W(r) = \exp(-m_W^2 r^2)$, $m_W = 300$ MeV. For simplicity a universal profile has been assumed, which is similar to that of the pomeron. No specific space-time structure is imposed leaving the central, spin-spin and tensor unrelated.
In general, the potentials in the s-channel irreps are related to those in the t- and u-channel by the crossing matrices X_{st}, X_{su}. For the so-called signatured potentials $V^{(\pm)} = [V(t) \pm V(u)]/2$ these can be combined. In Table 27 the SU(3) crossing matrices $X^{(\pm)}$, derived from Ref. [110], for the signatured potentials are given. The SU(3)-singlet exchange gives no distinction for the s-channel irreps and therefore is not included in the new $SU(3)$-symmetric potentials. Then, the s-channel potentials in the $\{\mu\}$-irrep corresponding to (15.2) are

$$W^{(\pm)}_{\mu,c}(r) = \sum_{\mu'} X^{(\pm)}(\mu, \mu')\, C_{\{\mu'\}}\, f_W(r), \tag{15.3}$$

and similarly for the spin-spin and tensor potentials. At present, experimentally it is not clear from which states the major attractive contribution to U_Ξ comes. Therefore, in [7] the results for two choices of the C,S,T parameters were worked out: ESC16$^{(\star)}$(A) and ESC16$(^\star)$(B). In these applications only central and spin-spin extra gaussian potentials are included. In both cases, the fitted meson coupling constants are about equal to those obtained with ESC16, which is also the case for the MPE couplings. Also, it appeared that the QPC-pattern of the baryon-baryon-meson g_{BBM}-couplings is preserved. The results are:
ESC16$^{(\star)}$(A): In this case it is assumed that $S_{\{10\}} = 0$. The central and spin-spin parameters of the new potentials in ESC16$^{(\star)}$ from the fit are listed in Table 28. No new tensor potentials were included. As can be seen in Table 29, the well-depths for ESC16$^{(\star+)}$ are much improved qualitatively compared to ESC16. In this table the "exp" values are

Table 27: The st- and su-crossing matrix $X^{(\pm)} = [X_{st} \pm X_{su}]/2$. Here $(\pm)$ refers to the symmetric $(27, 8_s, 1)$ and the asymmetric $(8_s, 10, 10^*)$ irreps respectively.

		$\mu'_{\beta'\gamma'}(t,u)$					
		27	8_s	1	8_a	10^*	10
	27	7/40	1/5	1/8	—	—	—
$\mu_{\beta\gamma}(s)$	8_s	27/40	–3/10	1/8	—	—	—
	1	27/8	1	1/8	—	—	—
	8_a	—	—	—	1/2	0	0
$\mu_{\beta\gamma}(s)$	10	—	—	—	0	1/4	1/4
	10^*	—	—	—	0	1/4	1/4

Table 28: ESC16$^{(\star)}$(A): Coupling constants SU(3)-symmetric gaussian potentials.

$\{\mu\}$	{27}	$\{8_s\}$	$\{8_a\}$	$\{10^*\}$	{10}
$C_{\{\mu\}}$	–0.41	–0.19	–6.64	+0.12	–2.66
$S_{\{\mu\}}$	–0.13	+0.90	+7.19	+0.49	0.0
$T_{\{\mu\}}$	—-	—-	—-	—-	—-

the experimental nuclear saturation point E_N, the U_Λ and U_Σ well-depth's from Ref. [6], and for U_Ξ the [108] datum. The ESC16$^{(\star+)}$ model includes, in distinction to ESC16$^{(\star)}$, three-body-forces (TBF's) calculated from the meson-pair interactions. The partial wave contributions to the U_Ξ-well-depth are displayed in Table 30. The attraction for U_Ξ comes from the T=0 states, in particular the $\Xi N(^1S_0, T = 0)$- and the $\Xi N(^3S_1, T = 0)$-state. The T=1 states give repulsion which comes mainly from the $\Xi N(^1S_0, T = 1)$-state. Note that the TBF contribution in Table 29 is repulsive for all well-depth's. Hence, the TBF used here would not lead to the desired attractive ΞN well-depth in the ESC16 model.

In the ESC16$^{(\star+)}$ model there is enough flexibility to tune U_Ξ to a smaller value by refitting, eventually with an extended combined fit including next to the NN⊕YN data, also the well depth's treated as pseudo-data.

Table 29: ESC16$^{(\star)}$(A): The nuclear saturation energy $E_N = B/A$, the well-depths U_Λ, U_Σ, and U_Ξ with SU(3)-symmetric interactions and three-body forces (TBF) at $k_F = 1.35$ fm, and $\Lambda_{FM} = 2500$ MeV. $E_N = T_N + U_N$, with $T_N = 22.626$ MeV.

	E_N	U_Λ	U_Σ	U_Ξ
"exp"	-16.3	-37.9	+9.9	-14.0
ESC16$^{(\star)}$	-19.9	-48.9	-26.1	-36.5
ESC16$^{(\star+)}$	-16.4	-36.7	+8.0	-17.8

ESC16$^{(\star)}$(B): In this case R-conjugation symmetry [111] is assumed, which implies that $C_{10} = C_{10^*}, S_{10} = S_{10^*}$, and $T_{10} = T_{10^*}$. (R-conjugation is not an SU(3)-symmetry, but an approximate symmetry of the ESC-model. It forbids e.g. the $^3P_1 \leftrightarrow ^1P_1$ transition, which is allowed under SU(3).) The results for this model are presented in Tables 31, 32, and 33. Comparison of Table 30 and Table 33 shows that the major attractive contribution comes from the $(^1S_0, T = 0)$- and $(^3S_1, T = 0)$- partial wave for ESC16$^{(\star)}$(A) and ESC16$^{(\star)}$(B) respectively. These results show that the extra freedom generated by the introduction of the SU(3)-symmetric Gaussian potentials $W^{(\pm)}_{\mu,\nu}(r), (\nu = c, s, t)$ leads to BB-interactions, which provide a good basis for calculations in $S \leq -2$ hypernuclear physics, and the ALICE correlation data.

Table 30: ESC16$^{(\star)}$(A): Partial wave contributions to $U_\Xi(\rho_0)$ at normal density.

model		$^1S_0$	$^3S_1$	$^1P_1$	$^3P_0$	$^3P_1$	$^3P_2$	U_Ξ	Γ^c_Ξ
ESC16	$T=0$	2.1	–0.4	–0.2	-5.3	1.5	–1.2		
	$T=1$	9.2	7.6	1.0	0.8	–2.0	–0.5	+13.7	5.1
ESC16$^{(\star)}$	$T=0$	–23.5	–5.7	0.9	-2.6	1.3	–1.6		
	$T=1$	7.0	–9.0	1.3	0.3	–3.2	–1.6	-36.5	9.0
ESC16$^{(\star+)}$	$T=0$	–16.0	–4.7	0.8	-3.2	2.1	–1.5		
	$T=1$	10.3	–6.4	2.0	1.4	–3.2	0.7	-17.8	4.7

Table 31: ESC16$^{(\star)}$(B): Coupling constants SU(3)-symmetric gaussian potentials.

$\{\mu\}$	$\{27\}$	$\{8_s\}$	$\{8_a\}$	$\{10^*\}$	$\{10\}$
$C_{\{\mu\}}$	–0.11	–0.49	–6.01	–3.27	–3.27
$S_{\{\mu\}}$	–0.49	+1.74	+6.54	–0.60	–0.60
$T_{\{\mu\}}$	—-	—-	—-	—-	—-

Table 32: ESC16$^{(\star)}$(B): The nuclear saturation energy $E_N = B/A$, the well-depths U_Λ, U_Σ, and U_Ξ with SU(3)-symmetric interactions and three-body forces (TBF) at $k_F = 1.35$ fm, and $\Lambda_{FM} = 1750$ MeV. $E_N = T_N + U_N$, with $T_N = 22.626$ MeV.

	E_N	U_Λ	U_Σ	U_Ξ
"exp"	-16.3	-37.9	+9.9	-14.0
ESC16$^{(\star)}$	-20.2	-51.5	-27.3	-25.2
& TBF	-14.4	-32.8	+17.6	-9.1

Table 33: ESC16$^{(\star)}$(B): Partial wave contributions to $U_\Xi(\rho_0)$ at normal density.

model		$^1S_0$	$^3S_1$	$^1P_1$	$^3P_0$	$^3P_1$	$^3P_2$	U_Ξ	Γ^c_Ξ
ESC16	$T=0$	2.1	–0.4	–0.2	-5.3	1.5	–1.2		
	$T=1$	9.2	7.6	1.0	0.8	–2.0	–0.5	+13.7	5.1
ESC16$^{(\star)}$	$T=0$	–1.0	–8.6	0.7	-3.0	1.1	–1.8		
	$T=1$	4.0	–11.7	0.9	0.2	–3.6	–2.3	-25.2	2.5
ESC16$^{(\star+)}$	$T=0$	0.4	–9.6	0.4	-4.9	2.9	–2.2		
	$T=1$	7.9	–4.3	1.9	1.8	–3.9	0.6	-9.1	3.1

15.4. ΞN G-matrix interaction and Ξ-nucleus states.

In Ref. [7] the G-matrix calculations have been performed with the continuous (CON) choice, where off-shell potentials are taken into account continuously from on-shell ones in intermediate propagations of correlated pairs. A two-body $^{(2T+1)(2S+1)}L_J$-state is specified by spin S, isospin T, orbital and total angular momenta L and J, respectively. Imaginary parts of G-matrices appear due to energy-conserving transitions from ΞN to $\Lambda\Lambda$ channels in $^{11}S_0$ and $^{13}P_J$ states. A conversion width Γ^c_Ξ is obtained from an imaginary part of U_Ξ by multiplying -2. The result $U_\Xi(\rho_0)$ for ESC16 is shown in Table 34. The BNL-E885 experiment [108] suggests that a Ξ^- s.p. potential in $^{12}_{\Xi^-}$Be is given by the attractive Wood-Saxon (WS) potential with the depth ~ -14 MeV. Furthermore, the emulsion events of Ξ hypernuclei give clear evidence for attractive Ξ-nucleus potentials. The depth of the above WS potential is related to the potential energy $U_\Xi(\rho_0)$ in normal-density matter, when a Ξ-nucleus potential is modeled as a local-density potential $U_\Xi(\rho(r))$. Though their relation is only indirect, it is clear that the repulsive value of $U_\Xi(\rho_0)$ for ESC16 in Table 34 is in contradiction with the above-mentioned experimental indications of attractive Ξ-nucleus interactions.

In order to realize an attractive Ξ-nucleus interaction, next to the ESC16$^{(\star)}$(A,B) solution to this problem, in [7] also a phenomenological effective ΞN interaction V_{eff} composed of two terms, a $(\pi\omega)$-pair exchange interaction $V_{\pi\omega}$ and a $SU(3)$-singlet interaction $V_{singlet}$, has been added to the ESC16 interaction. The $V_{\pi\omega}$ spin-spin and tensor potential functions are given in Ref. [112], equation (C17). The effective interaction is given as

$$\begin{aligned} V_{eff}(r;\rho) &= (X_2 + X_3 f(\tilde{\rho}))\, V_{\pi\omega}(r) + X_s\, V_{singlet}(r), \\ f(\tilde{\rho}) &= \tilde{\rho}\, \exp(-\eta\tilde{\rho}) \end{aligned} \tag{15.4}$$

with $\tilde{\rho} = \rho/\rho_0$. Here, the first term is assumed to have density-dependent strength, where $f(\tilde{\rho})$ is modeled so that it dominates at low density and is negligible at higher densities. X_2 and X_3 are strengths of density-independent two-body part and density-dependent one. This term brings about a large attraction especially in $(TSP) = (11+)$ state, P denoting parity. X_s is the strength of the $SU(3)$-singlet interaction, which works in $(TSP) = (00+)$ and $(01-)$ states. The form of the singlet potential is chosen as $V_{singlet} = -m_s \exp(-m_s^2 r^2/4)$, $m_s = 760$ MeV and for the different BB-channels the weights are the coefficients of V_1 in Table 2.

Parameters X_2, X_3, η and X_s are determined so that the derived G-matrix interaction derived from ESC16+V_{eff} reproduces the experimental value of Ξ^- binding energies B_{Ξ^-} in Ξ^-+^{14}N system [113, 107]. For the analysis, studied have been the four parameter sets A1, A2, B1 and B2, specified by (X_2, X_3, X_s)= (2.85, 0.0, 0.0), (2.55, 1.60, 0.0), (1.65, 0.0, 10.0) and (1.07, 3.00, 10.0), respectively, η being taken as 1.6. In the case of B1 and B2, the Pauli-blocking effect for [51]-configuration is not taken into account in the ESC16 construction. These four sets for V_{eff} give reasonable values of $B_{\Xi^-}(1S)$ and $B_{\Xi^-}(2P)$ in the Ξ^-+^{14}N system.

Table 34 shows the potential energies U_Ξ and their partial-wave contributions in $^{(2T+1)(2S+1)}L_J$ states at normal density ρ_0 for ESC16, A1, A2, B1 and B2. The U_Ξ value for ESC16 turns out to be repulsive. Comparing the partial-wave contributions for ESC16 with those for A1 or A2, one finds that the main difference is in $^{33}S_1$-state contributions, being repulsive in the former and strongly attractive in the latter. The negative value of U_Ξ in the case of A1 or A2 is due to the large $^{33}S_1$ attractive contribution of the ΞN-$\Lambda\Sigma$-$\Sigma\Sigma$ tensor-coupling term in the $(\pi\omega)$-pair exchange interaction in Eqn.(15.4). In the case of B1 or B2, the $^{33}S_1$ contributions are not so attractive, but instead the $SU(3)$-singlet interaction in $^{11}S_0$ state contributes attractively to give the negative value of U_Ξ. The calculated values of $\Gamma^c_\Xi(\rho_0)$ are given in the Table 34, the dominant contributions of which come from the $\Lambda\Lambda$-ΞN-$\Sigma\Sigma$ coupling interaction in the $^{11}S_0$ state. Here, it should be noted that the Γ^c_Ξ values for B1 and B2 are far smaller than those for A1 and A2.

The calculated values for the HAL-QCD potential (t13) are also given in the Table 34. Here P-state values are lacking because only the S-state potentials are given in Ref.[114]. There appear the two distinct features in the HAL-QCD result: One is the strongly attractive value of partial-wave contribution in $^{11}S_0$ state. It should be noted that the value in this state is given genuinely by the interaction because of the statistical weight factor $(2T+1)(2J+1) = 1$. The other is the small value of Γ^c_Ξ. Concerning these features, B1/B2 are more similar to HAL-QCD than A1/A2 owing to the $SU(3)$-singlet interactions. For reference, let us show the calulated values of $U_\Xi(\rho_0)$ for the t12 and t11 versions of the HAL-QCD potential, being -14.1 MeV and -16.2 MeV, respectively. Thus, these versions lead to overbinding values of B_Ξ in comparison with the experimental data.

It is interesting to compare these results with those by the chiral NLO interactions. Their G-matrix results are given in Ref.[115], where their calculated values of $U_\Xi(\rho_0)$ and their partial-wave contributions can be found in Fig.3

Table 34: $U_\Xi(\rho_0)$ and partial wave contributions in $^{(2T+1)(2S+1)}L_J$ states for ESC16 and ESC16+V_{eff} (A1, A2, B1, B2) calculated with the CON choice. Γ^c_Ξ denotes ΞN-$\Lambda\Lambda$ conversion width. Also the calculated values are given for the HAL-QCD potential [114]. All entries are in MeV.

	ESC16	A1	A2	B1	B2	HAL-QCD
X_2	0.0	2.85	2.55	1.65	1.07	
X_3	0.0	0.0	1.6	0.0	3.0	
X_s	0.0	0.0	0.0	10.	10.	
$^{11}S_0$	2.1	1.4	1.4	−4.0	−4.0	−4.9
$^{13}S_1$	−0.4	−2.2	−2.2	−2.8	−2.8	−2.2
$^{11}P_1$	−0.2	−0.3	−0.3	−0.3	−0.3	
$^{13}P_0$	−5.3	−3.5	−3.5	−2.0	−2.0	
$^{13}P_1$	1.5	1.3	1.3	1.7	1.7	
$^{13}P_2$	−1.2	−1.2	−1.2	−2.3	−2.3	
$^{31}S_0$	9.2	9.9	9.9	6.8	6.8	1.8
$^{33}S_1$	7.6	−13.5	−13.9	−4.7	−4.9	−5.4
$^{31}P_1$	1.0	1.3	1.3	1.0	1.0	
$^{33}P_0$	0.8	1.0	1.0	0.8	0.7	
$^{33}P_1$	−2.0	−2.8	−2.8	−3.0	−3.0	
$^{33}P_2$	0.5	0.1	0.1	−1.0	−1.0	
U_Ξ	+13.7	−8.5	−9.0	−10.1	−10.4	−10.6
Γ^c_Ξ	5.1	5.7	5.7	0.5	0.5	0.2

and Fig.2 (the values at $k = 0$ fm^{-1} in the figues), respectively. Then, their $U_\Xi(\rho_0)$ value is rather close to those for A1/A2 and B1/B2. The $^{11}S_0$ and $^{13}S_1$ ($^{31}S_0$ and $^{33}S_1$) contributions are similar to those for B1/B2 (A1/A2).

For the results on the finite Ξ^--nuclear systems: see Ref. [7], section VIIC. Here, the same method as for the Λ-nuclei has been used. A Ξ-nucleus folding potential $U_\Xi(\mathbf{r}, \mathbf{r}')$ for each particular system is obtained from $\mathcal{G}^{TS}_{(\pm)}(r; k_f)$, similarly as for $U_\Lambda(\mathbf{r}, \mathbf{r}')$ in Eqn.'s (14.7) and (14.8). It is assumed that a core nucleus is spherical, having zero spin and isospin. The densities $\rho(r)$ and mixed densities $\rho(r, r')$ have been obtained using Skyrme-HF wave functions. Using a local approximation for U_{ex} gives a local Ξ-nucleus potential $U_\Xi(r; k_f)$ for a spherical core. The isospin dependence of $\mathcal{G}^{TS}_{(\pm)}(r; k_F)$ leads to a Lane term. Only diagonal parts of the $\mathbf{t}_\Xi \cdot \mathbf{T}_c$ term have been taken into account. Results for binding energies B_{Ξ^-}, conversion widths $\Gamma^c_{\Xi^-}$, and radii $\sqrt{\langle r^2 \rangle}$, have been worked out for $\Xi^- +^{12} C, \Xi^- +^{14} N, \Xi^- +^{16} O$ and $\Xi^- +^{27}$Al, which have been shown in [7], Table XVII. These calculation also have been done for HAL-QCD.

16. ESC16-model $YY(S = -3, -4)$-Results

In this section the properties and results in [8] of the ESC16, and ESC16$^{(\star)}$ potentials for the S=-3,-4 sectors are presented. It appeared that the results for S=-3,-4 for the different models are not significantly different. Showed are the detailed results for ESC16, which are sufficient to represent the possible kinds of results. In the following, the model predictions for scattering lengths, bound states, and cross sections are shown.

16.1. Effective-range parameters

The (multi-channel) effective-range expansion, see [116], reads

$$p^{L+1/2}(\bar{K}^J)^{-1}p^{L+1/2} - A^{-1} + \frac{1}{2}(p^2 - p_0^2)^{1/2}\, R\, (p^2 - p_0^2)^{1/2},$$

where $\bar{K}^J$ is the mutilated K^J matrix with the $^3D_1$ channels being cut out, A^{-1} is the inverse scattering-length matrix, R the effective-range matrix, $p^{L+1/2}$ and $(p^2 - p_0^2)^{1/2}$ are the diagonal CM momentum matrices with elements $p_i^{L+1/2}$ and $(p_i^2 - p_{0i}^2)^{1/2}$. The low-energy parameters, *i.e.* scattering-lengths and effective-ranges, are shown for the S=-4 channels. For the low-energy parameters of the S=-3 channels $\Lambda\Xi, \Sigma\Xi$ having $I = 1/2, 3/2$, see Ref. [8]. Here A and R are matrices, which makes a thorough analysis complicated.

16.2. S=-4 Results

The following S=-4 low-energy parameters of ESC16 are obtained, where the C denotes Coulomb included

$$\begin{aligned} a^C_{\Xi\Xi}(^1S_0) &= -1.81\ [fm],\ \ r^C_{\Xi\Xi}(^1S_0) = 3.89\ [fm], \\ a_{\Xi\Xi}(^1S_0) &= -1.90\ [fm],\ \ r_{\Xi\Xi}(^1S_0) = 4.28\ [fm], \\ a_{\Xi\Xi}(^3S_1) &= +0.52\ [fm],\ \ r_{\Xi\Xi}(^3S_1) = 2.74\ [fm]. \end{aligned}$$

For ESC16$^{(\star)}$(A):

$$\begin{aligned} a_{\Xi\Xi}(^1S_0) &= -1.69\ [fm],\ \ r_{\Xi\Xi}(^1S_0) = 4.71\ [fm], \\ a_{\Xi\Xi}(^3S_1) &= +0.48\ [fm],\ \ r_{\Xi\Xi}(^3S_1) = 3.41\ [fm]. \end{aligned}$$

For ESC16$^{(\star)}$(B):

$$\begin{aligned} a_{\Xi\Xi}(^1S_0) &= -1.86\ [fm],\ \ r_{\Xi\Xi}(^1S_0) = 4.45\ [fm], \\ a_{\Xi\Xi}(^3S_1) &= +0.49\ [fm],\ \ r_{\Xi\Xi}(^3S_1) = 3.16\ [fm]. \end{aligned}$$

Comparison with the NN low-energy parameters in Table 13, shows that the interactions in the $\Xi\Xi$-channels is weaker, and there is no S=-4 analogon of the deuteron.

*16.3. Bound states in **S** waves*

The effective range formula for the pole position of a possible bound state in momentum space is

$$\kappa_\pm = (1 \pm \sqrt{1 - 2r/a})/r,\ B_\pm = -\kappa_\pm^2/(2m_{red}),$$

where the momentum is $p_\pm = i\kappa_\pm$. The pole closest to the lowest threshold is given by κ_-, and (usually) κ_+ is outside the region of the approximate validity of the effective-range formula. which for $\Xi\Xi(^1S_0)$ gives $\kappa_- < 0$, meaning an anti-bound state, and κ_+ is too large for the effective range expansion to be valid. In the case of $\Xi\Xi(^3S_1)$ the root is imaginary, and so no bound state. (Apparently, there is enough SU(3)- and R-symmetry breaking to prevent a deuteron-like bound state in this channel.) Similar analysis shows that also in the other channels, there do not occur bound states.
A discussion of the possible bound-states, using the SU(3) content of the different $S = 0, -1, -2$ channels is given in [35]. In contrast to the NSC97 models, no S<0 bound states are found in the ESC16 models.

16.4. Partial Wave Phase Parameters

For the *BB*-channels below the inelastic threshold, for the parametrization of the amplitudes the standard nuclear-bar phase shifts of [117] are used. The information on the elastic amplitudes above thresholds is most conveniently given using the BKS-phases [118, 119, 120, 121]. For uncoupled partial waves, the elastic *BB* S-matrix element is parametrized as

$$S = \eta e^{2i\delta}\ ,\ \ \eta = \cos(2\rho)\ . \tag{16.1}$$

For coupled partial waves the elastic *BB*-amplitudes are 2×2-matrices. The BKS S-matrix parametrization reads

$$S = e^{i\delta} e^{i\epsilon} N\ e^{i\epsilon} e^{i\delta}\ , \tag{16.2}$$

where

$$\delta = \begin{pmatrix} \delta_\alpha & 0 \\ 0 & \delta_\beta \end{pmatrix},\ \ \epsilon = \begin{pmatrix} 0 & \epsilon \\ \epsilon & 0 \end{pmatrix}, \tag{16.3}$$

and N is a real, symmetric matrix parameterized as

$$N = \begin{pmatrix} \eta_{11} & \eta_{12} \\ \eta_{12} & \eta_{22} \end{pmatrix}. \tag{16.4}$$

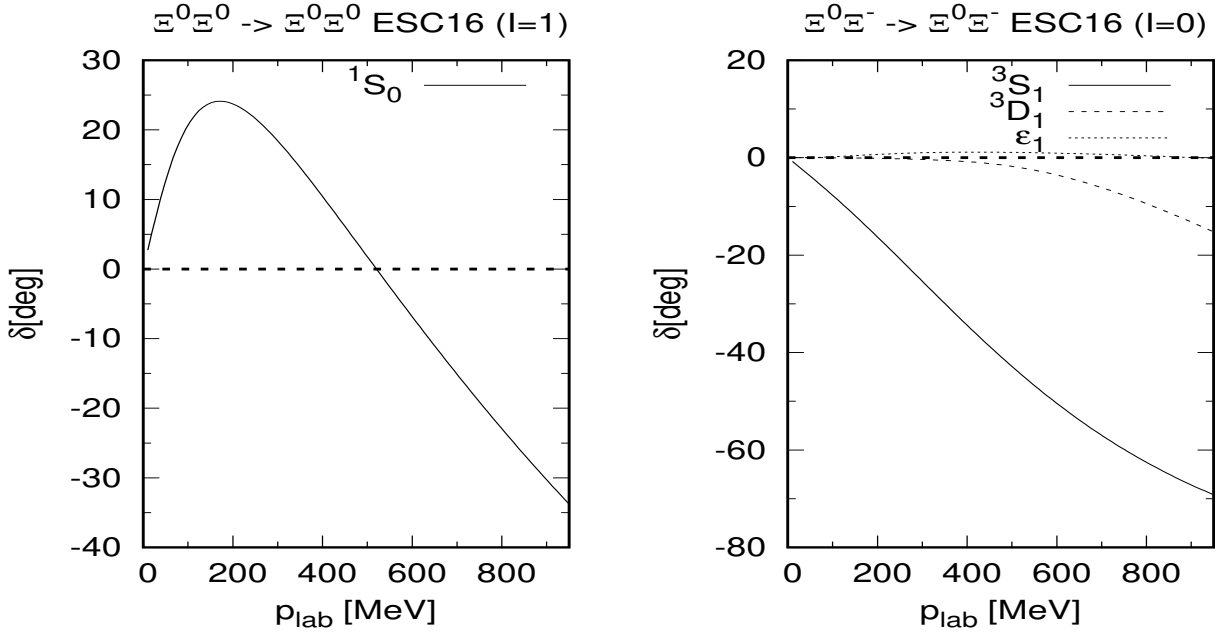

Figure 26: ESC16 $\Xi^0\Xi^0(^1S_0, I = 1)$- and $\Xi^0\Xi^-(^3S_1, I = 0)$ phases.

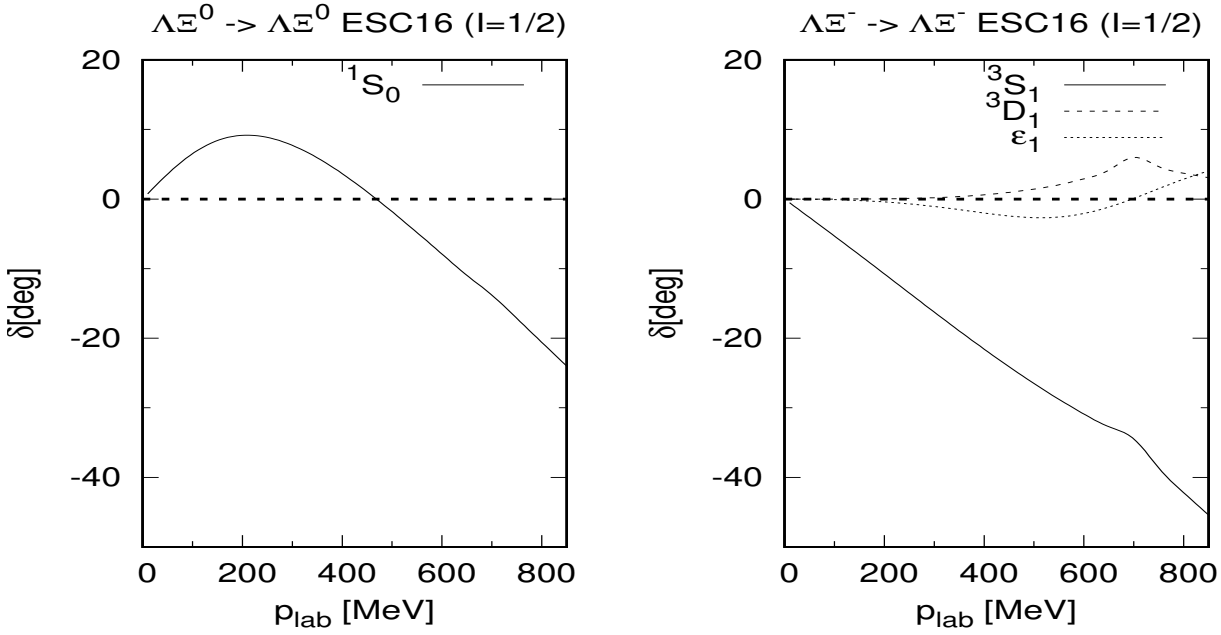

Figure 27: ESC16 $\Lambda\Xi$ $I = 1/2$ phases.

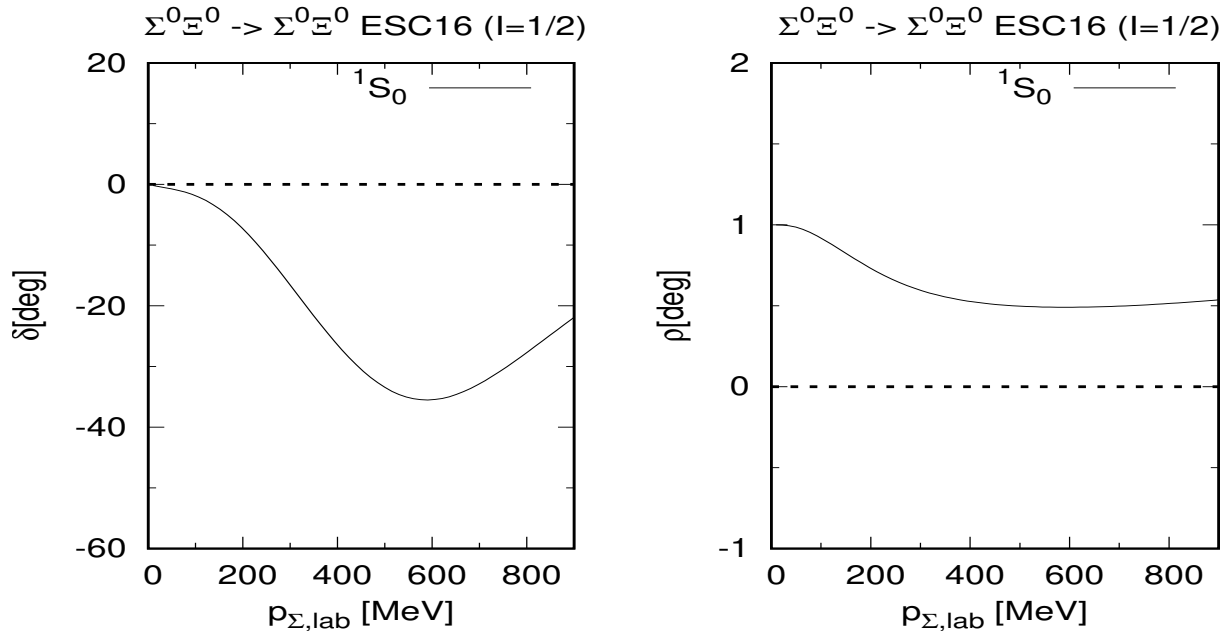

Figure 28: ESC16 $I = 1/2$ ${}^1S_0(\Sigma^0\Xi^0)$ phases and η-inelasticities.

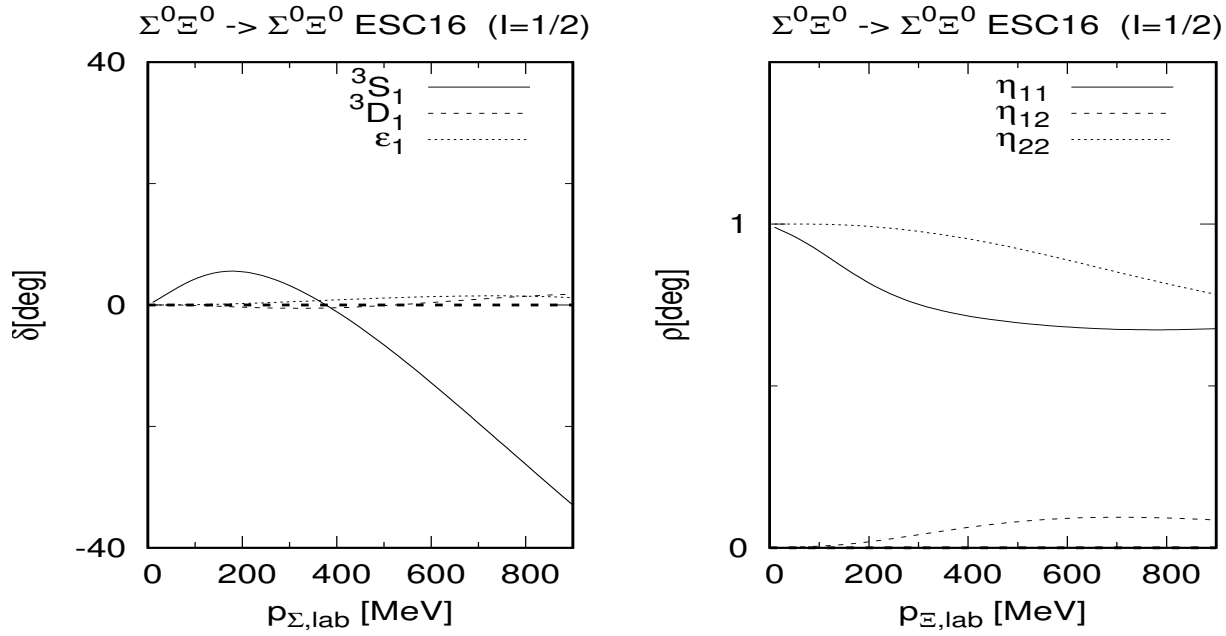

Figure 29: ESC16 $I = 1/2$ ${}^3C_1(\Sigma^0\Xi^0)$-phases and η-inelasticities.

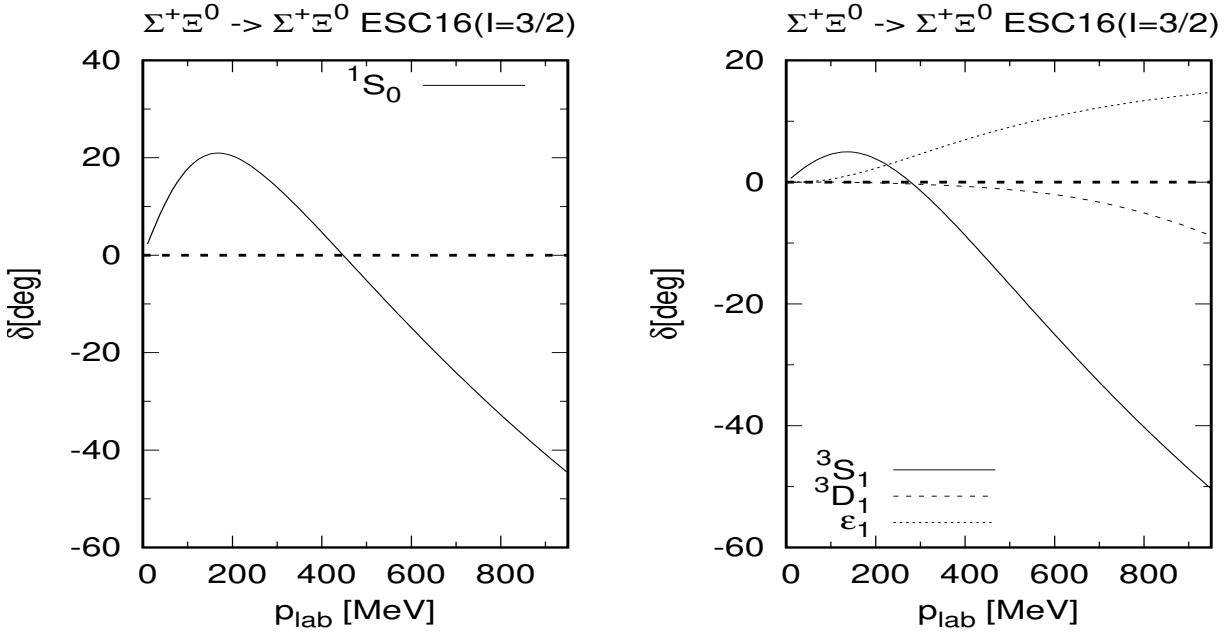

Figure 30: ESC16 $I = 3/2$ $\Sigma^+\Xi^0$-phases.

In Fig. 26 the S=-4 ESC16 nuclear-bar phases for $\Xi^0\Xi^0(^1S_0, I = 1)$ and $\Xi^0\Xi^-(^3S_1, I = 0)$ are shown. Fig. 27 shows the $\Lambda\Xi^0(^1S_0)$ and $\Lambda\Xi^-(^3S_1 - ^3D_1)$ phase parameters. Fig. 28 and Fig. 29 show for ESC16 the $\Sigma^0\Xi^0(I = 1/2)$ BKS phase shift and inelasticity parameters for $^1S_0$ and $^3S_1$ respectively. Similarly, Fig. 30 shows the $\Sigma^+\Xi^0(I = 3/2)$ phase shifts.

The $\Xi^-\Xi^-, \Xi^0\Xi-, \Xi^0\Xi^0$ nuclear-bar phase shifts for I=1 and I=0 as a function of the momentum and energy are given in the tables in [8], Appendix D for ESC16. Similarly, for the BKS-parameters $\Lambda\Xi^0, \Lambda\Xi(I = 1/2), \Sigma\Xi^0(I = 1/2)$, and $\Sigma^+\Xi^0(I = 3/2)$. the inelasticity parameters ρ and $\eta_{11}, \eta_{12}, \eta_{22}$, which contains the information to construct the $\delta-$, $\epsilon-$, N- and S-matrix. The $\Xi\Xi(^1S_0, I = 1)$ phase shift is in agreement with LQCD, see Ref. [122] Fig.2. For example at $p_{lab} = 200$ MeV/c, which means $T_{cm} = 3.8$ MeV, ESC16 has $\delta(^1S_0, I = 1) = 23.71$ deg, and ESC16$^{(\star)}(A)$ has $\delta(^1S_0, I = 1) = 21.45$ deg, which both match with the LQCD result.
Notice that the $\Xi\Xi(^3S_1, I = 0)$-phase shows repulsion, which qualitatively agrees with the LQCD result.

17. Neutron-stars, Hadronic Matter, QHT, BQM

17.1. ESC-model and 2.1$M_\odot$ Neutron-star's

1. Neutron stars (NS's) appear at the evolutionary endpoint of heavy stars as remnants of the collapsed core after the "supernova explosion". The result of the collapse is dominated by a degenerate neutron system, where equilibrium is achieved at a minimum of the total energy. Landau (1932) estimated that the maximum number of baryons for equilibrium is, see *e.g.* [123], $N_{max} \sim (\hbar c/G_N m_B^2)^{3/2} \sim 2 \times 10^{57}$ giving a mass $M_{max} \sim 1.5 M_\odot$. The discovery of many pulsars, after the first one in 1967, with a mass close to $1.44 M_\odot$, which are identified being neutron stars.
2. In studies of neutron stars, a key role is played by the equation of state (EoS) for dense nuclear matter. The calculation of the EoS, using the Bruckner-Hartree-Fock G-matrix approach, with only ESC meson-exchange interactions, gives $M_{NS} \approx 1.35 M_\odot$ [124]. With hyperon-mixing, *e.g.* Λ etc., in neutron-matter softens the EoS and the maximum mass is reduced considerably, which makes the discrepancy between the meson-exchange model and the NS observations even more severe. This problem, called "hyperon-puzzle", is addressed in this review.
3. Recently, massive neutron stars with masses over $2M_\odot$ have been reliably established by the observations of J1614−2230 [125], J0348+0432 [126], J0740+6620 [127] and J0952-0607 [128]. Also for these massive neutron stars over $2M_\odot$, the softening of the EoS by hyperon mixing in neutron-star matter is an even more real problem. The EoS softening is caused by the conversion of high-momentum neutrons at Fermi surfaces to low-momentum hyperons via strangeness non-conserving weak interactions, overcoming the mass difference between nucleons and hyperons utilizing the Fermi energy. Generally, such mechanisms can be due to the possible appearance of other hadronic degrees of freedom, such as Δ isobars [129], meson condensates [130, 131, 132, 133, 134] or quark phases [135, 136, 137, 138, 139, 140, 141, 142, 143, 144] and [10, 11]. Since such mechanisms of EoS softening are inevitable in neutron-star matter, it has been one of the central issues in this field to model EoSs, giving star masses over $2M_\odot$.
4. From the analyses of the X-ray data taken by the *Neutron Star Interior Composition Explorer* (NICER) and the X-ray Multi-Mirror (XMM-Newton) observatory, the radius information of NS's has been obtained for the massive NS PSR J0740+6620 with $2.1M_\odot$ and $1.4M_\odot$ NSs, whose radii are denoted as $R_{2.1M_\odot}$ and $R_{1.4M_\odot}$. The radius information of massive NS's gives important constraints for neutron-star EoSs, which are demonstrated critically by reproducing the neutron-star radii [11].
   A more precise measurement of the radius PSR J0740+6620 using updated NICER data yielded $R = 12.49^{+1.28}_{-0.88}$ km with the determined mass $M = 2.08 \pm 0.07 M_\odot$ [145]. Adopting their median values of $M = 2.1 M_\odot$ and $R_{2.1M_\odot} = 12.5$ km as data, they are compared with the calculated results. Then, these values are used as the criteria for EoSs, which is far more severe than the one using only the mass values as $2M_\odot$. In mass and radius (MR) relations of neutron stars , the criterion for MR curves is to reach the MR point of ($M = 2.1 M_\odot, R_{2.1M_\odot} =$ 12.5 km).
5. Several mechanisms have been proposed to reproduce masses over $2M_\odot$, solving the "hyperon-puzzle". Among them, the baryonic approach is to introduce repulsive three-body forces at the baryonic level [146, 147, 148, 149, 150], and [87, 88, 89]. In [87, 88, 89], the multi-pomeron exchange potential (MPP) was introduced as a model of universal repulsions among three and four baryons based on the extended soft core (ESC) baryon-baryon interaction model [5, 6, 7, 8]. With the MPP modeling of hyperonic three-body repulsions, the EoS softening by hyperon mixing is not satisfactorily recovered for heavy neutron stars ($M_{NS} \sim 2M_\odot$): The maximum masses do not significantly exceed $2M_\odot$, even if MPP repulsions are taken strongly enough. It seems difficult to reproduce both $M_{max} \sim 2.1 M_\odot$ and $R_{2.1M_\odot} \sim 12.5$ km by hadronic-matter EoSs with hyperon mixing.
6. The challenging subject is to study quark deconfinement phase transitions from a hadronic-matter EoS to a sufficiently stiff quark-matter EoS, giving $M_{max} \sim 2.1 M_\odot$ and $R_{2.1M_\odot} \sim 12.5$ km. It is known that quark-hadron phase transitions should be "crossover" or at most weak first-order to obtain EoSs stiff enough, because strong first-order transitions soften EoSs remarkably [135, 136, 137, 138, 139, 140, 141, 142, 143, 144], and [10]. Then, it seems essential that repulsive effects in quark phases are present to result in massive stars over $2M_\odot$. Without such repulsive effects, the quark mixing in neutron-star matter brings about a remarkable softening

of the EoS and a maximum mass is reduced to a value far less than $2M_\odot$, where the EoS softening caused by the conversion of high-momentum neutrons to low-momentum quarks. Our approach to this problem is given by the quark-hadron transition (QHT) model [10, 11], including the quark-quark (QQ) repulsions composed of meson-exchange and one-gluon-exchange potentials.

7. Another type of quark phase in neutron-star interiors is given by the so-called quarkyonic matter, see [151, 152, 153, 154, 155, 156, 157, 158], and [11], where the degrees of freedom inside the Fermi sea are treated as free quarks and nucleons exist at the surface of the Fermi sea. In the quarkyonic matter, the existence of free quarks inside the Fermi sphere gives nucleons extra kinetic energy by pushing them up to higher momenta, leading to increasing pressure. In the typical quarkyonic matter formalism [153], the thickness parameter Δ for the neutron Fermi layer plays a decisive role for neutron star MR curves, where no important conclusions can be drawn regarding the underlying quark-quark (QQ) and quark-baryon (QB) interactions. In Ref. [12], the nucleon-quark mixed (NQM) model composed of nucleons and u- and d-quarks in the Bruckner-Hartree-Fock (BHF) framework has been proposed, which is suitable to clarify the effects of QN and QQ interactions. This model can be easily extended to the baryon-quark mixed (BQM) model composed of nucleons, hyperons, u-, d- and s-quarks. In these models, quark densities in mixed matter are determined by equilibrium conditions between chemical potentials of baryons and free quarks without the use of *ad hoc* parameters such as the Fermi-layer thickness Δ.

17.2. EoS in the BHF framework

Here, the expressions for the baryon-quark mixed matter are given, in which those for baryonic matter and quark matter are included as limiting cases. The system of baryon-quark mixed matter is composed of baryons (n, p^+, Λ), free quarks (u, d, s) and electrons (e^-), where a baryon number density ρ_B is given by a sum of n-, p- and Λ-densities, $\rho_B = \rho_n + \rho_p + \rho_\Lambda$, and a quark number density ρ_Q by a sum of u-, d- and s-quark densities, $\rho_Q = \rho_u + \rho_d + \rho_s$. In the BHF framework, bare two-body BB, QQ, and QB potentials are renormalized into G-matrix interactions, namely, effective two-body interactions: G-matrix interactions $\mathcal{G}_{BB'}, \mathcal{G}_{QB}$, and $\mathcal{G}_{QQ'}$, with $B, B' = n, p, \Lambda$ and $Q, Q' = u, d, s$, are derived from the bare BB, QB and QQ interactions. They are given for each (T, S, P) state, with T, S, and P being isospin, spin, and parity in a two-body state, respectively.

Potential densities of B and Q are given by

$$U_{BB}(k) = \sum_{B'=n,p,\Lambda} U_B^{(B')}(k) = \sum_{B'=n,p,\Lambda} \sum_{k'<k_F^{(B')}} \langle kk'|\mathcal{G}_{BB'}|kk'\rangle \tag{17.1}$$

$$U_{BQ}(k) = \sum_{Q'=u,d,s} U_B^{(Q')}(k) = \sum_{Q'=u,d,s} \sum_{k'<k_F^{(Q')}} \langle kk'|\mathcal{G}_{BQ'}|kk'\rangle \tag{17.2}$$

$$U_{QQ}(k) = \sum_{Q'=u,d,s} U_Q^{(Q')}(k) = \sum_{Q'=u,d,s} \sum_{k'<k_F^{(Q')}} \langle kk'|\mathcal{G}_{QQ'}|kk'\rangle \tag{17.3}$$

$$U_{QB}(k) = \sum_{B'=n,p,\Lambda} U_Q^{(B')}(k) = \sum_{B'=n,p,\Lambda} \sum_{k'<k_F^{(B')}} \langle kk'|\mathcal{G}_{QB'}|kk'\rangle \tag{17.4}$$

where k_F^B and k_F^Q are Fermi momenta of baryon B and quark Q, respectively, and spin and isospin quantum numbers are implicit.

The quark energy density for $Q = u, d, s$ in baryon-quark mixed matter is given by

$$\varepsilon_Q = m_Q\rho_Q + g_s N_c \int_0^{k_F^Q} \frac{d^3k}{(2\pi)^3} \left\{ \sqrt{\hbar^2k^2 + m_Q^2} + \frac{1}{2}U_{QQ}(k) + \frac{1}{2}U_{QB}(k) \right\}, \tag{17.5}$$

where Fermion spin and quark-color degeneracy give factors $g_s = 2$ and $N_c = 3$.

The baryon energy density for $B = n, p, \Lambda$ is given by

$$\varepsilon_B = m_B\rho_B + \tau_B + v_B = m_B\rho_B + g_s \int_0^{k_F^B} \frac{d^3k}{(2\pi)^3} \left\{ \sqrt{\hbar^2k^2 + m_B^2} + \frac{1}{2}U_{BB}(k) + \frac{1}{2}U_{BQ}(k) \right\}. \tag{17.6}$$

The expression of ε_Q (ε_B) in quark (baryonic) matter is obtained by omitting U_{QB} (U_{BQ}).

In baryon-quark mixed matter, the total energy density is given by $\varepsilon = \varepsilon_n + \varepsilon_p + \varepsilon_\Lambda + \varepsilon_u + \varepsilon_d + \varepsilon_s + \varepsilon_e$. Chemical potential $\mu_i (i = n, p, \Lambda, u, d, s, e)$ and pressure P are expressed as

$$\mu_i = \frac{\partial \varepsilon_i}{\partial \rho_i} , \tag{17.7}$$

$$P = \sum_{i=n,p,\Lambda,u,d,s,e} \mu_i \rho_i - \varepsilon . \tag{17.8}$$

17.3. BB interactions and hadronic matter

The hadronic matter is defined as β-stable [12] baryonic matter. As a starting point for investigating the baryon-quark mixed matter, recapitulated is a typical hadronic matter EoS composed of n, p^+, Λ, e^- in the BHF framework with the use of ESC baryon-baryon (BB) interactions V_{BB} and three-body parts V_{BBB} [87, 88, 89]. V_{BBB} is composed of attractive and repulsive parts. The repulsive part contributes increasingly in high-density regions, being indispensable for stiff EoSs. The BB G-matrix interactions $\mathcal{G}_{BB}$ are derived from BB bare interactions V_{BB} or $V_{BB} + V_{BBB}$ [87]. They are given for each (BB', T, S, P) state, T, S, and P being the isospin, spin, and parity, respectively, and represented as $\mathcal{G}^{TSP}_{BB'}$. In β-stable hadronic matter composed of n, p^+, Λ, e^-, equilibrium conditions are given as

1. chemical equilibrium conditions,
$$\mu_n = \mu_p + \mu_e \ , \ \mu_n = \mu_\Lambda. \tag{17.9}$$
2. charge neutrality
$$\rho_p = \rho_e \tag{17.10}$$
3. baryon number conservation
$$\rho = \rho_n + \rho_p + \rho_\Lambda. \tag{17.11}$$

As is well known, the nuclear matter EoS is stiff enough to assure neutron-star masses over $2M_\odot$, if the strong three-nucleon repulsion is taken into account. However, there appears a remarkable softening of the EoS when exotic degrees of freedom, such as hyperon-mixingr, are included. As one of the ideas to avoid this "hyperon puzzle", it was proposed that the three-body repulsions worked universally for every kind of baryons [146]. In [87, 88, 89] the multi-pomeron exchange potential (MPP) was introduced as a (physical) model of universal repulsions among three and four baryons. The recent ESC works are mentioned in [5, 6, 7, 8].

In [89], they propose three versions of MPP (MPa, MPa$^+$, MPb), where MPa and MPa$^+$ (MPb) include the three and four body (only three-body) repulsions. The obtained MR curves for nucleonic-matter EoSs are given in [89] (Fig.3), where the curves move upwards with increasing MPP repulsions. The important criterion is the value of $R_{1.5M_\odot}$: There are given $R_{1.5M_\odot}$ = 12.5 km (MPb), 13.1 km (MPa), 13.4 km (MPa$^+$) in [89] (Table IV). Considering that the median values of the observed data of $R_{1.4M_\odot}$ are about 12.4 km, adopted is here the MPb version of MPP for three-body repulsions. It should be noted that the value of $R_{1.5M_\odot}$ for the nucleonic-matter EoS does not change much by mixings of hyperons or free quarks, as shown later, if their onset densities are larger than about $2\rho_0$. It is commented that the three-nucleon repulsion included in MPb is stronger than the corresponding one (UIX) in the standard model in [159], giving rise to $R_{1.5M_\odot} \approx 11.6$ km [160]. Values of M_{max} and $R_{2M_\odot}$ are obtained from the EoSs including MPb for hadronic matter with (without) Λ mixing, which are $M_{max}/M_\odot = 2.06$ (2.19) and $R_{2M_\odot}$ = 11.3 km (11.8 km) for the EoS with (without) Λ mixing. Thus, it is difficult to satisfy the criterion reproducing ($M = 2.1M_\odot, R_{2.1M_\odot}$ = 12.5 km) by hadronic-matter EoS, even if MPP repulsions are included.

Nucleonic matter given by ESC+MPb is denoted as NUCM, and baryonic matter given by ESC+MPb (ESC only) as BRYM (BRYM0), where nucleonic (baryonic) matter is composed of n, p^+, e^- (n, p^+, Λ, e^-).

[12] In β-stable matter the process $n \to p^+ + e^- + \bar{\nu}_e$ is blocked by the occupied electron states.

17.4. QQ interaction and QHT model

The bare QQ repulsive interaction is given by [161]

$$V_{QQ} = V_{EME} + V_{OGE} \tag{17.12}$$

where V_{EME} and V_{OGE} are the extended meson-exchange potential and the one-gluon-exchange potential, respectively. The parameters in the QQ potential are chosen to be consistent with physical observables.

The V_{EME} QQ potential is derived from the ESC *BB* potential so that the QQM couplings are related to the *BBM* couplings through folding procedures with Gaussian baryonic quark wave functions in the constituent quark model (CQM). Features of the V_{EME} NN potential persist in the V_{EME} QQ potential, which includes strongly repulsive components from vector-meson and pomeron exchanges between quarks, next to pseudoscalar, scalar, and axial-vector meson exchanges. No free parameter is included in V_{EME}.

Another repulsive component is given by V_{OGE} whose strength is determined by the quark-gluon coupling constant α_S, which is treated as a parameter to tune the QQ potential. The OGE-potential used is

$$V_{OGE}(r) = \frac{1}{4}(\boldsymbol{\lambda}_1 \cdot \boldsymbol{\lambda}_2)\alpha_S V_{vector}(m_{,}r) \tag{17.13}$$

where λ_a ($a = 1, 8$) are the Gell-Mann matrices in SU(3) color space, and $V_{vector}(m_G; r)$ is the OBE vector-exchange potential. The gluon mass is taken as $m_G = 420$ MeV [162].

In [161], the instanton potential V_{INS} and the multiple-pomeron exchange potentials among quarks V_{MPP} are included in V_{QQ} adding to V_{EME} and V_{OGE}. Here, they are omitted for simplicity, because attractive and repulsive contributions of V_{INS} and V_{MPP}, respectively, are rather canceled from each other, and the results for $V_{QQ} = V_{EME} + V_{OGE} + V_{INS} + V_{MPP}$ can be simulated well by those for $V_{QQ} = V_{EME} + V_{OGE}$ by adjusting the parameter α_S.

In the QHT model, quark-hadron phase transitions occur at the crossing points of the hadron pressure $P_H(\mu)$ and quark pressure $P_Q(\mu)$, being the onset densities of quark phases into the hadronic phases. To control onset densities, density-dependent quark masses are introduced, which are specified by the parameters ρ_c, γ and B_0 as follows

$$M_Q^*(\rho_Q) = \frac{M_0}{1 + \exp[\gamma(\rho_Q - \rho_c)]} + m_0 + C \tag{17.14}$$

with $C = M_0 - M_0/[1 + \exp(-\gamma\rho_c)]$ assuring $M_Q^*(0) = M_0 + m_0$, where ρ_Q is the number density of quark matter, and M_0 and m_0 are taken as 300 (360) MeV and 5 (140) MeV for u and $d(s)$ quarks. The effective quark mass $M_Q^*(\rho_Q)$ should be used together with $B(\rho_Q) = M_Q^*(0) - M_Q^*(\rho_Q) + B_0$, meaning the energy density difference between the perturbative vacuum and the true vacuum.

Then, the four parameters (α_S, ρ_c, γ and B_0) determine EoSs and neutron-star *MR* curves. The parameters are chosen such that the maximum masses M_{max} are as large as possible under onset densities of $2\rho_0$: The chosen parameters are $\alpha_S = 0.69, \rho_c = 7.5\rho_0, \gamma = 1.2$ and $B_0 = 10.0$. In the following section, the results for this parameter set are shown in order to demonstrate that it is possible to satisfy the criterion ($M = 2.1M_\odot, R_{2.1M_\odot} = 12.5$ km) in the QHT model.

In the EoS of β-stable quark matter composed of u,d,s,e$^-$, the equilibrium conditions are given as

1. chemical equilibrium conditions,
$$\mu_d = \mu_s = \mu_u + \mu_e, \tag{17.15}$$
2. charge neutrality
$$0 = \frac{1}{3}(2\rho_u - \rho_d - \rho_s) - \rho_e, \tag{17.16}$$
3. baryon number conservation
$$\rho_B = \frac{1}{3}(\rho_u + \rho_d + \rho_s) = \frac{1}{3}\rho_Q. \tag{17.17}$$

In order to construct the hybrid EoS including a transition from the hadronic phase to the quark phase, use is made of the replacement interpolation method [142, 11], being a simple modification of the Maxwell and Glendenning (Gibbs) construction [163]. The EoS of hadronic and quark phases and that of the mixed phase are described with the relations between the pressures and chemical potentials $P_H(\mu), P_Q(\mu)$ and $P_M(\mu)$, respectively. The critical chemical potential μ_c for the transition from the hadronic to the quark phase is obtained from the Maxwell condition

$$P_Q(\mu_c) = P_H(\mu_c) = P_c. \tag{17.18}$$

The pressure of the mixed phase is represented by a polynomial ansatz. Matching densities ρ_H and ρ_Q are obtained with use of $\rho(\mu) = dP(\mu)/d\mu$. There is no room for hyperon-mixing in the QHT model when the transition densities to quark phases are lower than the onset densities of hyperons in the hadronic phases.

17.5. QB interaction and the BQM model

In BHF calculations of baryon-quark mixed (BQM) matter, quark-quark (QQ) and quark-baryon (QB) two-body interactions are needed as well as *BB* interactions. In the present BQM calculations, for simplicity, QQ interactions are omitted because quark densities are lower than baryon densities, and their contributions to EoSs are small.

In [161] QN potentials $V_{EME}^{(QN)}$ are derived together with QQ potentials $V_{EME}^{(QQ)}$, in which meson-quark-quark and meson-nucleon-nucleon couplings are determined consistently in the framework of the CQM. These meson-exchange QN potentials are weakly repulsive and not useful to stiffen the EoSs. On the other hand, the $V_{DQE}^{QN)}$ potential is derived from a phenomenological description of the confinement-deconfinement mechanism via a nucleon-triquark coupling. Here, for the triquark [164] a quark-diquark presentation is exploited. The diquark-exchange (DQE) potential $V_{DQE}^{(QN)}$ derived in [165, 166, 167] is repulsive, its strength is given by the baryon-triquark coupling λ_3. Then, $V_{EME}^{(QN)}$ is omitted in the present BQM calculations, because results for $V^{(QN)} = V_{EME}^{(QN)} + V_{DQE}^{(QN)}$ with some value of λ_3 can be simulated well by those for $V^{(QN)} = V_{DQE}^{(QN)}$ with a slightly larger value of λ_3.

The $V_{DQE}^{(QN)}$ potential with $N = n, p$ and $Q = u, d$ is derived from a phenomenological description of a confinement-deconfinement mechanism via a nucleon-triquark coupling, using for the triquark [164] a quark-diquark presentation. This leads to an effective NJL-type quark-nucleon interaction,

$$\mathcal{L}_{int}^{(2)} = \lambda_3^2(\bar{\psi}\gamma_5\gamma_\mu\boldsymbol{\tau}Q) \cdot \bar{Q}\gamma_5\gamma^\mu\boldsymbol{\tau}\psi)/\mathcal{M}^2, \tag{17.19}$$

where the ratio $\lambda_3/\mathcal{M}$ is a free (density dependent) parameter. In (17.19) the isospinor is denoted by Q=(u,d). The diquark-exchange central potential is

$$\begin{aligned} V_{DQE}^{(QN)}(r) &= -\lambda_3^2 \frac{\Lambda}{4\pi\sqrt{\pi}} \frac{\Lambda^2}{\mathcal{M}^2} (\boldsymbol{\tau}_1 \cdot \boldsymbol{\tau}_2)(\boldsymbol{\sigma}_1 \cdot \boldsymbol{\sigma}_2)\, \mathcal{P}_x \cdot \\ &\quad \times \left[1 - \frac{\Lambda^2}{m_N m_Q}\left(1 - \frac{3(m_N - m_Q)^2}{16 m_N m_Q}\right)\left(1 - \frac{\Lambda^2 r^2}{6}\right)\right] \exp\left[-\frac{\Lambda^2 r^2}{4}\right], \end{aligned} \tag{17.20}$$

where the nucleon-triquark coupling λ_3 is dimensionless, and $\mathcal{P}_x$ is the space-exchange operator. The cut-off Λ and the scale mass $\mathcal{M}$ are adjustable parameters. Choosing $\mathcal{M} = M_N$ in vacuum QCD-sum-rules [168] predict $\lambda_3 \approx \sqrt{e/2}(2\pi)^{-2}[M_N/(\hbar c)]^3$ giving $\lambda_3/\sqrt{4\pi} \approx 0.96$. *The remarkable feature of the DQE qN-potential (17.20) is that it gives repulsion in all partial waves.* The sign in Eq. (17.20) comes from the diquark propagator, which differs a (-)-sign from the $\bar{Q}Q$-exchange propagator. In Appendix L is given a more complete derivation of the $V_{DQE}^{(QN)}$ potential. In the present framework, λ_3 is treated as a parameter to adjust resulting EoSs.

The flavor SU(3) generalized quark-baryon diquark exchange potential is denoted as $V_{DQE}^{(QB)}$ with $B = n, p, \Lambda$ and $Q = u, d, s$. In [169] the following relations are derived: $V_{DQE}^{(u\Lambda)} = V_{DQE}^{(un)}/2$, $V_{DQE}^{(d\Lambda)} = V_{DQE}^{(dp)}/2$, $V_{DQE}^{(s\Lambda)} = V_{DQE}^{(un)}$, and $V_{DQE}^{(sN)} = 0.0$ with $N = n, p$.

In BQ-mixed matter composed of n, p, Λ, u, d, s and e, their partial densities are denoted as $\rho_n, \rho_p, \rho_\Lambda, \rho_u, \rho_d, \rho_s$ and ρ_e, respectively. Their mixing ratios are defined as $y_p = \rho_p/\rho_n$, y_Λ/ρ_n, $y_u = \rho_u/\rho_n$, $y_d = \rho_d/\rho_n$, $y_s = \rho_s/\rho_n$, $y_e = \rho_e/\rho_n$, respectively. The equilibrium conditions are given as

1. chemical equilibrium conditions,

$$\mu_n = \mu_p + \mu_e \ , \ \mu_n = \mu_\Lambda \ ,$$
$$\mu_n = \mu_u + 2\mu_d \ , \ \mu_p = 2\mu_u + \mu_d \ , \ \mu_\Lambda = \mu_u + \mu_d + \mu_s \ , \tag{17.21}$$

2. charge neutrality

$$0 = \rho_p + \frac{1}{3}(2\rho_u - \rho_d - \rho_s) - \rho_e \ , \tag{17.22}$$

3. baryon number conservation

$$\rho = \rho_n + \rho_p + \rho_\Lambda + \frac{1}{3}\rho_Q, \tag{17.23}$$

where ρ is total density and $\rho_Q = \rho_u + \rho_d + \rho_s$. The mixing ratios have to be determined from the equilibrium conditions, which are applied in an approximate way as follows. As a first simplification, y_p and y_Λ are determined by the equilibrium conditions $\mu_n = \mu_p + \mu_e$ and $\mu_n = \mu_\Lambda$ in hadronic matter, which is brought into BQ-mixed matter. Then, μ_n, μ_u, μ_d and μ_s are given as functions of $y_d = \rho_d/\rho_n$ and $y_u = \rho_u/\rho_n$. In Eq. (17.21) μ_n becomes the expression $\mu_n(\rho_n, y_u, y_d, y_s) = \mu_u(y_n) + 2\mu_d(y_d)$. This equation has to be solved together with the equations $\mu_p = 2\mu_u + \mu_d$ and $\mu_\Lambda = \mu_u + \mu_d + \mu_s$. As the second simplification, the ratios y_d, y_u, and y_s in the quark parts are assumed to be related to y_p and y_Λ in the baryonic parts by $2y_d + y_u = 1, y_d + 2y_u = y_p$ and $y_u + y_d + y_s = y_\Lambda$. Then, $\mu_n(\rho_n, y_u, y_d, y_s)$ in Eq. (17.21) is given as by a function of variables ρ_n and y_d. Using solved y_d values, y_u and y_s are determined by the above relations. Thus, mixing ratios of quark components are obtained by solving Eq. (17.21), which leads to energy densities and pressures as a function of ρ. Forms of $y_q(\rho)$ with q=u,d,s, especially onset densities of quark components, play decisive roles for EoSs and neutron-star *MR* curves.

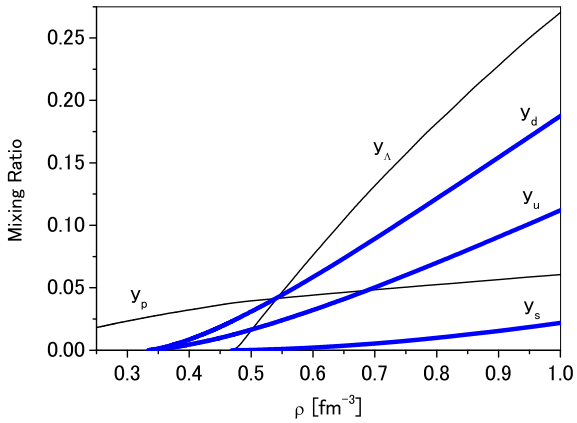

Figure 31: Mixing ratios in the BQM-b case are drawn as a function of total density ρ, onset densities of Bq states being $2.0\rho_0$ ($\kappa = 1.12$). Thin solid curves are for y_p and y_Λ. Thick solid ones are for y_d, y_u and y_s.

In the following section, two types of matter are investigated: (i) NQ-mixed matter composed of n, p, u, d and e, and (ii) BQ-mixed matter composed of n, p, Λ, u, d, s and e. Baryonic parts of NQM and BQM are given by NUCM and BRYM, respectively. BQM is denoted as BQM0 when its baryonic part is given by BRYM0. Namely, MPP repulsions are included (omitted) in the ΛN parts of BQM (BQM0). A value of λ_3 is chosen to reproduce a given value of the onset density of BQ-mixed states into baryonic states:

λa case : $\lambda_3/\sqrt{4\pi} = 0.46$ giving onset density $2.0\rho_0$; λb case : $\lambda_3/\sqrt{4\pi} = 0.41$ giving onset density $1.7\rho_0$

These cases are denoted as NQM-λa and NQM-λb (BQM-λa and BQM-λb) in the NQM (BQM) case. On the other hand, the choice of $\lambda_3/\sqrt{4\pi} = 0.96$ gives rise to the onset density $4.6\rho_0$. When the onset density is of such a large value, BQ-mixed states are not related to *MR* curves before reaching maximum masses.

In Fig. 31, mixing ratios in the BQM-λa case are drawn as a function of total density ρ, where y_p and y_Λ are given by thin solid curves, and y_u, y_d, y_s by thick solid curves. It should be noted that the intersections with the ρ axis show the onset densities, being 0.34 fm^{-1} ($2.0\rho_0$) for y_u and y_d, and 0.50 fm^{-1} for y_Λ and y_s.

18. NS-matter Results

In Fig. 32, pressures P for models NQM, QHT, and NUCM EoSs are drawn as a function of ρ with $\rho = \rho_n + \rho_p + \rho_Q/3$ ($\rho_Q = 0$ in QHT and NUCM models). The three solid curves are for NQM-λa and NQM-λb, marked in the figure by λa and λb, respectively. The dashed and the dot-dashed curves are for QHT and NUCM EoSs, respectively.

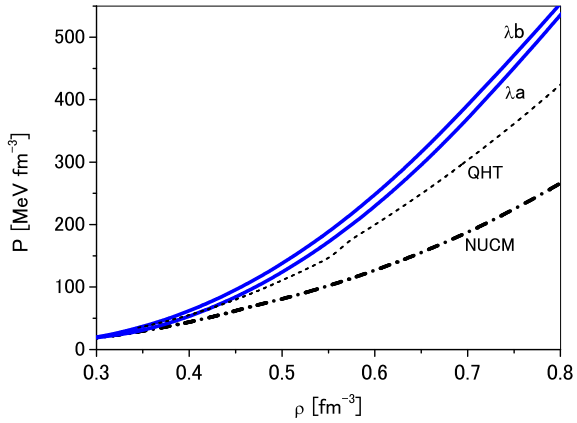

Figure 32: Pressures P for NQM, QHT, and NUCM EoSs are plotted as a function of $\rho = \rho_n + \rho_p + \rho_Q/3$. Solid curves marked by λa and λb are for NQM-λa and NQM-λb, respectively. The dashed and dot-dashed curves are for QHT and NUCM EoSs, respectively.

In Fig. 33 pressures P for NQM, QHT, and NUCM EoSs are drawn as a function of the energy density ε, that is $P(\varepsilon)$. The dot-dashed curve shows pressures in NUCM matter. The three solid curves show the cases of NQM-λa and NQM-λb, marked in the figure by λa and λb, respectively. The dashed curve is for QHT matter. The branching points of these four curves from the dot-dashed curve are related to the quark onset densities. Derivatives of $P(\varepsilon)$ are related to the sound velocities given by $c_s^2 = \partial P/\partial\varepsilon$. Derivatives of NQM and QHT curves (sound velocities) are larger than that of the nucleonic (NUCM) matter curve, which means that the former EoSs are stiffer than the latter one owing to the mixing of and the transition to quark states, respectively.

In Fig. 34, pressures $P(\varepsilon)$ for BQM, BRYM, BQM0, and BRYM0 EoSs are drawn as a function of energy density ε, where the thick (thin) curves are obtained in the case of including (omitting) the MPP repulsions in the ΛN parts. The dot-dashed curves are pressures in baryonic (BRYM and BRYM0) matter. The larger derivative (stiffness) of the thick (BRYM) curve than that of the thin (BRM0) one is caused by the MPP repulsion (recovery of the EoS softening by hyperon mixing). The thick (thin) solid curves are obtained for BQM-λa and BQM-λb (BQM0-λa and BQM0-λb) with (without) MPP repulsions in the ΛN parts, marked in the figure by λa and λb, respectively. The branching points of these six curves from the dot-dashed curves are related to the quark onset densities. The larger derivatives (stiffness) of the solid curves than those of the dot-dashed ones are caused by the diquark exchange repulsions between neutrons and quarks.

18.1. MR graphs

The EoSs for several neutron-star models are connected to the crust EoS [170, 171] at $\rho \sim 0.2$ fm^{-3} with smooth interpolations. Star masses M as a function of the radius R, that is $M(R)$, are obtained by solving the TOV equations with these EoSs. In the following figures for MR curves, the regions given by $M = 2.08 \pm 0.07 M_\odot$ and $R = 12.49^{+1.28}_{-0.88}$ km [145] are drawn by dotted rectangles, and the MR point of ($M = 2.1 M_\odot, R_{2.1M_\odot} = 12.5$ km) is indicated by a cross

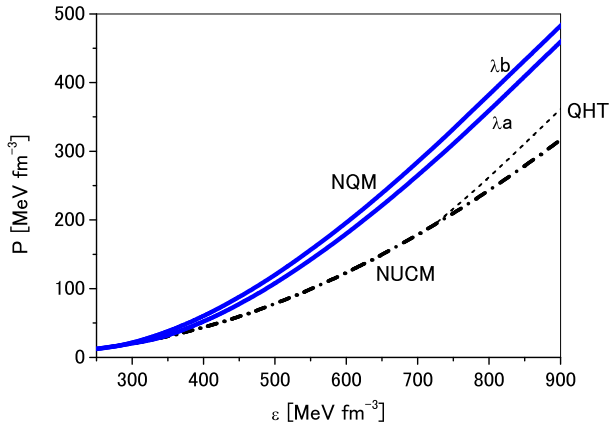

Figure 33: Pressures P for NQM, QHT, and NUCM EoSs are plotted as a function of the energy density ε. Solid curves marked by λa and λb are for NQM-λa and NQM-λb, respectively. The dot-dashed and dashed curves are for NUCM and QHT EoSs, respectively.

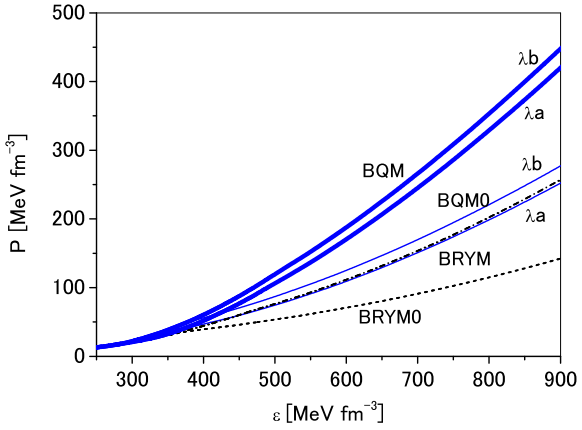

Figure 34: Pressures P for BQM, BRYM, BQM0 and BRYM0 EoSs as a function of energy density ε. Thick (thin) curves are obtained for BQM (BQM0) including (omitting) MPP repulsions in the ΛN parts. Thick (thin) dot-dashed curves are the pressure for BRYM (BRYM0) EoS. Thick (thin) solid curves are for BQM-λa and BQM-λb (BQM0-λa and BQM0-λb) with (without) MPP repulsions in the ΛN parts, marked by λa and λb, respectively.

symbol. In the analysis of MR curves, our critical guideline is that the obtained MR-curve reaches above this cross symbol. In Fig. 35 star masses are given as a function of radius R for NQM, QHT, and NUCM EoSs, corresponding

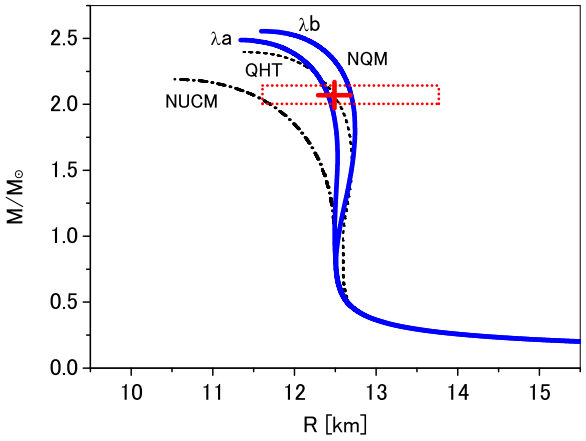

Figure 35: Star masses as a function of radius R for NQM, QHT, and NUCM EoSs. The dot-dashed curve marked by NUCM presents the nucleonic matter EoS. The solid curves marked by λa and λb present the NQM-λa and NQM-λb EoS, respectively. The dashed curve presents the QHT EoS,

to the $P(\varepsilon)$ curves in Fig. 33. The dot-dashed curve marked by NUCM presents the nucleonic matter EoS. The solid curves marked by λa and λb present the NQM-λa and NQM-λb EoSs, respectively. The dashed curve presents the QHT EoS. It should be noted that the solid curves for NQM EoSs are pushed up from the dot-dash curve EoS for NUCM by the increasing the diquark exchange repulsions between neutrons and quarks, while the dashed curve for the QHT EoS is obtained by the repulsive quark-quark interactions. In Fig. 36 star masses are given as a function

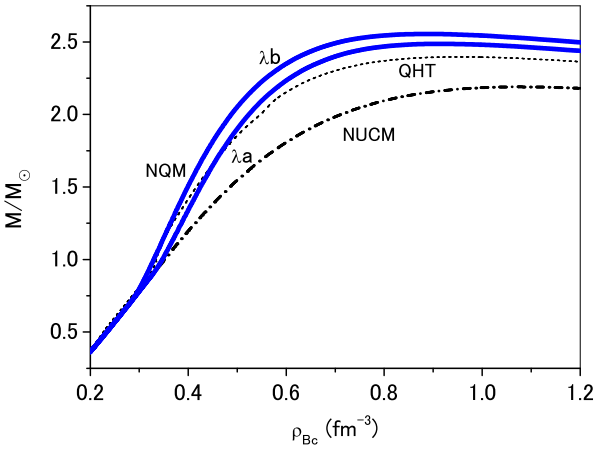

Figure 36: Star masses as a function of central baryon density ρ_{Bc}. The dot-dashed curve marked by NUCM presents the nucleonic matter EoS. The solid curves marked by λa and λb present the NQM-λa and NQM-λb EoS, respectively. The dashed curve presents the QHT EoS.

of central baryon density ρ_{Bc}, that is $M(\rho_{Bc})$. The dot-dashed curve marked by NUCM presents the nucleonic matter EoS. The solid curves marked by λa λb present the NQM-λa and NQM-λb EoSs, respectively. The dashed curve presents the QHT EoS. The behaviors of $M(\rho_{Bc})$ curves respond well to the corresponding $P(\rho)$ curves in Fig. 32. The

$P(\rho)$ curves, as well as the $M(\rho_{Bc})$ curves, are noted to be above the dot-dashed curves for the nucleonic EoS.

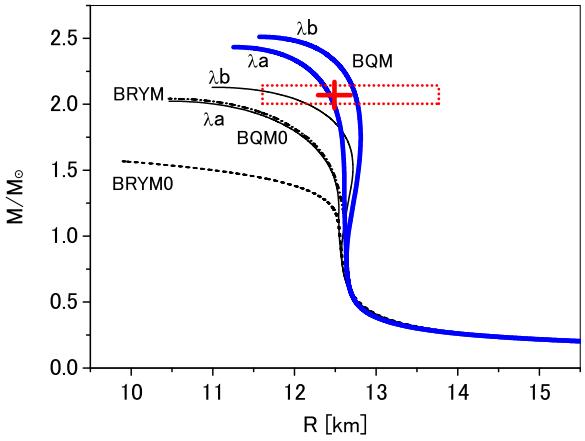

Figure 37: Star masses as a function of the radius R for BQM and BQM0 EoSs. The thick (thin) dot-dashed curve marked by BRYM (BRYM0) presents the baryonic matter EoS including (omitting) MPP repulsions in the ΛN parts. Thick (thin) solid curves marked by λa and λb present the BQM-λa and BQM-λb EoS, respectively,

In Fig. 37 star masses are given as a function of radius R for the BQM and BQM0 EoSs, corresponding to the $P(\varepsilon)$ curves in Fig. 34. The thick (thin) curve is obtained for the BQM (BQM0) EoS including (omitting) MPP repulsions in the ΛN parts. The thick (thin) dot-dashed curve is obtained for the BRYM (BRYM0) EoS. Thick (thin) solid curves marked by λa and λb present BQM-λa and BQM-λb (BQM0-λa and BQM0-λb) EoSs, respectively. In both cases of BQM and BQM0, the solid curves for BQM and BQM0 EoSs are pushed up from the dot-dashed curves for BRYM and BRYM0 EoSs, respectively, by the diquark exchange repulsions between neutrons and quarks. The solid curves for NQM EoSs in Fig. 35 are similar to those for BQM EoSs in Fig. 37, because the MR curve for BRYM EoS is similar to that for NUCM EoS, owing to the MPP repulsions in the ΛN parts, recovering the EoS softening by Λ mixing.

Table 35: Values of maximum masses $M_{max}/M_\odot$ and radii $R_{2.1M_\odot}$ (km) at $2.1M_\odot$ obtained for NQM, BQM, BQM0 and QHT EoSs with onset densities $2.0\rho_0$ (λa) and $1.7\rho_0$ (λb). Maximum masses are shown for NUCM, BRYM, and BRYM0.

	$M_{max}/M_\odot$	$R_{2.1M_\odot}$ (km)
NQM-λa	2.49	12.4
NQM-λb	2.53	12.6
BQM-λa	2.43	12.4
BQM-λb	2.48	12.6
BQM0-λa	2.02	
BQM0-λb	2.09	
NUCM	2.19	11.4
BRYM	2.04	
BRYM0	1.57	
QHT	2.40	12.4
Observations	> 2.1	~ 12.5

Table 35 summarizes the values of the maximum masses $M_{max}/M_\odot$ and radii $R_{2.1M_\odot}$ (km) found in Fig. 35 and Fig. 37, where the values of $R_{2.1M_\odot}$ turn out to be consistent with the observed data $R = 12.49^{+1.28}_{-0.88}$ km [145] in the

cases of NQM and BQM EoSs with onset densities of BQ-mixed states (λa) $2.0\rho_0$, (λb) $1.7\rho_0$. Also, values for the QHT EoSs are consistent with the data. The small value of $M_{max} = 1.57M_\odot$ for BRYM0 is due to the EoS softening by hyperon-mixing: "hyperon puzzle". The value of $M_{max} = 2.04M_\odot$ for BRYM means that the EoS softening is substantially recovered by including the MPP repulsion in ΛN parts, but this M_{max} is still small compared to $2.1M_\odot$. The value of $M_{max} = 2.02\ (2.09)M_\odot$ for BQM0-λa (λb) means that the EoS softening can be recovered by the strong qN diquark exchange repulsions, even if the MPP repulsions are not included in ΛN parts.

18.2. NS-matter Concluding Remarks

The recent NICER radius observation of the massive neutron stars gives important criteria for neutron-star EoSs: The recent observations indicate that neutron-star MR curves have to reach the MR point of ($M = 2.1M_\odot, R_{2.1M_\odot} =$ 12.5 km). It is difficult for a hadronic-matter EoS to meet this criterion. A promising idea for achieving this criterion, it is necessary to focus on possible repulsive effects of quark phases. Our approach to this problem is to derive neutron-star EoSs based on the quark-hadron transition (QHT) model [10, 11] and the baryon-quark mixed (BQM) model [12] in the BHF framework. In the QHT model, roles to stiffen EoSs are played by QQ repulsions composed of meson-exchange and one-gluon-exchange potentials stiffen EoSs. In the BQM model, (i) the quark densities are determined by equilibrium conditions between the chemical potentials of baryons and free quarks, and (ii) QB repulsions play important roles in stiffening the EoSs.

Features of neutron-star EoSs are demonstrated by pressures as a function of energy density $P(\varepsilon)$ and neutron-star MR curves. The stiffness of QHT EoS is controlled by the strengths of QQ repulsions and density-dependent quark masses, which result in reasonable MR curves. The stiffness of BQM EoSs and onset densities of BQ-mixed states are controlled by the strengths of QB diquark exchange repulsions through chemical equilibrium conditions between baryons and free quarks. By adjusting QB repulsions to give onset densities of about $2\rho_0$, MR curves for BQM matter EoSs are pushed up above the MR point of ($M = 2.1M_\odot, R_{2.1M_\odot} = 12.5$ km). In QHT EoSs, similar characteristic behaviors appear when QQ repulsions are changed.

The criterion to reach the MR point indicated by the updated NICER data gives a far more severe criterion for neutron-star EoSs than that for only the mass value, such as $2M_\odot$. It is difficult for hadronic matter EoSs to meet this criterion for MR curves. In our modeling of baryon-quark mixed matter, the resulting MR curves are easily pushed up above the MR point owing to the QB diquark exchange repulsion [165, 166, 167].

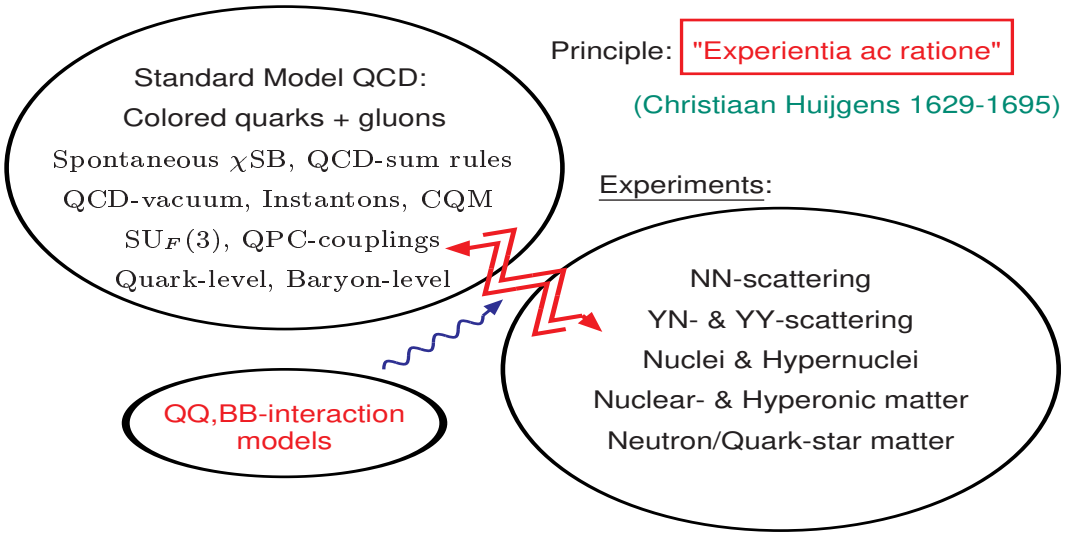

Figure 38: Mediator role ESC-model: Concepts and Experimental data

19. General background of the ESC-model

The general physics background, within the context of QCD, for the Nijmegen soft-core models has been briefly outlined in Ref. [5]. The mediator role of the ESC-model between theoretical concepts and experimental observables is illustrated in Fig. 38. The effective description of the baryon interactions at low and intermediate energies, in terms of baryons and mesons, can be understood from the standard-model (SM) by noting the following:

(i) SM-model: The strongly interacting sector of the SM-model contains three families of colored quarks: (ud), (cs), (tb). Integrating out the heavy quarks (c,b,t) leads to a QCD-world with effective interactions for the (u,d,s) quarks.

(ii) For low momenta, this QCD-world is assumed to be characterized by a phase transition due to a spontaneous Nambu-Goldstone chiral-symmetry breaking (SCSB) of the vacuum. Thereby, the quarks get dressed and become the so-called constituent quarks. The emerging picture is that of the constituent-quark-model (CQM) [172], with hadrons and confined quarks in vacuum.. At low momenta and for distances beyond 0.1 fm, a phase transition transforms the QCD-world into a complex hadronic-world where the quarks become constituent quarks and hadrons with interactions mediated by meson exchange.

(iii) Lattice approach: An alternative framework is the strong coupling lattice QCD (SCQCD) to study qualitatively the low energy meson-baryon and baryon-baryon physics, see Ref. [173] for applications and references. Here, the lattice spacing $a \geq 0.11\ fm$ provides a momentum scale for which the QCD coupling $g \geq 1.1$. Emerging is a picture where the meson-baryon coupling constants get large, and quark-exchange effects small. The latter is due to the suppression caused by the gluonic overlaps involved. For a similar reason, it has been argued [174] that the pomeron is exchanged between the individual quarks of the baryons. In this picture, the Nijmegen soft-core approach to baryon-baryon interactions is natural.

(iv) Out-integration: For an economic description of the ground state baryon SU(3)-octet states and their interactions, employing the generating-functional path-integral formalism, see *e.g.* [28, 175], the out-integration of the heavy meson and baryon degrees of freedom can be performed with the renormalization procedure a la Wilson [176].

(v) For the mesons, the restriction to mesons with $M \leq 1.5\ \mathrm{GeV}/c^2$, one arrives at a so-called *effective field theory* as the arena for our description of the low- and intermediate-energy baryon-baryon scattering. In this picture, the Nijmegen soft-core approach to baryon-baryon interactions is motivated naturally.

(vi) Instantons: In [177, 178, 179], the complex structure of the QCD vacuum is understood as a liquid of instantons and anti-instantons [180], and the valence quarks acquire a dynamical or constituent mass [181, 178, 179]. With the empirical value of the gluon condensate [182] as input, the instanton density and radius become [183] $n_c = 8 \cdot 10^{-4}\ \mathrm{GeV}^{-4}$, and $\rho_c = (600\ \mathrm{MeV})^{-1} \approx 0.3$ fm respectively. Also, with these parameters the non-perturbative vacuum expectation value for the quark fields are $\langle vac|\bar{\psi}\psi|vac\rangle \approx -10^{-2}\ \mathrm{GeV}^3$ and the quark effective (u,d) masses ≈ 200 MeV, i.e. much larger than the almost massless "current masses". In the calculation of light quarks in the instanton vacuum [179] the effective quark mass $m_Q(p = 0) = 345$ MeV was calculated, which is remarkably close to the constituent mass $M_N/3$.

(vii) Spectra: The spectra of the nucleons, Δ resonances, and the hyperons Λ, Σ, Ξ are described in detail by the Glozman-Riska model [184]. This is a modern version of the constituent quark model (CQM) [185], which is based on the Nambu-Goldstone spontaneous chiral-symmetry breaking (SCSB) with quarks interacting by the exchange of the $SU(3)_F$ octet of pseudoscalar mesons. The pseudoscalar octet members are the Nambu-Goldstone bosons (NGBs) associated with the hidden (approximate) chiral symmetry of QCD. The confining potential is chosen to be harmonic, as is rather common in constituent quark models. In line with this, harmonic wave functions were used in the derivation of the connection between the meson-baryon and meson-quark couplings [9]. Also, in [186], a good description of the baryon octet masses has been given with harmonic confinement, constituent quark masses, and meson-exchange.

(viii) Mesons: Very notable is the role of the instantons for the light meson spectrum. They give a non-perturbative effective gluonic interaction between quarks in QCD. For example, the instanton-induced interaction, as proposed by 't Hooft [187], generates at low momenta the constituent quark mass [179], i.e. breaks chiral symmetry. This interaction supplies a strong attractive attraction in the pseudoscalar-isovector quark-antiquark system - pions -, which makes them anomalously light, with zero mass in the chiral limit. This is the mechanism by which

the pions, being quark-antiquark bound states, appear as NGBs of the SCSB symmetry. This strongly attractive interaction is absent in vector mesons [188, 189], making the masses of the vector mesons $\approx 2m_Q$ in accordance with $m_\rho \approx m_\omega \approx 2m_Q$. Since $\alpha_s \approx 0.3$ the one-gluon-exchange (OGE) is weak, and therefore the $\pi - \rho$ mass splitting is not due to the perturbative color-magnetic spin-spin interaction between the quark and antiquark.

The 't Hooft [187] four-fermion instanton mediated interaction for the light flavor doublet $\psi = (u, d)$, in the form of a generalized Nambu-Jona-Lasinio Lagrangian [190], is

$$\mathcal{L}_I = g_I \left[(\bar{\psi}\psi)^2 - (\bar{\psi}\gamma_5 \boldsymbol{\tau}\psi)^2 - (\bar{\psi}\boldsymbol{\tau}\psi)^2 + (\bar{\psi}\gamma_5\psi)^2 \right]. \tag{19.1}$$

Here, the strength of the interaction g_I and the ultraviolet cut-off scale $1/r_0$ are related in the instanton liquid model [191]. In [192] it is shown that the t-channel iteration of the instanton interaction (19.1) leads to isoscalar and isovector pseudoscalar and scalar exchange quark-quark potentials. Since these potentials are already included in the ESC-model, the four-fermion instanton interaction does not lead to extra potentials.
The dynamical basis for the "kinematic broken" SU(3) symmetry is the (approximate) permutation symmetry w.r.t. the constituent (u,d,s)-quarks. This has its roots in the approximate equality of the quark masses, and more importantly, that the gluons have no flavor.

(ix) SU(3)-symmetry: The dynamical basis for the "kinematic broken" SU(3)-symmetry is the (approximate) permutation symmetry w.r.t. the constituent masses of the (u,d,s)-quarks. This has its roots in the approximate equality of the "current-quark" masses, and more importantly the gluons carry no flavor.

(x) BQ and QQ: The connection between the baryon and quark level the CQM [185] with $m_Q \approx M_N/3$ [9] is important. This opened the possibility to relate the ESC BB-potentials to the BQ- and QQ-potentials with no extra parameters. The latter potentials have been applied in the study of heavy neutron stars, where quark matter plays an important role, see Refs. [10, 11, 12], and this review sections 17 and 18.

20. Summary, Baryon-Baryon models, and Prospects

The ESC approach to baryon-baryon (BB) is a meson-exchange interaction model with (Gaussian) form factors. Here, besides pseudoscalar, also vector, scalar, and axial-vector mesons are included, which is important for an accurate description of the phase shifts at the higher energies. Also, in this approach, flavor SU(3) (broken) symmetry has been incorporated succesfully to connect the different BB-channels.

Novel in this review is the presentation of the ESC-model in the framework of the Kadyshevsky formalism. The advantages of the Kadyshevsky formalism is that it is (i) a relativistic field theory, (ii) at the same time in its appearance close to the so called old perturbation theory (OPT), and (iii) the particles in the intermediate states are on-mass-shell, which is ideal for the implementation of form factors, in particularly Gaussian ones. Furthermore, in momentum space one can do the calculations taking the full relativistic momentum dependence of the nucleons and mesons into account, similar to the method of Ref. [193] for the Lippmann-Schwinger equation. In the ESC-model an expansion is made in $1/M$ after which the transformation to configuration space is performed. Then, the potentials used in the ESC-models are retrieved, in particular for the TME and MPE ones [29, 30].

20.1. Present state of the ESC-model

Compared to ESC04 [2, 3], the model has been developed further. The new version ESC16 has, in addition to meson-exchange, also incorporated quark-core effects. Furthermore, the multi-gluon sector has been completed by the inclusion of the odderon. Moreover, the treatment of the axial-vector mesons is now in a very satisfactory shape by employing the B-field formalism. The ESC-model approach to the nuclear force opened the possibility of making a connection between the present available baryon-baryon experimental data on the one hand, and with the underlying quark structure of the baryons and mesons, on the other hand. Namely, a successful description of both the *NN*- and *YN*-scattering data is obtained with meson-baryon coupling parameters that all comply with the QPC-model. Note here that, in particular, the QPC-model treats the vector and scalar mesons on an equal footing. Apart from its role in $\pi\pi$ and πK scattering, the $f_0(620)$ has been shown to be present in relativistic nuclear scattering as well [194]. Note that by studying the relation between the QPC-processes and the BBM-couplings, the the ratio $\gamma(^3P_0)/\gamma(^3S_1) = 2:1$ is determined. In the literature, the $^3P_0$-QPC and the $^3S_1$-QPC in the SCQCD [173] has been studied in [195] and [196] respectively. For the ESC04 and ESC16 models, an estimate is given of the relative importance of the QPC processes. Also, the $F/(F+D)$-ratios of the OBE and MPE coupling constants are given by the QPC-model.

20.2. Combined fit NN and YN data

In fitting the NN-data, the Nijmegen PWA(1993) is used. Although phase shift analyses, with a more extended data base comprising more recent data, e.g. [197] are available in principle, apart from fine-tuning, no major changes are to be expected. For example, it appeared that measured spin correlations like A_{xx} and A_{yy} from [198] respectively [199] are successfully described by PWA(1993). In Fig. 2 of Ref. [197], the Granada phase shifts are compared to the Nijmegen PWA(1993). From this figure, it is clear that both analyses overlap very strongly. The inclusion of the TME and MPE potentials with PS-VC, PS-SC, SC-SC, SC-VC, etc. did not improve the NN-fit.

The combined fit for NN and YN is extremely good in ESC16 [5, 6]. This, by obeying the strong constraint of having no bound-states in the $S = -1$ systems. Also, bound-states are absent for the $S = -2, -3, -4$ channels. It is for the first time that the quality of the NN-fit does not suffer from the inclusion of the YN-data. The ΛN p-waves seem to be better, which is the result of the truly simultaneous $NN + YN$-fitting. This is also reflected in the better Scheerbaum K_Λ-value [91], making the well-known small spin-orbit splitting smaller, see Ref. [200].

20.3. G-matrix calculations

The G-matrix results showed for ESC04 that basic features of hypernuclear data are reproduced nicely, improving on the soft-core OBE-models NSC89 [34] and NSC97 [35]. Despite this superiority of ESC04 for hypernuclear data, some problems remained. In particular, the well depth U_Σ was attractive, which is very unlikely in view of several other studies, e.g. Refs. [201, 202] and [96, 203]. Furthermore, it has been shown [204] that the EoS for nuclear matter is too soft for the soft-core models. From this, one learns that a good fit to the present scattering data not necessarily means success in the G-matrix results. To explain this, one can think of two reasons: (i) the G-matrix results are sensitive to the two-body interactions below 1 fm, whereas the present YN-scattering data are not, (ii) other than two-body forces play an important role. The problem with U_Σ hints at a special feature in the $\Sigma^+ p(^3S_1)$-channel. As shown in the ESC16 Ref. [6], it can be solved partly by the inclusion of quark-core effects. Furthermore, for the stiffening of the EoS, a natural possibility is the presence of TBF in nuclear and hyperonic matter, see Ref. [204]. This also solves the nuclear saturation problem [3].

It is important to stress the role of the information on hypernuclei in our analysis, via the G-matrix calculations. The ESC16-solution is required to have (i) no BB-bound states in $S = -1$, (ii) $U_{ss} > 1$, and $U_\Sigma > 0$. A very adequate description of the well-depth U_N, U_Λ, U_Σ, and U_Ξ can be obtained by including extra two- and three-body forces from meson-pairs (PS-SC, PS-VC, SC-SC, SC-VC, VC-VC, etc.) and those from the Fujita-Miyazawa interaction [205].

20.4. Synopsis A:

Summarizing the results of the ESC-model approach to baryon-baryon interactions, it has been shown that ESC models are able to give, with a single parameter-set, extremely satisfactory descriptions of the NN⊕YN-data, and at the same time lead to successful G-matrix results. For the coupling constants: (i) flavor SU(3)-symmetry can be maintained, and (ii) the predictions of the QPC-model are matched. Therefore, the ESC-models, ESC04 and ESC16, can be considered as very useful for the determination of the baryon-baryon interactions for low-energy scattering, meson-baryon couplings, and the description of hypernuclei in the context of kinematically broken SU(3)-symmetry. The values for many parameters, which in previous Nijmegen work were considered to be free to a large extent, follow now rather well the pattern shown in quark-model predictions. This is particularly the case for the $F/(F + D)$-ratios of the BBM-coupling constants. Furthermore, the ESC-model description of the $S = 0, -1$ BB-systems, the applications to the $S = -2, -3, -4$ BB-systems, as well as the G-matrix treatment of nuclear and hyperonic matter, have a rather sound physical basis.

20.5. Nuclear and Hyperonic Matter

As is well known, the experimental nuclear saturation properties: the density ρ_N, the binding energy per nucleon E/A, and the compression modulus K, cannot be reproduced quantitatively with nuclear two-body interactions only, see e.g. Ref. [206]. The inclusion of many-nucleon interactions is essential for giving the correct energy curve $E(\rho_N)$. Here, the three-nucleon interaction, composed of an attractive (TNA) and a repulsive (TNR) part, seems to be most important. Soft-core two-baryon potentials lead to a too soft equation of state (EoS). For example, ESC16 gives for the mass of the neutron star $1.35 M_\odot$ [124], implying for this model the necessity for a TNR contribution. Furthermore, at high densities, hyperon-mixing in neutron-star matter brings about a significant softening of the EoS, which gives a

reduction of the TNR effect for the maximum mass [204, 207, 208]. To compensate for this adverse effect, Nishizaki, Takatsuka and one of the authors (Y.Y.) [204] made the conjecture: there is a universal three-baryon repulsion (TBR), that operates for *YNN* and *YYN*, as well as for *NNN*. In QCD the gluons are flavor blind and therefore it is natural to relate this universal TBR to multi-gluon exchange. Because in QCD, the pomeron is a (non-perturbative) multi-gluon effect, which gives repulsion at low energies, in the ESC-models the TBR is associated with triple and quartic pomeron exchange [209, 210], as illustrated in Fig. 39.

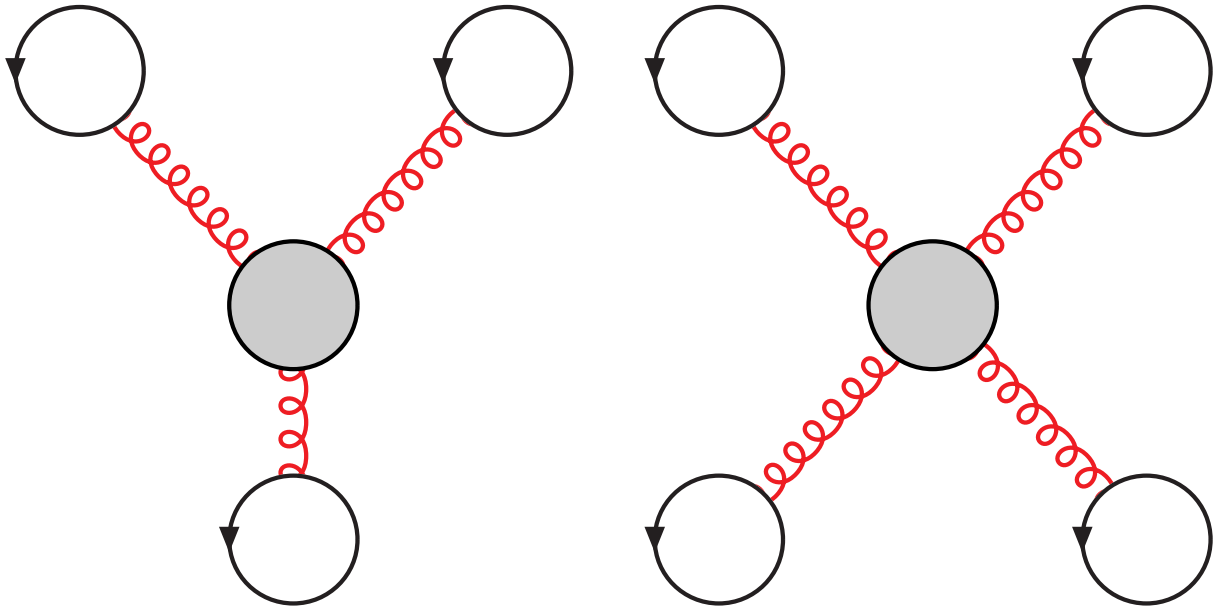

Figure 39: Triple- and quartic-pomeron 3- and 4-body interaction.

Then, to stiffen the EoS, together with a phenomenological TNA, we include in the G-matrix matter calculations with ESC16 the universal repulsive multi-gluon three-body (and four-body) forces in the form of the multi-pomeron exchange potential (MPP) [211, 13]. As demonstrated in [86, 87, 88, 89], the inclusion of TNA+MPP gives the proper nuclear saturation point, and makes the EoS of neutron matter stiff enough to assure the large observed values of two massive neutron stars with mass $1.97 \pm 0.04 M_\odot$ for PSR J1614-2230 [125] and $2.01 \pm 0.04 M_\odot$ for PSR J0348+0432 [126]. So, with the introduction of TNA+MPP, three things are achieved: (i) the right nuclear saturation point, (ii) the proper description of the neutron star masses, and (iii) better hyperonic well depths U_Y for $Y = \Lambda, \Sigma$ [6].

20.6. Baryon-quark and Quark-quark interactions

Recently, the ESC model has been extended to baryon-quark (BQ) and quark-quark (QQ) ESC-like potentials, utilizing the connection with the BB-interactions in the constituent quark model (CQM) [9]. Since in mixed nuclear-quark matter for baryon densities beyond $(2-3)\rho_N$ partially deconfinement of the quarks occurs, which opens the possibility of QB-interactions via diquark-exchange (DQE), which appears to be strongly repulsive. The meson-exchange BB-, BQ-, QQ-interactions and DQE-exchange have been applied in the Bruckner-Hartree-Fock (BHF) framework to mixed quark-baryon matter calculations for (heavy) neutron stars [10, 11, 12], and the latest version described in the review. As reported in this review, the BHF calculations, with the ESC interactions, of the in recent years discovered heavy neutron stars, is successful describing both the mass and the radius.

20.7. Synopsis B:

The extension of the ESC-interactions to the quark-level, exploiting the CQM relations, is a promising way to study mixed baryon-quark matter. This enables to study deconfinement, in for example heavy neutron stars and other very compact stellar objects, in a unified manner. Furthermore, this may also be relevant for supernovae modeling.

20.8. Baryon-Baryon models

The study of NN, YN, etc. has a very respectable history and literature. After the discovery of the neutron(1932), the advent of nuclear and particle physics in the thirties of the 20th century, quite an extensive and rich amount of experimental and theoretical work emerged from a worldwide scientific activity. The observation of cosmic-rays and research with particle accelerators has led to the discovery of many new baryons and mesons, see [42].
It appeared that the OPE and TPE potentials were not able to describe the NN data at 150, 210 and 300 MeV, because of an unsufficient spin-orbit interaction [212]. Therefore, next to OPE and TPE, the vector, scalar and axial-vector meson-exchanges have been added to the BB interaction, leading to OBE models, with or without TPE, developed by groups in *e.g.* Kyoto [213], Texas A& M [214], Paris [215], Bonn [216], Nijmegen [33, 81], etc.. Later, it became the opinion that the OBE interactions have too many free parameters: meson-baryon coupling constants and cut-off or form factor parameters. As the coupling constants are concerned, this feature does not apply strictly to the Nijmegen ESC models, where the physical constraints from the QPC-model and SU(3) symmetry are used, see Appendix I and [2] etc. In the nineties chiral-effective-field theory models have been developed [217, 218, 219], using the Weinberg theory of handling non-renormalizable pion-exchange interactions, using counter terms in the form of contact terms. Quark model related baryon-baryon interactions have been developed in the resonating-group-method (RGM), see [220], and most recently in the Lattice QCD models [114, 122, 221].

20.9. Prospects

The field of baryon-baryon interactions, which started with the discovery of the hyperons around 1950, is at present a very active area of research experimentally. This, because of the recent experiments (i) B-correlations: CERN-LHC [31], RHIC-STAR [32], (ii) S=-1: CLAS Collaboration [222] and J-PARC E40 Collaboration [223, 224, 225] (iii) S=-2: J-PARC E42 Collaboration [226], and BEPCII-BESIII Collaboration [227].

Reasons and topics for the further development of the ESC-model are: (i) Inclusion of the new data from the recent experiments, (ii) Extension of the TME-potentials with PS-PS, PS-SC, PS-VC, etc. contributions, (iii) ESC-model and G-matrix calculations, using the relativistic momentum-space Kadyshevsky interactions, and (iv)The NS-model can be extended to non-zero temperatures.

Acknowledgements

We are grateful to J.J. de Swart[‡], H. Bandō[‡], Y. Akaishi, T. Motoba, E. Hiyama, K. Itonaga, Y. Yasutake, V.G.J. Stoks, M. Rentmeester, R.A. Bryan[‡], B.F. Gibson, H.-J. Schulze, and D. Blaschke for their collaboration, stimulating discussions, and interest.

Appendix A. Kadyshevsky-Rules in Momentum-Space

In this appendix the rules for the Kadyshevsky graphs [14, 15, 16] are given. Following the setup of Appendix B in [55], where the rules for the Feynman graphs are given, the differences will then come to the surface most transparently. Starting from the expression of the S-operator, one has

$$\begin{aligned} S &= 1 + \sum_{n=1}^{\infty} \left(\frac{i}{\hbar}\right)^n \int_{-\infty}^{+\infty} \dots \int_{-\infty}^{+\infty} \theta(x_n^0 - x_{n-1}^0)\theta(x_{n-1}^0 - x_{n-2}^0) \dots \theta(x_2^0 - x_1^0) \\ &\quad \times \mathcal{L}_I(x_n)\, \mathcal{L}_I(x_{n-1}) \dots \mathcal{L}_I(x_1) \cdot d^4x_n \dots d^4x_1 \equiv 1 + \sum_{n=1}^{\infty} S_n, \end{aligned} \tag{A.1}$$

where [14] is followed, and introduce the time-like vector n^μ with $n^2 = n_0^2 - \mathbf{n}^2 = 1, n_0 > 0$. Then (A.1) can be brought into a completely 4-dimensional form by the replacement

$$\theta(x^0) \to \theta(x \cdot n) \ , \quad n \cdot x = n_0 x^0 - \mathbf{n} \cdot \mathbf{x}. \tag{A.2}$$

This gives ($\hbar = 1$)

$$S_n = i^n \int_{-\infty}^{+\infty} \dots \int_{-\infty}^{+\infty} \theta[n\cdot(x_n - x_{n-1})]\theta[n\cdot(x_{n-1} - x_{n-2})]\dots\theta[n\cdot(x_2 - x_1)]\cdot \times \mathcal{L}_I(x_n)\,\mathcal{L}_I(x_{n-1})\dots\mathcal{L}_I(x_1)\cdot d^4x_n\dots d^4x_1\ . \tag{A.3}$$

From the expression (A.3) one can work out the rules for the Kadyshevsky graphs in a way that parallels the derivation of the Feynman rules. The differences come from the treatment of the θ-functions. In the case of the Feynman graphs, one includes the θ-functions into the propagators by applying the Wick-expansion to the T-products of the field operators. In the case of the Kadyshevsky graphs one employs a four-dimensional form of the θ-functions, exploiting (A.2),

$$\theta(n\cdot x) = -\frac{1}{2\pi i}\int_{-\infty}^{+\infty} d\kappa \frac{\exp\left[-i\kappa(n\cdot x)\right]}{\kappa + i\epsilon}\ , \tag{A.4}$$

and one applies the Wick-expansion to the ordinary products of the field operators. Then, the propagators are given by

$$\begin{aligned}
\langle 0|\phi(x)\phi(y)|0\rangle &= D^{(+)}(x-y) = \int \frac{d^4q}{(2\pi)^3}\theta(q_0)\delta(q^2 - m^2)\\
\langle 0|A_\mu(x)A_\nu(y)|0\rangle &= D^{(+)}_{\mu\nu}(x-y) = -g_{\mu\nu}\int \frac{d^4q}{(2\pi)^3}\theta(q_0)\delta(q^2)\\
\langle 0|\psi(x)_\beta\bar\psi(y)_\alpha|0\rangle &= S^{(+)}_{\beta\alpha}(x-y) = \int \frac{d^4p}{(2\pi)^3}\theta(p_0)\,(\not p + M)_{\beta\alpha}\,\delta(p^2 - M^2)\ .
\end{aligned} \tag{A.5}$$

In the Kadyshevsky theory the considered Hilbert space is enlarged by admitting states containing 'quasi-particles'. The latter carry only 4-momentum, and serve to have formally four-momentum conservation at each vertex. The quasi-particles refer to the κ-variables in the Fourier transforms (A.4) of the θ-functions appearing in (A.3). These quasi-particle states $|\kappa_1,\dots\rangle$ are normalized by

$$\langle\kappa_1'\dots|\kappa_1,\dots\rangle = \delta(\kappa_1' - \kappa_1)\dots \tag{A.6}$$

The θ-functions in (A.3) connect only internal points of the graphs. To handle integral equations, occurring in for example the Bethe-Salpeter and Schwinger-Dyson equations, one needs to consider amplitudes with external quasi-particles as well as internal quasi-particles. The external quasi-particle entering a vertex is included only in the four-momentum conservation rule of that vertex, including both the external and the internal quasi-particle 4-momentum.

After these preliminary remarks, listed are the momentum-space rules for the computation of the $-M_{\kappa',\kappa}$-amplitudes, defined by

$$S_{\kappa',\kappa} = 1_{\kappa',\kappa} - (2\pi)^4 i\delta^4(P_f + \kappa' n - P_i - \kappa n)\ M_{\kappa',\kappa}. \tag{A.7}$$

The invariant amplitude $-M_{\kappa',\kappa}$ is computed by drawing all connected Feynman graphs for the considered process. The amplitude [13]

$$-(2\pi)^4\delta(\sum_i p_{i,out} + \kappa' n - \sum_i p_{i,in} - \kappa n)\ M_{\kappa',\kappa}(G) \tag{A.8}$$

corresponding to graph G is built up by associating factors with the elements of the graph, listed below:

I. Those factors, independent of the specific details of the interactions, are given by the following rules:

1. Draw the Feynman graph G. Arbitrarily number its vertices and orient each internal line from the vertex with the larger number to the vertex with the smaller number, assigning to it a 4-momentum p. Then, *without changing the orientation*, change the (single) internal fermion lines to double (antifermion) lines, such as to conserve the fermion number in every vertex.

[13] Notice here the (-)-sign, which is due to the (-)-sign in (A.7).

2. Connect with thin lines the first vertex with the second, the second with the third, etc. Orient them in the direction of increasing numbers and assign to them a 4-momentum $\kappa_s n$, where $s = 1, 2, \ldots, n-1$ is the number of the vertex which a given dotted line leaves. Attach to the first vertex an incoming external dotted line with 4-momentum $\kappa_i n$, and to the last vertex n an outgoing external dotted line with 4-momentum $\kappa_f n$.

3. For incoming (outgoing) boson and fermion lines: identical to the rules for Feynman graphs [55, 16], see Table A.36 [14].

Table A.36: Kadyshevski rules external lines.

Line	Particle	State	Factor in m.e.
$\bullet - - < - - \; q\; \alpha$	fermion	in	$[(2\pi)^{3/2}\sqrt{M/E(\mathbf{q})}]\; u_\alpha(\mathbf{q})$
$\bullet ===<=== \; q\; \alpha$	antifermion	in	$[(2\pi)^{3/2}\sqrt{M/E(\mathbf{q})}]\; \bar{v}_\alpha(\mathbf{q})$
$\bullet - -- < - - -$ k	meson	in	$[(2\pi)^{3/2}/\sqrt{2\omega(\mathbf{k})}]$
$-- < - - \bullet \; p\; \beta$	fermion	out	$[(2\pi)^{3/2}\sqrt{M/E(\mathbf{p})}]\; \bar{u}_\beta(\mathbf{p})$
$==<== \bullet \; p\; \beta$	antifermion	out	$[(2\pi)^{3/2}\sqrt{M/E(\mathbf{p})}]\; v_\beta(\mathbf{p})$
$\cdots\cdots < \cdots\cdots \bullet$ k	meson	out	$[(2\pi)^{3/2}/\sqrt{2\omega(\mathbf{k})}]$

4. For each internal dotted line with momentum κn a factor

$$G_0(\kappa) = -\frac{1}{\kappa + i\epsilon}\ . \tag{A.9}$$

5. For each internal boson line with mass m and momentum q a factor

$$\Delta^{(+)}(q) = \theta(q_0)\delta(q^2 - m^2). \tag{A.10}$$

6. For each internal fermion line with mass M and momentum p and *positive energy* a factor

$$S^{(+)}_{\beta\alpha}(p) = (\not{p} + M)_{\beta\alpha}\,\theta(p_0)\delta(p^2 - M^2). \tag{A.11}$$

For each internal fermion line with momentum p and *negative energy* a factor

$$S^{(-)}_{\beta\alpha}(p) = (\not{p} - M)_{\beta\alpha}\,\theta(-p_0)\delta(p^2 - M^2), \tag{A.12}$$

in accordance with Table A.37 [16].

7. For each internal photon line, using the Feynman gauge, a factor

$$D^{(+)}(q)_{\mu\nu} = -g_{\mu\nu}\theta(q_0)\delta(q^2)\ . \tag{A.13}$$

8a. For each vertex, number s, a factor

$$(2\pi)^4\delta^4\left(\sum_i p_{i,out} + \kappa_{s+1} - \sum_i p_{i,in} - \kappa_s\right), \tag{A.14}$$

where $p_{i,out}$ and $p_{i,in}$ are the outgoing respectively the incoming momenta at the vertex with number s.

[14] In this table the Dirac-spinors of [55] are used, and not those of [16].

Table A.37: Kadyshevski rules internal lines.

Line	Particle	Pairing	Factor in m.e.
j' • −− < − − • j	fermion	$\psi_\beta(q_{j'}\bar{\psi}_\alpha(p_j); j' < j$	$S^{(+)}_{\beta\alpha}(p_j, M)$
j'• ===<=== • j	antifermion	$\bar{\psi}_\alpha(p_j\psi_\beta(q_{j'}); j' < j$	$S^{(+)}_{\beta\alpha}(q_j, -M)$
j' • · · · · · < · · · · · • j	meson	$\phi(k_{j'}\phi(k_j); j' < j$	$\Delta^{(+)}(k_j)$

8b. Integrate over each internal particle line , momentum l: $\int d^4l/(2\pi)^3$.

9. Integrate over each internal quasi-particle (dotted) line with momentum $\kappa_s n$: $\int_{-\infty}^{+\infty} d\kappa_s/(2\pi)$.

10. *Not* a factor -1 for each closed loop.

11. A factor -1 between graphs which differ only by an interchange of two external fermions. This not only for the interchange of identical fermions in the final state, but also for the interchange of *e.g.* an initial fermion and a similar anti-fermion in the final state.

12. Repeat the operations (1)-(11) for all $n!$ numberings of the vertices of the given Feynman graph and sum.

II. Those factors coming from the structure and type of vertices are given for each vertex by the matrix element $\langle \ldots | \mathcal{L}_I(0) | \ldots \rangle$. Therefore, they are, apart from a factor $(-i)$, identical to that given in [55], Appendices B.

To exhibit the δ-functions for the baryons in the calculations of the amplitudes the fermion and boson propagators are written as

$$S^{(\pm)}(p) = \widetilde{S}^{\pm)}(p)\, \delta_\pm(p^2 - M^2),\ \Delta^{(+)}(q) = \delta_+(q^2 - m^2). \tag{A.15}$$

Appendix B. Orientation Kadyshevsky graphs for the planar and crossed box graphs

Here, the Kadyshevsky prescription [14, 15, 16] is used for the orientation of the internal lines in the 4th order graphs for fermion-fermion scattering. In the figure below, the vertices for the 4! = 24 box-graphs are ordered, and find that only six configurations have exclusively positive baryons, *i.e.* correspond to BB-scattering/interaction. There are 12 graphs with one anti-fermion in the intermediate states, and 6 graphs with two anti-fermions in the intermediate states. The latter correspond to the so-called 1Z- and 2Z-graphs, which are important for Quark-quark (QQ) interactions. In Fig. B.40 at the left corners of each graph, there are incoming positive-energy nucleon lines, and at the right corners there are outgoing positive-energy nucleon lines. If at any vertex the arrows of the nucleon lines are opposite, the pair-suppression mechanism makes these graphs negligible in the case of BB-scattering. However, for quark-quark interaction this is not the case.

Inspection of the graphs in Fig. B.40 shows that there are only six graphs that survive in the limit of strong pair-suppression. They are: the first three graphs in row one, the third and fifth graphs in row two, and the fifth graph in row five.

In the two-fermion scattering processes, the incoming lines enter from the right and the outgoing lines leave the graphs on the left. The graphs are indexed with (r,c), where r is the row number, and c the column number for the internal fermion lines:

1. The $[+,+]$*-graphs are: (1,1), (1,2), (1,3), (2,3), (2,5), (3,5).*
2. The $[+,-]$*-graphs are: (1,4), (1,5), (1,6), (2,4), (2,6), (3,6).*
3. The $[-,+]$*-graphs are: (2,1), (3,1), (3,2), (4,1), (4,3), (4,5).*
4. The $[-,-]$*-graphs are: (2,2), (3,2), (3,4), (4,2), (4,4), (4,6).*

The crossed graphs are obtained by simply crossing the meson lines in the graphs.

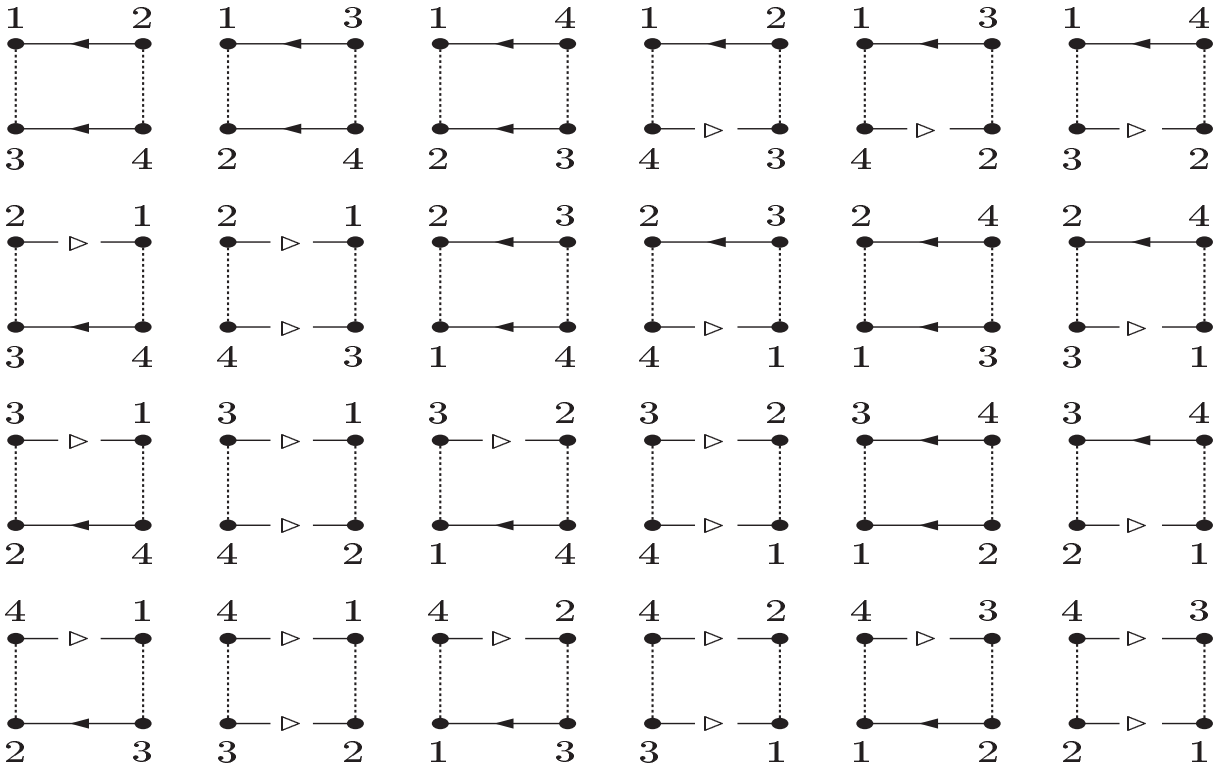

Figure B.40: *Kadyshevsky vertex configurations. The solid-filled arrow lines denote baryons with positive energy, and the solid open-arrow lines denote baryons with negative energy. The dashed lines refer to the mesons.*

Appendix C. Fourth-order Kadyshevsky Graphs σ = [++]

Appendix C.1. The planar-box graphs

Following the rules of Appendix A, drawn are the planar two-meson exchange graphs in Figs. C.41-C.43. Here, the numbering of the vertices can be read off by following the quasi-particle lines, beginning with the entering κ-line. The quasi-particle lines κ_i for $i = 1, 2, 3$ are then defined according to Appendix A. Then, again following the rules of Appendix A, below the resulting amplitudes are listed. Graph (a) in the planar-box Kadyshevsky graphs Fig. C.41

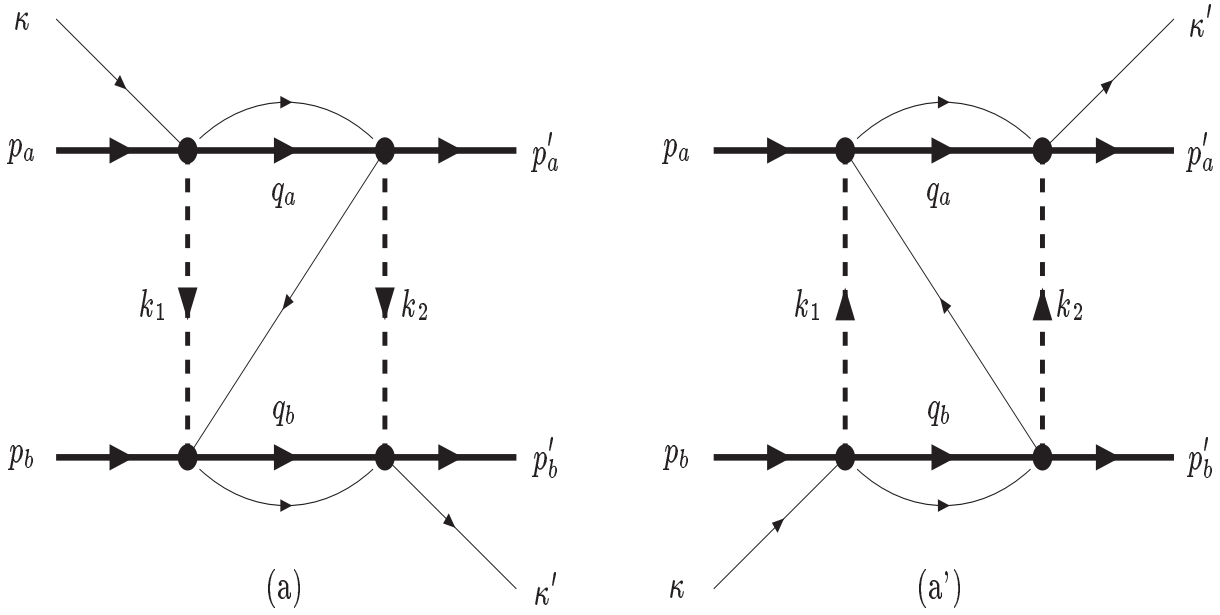

Figure C.41: *Planar Kadyshevsky graphs. The solid lines denote baryons. The dashed lines refer to the mesons.*

gives for the fourth-order kernel [15]

$$
\begin{aligned}
(2\pi)^4\delta^4\left(p'_a+p'_b+\kappa' n-p_a-p_b-\kappa n\right)\, M^{(//,a)}_{\kappa',\kappa} = -\left\{\frac{M_a^2M_b^2}{E_a(\mathbf{p}'_a)E_b(\mathbf{p}'_b)E_a(\mathbf{p}_aE_b(\mathbf{p}_b)}\right\}^{1/2}\int\frac{d^4q_a}{(2\pi)^3}\int\frac{d^4q_b}{(2\pi)^3}\cdot\\
\times\int\frac{d^4k_1}{(2\pi)^3}\int\frac{d^4k_2}{(2\pi)^3}\,\delta_+\left[k_1^2-m_1^2\right]\delta_+\left[k_2^2-m_2^2\right]\cdot\delta_+\left[q_a^2-M_a^2\right]\delta_+\left[q_b^2-M_b^2\right]\cdot\\
\times\left[\bar u(p'_a)\Gamma_2^{(a)}\widetilde S^{(+)}(q_a)\Gamma_1^{(a)}u(p_a)\right]\,\left[\bar u(p'_b)\Gamma_2^{(b)}\widetilde S^{(-)}(q_b)\Gamma_1^{(b)}u(p_b)\right]\\
\times\int_{-\infty}^{\infty}\frac{d\kappa_1}{2\pi}\int_{-\infty}^{\infty}\frac{d\kappa_2}{2\pi}\int_{-\infty}^{\infty}\frac{d\kappa_3}{2\pi}\,\frac{1}{\kappa_1-i\epsilon}\,\frac{1}{\kappa_2-i\epsilon}\,\frac{1}{\kappa_3-i\epsilon}\cdot\\
\times(2\pi)^4\delta^4\left(\kappa_1 n+p'_a-q_a-k_2-\kappa n\right)(2\pi)^4\delta^4\left(\kappa_3 n+p_a-q_a-k_1-\kappa' n\right)\cdot\\
\times(2\pi)^4\delta^4\left(\kappa_2 n-\frac{1}{2}(\kappa'+\kappa)n-(q_a+q_b)+\frac{1}{2}(p'_a+p'_b+p_a+p_b)\right).
\end{aligned}
\tag{C.1}
$$

Note that the expression for the amplitude in (C.1) for only positive-energy nucleons in the intermediate state is manifestly covariant. With the δ-functions, all κ-integrals can be carried out. Also, the integrations over the zero-components can be carried out, thanks to the on-mass-shell δ_+-functions. This is done in the CM-system, where one

[15] In this Appendix C and Appendix E the subscripts in Γ_X's, where $X = S, PV, V, \mu$, etc., see (7.2), are suppressed.

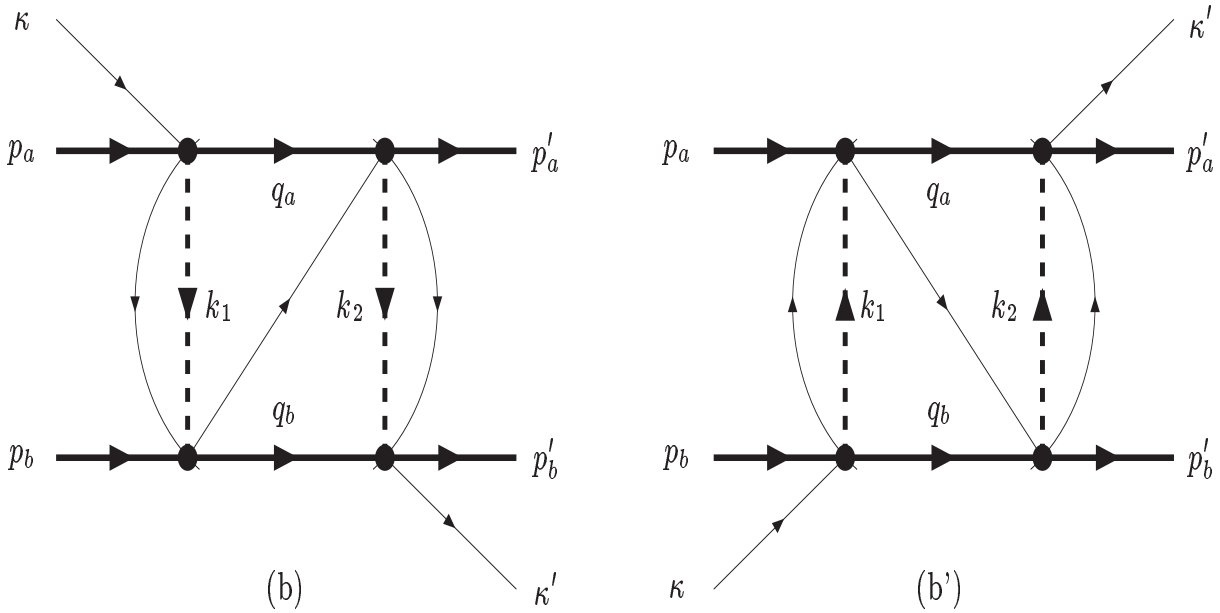

Figure C.42: *Planar Kadyshevsky graphs. The solid lines denote baryons. The dashed lines refers to the mesons.*

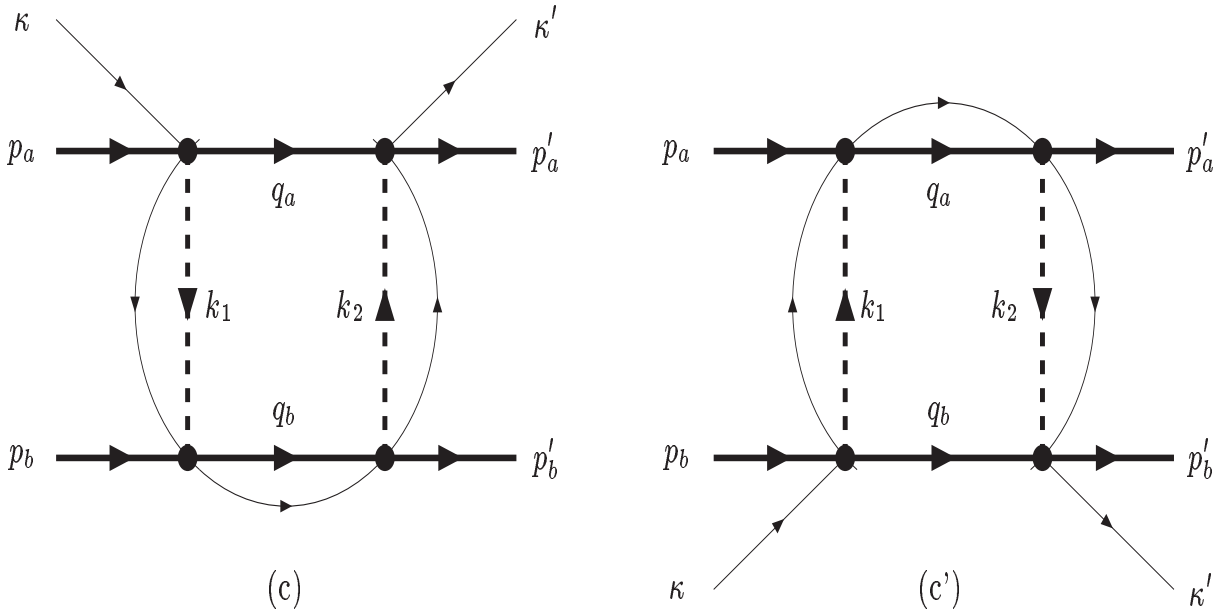

Figure C.43: *Planar Kadyshevsky graphs. The solid lines denote baryons. The dashed lines refers to the mesons.*

can use the specific form of the n^μ-vector. The result for graph (a) is

$$M^{(//,a)}_{\kappa',\kappa}(p'_a s'_a, p'_b s'_b; p_a s_a, p_b s_b) = \left\{ \frac{M_a^2 M_b^2}{E_a(\mathbf{p}'_a) E_b(\mathbf{p}'_b) E_a(\mathbf{p}_a E_b(\mathbf{p}_b)} \right\}^{1/2} \cdot (2\pi)^3 \int d^3q \cdot$$
$$\times \int \frac{d^3k_1}{(2\pi^3)2\omega_1} \int \frac{d^3k_2}{(2\pi^3)2\omega_2} \delta^{(3)}(\mathbf{k}_1 - \mathbf{p} + \mathbf{q}) \delta^{(3)}(\mathbf{k}_2 + \mathbf{p}' - \mathbf{q}) \cdot$$
$$\times \frac{M_a M_b}{E_a(\mathbf{q}) E_b(\mathbf{q})} \sum_{s''_a, s''_b} \Big[\bar{u}(\mathbf{p}'_a, s'_a) \Gamma_2^{(a)} u(\mathbf{q}_a, s''_a) \cdot \bar{u}(\mathbf{q}_a, s''_a) \Gamma_1^{(a)} u(\mathbf{p}_a, s_a) \Big] \cdot$$
$$\times \Big[\bar{u}(\mathbf{p}'_b, s'_b) \Gamma_2^{(b)} u(\mathbf{q}_b, s''_b) \cdot \bar{u}(\mathbf{q}_b, s''_b) \Gamma_1^{(b)} u(\mathbf{p}_b, s_b) \Big] \cdot D^{(//,a)}_{\kappa',\kappa}(\omega_1, \omega_2). \tag{C.2}$$

Similar calculations are carried through for the graphs (a'),(b),(b'),(c), and (c'). In the CM-system, this leads to the denominators ($\sigma = [++]$)

$$\begin{aligned}
D^{(//,a)}_{\kappa',\kappa}(\omega_1,\omega_2) &= \frac{1}{\omega_1 - \kappa + [E_a(\mathbf{q}) - E_a(\mathbf{p})] + i\epsilon} \cdot \frac{1}{\omega_2 - \kappa' + [E_b(\mathbf{q}) - E_b(\mathbf{p}')] + i\epsilon} \cdot \\
&\quad \times \frac{1}{\omega_1 + \omega_2 - \frac{1}{2}(\kappa' + \kappa) + \frac{1}{2}[E_a(\mathbf{p}') - E_b(\mathbf{p}') - E_a(\mathbf{p}) + E_b(\mathbf{p})] + i\epsilon}, \\
D^{(//,a')}_{\kappa',\kappa}(\omega_1,\omega_2) &= \frac{1}{\omega_1 - \kappa - [E_b(\mathbf{p}) - E_b(\mathbf{q})] + i\epsilon} \cdot \frac{1}{\omega_2 - \kappa' - [E_a(\mathbf{p}') - E_a(\mathbf{q})] + i\epsilon} \cdot \\
&\quad \times \frac{1}{\omega_1 + \omega_2 - \frac{1}{2}(\kappa' + \kappa) - \frac{1}{2}[E_a(\mathbf{p}') - E_b(\mathbf{p}') - E_a(\mathbf{p}) + E_b(\mathbf{p})] + i\epsilon}, \\
D^{(//,b)}_{\kappa',\kappa}(\omega_1,\omega_2) &= \frac{1}{\omega_1 - \kappa - [E_a(\mathbf{p}) - E_a(\mathbf{q})] + i\epsilon} \cdot \frac{1}{\omega_2 - \kappa' - [E_b(\mathbf{p}') - E_b(\mathbf{q})] + i\epsilon} \cdot \\
&\quad \times \frac{1}{-\frac{1}{2}(\kappa' + \kappa) - \frac{1}{2}[E_a(\mathbf{p}') + E_b(\mathbf{p}') + E_a(\mathbf{p}) + E_b(\mathbf{p})] + (E_a(\mathbf{q}) + E_b(\mathbf{q})) + i\epsilon}, \\
D^{(//,b')}_{\kappa',\kappa}(\omega_1,\omega_2) &= \frac{1}{\omega_1 - \kappa - [E_b(\mathbf{p}) - E_b(\mathbf{q})] + i\epsilon} \cdot \frac{1}{\omega_2 - \kappa' - [E_a(\mathbf{p}') - E_a(\mathbf{q})] + i\epsilon} \cdot \\
&\quad \times \frac{1}{-\frac{1}{2}(\kappa' + \kappa) - \frac{1}{2}[E_a(\mathbf{p}') + E_b(\mathbf{p}') + E_a(\mathbf{p}) + E_b(\mathbf{p})] + (E_a(\mathbf{q}) + E_b(\mathbf{q})) + i\epsilon}, \\
D^{(//,c)}_{\kappa',\kappa}(\omega_1,\omega_2) &= \frac{1}{\omega_1 - \kappa - [E_a(\mathbf{p}) - E_a(\mathbf{q})] + i\epsilon} \cdot \frac{1}{\omega_2 - \kappa' - [E_a(\mathbf{p}') - E_a(\mathbf{q})] + i\epsilon} \cdot \\
&\quad \times \frac{1}{-\frac{1}{2}(\kappa' + \kappa) - \frac{1}{2}[E_a(\mathbf{p}') + E_b(\mathbf{p}') + E_a(\mathbf{p}) + E_b(\mathbf{p})] + (E_a(\mathbf{q}) + E_b(\mathbf{q})) + i\epsilon}, \\
D^{(//,c')}_{\kappa',\kappa}(\omega_1,\omega_2) &= \frac{1}{\omega_1 - \kappa - [E_b(\mathbf{p}) - E_b(\mathbf{q})] + i\epsilon} \cdot \frac{1}{\omega_2 - \kappa' - [E_b(\mathbf{p}') - E_b(\mathbf{q})] + i\epsilon} \cdot \\
&\quad \times \frac{1}{-\frac{1}{2}(\kappa' + \kappa) - \frac{1}{2}[E_a(\mathbf{p}') + E_b(\mathbf{p}') + E_a(\mathbf{p}) + E_b(\mathbf{p})] + (E_a(\mathbf{q}) + E_b(\mathbf{q})) + i\epsilon}.
\end{aligned} \tag{C.3a}$$

Appendix C.2. The crossed-box graphs

Following the rules of Appendix A, drawn are the crossed two-meson exchange graphs in Figs. C.44-C.46. Here, the numbering of the vertices can be read off by following the quasi-particle lines, beginning with the entering κ-line. The quasi-particle lines κ_i for $i = 1, 2, 3$ are then defined according to Appendix A. Then, again following the rules of Appendix A, listed below are the resulting amplitudes. Graph (a) in the crossed-box Kadyshevsky graphs Fig. C.44

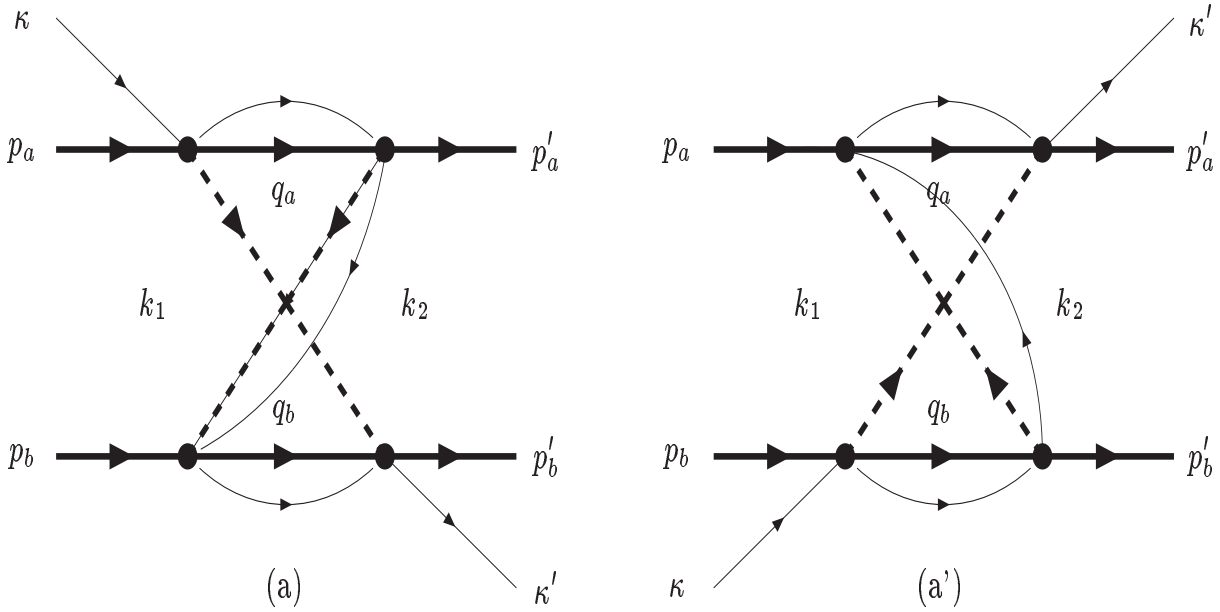

Figure C.44: *Crossed Kadyshevsky graphs. The solid lines denote baryons. The dashed lines refers to the mesons.*

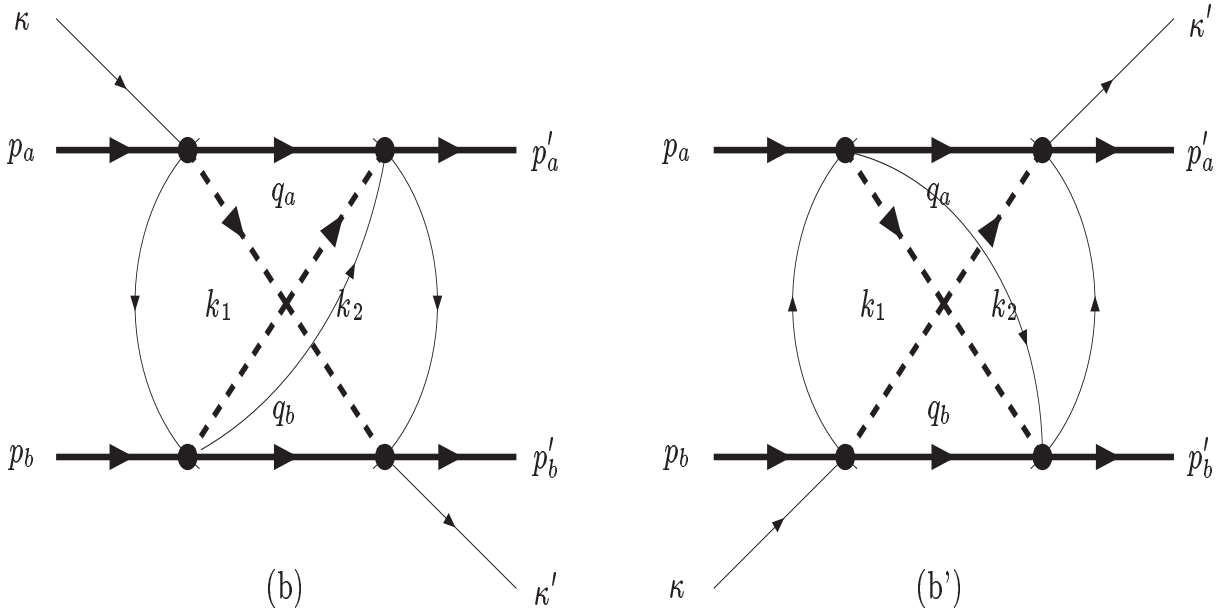

Figure C.45: *Crossed Kadyshevsky graphs. The solid lines denote baryons. The dashed lines refers to the pseudo-scalar mesons. The thin lines denote the quasi-momentum particles.*

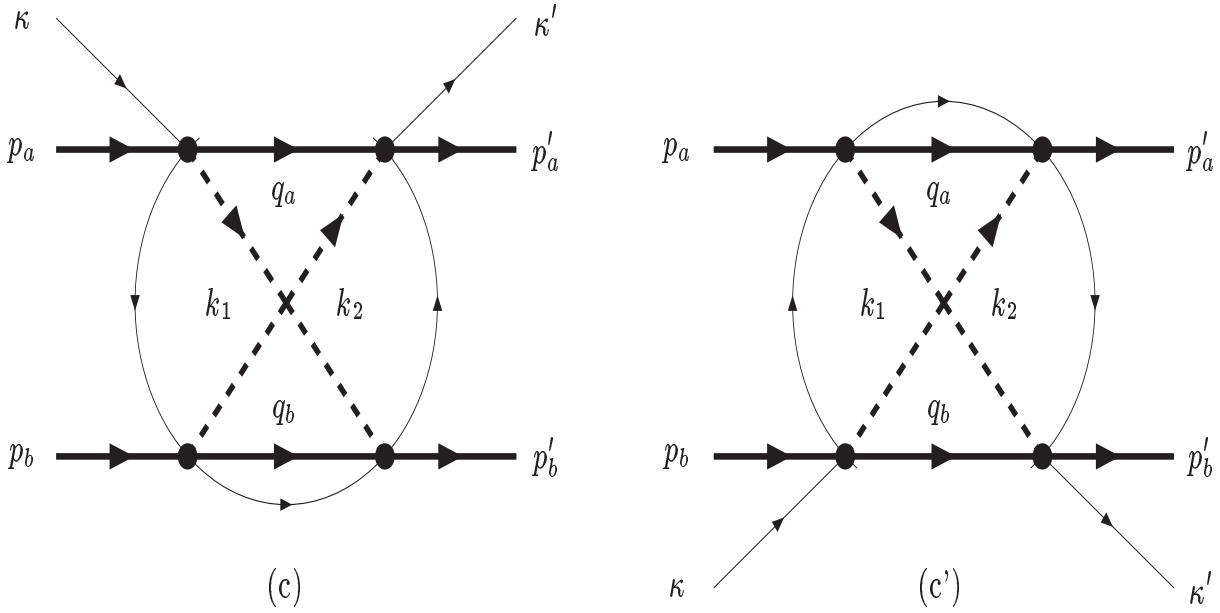

Figure C.46: *Crossed Kadyshevsky graphs. The solid lines denote baryons. The dashed lines refers to the pseudo-scalar mesons. The thin lines denote the quasi-momentum particles.*

gives for the fourth-order kernel, with only positive-energy spinors for the intermediate nucleons,

$$M^{(X,a)}_{\kappa',\kappa}\left(p'_a, p'_b; p_a, p_b\right) = -\left\{\frac{M_a^2 M_b^2}{E_a(\mathbf{p}'_a)E_b(\mathbf{p}'_b)E_a(\mathbf{p}_a E_b(\mathbf{p}_b)}\right\}^{1/2} \int \frac{d^4q_a}{(2\pi)^3}\int \frac{d^4q_b}{(2\pi)^3}\int \frac{d^4k_1}{(2\pi)^3}\int \frac{d^4k_2}{(2\pi)^3}\cdot$$
$$\times\delta_+\left[q_a^2 - M_a^2\right]\delta_+\left[q_b^2 - M_b^2\right]\cdot\delta_+\left[k_1^2 - m_1^2\right]\delta_+\left[k_2^2 - m_2^2\right]\cdot$$
$$\times\left[\bar{u}(p'_a)\Gamma_2^{(a)}\widetilde{S}^{(+)}(q_a)\Gamma_1^{(a)}u(p_a)\right]\left[\bar{u}(p'_b)\Gamma_1^{(b)}\widetilde{S}^{(-)}(q_b)\Gamma_2^{(b)}u(p_b)\right]\cdot$$
$$\times\int_{-\infty}^{\infty}\frac{d\kappa_1}{2\pi}\int_{-\infty}^{\infty}\frac{d\kappa_2}{2\pi}\int_{-\infty}^{\infty}\frac{d\kappa_3}{2\pi}\frac{1}{\kappa_1 - i\epsilon}\frac{1}{\kappa_2 - i\epsilon}\frac{1}{\kappa_3 - i\epsilon}\cdot$$
$$\times(2\pi)^4\delta^4\left(\kappa_1 n + p'_a - q_a - k_2 - \kappa n\right)(2\pi)^4\delta^4\left(\kappa_3 n + p_a - q_a - k_1 - \kappa' n\right)\cdot$$
$$\times(2\pi)^4\delta^4\left(\kappa_2 n - \frac{1}{2}(\kappa' + \kappa) - (k_1 + k_2) + \frac{1}{2}(p'_b + p'_a + p_b + p_a) - (q_a + q_b)\right). \qquad \text{(C.4)}$$

With the δ-functions, all κ-integrals can be carried out. Also, the integrations over the zero-components can be carried out, thanks to the on-mass-shell δ_+-functions. The result for graph (a) is

$$M^{(X,a)}_{\kappa',\kappa}(p'_a s'_a, p'_b s'_b; p_a s_a, p_b s_b) = \left\{\frac{M_a^2 M_b^2}{E_a(\mathbf{p}'_a)E_b(\mathbf{p}'_b)E_a(\mathbf{p}_a E_b(\mathbf{p}_b)}\right\}^{1/2}\cdot$$
$$\times(2\pi)^3\int d^3q_a\int d^3q_b\,\delta^{(3)}(\mathbf{q}_a - \mathbf{q}_b + \mathbf{p}_a - \mathbf{p}'_b)\cdot$$
$$\times\int\frac{d^3k_1}{(2\pi^3)2\omega_1}\int\frac{d^3k_2}{(2\pi^3)2\omega_2}\delta^{(3)}(\mathbf{k}_1 - \mathbf{p}_a + \mathbf{q}_a)\delta^{(3)}(\mathbf{k}_2 + \mathbf{p}'_a + \mathbf{q}_a)\cdot$$
$$\times\frac{M_a M_b}{E_a(\mathbf{q})E_b(\mathbf{q})}\sum_{s''_a, s''_b}\left[\bar{u}(\mathbf{p}'_a, s'_a)\Gamma_2^{(a)}u(\mathbf{q}_a, s''_a)\cdot\bar{u}(\mathbf{q}_a, s''_a)\Gamma_1^{(a)}u(\mathbf{p}_a, s_a)\right]\cdot$$
$$\times\left[\bar{u}(\mathbf{p}'_b, s'_b)\Gamma_1^{(b)}u(\mathbf{q}_b, s''_b)\cdot\bar{u}(\mathbf{q}_b, s''_b)\Gamma_2^{(b)}u(\mathbf{p}_b, s_b)\right]\cdot D^{(X,a)}_{\kappa',\kappa}(\omega_1, \omega_2). \qquad \text{(C.5)}$$

Similar calculations are carried through for the graphs (a'),(b),(b'),(c), and (c'). In the CM-system, this leads to

$$
\begin{aligned}
D^{(X,a)}_{\kappa',\kappa}(\omega_1,\omega_2) &= \frac{1}{\omega_1-\kappa+\left[E_a(\mathbf{q})-E_a(\mathbf{p})\right]+i\epsilon}\cdot\frac{1}{\omega_1-\kappa'+\left[E_b(\mathbf{q})-E_b(\mathbf{p}')\right]+i\epsilon}\cdot\\
&\quad\times\frac{1}{\omega_1+\omega_2-\frac{1}{2}(\kappa'+\kappa)+\frac{1}{2}\left[E_a(\mathbf{p}')-E_b(\mathbf{p}')-E_a(\mathbf{p})+E_b(\mathbf{p})\right]+i\epsilon},\\
D^{(X,a')}_{\kappa',\kappa}(\omega_1,\omega_2) &= \frac{1}{\omega_2-\kappa+\left[E_b(\mathbf{q})-E_b(\mathbf{p})\right]+i\epsilon}\cdot\frac{1}{\omega_2-\kappa'+\left[E_a(\mathbf{q})-E_a(\mathbf{p}')\right]+i\epsilon}\cdot\\
&\quad\times\frac{1}{\omega_1+\omega_2-\frac{1}{2}(\kappa'+\kappa)-\frac{1}{2}\left[E_a(\mathbf{p}')-E_b(\mathbf{p}')-E_a(\mathbf{p})+E_b(\mathbf{p})\right]+i\epsilon},\\
D^{(X,b)}_{\kappa',\kappa}(\omega_1,\omega_2) &= \frac{1}{\omega_1-\kappa+\left[E_a(\mathbf{q})-E_a(\mathbf{p})\right]+i\epsilon}\cdot\frac{1}{\omega_1-\kappa'+\left[E_b(\mathbf{q})-E_b(\mathbf{p}')\right]+i\epsilon}\cdot\\
&\quad\times\frac{1}{\omega_1+\omega_2-\frac{1}{2}(\kappa'+\kappa)-\frac{1}{2}\left[E_a(\mathbf{p}')+E_b(\mathbf{p}')+E_a(\mathbf{p})+E_b(\mathbf{p})\right]+(E_a(\mathbf{q})+E_b(\mathbf{q}))+i\epsilon},\\
D^{(X,b')}_{\kappa',\kappa}(\omega_1,\omega_2) &= \frac{1}{\omega_2-\kappa+\left[E_b(\mathbf{q})-E_b(\mathbf{p})\right]+i\epsilon}\cdot\frac{1}{\omega_2-\kappa'+\left[E_a(\mathbf{q})-E_a(\mathbf{p}')\right]+i\epsilon}\cdot\\
&\quad\times\frac{1}{\omega_1+\omega_2-\frac{1}{2}(\kappa'+\kappa)-\frac{1}{2}\left[E_a(\mathbf{p}')+E_b(\mathbf{p}')+E_a(\mathbf{p})+E_b(\mathbf{p})\right]+(E_a(\mathbf{q})+E_b(\mathbf{q}))+i\epsilon},\\
D^{(X,c)}_{\kappa',\kappa}(\omega_1,\omega_2) &= \frac{1}{\omega_1-\kappa+\left[E_a(\mathbf{q})-E_a(\mathbf{p})\right]+i\epsilon}\cdot\frac{1}{\omega_2-\kappa'+\left[E_a(\mathbf{q})-E_a(\mathbf{p}')\right]+i\epsilon}\cdot\\
&\quad\times\frac{1}{\omega_1+\omega_2-\frac{1}{2}(\kappa'+\kappa)-\frac{1}{2}\left[E_a(\mathbf{p}')+E_b(\mathbf{p}')+E_a(\mathbf{p})+E_b(\mathbf{p})\right]+(E_a(\mathbf{q})+E_b(\mathbf{q}))+i\epsilon},\\
D^{(X,c')}_{\kappa',\kappa}(\omega_1,\omega_2) &= \frac{1}{\omega_2-\kappa+\left[E_b(\mathbf{q})-E_b(\mathbf{p})\right]+i\epsilon}\cdot\frac{1}{\omega_1-\kappa'+\left[E_b(\mathbf{q})-E_b(\mathbf{p}')\right]+i\epsilon}\cdot\\
&\quad\times\frac{1}{\omega_1+\omega_2-\frac{1}{2}(\kappa'+\kappa)-\frac{1}{2}\left[E_a(\mathbf{p}')+E_b(\mathbf{p}')+E_a(\mathbf{p})+E_b(\mathbf{p})\right]+(E_a(\mathbf{q})+E_b(\mathbf{q}))+i\epsilon}.
\end{aligned}
\tag{C.6a}
$$

Appendix D. Relation Kadyshevsky and Klein-Macke potentials

Appendix D.1. Relation Klein-Macke formalism planar graphs

To make the connection with the Klein-Macke formalism in [26], consider elastic scattering and $\kappa=\kappa'=0$. Then, the factors in the denominator $D^{(//,a)}_{\sigma;0,0}(\omega_1,\omega_2)$ in Eq. (C.3) are written as follows:

1. $\omega_1+E_a(\mathbf{q})-E_a(\mathbf{p})=\omega_1+E_a(\mathbf{q})+E_b(\mathbf{p})-\left[E_a(\mathbf{p})+E_b(\mathbf{p})\right]=$
   $\omega_1+\left[E_a(\mathbf{q})+E_b(\mathbf{p})\right]-W\Rightarrow\omega_1+A+A'',$

2. $\omega_2+E_b(\mathbf{q})-E_b(\mathbf{p}')=\omega_2+E_b(\mathbf{q})+E_a(\mathbf{p}')-\left[E_b(\mathbf{p}')+E_a(\mathbf{p}')\right]=$
   $\omega_2+\left[E_b(\mathbf{q})+E_a(\mathbf{p}')\right]-W\Rightarrow\omega_2+A'+B'',$

3. $\omega_1+\omega_2+\frac{1}{2}\left[E_a(\mathbf{p}')-E_b(\mathbf{p}')-E_a(\mathbf{p})+E_b(\mathbf{p})\right]=$
   $\omega_1+\omega_2+\frac{1}{2}\left[2E_a(\mathbf{p}')-(E_a(\mathbf{p}')+E_b(\mathbf{p}'))-(E_a(\mathbf{p})+E_b(\mathbf{p}))\right]+2E_b(\mathbf{p})\right]=$
   $\omega_1+\omega_2+(E_a(\mathbf{p}')+E_b(\mathbf{p}))-W)\Rightarrow\omega_1+\omega_2+A'+A.$

Here $\Rightarrow$ means taking equal masses $M_a = M_b$, and $A = E(\mathbf{p}) - W/2,\ A' = E(\mathbf{p}') - W'/2,\ A'' = E(\mathbf{q}) - W/2,\ B'' = A''$. The expressions for the on-shell denominators become

$$\begin{aligned}
D^{(//,a)}_{\sigma;0,0}(\omega_1,\omega_2) &\Rightarrow (\omega_1 + A + A'')^{-1}\ (\omega_2 + A' + A'')^{-1}\ [2A'']^{-1}\,,\\
D^{(//,a')}_{\sigma;0,0}(\omega_1,\omega_2) &\Rightarrow (\omega_1 + A + A'')^{-1}\ (\omega_2 + A' + A'')^{-1}\ [2A'']^{-1}\,,\\
D^{(//,b)}_{\sigma;0,0}(\omega_1,\omega_2) &\Rightarrow (\omega_1 + A + A'')^{-1}\ (\omega_2 + A' + A'')^{-1}\ (\omega_1+\omega_2)^{-1}\,,\\
D^{(//,b')}_{\sigma;0,0}(\omega_1,\omega_2) &\Rightarrow (\omega_1 + A + A'')^{-1}\ (\omega_2 + A' + A'')^{-1}\ (\omega_1+\omega_2)^{-1}\,,\\
D^{(//,c)}_{\sigma;0,0}(\omega_1,\omega_2) &\Rightarrow (\omega_1 + A + A'')^{-1}\ (\omega_2 + A' + A'')^{-1}\ [2A'']^{-1}\,,\\
D^{(//,c')}_{\sigma;0,0}(\omega_1,\omega_2) &\Rightarrow (\omega_1 + A + A'')^{-1}\ (\omega_2 + A + A'')^{-1}\ [2A'']^{-1}\,.
\end{aligned} \tag{D.1}$$

This demonstrates that the Klein-Macke formalism, at least for equal fermion masses, leads to equivalent expressions for the potentials as in [26].

Appendix D.2. Relation Klein-Macke formalism crossed graphs

Taking equal masses $M_a = M_b$, and the notation used in [26] $A = E(\mathbf{p}) - W/2,\ A' = E(\mathbf{p}') - W'/2,\ A'' = E(\mathbf{q}) - W/2,\ B'' = A''$, the expressions for the on-shell denominators become

$$\begin{aligned}
D^{(X,a)}_{\sigma;0,0}(\omega_1,\omega_2) &\Rightarrow (\omega_1 + A' + A'')^{-1}\ (\omega_2 + A + A'')^{-1}\ (\omega_1+\omega_2+2A'')^{-1}\,,\\
D^{(X,a')}_{\sigma;0,0}(\omega_1,\omega_2) &\Rightarrow (\omega_1 + A' + A'')^{-1}\ (\omega_2 + A + A'')^{-1}\ (\omega_1+\omega_2+2A'')^{-1}\,,\\
D^{(X,b)}_{\sigma;0,0}(\omega_1,\omega_2) &\Rightarrow (\omega_2 + A' + A'')^{-1}\ (\omega_2 + A + A'')^{-1}\ (\omega_1+\omega_2)^{-1}\,,\\
D^{(X,b')}_{\sigma;0,0}(\omega_1,\omega_2) &\Rightarrow (\omega_1 + A' + A'')^{-1}\ (\omega_1 + A + A'')^{-1}\ (\omega_1+\omega_2)^{-1}\,,\\
D^{(X,c)}_{\sigma;0,0}(\omega_1,\omega_2) &\Rightarrow (\omega_2 + A' + A'')^{-1}\ (\omega_2 + A + A'')^{-1}\ (\omega_1+\omega_2+2A'')^{-1}\,,\\
D^{(X,c')}_{\sigma;0,0}(\omega_1,\omega_2) &\Rightarrow (\omega_1 + A' + A'')^{-1}\ (\omega_1 + A + A'')^{-1}\ (\omega_1+\omega_2+2A'')^{-1}\,.
\end{aligned} \tag{D.2}$$

In Fig. 10 and 11 the OPT-graphs are shown, which lead for $\kappa = \kappa' = 0$ to the same pair-potentials using the Klein-Macke formalism in Ref. [26, 29].

Appendix D.3. Adiabatic Approximations [16]*, "non-adiabatic": in the denominators expansion of the baryon energies in* $1/M_B$*.*

In the adiabatic approximation $A = A' = 0$. The expressions for the denominators become:

Planar-graphs:

$$\begin{aligned}
D^{(//,a)}_{\sigma;0,0}(ad) &= \frac{1}{\omega_1}\,\frac{1}{2A''}\,\frac{1}{\omega_2} \quad , \quad D^{(//,a')}_{\sigma;0,0}(ad) = \frac{1}{\omega_1}\,\frac{1}{2A''}\,\frac{1}{\omega_2},\\
D^{(//,b)}_{\sigma;0,0}(ad) &= \frac{1}{\omega_1}\,\frac{1}{\omega_1+\omega_2}\,\frac{1}{\omega_2} \quad , \quad D^{(//,b')}_{\sigma;0,0}(ad) = \frac{1}{\omega_1}\,\frac{1}{\omega_1+\omega_2}\,\frac{1}{\omega_2},\\
D^{(//,c)}_{\sigma;0,0}(ad) &= \frac{1}{\omega_1}\,\frac{1}{2A''}\,\frac{1}{\omega_2} \quad , \quad D^{(//,c')}_{\sigma;0,0}(ad) = \frac{1}{\omega_1}\,\frac{1}{2A''}\,\frac{1}{\omega_2}.
\end{aligned} \tag{D.3}$$

[16] "Adiabatic" approximation: an effective potential between the interacting particles is calculated, neglecting during the exchange of the mesons the motion of the baryons, *i.e.* baryon energy differences are put to zero, see Ref. [26].

Crossed-graphs:

$$
\begin{aligned}
D^{(X,a)}_{\sigma;0,0}(ad) &= \frac{1}{\omega_1}\,\frac{1}{\omega_1+\omega_2}\,\frac{1}{\omega_2} \quad , \quad D^{(X,a')}_{\sigma;0,0}(ad) = \frac{1}{\omega_1}\,\frac{1}{\omega_1+\omega_2}\,\frac{1}{\omega_2}, \\
D^{(X,b)}_{\sigma;0,0}(ad) &= \frac{1}{\omega_2}\,\frac{1}{\omega_1+\omega_2}\,\frac{1}{\omega_2} \quad , \quad D^{(X,b')}_{\sigma;0,0}(ad) = \frac{1}{\omega_1}\,\frac{1}{\omega_1+\omega_2}\,\frac{1}{\omega_1}, \\
D^{(X,c)}_{\sigma;0,0}(ad) &= \frac{1}{\omega_2}\,\frac{1}{\omega_1+\omega_2}\,\frac{1}{\omega_2} \quad , \quad D^{(X,c')}_{\sigma;0,0}(ad) = \frac{1}{\omega_1}\,\frac{1}{\omega_1+\omega_2}\,\frac{1}{\omega_1}.
\end{aligned}
\tag{D.4}
$$

Notice that the spinor-numerator factors for the parallel graphs are the same, and so there is the symmetry $\omega_1 \leftrightarrow \omega_2$, as can be seen from the expressions above, and similarly for the crossed graphs.

Defining $D^{(//)}_{\sigma;0,0}(ad) = \sum_{i=a,b,c,a',b',c'} D^{(//,i)}(ad)$. Similarly $D^{(X)}_{\sigma;0,0}(ad)$ for the crossed graphs. The denominator for the parallel graphs is

$$
D^{(//)}_{\sigma;0,0}(ad) \;=\; \frac{1}{\omega_1}\,\frac{4}{2A''}\,\frac{1}{\omega_2} + \frac{2}{\omega_1\omega_2}\,\frac{1}{\omega_1+\omega_2}. \tag{D.5}
$$

and for the crossed graphs

$$
D^{(X)}_{\sigma;0,0}(ad) \;=\; \frac{2}{\omega_1\omega_2}\left[1+\frac{\omega_1}{\omega_2}+\frac{\omega_2}{\omega_1}\right]\frac{1}{\omega_1+\omega_2}. \tag{D.6}
$$

Comparison: The denominators $D^{(//,a)}(ad), D^{(//,a')}(ad)$ corresponds to the so-called TMO-graphs. Subtracting the one-meson-exchange iterated graph $D^{(//,a)}(ad), D^{(//,a')}(ad) \Rightarrow 0$. This subtraction avoids *"double counting"* when used in the integral equations. Taking into account the leading non-adiabatic corrections, see for details [26], one obtains in total

$$
D^{(//,a)}_{\sigma;0,0}(ad) + D^{(//,a')}_{\sigma;0,0}(ad) \Rightarrow -\frac{1}{\omega_1\omega_2}\left(\frac{1}{\omega_1}+\frac{1}{\omega_2}\right). \tag{D.7}
$$

contributions, including the 1/M corrections from the TMO-graphs, for the planar graphs in formulas (8.1)-(9.4)

$$
D^{(//)}(ad) \;=\; \frac{1}{\omega_1\omega_2}\left[\frac{1}{\omega_1+\omega_2}-\frac{1}{\omega_1}-\frac{1}{\omega_2}\right],
$$

and for the crossed graphs in formulas (8.3)-(8.5)

$$
D^{(X)}(ad) \;=\; \frac{1}{\omega_1\omega_2}\left[\frac{1}{\omega_1}+\frac{1}{\omega_2}-\frac{1}{\omega_1+\omega_2}\right] = -D^{(//)}(ad).
$$

In Fig. 10 and 11 the OPT-graphs are shown, which lead for $\kappa = \kappa' = 0$ to the same pair-potentials using the Klein-Macke formalism in Ref. [26, 29].

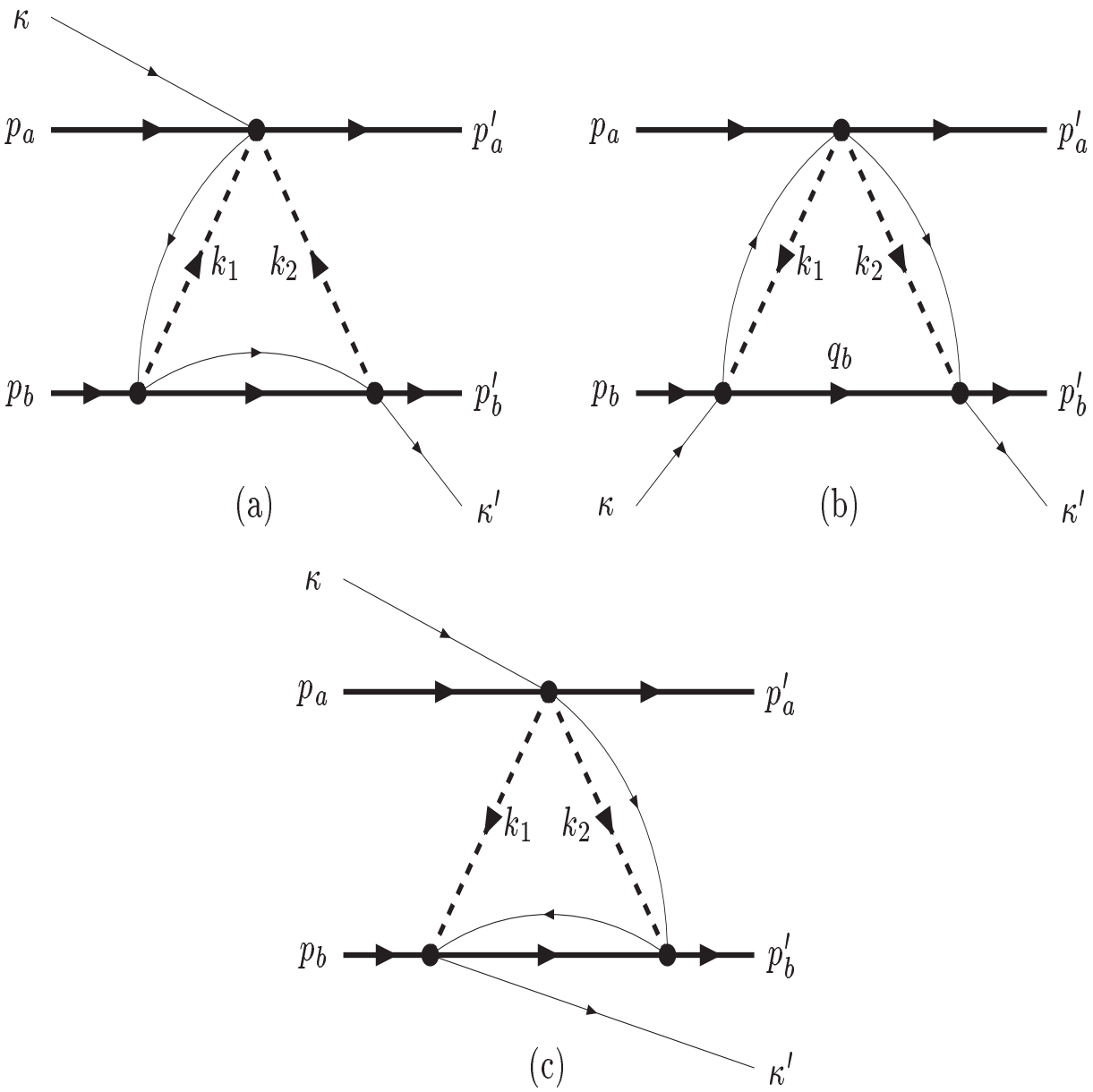

Figure D.47: *Pair Kadyshevsky graphs. The solid lines denote the nucleons, and the dashed lines the mesons. The dotted lines denote the quasi-momentum particles. In (a) and (c), the intermediate momentum is q_b as in (b).*

Appendix E. One-pair and Two-pair Kadyshevsky graphs $\sigma = [+]$

Appendix E.1. One-pair Kadyshevsky graphs $\sigma = [+]$

Graph (a) in the Kadyshevsky graphs Fig. D.47 gives for the one-pair exchange matrix element

$$
\begin{aligned}
&(2\pi)^4\delta^4\left(p'_a+p'_b+\kappa' n-p_a-p_b-\kappa n\right)\; M^{(pair,a)}_{\kappa',\kappa}=\left\{\frac{M_a^2M_b^2}{E_a(\mathbf{p}'_a)E_b(\mathbf{p}'_b)E_a(\mathbf{p}_a)E_b(\mathbf{p}_b)}\right\}^{1/2}\cdot\\
&\times\left[\bar u(p'_a)\Gamma^{(a)}_{2-pair}u(p_a)\right]\int\frac{d^4k_1}{(2\pi)^3}\int\frac{d^4k_2}{(2\pi)^3}\cdot\delta_+\left[k_1^2-m_1^2\right]\delta_+\left[k_2^2-m_2^2\right]\cdot\\
&\times\int_{-\infty}^{\infty}\frac{d\kappa_1}{2\pi}\int_{-\infty}^{\infty}\frac{d\kappa_2}{2\pi}\int_{-\infty}^{\infty}\frac{d\kappa_3}{2\pi}\frac{1}{\kappa_1-i\epsilon}\frac{1}{\kappa_2-i\epsilon}\frac{1}{\kappa_3-i\epsilon}\cdot\\
&\times\int\frac{d^4q_b}{(2\pi)^3}\,\delta_+\left[(q_b^2-M_b^2\right]\cdot\left[\bar u(p'_b)\Gamma_2^{(b)}\widetilde S_F^{(+)}(q_b)\Gamma_1^{(b)}u(p_b)\right]\cdot\\
&\times(2\pi)^4\delta^4\left(p'_a+\kappa_1 n-p_a-\kappa n-k_1-k_2\right)(2\pi)^4\delta^4\left(p'_b-\kappa_2 n+k_2-q_b+\kappa' n\right)\cdot\\
&\times(2\pi)^4\delta^4\left(q_b-\kappa_1 n-p_b+\kappa_2 n+k_1\right)
\end{aligned}
\tag{E.1}
$$

Graph (b) in the Kadyshevsky graphs Fig. D.47 gives for the one-pair exchange matrix element

$$
\begin{aligned}
&(2\pi)^4\delta^4\left(p'_a+p'_b+\kappa' n-p_a-p_b-\kappa n\right)\; M^{(pair,b)}_{\kappa',\kappa}=\left\{\frac{M_a^2M_b^2}{E_a(\mathbf{p}'_a)E_b(\mathbf{p}'_b)E_a(\mathbf{p}_a)E_b(\mathbf{p}_b)}\right\}^{1/2}\cdot\\
&\times\left[\bar u(p'_a)\Gamma^{(a)}_{2-pair}u(p_a)\right]\int\frac{d^4k_1}{(2\pi)^3}\int\frac{d^4k_2}{(2\pi)^3}\,\delta_+\left[k_1^2-m_1^2\right]\delta_+\left[k_2^2-m_2^2\right]\cdot\\
&\times\int_{-\infty}^{\infty}\frac{d\kappa_1}{2\pi}\int_{-\infty}^{\infty}\frac{d\kappa_2}{2\pi}\int_{-\infty}^{\infty}\frac{d\kappa_3}{2\pi}\frac{1}{\kappa_1-i\epsilon}\frac{1}{\kappa_2-i\epsilon}\frac{1}{\kappa_3-i\epsilon}\cdot\\
&\times\int\frac{d^4q_b}{(2\pi)^3}\,\delta_+\left[(q_b^2-M_b^2\right]\cdot\left[\bar u(p'_b)\Gamma_2^{(b)}\widetilde S_F^{(+)}(q_b)\Gamma_1^{(b)}u(p_b)\right]\cdot\\
&\times(2\pi)^4\delta^4\left(p'_a+\kappa_2 n-p_a-\kappa_1 n+k_1+k_2\right)(2\pi)^4\delta^4\left(p'_b-\kappa_2 n-q_b-k_2+\kappa' n\right)\cdot\\
&\times(2\pi)^4\delta^4\left(q_b+\kappa_1 n-p_b-k_1-\kappa n\right)
\end{aligned}
\tag{E.2}
$$

Graph (c) in the Kadyshevsky graphs Fig. D.47 gives for the one-pair exchange matrix element

$$
\begin{aligned}
&(2\pi)^4\delta^4\left(p'_a+p'_b+\kappa' n-p_a-p_b-\kappa n\right)\; M^{(pair,c)}_{\kappa',\kappa}=\left\{\frac{M_a^2M_b^2}{E_a(\mathbf{p}'_a)E_b(\mathbf{p}'_b)E_a(\mathbf{p}_a)E_b(\mathbf{p}_b)}\right\}^{1/2}\cdot\\
&\times\left[\bar u(p'_a)\Gamma^{(a)}_{2-pair}u(p_a)\right]\int\frac{d^4k_1}{(2\pi)^3}\int\frac{d^4k_2}{(2\pi)^3}\,\delta_+\left[k_1^2-m_1^2\right]\delta_+\left[k_2^2-m_2^2\right]\cdot\\
&\times\int_{-\infty}^{\infty}\frac{d\kappa_1}{2\pi}\int_{-\infty}^{\infty}\frac{d\kappa_2}{2\pi}\int_{-\infty}^{\infty}\frac{d\kappa_3}{2\pi}\frac{1}{\kappa_1-i\epsilon}\frac{1}{\kappa_2-i\epsilon}\frac{1}{\kappa_3-i\epsilon}\cdot\\
&\times\int\frac{d^4q_b}{(2\pi)^3}\,\delta_+\left[(q_b^2-M_b^2\right]\cdot\left[\bar u(p'_b)\Gamma_2^{(b)}\widetilde S_F^{(+)}(q_b)\Gamma_1^{(b)}u(p_b)\right]\cdot\\
&\times(2\pi)^4\delta^4\left(p'_a-p_a-\kappa n+\kappa_1 n+k_1+k_2\right)(2\pi)^4\delta^4\left(q_b+\kappa_2 n-p_b-\kappa_1 n+k_1\right)\cdot\\
&\times(2\pi)^4\delta^4\left(p'_b-q_b-\kappa_1 n-k_2+\kappa_2 n\right)
\end{aligned}
\tag{E.3}
$$

The result of the integration gives for graph (a)

$$M^{(pair,a)}_{\kappa',\kappa}(p'_a s'_a, p'_b s'_b; p_a s_a, p_b s_b) = \left\{ \frac{M_a^2 M_b^2}{E_a(\mathbf{p}'_a) E_b(\mathbf{p}'_b) E_a(\mathbf{p}_a) E_b(\mathbf{p}_b)} \right\}^{1/2} \left[\bar{u}(\mathbf{p}'_a, s'_a) \Gamma^{(a)}_{pair} u(\mathbf{p}_a, s_a) \right] \cdot$$
$$\times \int \frac{d^3k_1}{(2\pi)^3 2\omega_1} \int \frac{d^3k_2}{(2\pi)^3 2\omega_2} \int \frac{d^3q}{2E_b(\mathbf{q})} \delta^{(3)}(\mathbf{q} - (\mathbf{p}' + \mathbf{p} - \mathbf{k}_1 + \mathbf{k}_2)/2) \cdot$$
$$\times \left[\bar{u}(\mathbf{p}'_b, s'_b) \Gamma^{(b)}_2 (\not{q} + M_b) \Gamma^{(b)}_1 u(\mathbf{p}_b, s_b) \right] \cdot D^{(pair,a)}_{\kappa',\kappa}(\omega_1, \omega_2) \cdot$$
$$\times (2\pi)^3 \delta^{(3)}(\mathbf{p}' - \mathbf{p} + \mathbf{k}_1 + \mathbf{k}_2), \tag{E.4}$$

with $q_0 = E_b(\mathbf{q})$. Similarly for graphs (b) and (c). For the CM-amplitudes one obtains

$$D^{(pair,a)}_{\kappa',\kappa}(\omega_1, \omega_2) = + \frac{1}{\omega_1 + \omega_2 + \frac{1}{2}(\kappa' + \kappa) + \frac{1}{2}[E_b(\mathbf{p}') - E_b(\mathbf{p}) - E_a(\mathbf{p}') + E_a(\mathbf{p})] + i\epsilon} \cdot$$
$$\times \frac{1}{\omega_1 + \kappa' - E_b(\mathbf{p}) + E_b(\mathbf{q}) + i\epsilon}, \tag{E.5a}$$
$$D^{(pair,b)}_{\kappa',\kappa}(\omega_1, \omega_2) = - \frac{1}{\omega_2 - \kappa + [E_b(\mathbf{p}') - E_b(\mathbf{q})] + i\epsilon} \cdot$$
$$\times \frac{1}{\omega_1 + \frac{1}{2}(\kappa' + \kappa) + \frac{1}{2}\left[E_a(\mathbf{p}') + E_b(\mathbf{p}') - E_a(\mathbf{p}) + E_b(\mathbf{p})\right] - E_b(\mathbf{q}) + i\epsilon}, \tag{E.5b}$$
$$D^{(pair,c)}_{\kappa',\kappa}(\omega_1, \omega_2) = + \frac{1}{\omega_1 + \omega_2 + \frac{1}{2}[E_b(\mathbf{p}') - E_a(\mathbf{p}') - E_b(\mathbf{p}) + E_a(\mathbf{p})] + i\epsilon} \cdot$$
$$\times \frac{1}{\omega_2 + E_b(\mathbf{p}') - E_b(\mathbf{q}) - \kappa + i\epsilon}. \tag{E.5c}$$

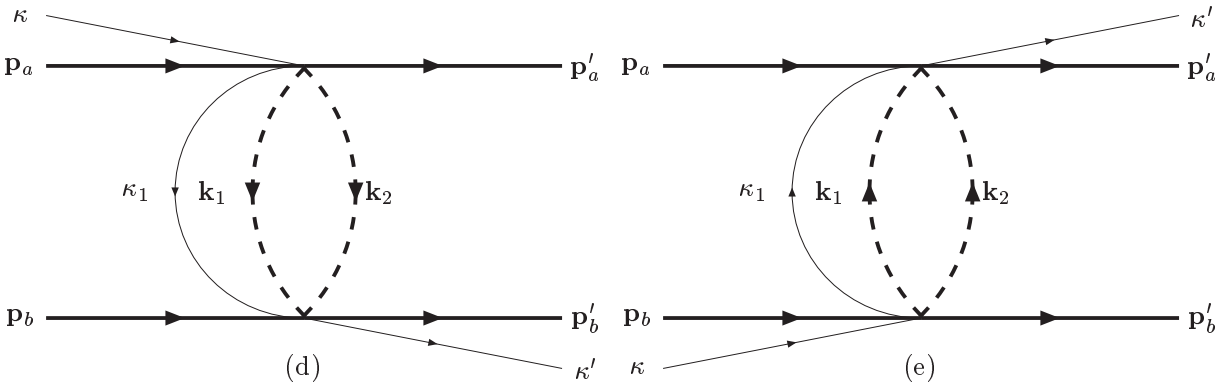

Figure E.48: *Two-pair Kadyshevsky graphs.*

Appendix E.2. Two-pair Kadyshevsky graphs

Graph (d) in the Kadyshevsky graphs Fig. E.48 gives for the two-pair exchange matrix element

$$
\begin{aligned}
&-(2\pi)^4\delta^4\left(p'_a+p'_b+\kappa' n-p_a-p_b-\kappa n\right)\; M^{(pair,d)}_{\kappa',\kappa}=\left\{\frac{M_a^2M_b^2}{E_a(\mathbf{p}'_a)E_b(\mathbf{p}'_b)E_a(\mathbf{p}_a)E_b(\mathbf{p}_b)}\right\}^{1/2}\int\frac{d^4k_1}{(2\pi)^3}\int\frac{d^4k_2}{(2\pi)^3}\;\cdot\\
&\times\delta_+\left[k_1^2-m_1^2\right]\delta_+\left[k_2^2-m_2^2\right]\cdot\int_{-\infty}^{\infty}\frac{d\kappa_1}{2\pi}\int_{-\infty}^{\infty}\frac{d\kappa_2}{2\pi}\int_{-\infty}^{\infty}\frac{d\kappa_3}{2\pi}\frac{1}{\kappa_1-i\epsilon}\frac{1}{\kappa_2-i\epsilon}\frac{1}{\kappa_3-i\epsilon}\cdot\\
&\times(2\pi)^4\delta^4\left(p'_a-p_a+\kappa_1 n-\kappa n+k_1+k_2\right)\;(2\pi)^4\delta^4\left(p'_b-p_b+\kappa' n-k_1-\kappa_1 n\right)\\
&\times\left[\bar u(p'_a)\Gamma^{(a)}_{pair}u(p_a)\right]\;\left[\bar u(p'_b)\,\Gamma^{(b)}_{pair}u(p_b)\right]
\end{aligned}
\tag{E.6}
$$

For graph (e) the two-pair matrix element is

$$
\begin{aligned}
&-(2\pi)^4\delta^4\left(p'_a+p'_b+\kappa' n-p_a-p_b-\kappa n\right)\; M^{(pair,e)}_{\kappa',\kappa}=\left\{\frac{M_a^2M_b^2}{E_a(\mathbf{p}'_a)E_b(\mathbf{p}'_b)E_a(\mathbf{p}_a)E_b(\mathbf{p}_b)}\right\}^{1/2}\int\frac{d^4k_1}{(2\pi)^3}\int\frac{d^4k_2}{(2\pi)^3}\;\cdot\\
&\times\delta_+\left[k_1^2-m_1^2\right]\delta_+\left[k_2^2-m_2^2\right]\cdot\int_{-\infty}^{\infty}\frac{d\kappa_1}{2\pi}\int_{-\infty}^{\infty}\frac{d\kappa_2}{2\pi}\int_{-\infty}^{\infty}\frac{d\kappa_3}{2\pi}\frac{1}{\kappa_1-i\epsilon}\frac{1}{\kappa_2-i\epsilon}\frac{1}{\kappa_3-i\epsilon}\cdot\\
&\times(2\pi)^4\delta^4\left(p'_a-p_a-\kappa_1 n+\kappa' n-k_1-k_2\right)\;(2\pi)^4\delta^4\left(p'_b-p_b-\kappa n+\kappa_1 n+k_1+k_2\right)\\
&\times\left[\bar u(p'_a)\Gamma^{(a)}_{pair}u(p_a)\right]\;\left[\bar u(p'_b)\,\Gamma^{(b)}_{pair}u(p_b)\right]
\end{aligned}
\tag{E.7}
$$

The result of the integration for graph (d) is

$$
\begin{aligned}
M^{(pair,d)}_{\kappa',\kappa}(p'_as'_a,p'_bs'_b;p_as_a,p_bs_b)&=\left\{\frac{M_a^2M_b^2}{E_a(\mathbf{p}'_a)E_b(\mathbf{p}'_b)E_a(\mathbf{p}_a)E_b(\mathbf{p}_b)}\right\}^{1/2}\cdot\\
&\times\int\frac{d^3k_1}{(2\pi)^32\omega_1}\int\frac{d^3k_2}{(2\pi)^32\omega_2}(2\pi)^3\delta^{(3)}(\mathbf{p}'-\mathbf{p}+\mathbf{k}_1+\mathbf{k}_2)\cdot\\
&\times\left[\bar u(\mathbf{p}'_a,s'_a)\Gamma^{(a)}_{pair}u(\mathbf{p}'_a,s'_a)\right]\cdot\left[\bar u(\mathbf{p}'_b,s'_b)\Gamma^{(b)}_{pair}u(\mathbf{p}_b,s_b)\right]\cdot D^{(pair,d)}_{\kappa',\kappa}(\omega_1,\omega_2),
\end{aligned}
\tag{E.8}
$$

and similarly for graph (e). For the CM-amplitudes one obtains

$$
D^{(pair,d)}_{\kappa',\kappa}(\omega_1,\omega_2)\;=\;+\frac{1}{\omega_1+\omega_2-\frac{1}{2}(\kappa'+\kappa)-\frac{1}{2}[E_b(\mathbf{p}')-E_a(\mathbf{p}')-E_b(\mathbf{p})+E_a(\mathbf{p})]+i\epsilon},
\tag{E.9a}
$$

$$
D^{(pair,e)}_{\kappa',\kappa}(\omega_1,\omega_2)\;=\;+\frac{1}{\omega_1+\omega_2-\frac{1}{2}(\kappa'+\kappa)-\frac{1}{2}[E_a(\mathbf{p}')-E_b(\mathbf{p}')-E_a(\mathbf{p})+E_b(\mathbf{p})]+i\epsilon}.
\tag{E.9b}
$$

Note that this also gives the constraint $E_b(\mathbf{p}')+E_a(\mathbf{p}'+\kappa' n=E_b(\mathbf{p}+E_a(\mathbf{p}+\kappa n$, which is consistent with energy conservation including κ' and κ.
In Fig. 13 the OPT-graphs are shown, which lead for $\kappa=\kappa'=0$ to the same pair-potentials using the Klein-Macke formalism in Ref. [30].

Appendix F. Exact Reduction Dirac-spinors to Pauli-spinors

The transition from Dirac spinors to Pauli spinors is given here, without approximations. The notations $\mathcal{E}=E+M$ and $\mathcal{E}'=E'+M'$, where $E=E(p,M)$ and $E'=E(p',M')$, are used. Also, omitted are, on the right-hand side in the

expressions below, the final and initial Pauli spinors $\chi'^{\dagger}$ and χ, respectively, which are self-evident. The expressions below are derived using the Dirac spinors [55]

$$u(\mathbf{p}) = \sqrt{\frac{E+M}{2M}} \begin{pmatrix} \chi \\ \frac{\sigma\cdot\mathbf{p}}{E+M}\,\chi \end{pmatrix}, \quad v(\mathbf{p}) = \sqrt{\frac{E+M}{2M}} \begin{pmatrix} \frac{\sigma\cdot\mathbf{p}}{E+M}\,\chi \\ \chi \end{pmatrix}. \tag{F.1}$$

With these Dirac spinors, the matrix elements are

$$\bar{u}(\mathbf{p}')\gamma_5 u(\mathbf{p}) = -\sqrt{\frac{\mathcal{E}'\mathcal{E}}{4M'M}}\left[\frac{\boldsymbol{\sigma}\cdot\mathbf{p}'}{\mathcal{E}'} - \frac{\boldsymbol{\sigma}\cdot\mathbf{p}}{\mathcal{E}}\right], \tag{F.2a}$$

$$\bar{u}(\mathbf{p}')\gamma_5\gamma^0 u(\mathbf{p}) = -\sqrt{\frac{\mathcal{E}'\mathcal{E}}{4M'M}}\left[\frac{\boldsymbol{\sigma}\cdot\mathbf{p}'}{\mathcal{E}'} + \frac{\boldsymbol{\sigma}\cdot\mathbf{p}}{\mathcal{E}}\right], \tag{F.2b}$$

$$\begin{aligned}\bar{u}(\mathbf{p}')\gamma_5\boldsymbol{\gamma}\, u(\mathbf{p}) &= -\sqrt{\frac{\mathcal{E}'\mathcal{E}}{4M'M}}\left[\boldsymbol{\sigma} + \frac{(\boldsymbol{\sigma}\cdot\mathbf{p}')\,\boldsymbol{\sigma}\,(\boldsymbol{\sigma}\cdot\mathbf{p})}{\mathcal{E}'\mathcal{E}}\right] \\ &= -\sqrt{\frac{\mathcal{E}'\mathcal{E}}{4M'M}}\left[\left(1 - \frac{\mathbf{p}'\cdot\mathbf{p}}{\mathcal{E}'\mathcal{E}}\right)\boldsymbol{\sigma} - i\frac{\mathbf{p}'\times\mathbf{p}}{\mathcal{E}'\mathcal{E}}\right. \\ &\quad \left. + \frac{1}{\mathcal{E}'\mathcal{E}}\left(\boldsymbol{\sigma}\cdot\mathbf{p}\,\mathbf{p}' + \boldsymbol{\sigma}\cdot\mathbf{p}'\,\mathbf{p}\right)\right] \approx -\boldsymbol{\sigma},,\end{aligned} \tag{F.2c}$$

where are defined $\mathbf{k} = \mathbf{p}' - \mathbf{p}$, $\mathbf{q} = (\mathbf{p}' + \mathbf{p})/2$.

$$\bar{v}(\mathbf{p}')\gamma_5 u(\mathbf{p}) = -\sqrt{\frac{\mathcal{E}'\mathcal{E}}{4M'M}}\left[\left(1 - \frac{\mathbf{p}'\cdot\mathbf{p}}{\mathcal{E}'\mathcal{E}}\right) - i\frac{\mathbf{p}'\times\mathbf{p}\cdot\boldsymbol{\sigma}}{\mathcal{E}'\mathcal{E}}\right], \tag{F.3a}$$

$$\bar{v}(\mathbf{p}')\gamma_5\gamma^0 u(\mathbf{p}) = +\sqrt{\frac{\mathcal{E}'\mathcal{E}}{4M'M}}\left[\left(1 + \frac{\mathbf{p}'\cdot\mathbf{p}}{\mathcal{E}'\mathcal{E}}\right) + i\frac{\mathbf{p}'\times\mathbf{p}\cdot\boldsymbol{\sigma}}{\mathcal{E}'\mathcal{E}}\right], \tag{F.3b}$$

$$\bar{v}(\mathbf{p}')\gamma_5\boldsymbol{\gamma}\, u(\mathbf{p}) = +\sqrt{\frac{\mathcal{E}'\mathcal{E}}{4M'M}}\left[\left(\frac{\mathbf{p}'}{\mathcal{E}'} + \frac{\mathbf{p}}{\mathcal{E}}\right) + i\left(\frac{\boldsymbol{\sigma}\times\mathbf{p}'}{\mathcal{E}'} - \frac{\boldsymbol{\sigma}\times\mathbf{p}}{\mathcal{E}}\right)\right], \tag{F.3c}$$

and for the $\bar{u}\Gamma v$ one can use the identity $\bar{u}(\mathbf{p}')\Gamma\, v(\mathbf{p}) = \bar{v}(\mathbf{p})\,[\gamma_0\Gamma^{\dagger}\,\gamma_0]\,u(\mathbf{p}')$ [17].

Appendix G. OBE-Potentials in ESC16

The OBE-potentials in ESC16 are those contained already in ESC04 [2, 3], and some new additional contributions. The additions to the OBE-potentials w.r.t. the ESC04-models consist of the following elements: (i) extension of the baryon-baryon-meson vertex of the axial-vector mesons ($J^{PC} = 1^{++}$) by adding the derivative coupling, (ii) inclusion of the axial-vector mesons of the 2nd kind, having $J^{PC} = 1^{+-}$. In Ref. [5], the potentials for non-strange meson exchange have been given. Here, are listed the additions and the basic potentials for meson exchange with non-zero strangeness.

Appendix G.1. Additions to the OBE-Potentials in ESC16

The interaction Hamiltonian densities for the new couplings are

[17] Note the relations $v(\mathbf{p}) = \gamma_5\, u(\mathbf{p})$ and $\bar{v}(\mathbf{p}) = -\bar{u}(\mathbf{p})\gamma_5$, which explains the connections between the (F.2c) and (F.3c) expressions.

a) Axial-vector-meson exchange ($J^{PC} = 1^{++}$, 1^{st} kind):

$$\mathcal{H}_A = g_A[\bar{\psi}\gamma_\mu\gamma_5\psi]\phi_A^\mu + \frac{if_A}{\mathcal{M}}[\bar{\psi}\gamma_5\psi]\,\partial_\mu\phi_A^\mu. \tag{G.1}$$

In ESC04 the g_A-coupling was included, but not the derivative f_A-coupling.

b) Axial-vector-meson exchange ($J^{PC} = 1^{+-}$, 2^{nd} kind):

$$\mathcal{H}_B = \frac{if_B}{m_B}[\bar{\psi}\sigma_{\mu\nu}\gamma_5\psi]\,\partial_\nu\phi_B^\mu, \tag{G.2}$$

where m_B is the mass $b_1(1235)$. In ESC04 this coupling was not included. Like for the axial-vector mesons of the 1^{st}-kind included is an SU(3)-nonet with members $b_1(1235), h_1(1170), h_1'(1380)$. In the quark-model they are $Q\bar{Q}(^1P_1)$-states.

The inclusion of the Gaussian form factors is discussed in previous papers [34] and reviewed in [5]. For the approximations made in deriving the potentials from the relativistic Born-Approximation, see also Ref. [5]. Due to these approximations, the dependence on $\mathbf{q}^2$ is linearized, and one can write

$$V_i(\mathbf{k}^2, \mathbf{q}^2) = V_{ia}(\mathbf{k}^2) + V_{ib}(\mathbf{k}^2)\left(\mathbf{q}^2 + \frac{1}{4}\mathbf{k}^2\right), \tag{G.3}$$

where $i = 1 - 8$. The combination $(\mathbf{q}^2 + \mathbf{k}^2/4)$ leads to a purely non-local potential. The additional OBE-potentials are obtained in the standard way, see [33, 34]. The potential functions V_i of (G.3) are written in the form

$$V_i(\mathbf{k}^2, \mathbf{q}^2) = \sum_X \Omega_i^{(X)}(\mathbf{k}^2)\cdot\Delta^{(X)}(\mathbf{k}^2, m^2, \Lambda^2), \tag{G.4}$$

where m denotes the mass of the meson, Λ the cut-off in the gaussian form factor, and $X = P, V, S, A, B$, and D (P= pseudoscalar, V= vector, S= scalar, A= axial-vector, B= axial-vector, and D = Pomeron/Odderon). For meson-exchange the propagator $\Delta^{(X)}$-function is

$$\Delta^{(X)}(\mathbf{k}^2, m^2, \Lambda^2) = e^{-\mathbf{k}^2/\Lambda^2}/(\mathbf{k}^2 + m^2). \tag{G.5}$$

For X=S,A, included in the propagator is a zero by the factor $(1 - \mathbf{k}^2/U^2)$, with U=750 MeV [2, 3]. In the case X=D the propagator is replaced by

$$\Delta^{(D)}(\mathbf{k}^2, m^2, \Lambda^2) = \frac{1}{\mathcal{M}^2}e^{-\mathbf{k}^2/4m_D^2}. \tag{G.6}$$

Here, $\mathcal{M}$ is a universal scaling mass, taken to be the proton mass, which is also used in the derivative couplings above, as well as in the f_V- and f_A-coupling of the vector-mesons.

Appendix G.2. Meson-exchange with Non-zero Strangeness ($\Delta Y \neq 0$)

For the non-strange mesons, the mass differences at the vertices are neglected, taken at the YYM- and the NNM-vertex is the average hyperon and the average nucleon mass, respectively. This implies that the contributions to the Pauli-invariants P_7 and P_8 are not included. (See Ref. [57] for the definition of $P_i, i = 1, 8$). These exchanges lead to the so-called 'exchange-potentials'. For the invariants $O_1, \ldots, O_6$, see [57], the expressions analogous to those for the non-strange mesons given above apply. This, with the amendments that (i) in momentum and configuration space, there is a complete symmetric appearance of M_Y and M_N, (ii) in configuration space there appears the baryon-exchange operator $\mathcal{P} = -\mathcal{P}_x\,\mathcal{P}_\sigma$ operator, and (iii) for the anti-symmetric spin-orbit potential $\mathcal{P} \to \mathcal{P}_x$. Here, $\mathcal{P}_x$ and $\mathcal{P}_\sigma$ are the space-exchange and spin-exchange operators, respectvely. The details are given in Appendix K. Therefore, the $\Omega_i^{(X)}$ for these potentials can be obtained from those given in ref. [5] Eqs. (4.14)-(4.18), by replacing both M_Y and M_N by $(M_Y M_N)^{1/2}$. Furthermore, in the case of the vector and axial-B mesons the Proca-formalism [28, 228] is used,

which gives for the vector mesons non-negligible contributions from the second part of the vector-meson propagator $(k_\mu k_\nu/m^2)$ of the K^* meson:

$$-V_i^{K^*} = V_i^{(V)} - \frac{(M_3 - M_1)(M_4 - M_2)}{m^2}\, V_i^{(S)}, \tag{G.7}$$

where in $V_i^{(S)}$ the vector-meson-couplings have to be used, and M_Y and M_N must be replaced by $(M_Y M_N)^{1/2}$. In Eq. (G.7) $M_1 = M_4 = M_Y$ and $M_2 = M_3 = M_N$. For the axial-A mesons, the B-field formalism is exploited, see [5] Appendix A, and there is no second term in the propagator.

For the mesons with non-zero strangeness, K, K^*, κ, K_A and K_B, the mass differences at the vertices are not neglected, they are taken into account at the YNM-vertices the differences between the average hyperon and the average nucleon mass. This implies that included are contributions to the Pauli-invariants P_8. There are not contributions to P_7. Furthermore, mass differences in the YN-propagation are included via meson mass corrections in the strange-meson propagators.

(a) Pseudoscalar K-meson exchange:

$$\Omega_{2a}^{(P)} = -f_{13}^P f_{24}^P \left(\frac{\mathbf{k}^2}{3m_{\pi^+}^2}\right), \quad \Omega_{3a}^{(P)} = -f_{13}^P f_{24}^P \left(\frac{1}{m_{\pi^+}^2}\right), \tag{G.8a}$$

$$\Omega_{2b}^{(P)} = +f_{13}^P f_{24}^P \left(\frac{\mathbf{k}^2}{6m_{\pi^+}^2}\right), \quad \Omega_{3b}^{(P)} = +f_{13}^P f_{24}^P \left(\frac{1}{2m_{\pi^+}^2 M_Y M_N}\right). \tag{G.8b}$$

(b) Vector-meson K^*-exchange:

$$\begin{aligned}
\Omega_{1a}^{(V)} &= \left\{ g_{13}^V g_{24}^V \left(1 - \frac{\mathbf{k}^2}{2M_Y M_N}\right) - \left(g_{13}^V f_{24}^V + f_{13}^V g_{24}^V\right) \frac{\mathbf{k}^2}{4\mathcal{M}\sqrt{M_Y M_N}} \right. \\
&\quad \left. + f_{13}^V f_{24}^V \frac{\mathbf{k}^4}{16\mathcal{M}^2 M_Y M_N} \right\}, \quad \Omega_{1b}^{(V)} = g_{13}^V g_{24}^V \left(\frac{3}{2M_Y M_N}\right), \\
\Omega_{2a}^{(V)} &= -\frac{2}{3}\mathbf{k}^2\, \Omega_{3a}^{(V)}, \quad \Omega_{2b}^{(V)} = -\frac{2}{3}\mathbf{k}^2\, \Omega_{3b}^{(V)} \\
\Omega_{3a}^{(V)} &= \left\{ (g_{13}^V g_{24}^V + \left(g_{13}^V f_{24}^V + g_{24}^V f_{13}^V\right) \frac{\sqrt{M_Y M_N}}{\mathcal{M}}) - f_{13}^V f_{24}^V \frac{\mathbf{k}^2}{8\mathcal{M}^2} \right\} /(4M_Y M_N) \\
\Omega_{3b}^{(V)} &= -\left(g_{13}^V + f_{13}^V \frac{M_Y}{\mathcal{M}}\right)\left(g_{24}^V + f_{24}^V \frac{M_N}{\mathcal{M}}\right) /(8M_Y^2 M_N^2), \\
\Omega_4^{(V)} &= -\left\{ 12 g_{13}^V g_{24}^V + 8(g_{13}^V f_{24}^V + f_{13}^V g_{24}^V) \frac{\sqrt{M_Y M_N}}{\mathcal{M}} - f_{13}^V f_{24}^V \frac{3\mathbf{k}^2}{\mathcal{M}^2} \right\} /(8M_Y M_N) \\
\Omega_5^{(V)} &= -\left\{ g_{13}^V g_{24}^V + 4(g_{13}^V f_{24}^V + f_{13}^V g_{24}^V) \frac{\sqrt{M_Y M_N}}{\mathcal{M}} + 8 f_{13}^V f_{24}^V \frac{M_Y M_N}{\mathcal{M}^2} \right\} /(16 M_Y^2 M_N^2) \\
\Omega_6^{(V)} &= -\left\{ (g_{13}^V f_{24}^V - f_{13}^V g_{24}^V) \frac{1}{\sqrt{\mathcal{M}^2 M_Y M_N}} \right\}.
\end{aligned} \tag{G.9}$$

(c) Scalar-meson κ-exchange:

$$\begin{aligned}
\Omega_{1a}^{(S)} &= -g_{13}^S g_{24}^S \left(1 + \frac{\mathbf{k}^2}{4M_Y M_N}\right), \ \Omega_{1b}^{(S)} = +g_{13}^S g_{24}^S \frac{1}{2M_Y M_N}, \\
\Omega_4^{(S)} &= -g_{13}^S g_{24}^S \frac{1}{2M_Y M_N}, \ \Omega_5^{(S)} = g_{13}^S g_{24}^S \frac{1}{16 M_Y^2 M_N^2}, \ \Omega_6^{(S)} = 0.
\end{aligned} \tag{G.10}$$

(d) Axial-vector K_{1A}-exchange $J^{PC} = 1^{++}$:

$$\begin{aligned}
\Omega_2^{(A)} &= -g_{13}^A g_{24}^A \left[1 - \frac{2\mathbf{k}^2}{3M_Y M_N}\right] + \left[\left(g_{13}^A f_{24}^A + f_{13}^A g_{24}^A\right)\frac{\sqrt{M_Y M_N}}{\mathcal{M}} - f_{13}^A f_{24}^A \frac{\mathbf{k}^2}{2\mathcal{M}^2}\right]\frac{\mathbf{k}^2}{6M_Y M_N} \\
\Omega_{2b}^{(A)} &= -g_{13}^A g_{24}^A \left(\frac{3}{2M_Y M_N}\right) \\
\Omega_3^{(A)} &= -g_{13}^A g_{24}^A \left[\frac{1}{4M_Y M_N}\right] + \left[\left(g_{13}^A f_{24}^A + f_{13}^A g_{24}^A\right)\frac{\sqrt{M_Y M_N}}{\mathcal{M}} - f_{13}^A f_{24}^A \frac{\mathbf{k}^2}{2\mathcal{M}^2}\right]\frac{1}{2M_Y M_N} \\
\Omega_4^{(A)} &= -g_{13}^A g_{24}^A \left[\frac{1}{2M_Y M_N}\right] \;,\; \Omega_5^{(A)'} = -g_{13}^A g_{24}^A \left[\frac{2}{M_Y M_N}\right] \;,\; \Omega_6^{(A)} = 0.
\end{aligned} \tag{G.11}$$

Here, is used the B-field description with $\alpha_r = 1$, see [5], Appendix A. The detailed treatment of the potential proportional to P'_5, i.e. with $\Omega_5^{(A)'}$, is given in [5], Appendix B.

(e) Axial-vector K_{1B}-exchange $J^{PC} = 1^{+-}$:

$$\begin{aligned}
\Omega_{2a}^{(B)} &= +f_{13}^B f_{24}^B \frac{4M_N M_Y}{m_B^2}\left(1 - \frac{\mathbf{k}^2}{4M_Y M_N}\right)\left(\frac{\mathbf{k}^2}{12M_Y M_N}\right),\; \Omega_{2b}^{(B)} = +f_{13}^B f_{24}^B \frac{4M_N M_Y}{m_B^2}\left(\frac{\mathbf{k}^2}{8M_Y^2 M_N^2}\right) \\
\Omega_{3a}^{(B)} &= +f_{13}^B f_{24}^B \frac{4M_N M_Y}{m_B^2}\left(1 - \frac{\mathbf{k}^2}{4M_Y M_N}\right)\left(\frac{1}{4M_Y M_N}\right),\; \Omega_{3b}^{(B)} = +f_{13}^B f_{24}^B \frac{4M_N M_Y}{m_B^2}\left(\frac{3}{8M_Y^2 M_N^2}\right),
\end{aligned} \tag{G.12}$$

As in Ref. [34] in the derivation of the expressions for $\Omega_i^{(X)}$, given above, M_Y and M_N denote the mean hyperon and nucleon mass, respectively $M_Y = (M_1 + M_3)/2$ and $M_N = (M_2 + M_4)/2$, and m denotes the mass of the exchanged meson. Moreover, the approximation $1/M_N^2 + 1/M_Y^2 \approx 2/(M_N M_Y)$, is used, which is rather good since the mass differences between the baryons are not large.

Appendix G.3. One-Boson-Exchange Interactions in Configuration Space I

In configuration space, the *BB*-interactions are described by potentials of the general form, see *e.g.* Ref. [13],

$$\begin{aligned}
V &= \Big\{V_C(r) + V_\sigma(r)\boldsymbol{\sigma}_1\cdot\boldsymbol{\sigma}_2 + V_T(r)S_{12} + V_{SO}(r)\mathbf{L}\cdot\mathbf{S} + V_Q(r)Q_{12} \\
&\quad + V_{ASO}(r)\,\frac{1}{2}(\boldsymbol{\sigma}_1 - \boldsymbol{\sigma}_2)\cdot\mathbf{L} - \frac{1}{2M_Y M_N}\left(\boldsymbol{\nabla}^2 V^{n.l.}(r) + V^{n.l.}(r)\boldsymbol{\nabla}^2\right)\Big\}\cdot\mathcal{P}, \qquad \text{(G.13a)} \\
V^{n.l.} &= \Big\{\varphi_C(r) + \varphi_\sigma(r)\boldsymbol{\sigma}_1\cdot\boldsymbol{\sigma}_2 + \varphi_T(r)S_{12}\Big\}, \qquad \text{(G.13b)}
\end{aligned}$$

where *n.l.* stands for non-local, and

$$\begin{aligned}
S_{12} &= 3(\boldsymbol{\sigma}_1\cdot\hat{r})(\boldsymbol{\sigma}_2\cdot\hat{r}) - (\boldsymbol{\sigma}_1\cdot\boldsymbol{\sigma}_2), \qquad \text{(G.14a)} \\
Q_{12} &= \frac{1}{2}\Big[(\boldsymbol{\sigma}_1\cdot\mathbf{L})(\boldsymbol{\sigma}_2\cdot\mathbf{L}) + (\boldsymbol{\sigma}_2\cdot\mathbf{L})(\boldsymbol{\sigma}_1\cdot\mathbf{L})\Big], \qquad \text{(G.14b)}
\end{aligned}$$

The exchange operator $\mathcal{P} = 1$ for hypercharge Y zero exchange and $\mathcal{P} = -\mathcal{P}_x\mathcal{P}_\sigma$. Here, $\mathcal{P}_x$ and $\mathcal{P}_\sigma$ are the space- and spin-exchange operators, respectively. For the basic functions for the Fourier transforms with Gaussian form factors, see Refs. [33, 34]. For the details of the Fourier transform for the potentials with P'_5, which occur in the case of the axial-vector mesons with $J^{PC} = 1^{++}$, see [5], Appendix B.

(a) Pseudoscalar-meson K-exchange:

$$\begin{aligned}
V_{PS}(r) &= \frac{m}{4\pi}\left[f_{13}^P f_{24}^P\left(\frac{m^2}{m_{\pi^+}^2}\right)\left(\frac{1}{3}(\boldsymbol{\sigma}_1\cdot\boldsymbol{\sigma}_2)\,\phi_C^1 + S_{12}\phi_T^0\right)\right]\mathcal{P}, \qquad \text{(G.15a)} \\
V_{PS}^{n.l.}(r) &= -\frac{m}{4\pi}\left[f_{13}^P f_{24}^P\left(\frac{m^2}{2m_{\pi^+}^2}\right)\left(\frac{1}{3}(\boldsymbol{\sigma}_1\cdot\boldsymbol{\sigma}_2)\,\phi_C^1 + S_{12}\phi_T^0\right)\right]\mathcal{P}. \qquad \text{(G.15b)}
\end{aligned}$$

(b) Vector-meson K^*-exchange:

$$
\begin{aligned}
V_V(r) = \frac{m}{4\pi}\Bigg[&\left\{g_{13}^V g_{24}^V\left[\phi_C^0+\frac{m^2}{2M_YM_N}\phi_C^1\right]\right.\\
&\left.+\left(g_{13}^V f_{24}^V+f_{13}^V g_{24}^V\right)\frac{m^2}{4\mathcal{M}\sqrt{M_YM_N}}\,\phi_C^1+f_{13}^V f_{24}^V\frac{m^4}{16\mathcal{M}^2M_YM_N}\phi_C^2\right\}\\
&+\frac{m^2}{6M_YM_N}\left\{\left[g_{13}^V g_{24}^V+\left(g_{13}^V f_{13}^V+g_{24}^V f_{13}^V\right)\frac{\sqrt{M_YM_N}}{\mathcal{M}}+f_{13}^V f_{24}^V\frac{M_YM_N}{\mathcal{M}^2}\right]\phi_C^1+f_{13}^V f_{24}^V\frac{m^2}{8\mathcal{M}^2}\phi_C^2\right\}(\boldsymbol{\sigma}_1\cdot\boldsymbol{\sigma}_2)\\
&-\frac{m^2}{4M_YM_N}\left\{\left[g_{13}^V g_{24}^V+\left(g_{13}^V f_{24}^V+g_{24}^V f_{13}^V\right)\frac{\sqrt{M_YM_N}}{\mathcal{M}}\right)\phi_T^0+f_{13}^V f_{24}^V\frac{m^2}{8\mathcal{M}^2}\phi_T^1\right\}S_{12}\\
&-\frac{m^2}{M_YM_N}\left\{\left[\frac{3}{2}g_{13}^V g_{24}^V+\left(g_{13}^V f_{24}^V+f_{13}^V g_{24}^V\right)\frac{\sqrt{M_YM_N}}{\mathcal{M}}\right]\phi_{SO}^0+\frac{3}{8}f_{13}^V f_{24}^V\frac{m^2}{\mathcal{M}^2}\phi_{SO}^1\right\}\mathbf{L}\cdot\mathbf{S}\\
&+\frac{m^4}{16M_Y^2M_N^2}\left\{\left[g_{13}^V g_{24}^V+4\left(g_{13}^V f_{24}^V+f_{13}^V g_{24}^V\right)\frac{\sqrt{M_YM_N}}{\mathcal{M}}+8f_{13}^V f_{24}^V\frac{M_YM_N}{\mathcal{M}^2}\right]\right\}\cdot\\
&\times\frac{3}{(mr)^2}\phi_T^0Q_{12}+\frac{m^2}{M_YM_N}\left\{\left(g_{13}^V f_{24}^V-f_{13}^V g_{24}^V\right)\frac{\sqrt{M_YM_N}}{\mathcal{M}}\,\phi_{SO}^0\right\}\cdot\frac{1}{2}\,(\boldsymbol{\sigma}_1-\boldsymbol{\sigma}_2)\cdot\mathbf{L}\,\mathcal{P}_\sigma\Bigg]\,\mathcal{P},
\end{aligned}
\tag{G.16a}
$$

$$
\begin{aligned}
V_V^{n.l.}(r) = \frac{m}{4\pi}\Bigg[&\frac{3}{2}g_{13}^V g_{24}^V\phi_C^0+\frac{m^2}{6M_YM_N}\left\{\left[\left(g_{13}^V+f_{13}^V\frac{\sqrt{M_YM_N}}{\mathcal{M}}\right)\left(g_{24}^V+f_{24}^V\frac{\sqrt{M_YM_N}}{\mathcal{M}}\right)\right]\phi_C^1\right\}\,(\boldsymbol{\sigma}_1\cdot\boldsymbol{\sigma}_2)\\
&-\frac{m^2}{4M_YM_N}\left\{\left[\left(g_{13}^V+f_{13}^V\frac{\sqrt{M_YM_N}}{\mathcal{M}}\right)\left(g_{24}^V+f_{24}^V\frac{\sqrt{M_YM_N}}{\mathcal{M}}\right)\right]\phi_T^0\right\}\,S_{12}\Bigg].
\end{aligned}
\tag{G.16b}
$$

(c) Scalar-meson κ-exchange:

$$
V_S(r) = -\frac{m}{4\pi}\left[g_{13}^S g_{24}^S\left\{\left[\phi_C^0-\frac{m^2}{4M_YM_N}\phi_C^1\right]+\frac{m^2}{2M_YM_N}\phi_{SO}^0\,\mathbf{L}\cdot\mathbf{S}+\frac{m^4}{16M_Y^2M_N^2}\frac{3}{(mr)^2}\phi_T^0Q_{12}\right\}\right]\mathcal{P},
\tag{G.17a}
$$

$$
V_S^{n.l.}(r) = \frac{m}{4\pi}\left[\frac{1}{2}g_{13}^S g_{24}^S\phi_C^0\right]\mathcal{P}.
\tag{G.17b}
$$

(d) Axial-vector K_{1A}-meson exchange $J^{PC}=1^{++}$:

$$
\begin{aligned}
V_A(r) = -\frac{m}{4\pi}\Bigg[&\left\{g_{13}^A g_{24}^A\left(\phi_C^0+\frac{2m^2}{3M_YM_N}\phi_C^1\right)+\frac{m^2}{6M_YM_N}\left(g_{13}^A f_{24}^A+f_{13}^A g_{24}^A\right)\frac{\sqrt{M_YM_N}}{\mathcal{M}}\phi_C^1\right.\\
&\left.+f_{13}^A f_{24}^A\frac{m^4}{12M_YM_N\mathcal{M}^2}\phi_C^2\right\}(\boldsymbol{\sigma}_1\cdot\boldsymbol{\sigma}_2)\\
&-\frac{m^2}{4M_YM_N}\left\{\left[g_{13}^A g_{24}^A-2\left(g_{13}^A f_{24}^A+f_{13}^A g_{24}^A\right)\frac{\sqrt{M_YM_N}}{\mathcal{M}}\right]\phi_T^0-f_{13}^A f_{24}^A\frac{m^2}{2\mathcal{M}^2}\phi_T^1\right\}S_{12}\\
&+\frac{m^2}{2M_YM_N}g_{13}^A g_{24}^A\phi_{SO}^0\,\mathbf{L}\cdot\mathbf{S}\Bigg]\,\mathcal{P},
\end{aligned}
\tag{G.18a}
$$

$$
V_A^{n.l.}(r) = -\frac{m}{4\pi}\left[\frac{3}{2}g_{13}^A g_{24}^A\phi_C^0(\boldsymbol{\sigma}_1\cdot\boldsymbol{\sigma}_2)\right]\mathcal{P}.
\tag{G.18b}
$$

(e) Axial-vector K_{1B}-meson exchange $J^{PC}=1^{+-}$:

$$
\begin{aligned}
V_B(r) = -\frac{m}{4\pi}\frac{4M_NM_Y}{m^2}\Bigg[&f_{13}^B f_{24}^B\left\{\frac{m^2}{12M_YM_N}\left(\phi_C^1+\frac{m^2}{4M_YM_N}\phi_C^2\right)\boldsymbol{\sigma}_1\cdot\boldsymbol{\sigma}_2\right.\\
&\left.+\frac{m^2}{4M_YM_N}\left(\phi_T^0+\frac{m^2}{4M_YM_N}\phi_T^1\right)S_{12}\right\}\Bigg]\,\mathcal{P},
\end{aligned}
\tag{G.19}
$$

$$
V_B^{n.l.}(r) = -\frac{m}{4\pi}\frac{3M_NM_Y}{2m^2}\left[f_{13}^B f_{24}^B\left(\frac{1}{3}(\boldsymbol{\sigma}_1\cdot\boldsymbol{\sigma}_2)\,\phi_C^1+S_{12}\phi_T^0\right)\right]\mathcal{P}.
\tag{G.20}
$$

(f) Diffractive-exchange: Since in the ESC16-model the diffractive Pomeron and Odderon exchanges are SU(3) singlets, there are no contributions to $S \neq 0$-exchange potentials.

Above, in Eq.'s (G.15-G.20) the exchange operator is defined as

$$\mathcal{P} = -\mathcal{P}_x \mathcal{P}_\sigma, \tag{G.21}$$

where $\mathcal{P}_x$ and $\mathcal{P}_\sigma$ are the space- and spin-exchange operators respectively. The extra $(-\mathcal{P}_\sigma)$-operator in (G.16) for the anti-symmetric spin-orbit potential is explained in Appendix K. Notice that $-\mathcal{P}_\sigma \mathcal{P} = \mathcal{P}_x$, which is well defined for the coupled singlet-triplet systems.

Appendix G.4. One-Boson-Exchange Interactions in Configuration Space II

The extra potentials, due to the zeros in the scalar and axial-A vector form factors, are:

a) Scalar-mesons:

$$\Delta V_S(r) = -\frac{m}{4\pi}\frac{m^2}{U^2}\left[g^S_{13}g^S_{24}\left\{\left[\phi^1_C - \frac{m^2}{4M_Y M_N}\phi^2_C\right] + \frac{m^2}{2M_Y M_N}\phi^1_{SO}\,\mathbf{L}\cdot\mathbf{S} + \frac{m^4}{16M_Y^2 M_N^2}\phi^1_T\, Q_{12}\right\}\right]\mathcal{P}. \tag{G.22}$$

b) Axial-mesons: The extra contribution to the potentials comes from the zero in the axial-vector meson form factor are obtained from the expression (G.11) by making substitutions as follows

$$\Delta V_A^{(1)}(r) = V_A^{(1)}\left(\phi^0_C \to \phi^1_C, \phi^0_T \to \phi^1_T, \phi^0_{SO} \to \phi^1_{SO}\right)\cdot\frac{m^2}{U^2}\,. \tag{G.23}$$

Note that the similar $\Delta V_A^{(2)}(r)$ are not included, since they involve $\mathbf{k}^4$-terms in momentum-space. Then,

$$\begin{aligned} V_A^{(1)}(r) = -\frac{g^A_{13}g^A_{24}}{4\pi}\, m\Bigg[&\phi^0_C\,(\boldsymbol{\sigma}_1\cdot\boldsymbol{\sigma}_2) - \frac{1}{12M_Y M_N}\left(\nabla^2\phi^0_C + \phi^0_C\nabla^2\right)(\boldsymbol{\sigma}_1\cdot\boldsymbol{\sigma}_2) \\ &+\frac{3m^2}{4M_Y M_N}\,\phi^0_T\, S_{12} + \frac{m^2}{2M_Y M_N}\,\phi^0_{SO}\,\mathbf{L}\cdot\mathbf{S} \\ &+\frac{m^2}{4M_Y M_N}\frac{M_N^2 - M_Y^2}{M_Y M_N}\,\phi^{(0)}_{SO}\cdot\frac{1}{2}(\boldsymbol{\sigma}_1 - \boldsymbol{\sigma}_2)\cdot\mathbf{L}\Bigg]\,\mathcal{P}. \end{aligned} \tag{G.24}$$

Appendix H. ESC-couplings and the QPC-model

In the ESC-model for baryon-baryon, the meson-baryon couplings are in principle only restricted by the requirements of relativistic covariance, time-reversal and parity. However, dynamical input based on e.g. QCD, the QM, chiral-symmetry, and flavor SU(3), is essential in order to be able to link the NN-, YN-, and YY-systems. It appeared that in the ESC-model the $^3P_0$ quark-antiquark pair-creation model [45, 46] leads to a scheme for the meson-baryon-baryon couplings which is very similar to that found in the fits of the ESC-model [2, 3]. The couplings found in the ESC16-model fit very well in the $(^3P_0 + ^3S_1)$-scheme with a ratio $^3P_0/^3S_1 = 2:1$.

Appendix H.1. QPC-model Coupling Non-strange Mesons

According to the Quark-Pair-Creation (QPC) model, in the $^3P_0$-version [45, 46], the baryon-baryon-meson couplings are given in terms of the quark-pair creation constant γ_M, and the radii of the (constituent) Gaussian quark wave functions, by [46, 229]

$$g_{BBM}(\pm) = \gamma_M\,\frac{3}{\sqrt{2}}\,\pi^{-3/4}\,X_M\,(I_M, L_M, S_M, J_M)\;F_M^{(\pm)}\,, \tag{H.1}$$

where $\pm = -(-)^{L_f}$ with L_f is the orbital angular momentum of the final BM-state, $X_M(\ldots)$ is an isospin, spin, etc. recoupling coefficient, and

$$\begin{aligned} F^{(+)} &= \frac{3}{2}\ (m_M R_M)^{+1/2}\ (\Lambda_{QPC} R_M)^{-2}, \\ F^{(-)} &= \frac{3}{2}\ (m_M R_M)^{-1/2}\ (\Lambda_{QPC} R_M)^{-2} \cdot 3\sqrt{2}(M_M/M_B). \end{aligned} \tag{H.2}$$

are coming from the overlap integrals, calculated with a Gaussian cut-off Λ_{QPC} for the quark-pair coupling to the constituent quark in the baryon, see Ref. [5]. Here, the superscripts $\mp$ refer to the parity of the mesons M: $(-)$ for $J^{PC} = 0^{+-}, 1^{--}$, and $(+)$ for $J^{PC} = 0^{++}, 1^{++}$. The radii of the baryons, in this case nucleons, and the mesons are respectively denoted by R_B and R_M.

The QPC($^3P_0$) model gives several interesting relations, such as $g_\omega = 3g_\rho, g_\epsilon = 3g_{a_0}$, and $g_{a_0} \approx g_\rho, g_\epsilon \approx g_\omega$. These relations can be seen most easily by applying the Fierz transformation to the $^3P_0$-pair-creation Hamiltonian, see Appendix D.

From $\rho \to e^+e^-$, employing the current-field-identities (C.F.I's) one can derive, see for example [230], the following relation with the QPC-model

$$f_\rho = \frac{m_\rho^{3/2}}{\sqrt{2}|\psi_\rho(0)|} \Leftrightarrow \gamma\left(\frac{2}{3\pi}\right)^{1/2} \frac{m_\rho^{3/2}}{|'\psi_\rho(0)'|}, \tag{H.3}$$

which, neglecting the difference between the wave functions on the left and right-hand side, gives the pair creation constant $\gamma \to \gamma_0 = \frac{1}{2}\sqrt{3\pi} = 1.535$. However, in the QPC-model Gaussian harmonic oscillator wave functions are used, which does not account for the $1/r$-behavior, due to one-gluon exchange (OGE), at short distances. This is corrected by applying an OG-correction [231] to the wave function, which gives for γ [232]

$$\gamma = \gamma_0 \left(1 - \frac{16}{3}\frac{\alpha(m_M)}{\pi}\right)^{-1/2} . \tag{H.4}$$

In Table H.38 $\gamma(\mu)$ is shown, Using from [233] the parameterization

$$\alpha_s(\mu) = 4\pi/\left(\beta_0 \ln(\mu^2/\Lambda_{QCD}^2)\right) , \tag{H.5}$$

with $\Lambda_{QCD} = 100$ MeV and $\beta_0 = 11 - \frac{2}{3}n_f$ for $n_f = 3$, and taking the typical scale $m_M \approx 1$ GeV, the above formula gives

Table H.38: Pair-creation constant γ as a function of μ.

μ [GeV]	$\alpha_s(\mu)$	$\gamma(\mu)$
∞	0.00	1.535
80.0	0.10	1.685
35.0	0.20	1.889
1.05	0.30	2.191
0.55	0.40	2.710
0.40	0.50	3.94
0.35	0.55	5.96

$\gamma_M = 2.19$. This value will use later, when comparing the QPC-model predictions and the ESC16-model coupling constants.

The formulas (H.2) are valid for the simplest QPC model. For a realistic description of the coupling constants of the ESC16 model, two extensions are introduced: (i) inclusion of both the $^3P_0$- and the $^3S_1$-mechanism, (ii) inclusion of SU(6)-breaking. For details, see [234]. For the latter, used are the (56) and (70) SU(6)-irrep mixing [229], and a short-distance quark-gluon form factor. In Table H.39 shown are the $^3P_0 - ^3S_1$-model results and the values obtained in the ESC16-fit. In this table, fixed is $\gamma_M = 2.19$ for the vector-, scalar-, and axial-vector mesons. From Table H.38 one sees

that at the scale of $m_M \approx 1$ GeV, such a value is reasonable. Here, one has to realize that the QPC-predictions are kind of "bare" couplings, which allow vertex corrections from meson-exchange. For the pseudo-scalar, a different value has to be used, showing indeed some 'running'-behavior as expected from QCD. In [232], for the decays $\rho, \epsilon \rightarrow 2\pi$ etc. it was found $\gamma = 3.33$, whereas here $\gamma_\pi = 5.51$. For the mesonic decays of the charmonium states $\gamma = 1.12$. One notices the similarity between the QPC($^3P_0$)-model predictions and the fitted couplings. Of course, these results are sensitive to the r_M values. It appeared that for all solutions with a very good χ^2_{NN} the r_M values varied by ±0.2 fm.
The ESC16-couplings and the QPC-couplings agree very well. In particular, the SU(6)-breaking is improving the agreement significantly. All this strengthens the claim that the ESC16-couplings are realistic ones.

Table H.39: SU(6)-breaking in coupling constants, using (56) and (70)-irrep mixing with angle $\varphi = -22^o$ for the $^3P_0$- and $^3S_1$-model. Gaussian Quark-gluon cut-off $\Lambda_{QQG} = 986.6$ MeV. Ideal mixing for vector and scalar meson nonets. For pseudoscalar- and axial-nonets the mixing angles are -11.4^0 and -42.7^o, respectively, imposing the OZI-rule. Here, $\Lambda_{QPC} = 259.6$ MeV, $\gamma(\alpha_s = 0.30) = 2.19$ etc. The weights are A=0.789 and B=0.211 for the $^3P_0$ and $^3S_1$ respectively. The values in parentheses in the column QPC denote the results for $\varphi = 0^o$.

Meson	$r_M[fm]$	γ_M	$^3S_1$	$^3P_0$	QPC	ESC16
$\pi(140)$	0.30	5.51	$g = -1.37$	$g = +5.12$	3.76 (3.99)	3.65
$\eta'(957)$	0.60	2.22	$g = -1.61$	$g = +6.02$	4.41 (5.38)	4.32
$\rho(770)$	0.80	2.37	$g = -0.09$	$g = +0.65$	0.57 (0.68)	0.58
$\omega(783)$	0.70	2.35	$g = -0.48$	$g = +3.60$	3.12 (3.09)	3.11
$a_0(962)$	0.80	2.22	$g = +0.12$	$g = +0.46$	0.59 (0.61)	0.54
$\epsilon(620)$	0.70	2.37	$g = +0.63$	$g = +2.35$	2.98 (2.98)	2.98
$a_1(1270)$	0.60	2.09	$g = -0.09$	$g = -0.67$	-0.76 (-0.77)	-0.82
$f_1(1285)$	0.60	2.09	$g = -0.08$	$g = -0.60$	-0.68 (-0.69)	-0.76

Appendix I. Quark-Pair-Creation model

In this appendix, a short description of the evaluation of the BBM coupling constants in the QPC-model, using the Fierz-transformation technique, is given. Details are given in Ref. [234]. Here, apart from the Fierz-transformation, the techniques used are those of [46, 229, 232]. In Fig. I.49 the two kinds of processes, direct (a) and exchange (b), are shown.

The derivation of the BBM-couplings starts from the generalized $^3P_0$ (S) and $^3S_1$ (V) Pair-creation Hamiltonians

$$\begin{aligned} \mathcal{H}_I^{(S)} &= -4\gamma_{q\bar{q}}^{(S)} \left(\sum_i \bar{q}_i q_i \right) \cdot \left(\sum_j \bar{q}_j q_j \right), \\ \mathcal{H}_I^{(V)} &= -\gamma_{q\bar{q}}^{(V)} \left(\sum_i \bar{q}_{i,\alpha} (\lambda)^\alpha_{\ \beta} \gamma^\mu q_{i,\beta} \right) \otimes \left(\sum_j \bar{q}_{j,\gamma} (\lambda)^\gamma_{\ \delta} \gamma_\mu q_{j,\delta} \right) \end{aligned} \tag{I.1}$$

where $\gamma_{q\bar{q}}^{(V)}$ is a phenomenological constant, and the summations run as $i, j = u, d, s$. In this QPC model, there is in the fundamental process a (confined) scalar or gluon propagator. This implies, assuming a constant propagator, an extra

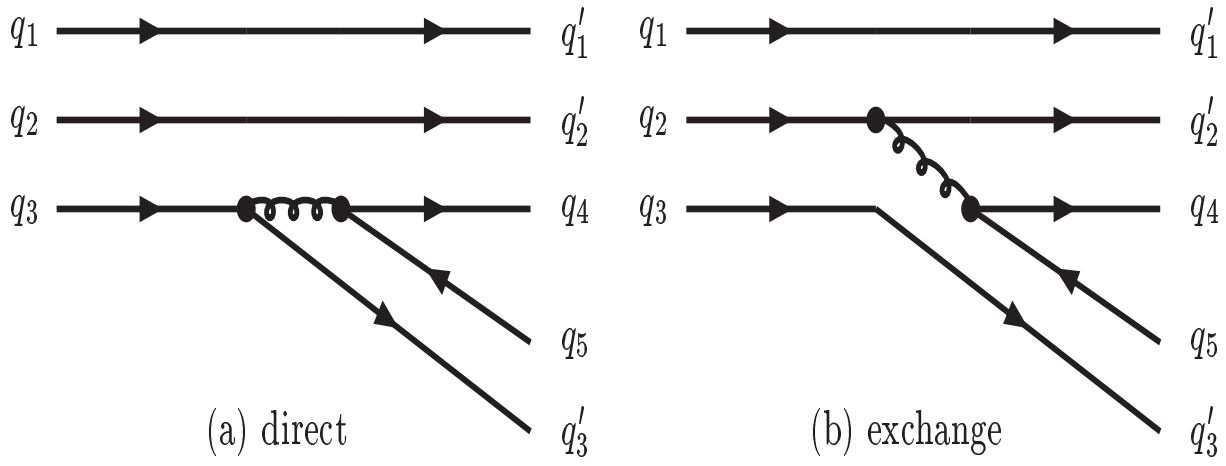

Figure I.49: $^3P_0$- *and* $^3S_1$*-quark-pair-creation (QPC)*

factor depending on a scalar or (massive) gluon exchange $(-i)^2.(\mp i/m_G^2) \sim \pm i/\Lambda_{QPC}^2$. meaning $\sim \pm iH_{int}$.
Rearrangement is supposed to take place when some mechanism creates a quark-antiquark pair in a baryon, where one quark from the baryon combines into a mesonic state with the anti-quark from the pair. The quark from the pair recombines with the two remaining quarks of the baryon to make the baryon in the final state. These rearrangements into mesons of different kinds can be understood from a Fierz transformation applied to (I.1). One has the identity [235]

$$\begin{aligned}
\mathcal{H}_I^{(S)} &= \gamma_{q\bar{q}}^{(S)} \sum_{i,j} \Big[+\ \bar{q}_i\, q_j \cdot \bar{q}_i\, q_j + \bar{q}_i\gamma_\mu q_j \cdot \bar{q}_j\gamma^\mu q_i \\
&-\frac{1}{2}\,\bar{q}_i\sigma_{\mu\nu} q_j \cdot \bar{q}_j\sigma^{\mu\nu} q_i - \bar{q}_i\gamma_\mu\gamma_5 q_j \cdot \bar{q}_j\gamma^\mu\gamma^5 q_i + \ \bar{q}_i\gamma_5 q_j \cdot \bar{q}_j\gamma^5 q_i \Big], \\
\mathcal{H}_I^{(V)} &= +\gamma_{q\bar{q}}^{(V)} \sum_{i,j} \Big[+\ \bar{q}_i\, q_j \cdot \bar{q}_i\, q_j - \frac{1}{2}\,\bar{q}_i\gamma_\mu q_j \cdot \bar{q}_j\gamma^\mu q_i \\
&-\frac{1}{2}\,\bar{q}_i\gamma_\mu\gamma_5 q_j \cdot \bar{q}_j\gamma^\mu\gamma^5 q_i - \ \bar{q}_i\gamma_5 q_j \cdot \bar{q}_j\gamma^5 q_i \Big].
\end{aligned} \tag{I.2}$$

Here, is considered only the flavor-spin Fierzing. [18] The appropriate Fierzing of the color structure is different for graph (a) and graph (b) in Fig. I.49: (i) For graph (a) the identity [235]

$$(\boldsymbol{\lambda})^\gamma_{\ \delta} \cdot (\boldsymbol{\lambda})^\beta_\alpha = \frac{16}{9}\delta^\gamma_\alpha\delta^\beta_\delta - \frac{1}{3}(\boldsymbol{\lambda})^\gamma_\alpha \cdot (\boldsymbol{\lambda})^\beta_\delta \tag{I.3}$$

is used. Since the mesons are colorless, the second term in (I.3) may be neglected, and color gives the simple factor 16/9.
(ii) In graph (b), there is in fact a sum over q_1 and q_2. Because the baryons are colorless, one has

$$(\boldsymbol{\lambda}_1)^\beta_\alpha + (\boldsymbol{\lambda}_2)^\beta_\alpha = -(\boldsymbol{\lambda}_3)^\beta_\alpha. \tag{I.4}$$

Therefore, for this graph, using (I.3), one has the identity

$$(\boldsymbol{\lambda}_5)^\gamma_{\ \delta} \cdot \sum_{i=1,2} (\boldsymbol{\lambda}_i)^\beta_\alpha = -\frac{16}{9}\delta^\gamma_\alpha\delta^\beta_\delta + \frac{1}{3}(\boldsymbol{\lambda}_5)^\gamma_\alpha \cdot (\boldsymbol{\lambda}_3)^\beta_\delta \tag{I.5}$$

[18] It should be noted that the terms for the couplings of the B-axial $J^{PC} = 1^{+-}$- and tensor $J^{PC} = 2^{++}$mesons are missing on the r.h.s. of (I.2). The same is true for the $^3P_0$-interaction (I.1).

Again, for colorless mesons the second term in (I.5) may be neglected, and color gives the simple factor $-16/9$.
The direct (a) and exchange (b) graphs give different color factors. Such a difference does not occur in the $^3P_0$-model. Now, it appears that the momentum overlap for type (b) is usually much smaller than for type (a), see Ref. [234] for details. This can be traced back to the use of a constant propagator for the (confined) gluon. Therefore, in the following, neglected are the processes described in graph (b). Then, the difference between the $^3P_0$- and $^3S_1$-model is, apart from an overall constant, exclusively given by the different coefficients in the flavor-spin Fierz-identities (I.2).

In the $^3S_1$-model for the interaction Hamiltonian for the pair-creation one uses the one-gluon-exchange (OGE) model [236, 237], see Fig. I.49. Considering one-gluon exchange, see Fig. I.49, one derives the effective vertex [236, 237] by using a (confined) constant $P_g(ji)$ gluon propagator between quark line i and line j: $P_g(ji) \sim \delta_{ji}/m_g^2$, where the (effective) gluon mass is taken to be $m_g \approx (0.8 fm^{-1}) \approx 250$ MeV [237]. Notice that the color factor for the coupling of colorless mesons to colorless baryons is always the same, and can be included into an effective coupling γ_S, i.e.

$$\frac{\pi\alpha_s(\boldsymbol{\lambda}_i \cdot \boldsymbol{\lambda}_j)}{m_G^2} \Rightarrow \gamma_{q\bar{q}}^{(V)}. \tag{I.6}$$

Here, a constant (confined) gluon-propagator $P_g = 1/m_G^2$R is used. As is clear from (I.1) $\gamma_{q\bar{q}}$ has the dimension $[\text{MeV}]^{-2}$. Also, notice that $m_G \approx \Lambda_{QPC}$, and therefore $\gamma_{q\bar{q}} \longrightarrow \gamma_{q\bar{q}}/\Lambda_{QPC}^2$. From the momentum conservation rules, one now gets different dependencies between the momenta as compared to the version of the $^3P_0$-model in [46, 232]. Hence, one has different momentum overlap-integrals.

From the results for the couplings of the mesons in the $^3P_0$-model, those for the $^3S_1$–model meson-couplings can be read off by comparing the coefficients in the Fierz-identities (I.2) and (I.1) for the corresponding operators. Here, it is assumed that the effect of color in the $^3P_0$- and $^3S_1$-model can be absorbed into $\gamma_V^{(S,V)}$, see below. For example, the prediction for the scalar-meson couplings will have the ratio $g_\epsilon(^3S_1) = \left[\gamma_V^{(V)}/\gamma_{q\bar{q}}^{(S)}\right] g_\epsilon(^3P_0)$. Apart from an overall constant, the couplings for the $^3S_1$-model can be read off from those of the $^3P_0$-model.

Appendix I.1. Meson-states, Meson- and baryon wave-functions

Below, the $\langle B, M|H_{int}|A\rangle$ matrix elements are listed for the different types of mesons. Restriction on the quark-level to process (a) in Fig. I.49, using the Fierzed form of the interaction Hamiltonian's in (I.1). So, below the results for

the $^3P_0$-model are given. Following [238], the meson creation operators are wriiten as

$$
\begin{aligned}
J^{PC}=0^{-+}: \qquad d^\dagger_{M,P}(\mathbf{k}) &= i\sum_{r,s=\pm}\int d^3k_1 d^3k_2\;\delta(\mathbf{k}-\mathbf{k}_1-\mathbf{k}_2)\;\cdot \\
&\quad\times\widetilde{\psi}^{(L=0)}_M(\mathbf{k}_1,\mathbf{k}_2)\;\varphi^{(0)}(r,s)\;b^\dagger(\mathbf{k}_1,r)\;d^\dagger(\mathbf{k}_2,s), \qquad \text{(I.7)}\\
J^{PC}=1^{--}:\; d^\dagger_{M,V}(\mathbf{k},m) &= \sum_{r,s=\pm}\int d^3k_1 d^3k_2\;\delta(\mathbf{k}-\mathbf{k}_1-\mathbf{k}_2)\;\cdot \\
&\quad\times\widetilde{\psi}^{(L=0)}_M(\mathbf{k}_1,\mathbf{k}_2)\;\varphi^{(1)}_m(r,s)\;b^\dagger(\mathbf{k}_1,r)\;d^\dagger(\mathbf{k}_2,s), \qquad \text{(I.8)}\\
J^{PC}=0^{++}:\; d^\dagger_{M,S}(\mathbf{k},m) &= \sum_{r,s=\pm}\int d^3k_1 d^3k_2\;\delta(\mathbf{k}-\mathbf{k}_1-\mathbf{k}_2)\;(-)^m\cdot \\
&\quad\times\widetilde{\psi}^{(L=1)}_{M,m}(\mathbf{k}_1,\mathbf{k}_2)\;\varphi^{(1)}_{-m}(r,s)\;b^\dagger(\mathbf{k}_1,r)\;d^\dagger(\mathbf{k}_2,s), \qquad \text{(I.9)}\\
J^{PC}=1^{++}:\; d^\dagger_{M,A}(\mathbf{k},m) &= \sum_{r,s=\pm}\int d^3k_1 d^3k_2\;\delta(\mathbf{k}-\mathbf{k}_1-\mathbf{k}_2)\;C(1,1,1;m_L,m_\sigma,m)\cdot \\
&\quad\times\widetilde{\psi}^{(L=1)}_{M,m_L}(\mathbf{k}_1,\mathbf{k}_2)\;\varphi^{(1)}_{m_\sigma}(r,s)\;b^\dagger(\mathbf{k}_1,r)\;d^\dagger(\mathbf{k}_2,s), \qquad \text{(I.10)}\\
J^{PC}=1^{+-}:\; d^\dagger_{M,B}(\mathbf{k},m) &= \sum_{r,s=\pm}\int d^3k_1 d^3k_2\;\delta(\mathbf{k}-\mathbf{k}_1-\mathbf{k}_2)\;\cdot \\
&\quad\times\widetilde{\psi}^{(L=1)}_{M,m}(\mathbf{k}_1,\mathbf{k}_2)\;\varphi^{(0)}(r,s)\;b^\dagger(\mathbf{k}_1,r)\;d^\dagger(\mathbf{k}_2,s), \qquad \text{(I.11)}\\
J^{PC}=2^{++}:\; d^\dagger_{M,T}(\mathbf{k},m) &= \sum_{r,s=\pm}\int d^3k_1 d^3k_2\;\delta(\mathbf{k}-\mathbf{k}_1-\mathbf{k}_2)\;C(1,1,2;m_L,m_\sigma,m)\cdot \\
&\quad\times\widetilde{\psi}^{(L=1)}_{M,m_L}(\mathbf{k}_1,\mathbf{k}_2)\;\varphi^{(1)}_{m_\sigma}(r,s)\;b^\dagger(\mathbf{k}_1,r)\;d^\dagger(\mathbf{k}_2,s), \qquad \text{(I.12)}
\end{aligned}
$$

for respectively the pseudoscalar-, vector-, scalar-, axial-vector mesons of the first (A_1 etc.) and second kind (B_1 etc.), and tensor mesons. These representations are the equal-time Bethe-Salpeter wave functions [239]:

$$
f_{\mathbf{k},\alpha}(x,y)\equiv\langle 0|T\left[q_i(x)q_j(y)\right]|M(\mathbf{k},\alpha\rangle\overset{x^0=y^0}{\longrightarrow}\left(0|q_i(\mathbf{x})q_j(\mathbf{y})|M(\mathbf{k},\alpha\right),
$$

using the definition $\theta[0]=1/2$. Here, a factor i is included in the definition of the $d^\dagger_{M,P}(\mathbf{k})$-operator. This is in order to have under time-reversal $\mathcal{T}|\pi_0(\mathbf{k})\rangle=|\pi_0(-\mathbf{k})\rangle$. The reason is that under time-reversal the spin-components change sign, which implies for the spin-singlet $\varphi^{(0)}(-r,-s)=-\varphi^{(0)}(r,s)$ etc.
The baryon and meson harmonic oscillator wave functions are

$$
\begin{aligned}
\widetilde{\psi}_N(\mathbf{k}_1,\mathbf{k}_2,\mathbf{k}_3) &= \left(\frac{\sqrt{3}R_A^2}{\pi}\right)^{3/2}\exp\left[-\frac{R_A^2}{6}\sum_{i<j}(\mathbf{k}_i-\mathbf{k}_j)^2\right],\\
\widetilde{\psi}^{(L=0)}_M(\mathbf{k}_1,\mathbf{k}_2) &= \left(\frac{R_M^2}{\pi}\right)^{3/4}\exp\left[-\frac{R_M^2}{8}(\mathbf{k}_1-\mathbf{k}_2)^2\right],\\
\widetilde{\psi}^{(L=1)}_{M,m}(\mathbf{k}_1,\mathbf{k}_2) &= \frac{R_M}{\sqrt{2}}\left(\frac{R_M^2}{\pi}\right)^{3/4}\left[-\boldsymbol{\epsilon}_m\cdot(\mathbf{k}_1-\mathbf{k}_2)\right]\;.\exp\left[-\frac{R_M^2}{8}(\mathbf{k}_1-\mathbf{k}_2)^2\right].
\end{aligned}
$$

Here, are used the spherical unit vectors $\boldsymbol{\epsilon}_{\pm1}=\mp\frac{1}{\sqrt{2}}(\mathbf{e}_1\pm i\mathbf{e}_2)\;\;,\;\;\boldsymbol{\epsilon}_0=\mathbf{e}_3$.

Appendix I.2. Coupling-constant Formulas

The matrix elements $\langle B_f(\mathbf{p}')\;M(\mathbf{k})|\mathcal{H}_I^{(S),(V)}|B_i(\mathbf{p})\rangle$ involve the momentum space overlap integrals, which can be performed in a straightforward manner [234]. The summary of the derived formulas in [234], in the case of the

$^3P_0$-model, for the divers (I=1)-couplings is:

$$g_P = +\pi^{-3/4}\,\gamma_{q\bar{q}}\,\frac{(m_P R_P)^{1/2}}{(\Lambda_{QPC}R_P)^2}\cdot(6\sqrt{2})\,,\; g_V = +\pi^{-3/4}\,\gamma_{q\bar{q}}\,\frac{(m_V R_V)^{1/2}}{(\Lambda_{QPC}R_V)^2}\cdot(3/\sqrt{2})\,,$$
$$g_S = +\pi^{-3/4}\,\gamma_{q\bar{q}}\,\frac{(m_S R_S)^{-1/2}}{(\Lambda_{QPC}R_S)^2}\cdot\frac{9m_S}{M_B}\,,\; g_A = -\pi^{-3/4}\,\gamma_{q\bar{q}}\,\frac{(m_A R_A)^{-1/2}}{(\Lambda_{QPC}R_A)^2}\cdot\frac{6m_A}{M_B},$$

with $\Lambda_{QPC} \approx 600$ MeV, and $R_M \approx 0.66$.

Appendix J. ESC-potentials and the Constituent Quark-model

The calculation of Table H.39 uses the constituent quark model (CQM) in the SU(6)-version of [46]. Since this calculation implicitly uses the direct coupling of the mesons to the quarks, it defines the QQM-vertex. Then, OBE-potentials can be derived by folding meson-exchange with the quark wave functions of the baryons. The BB-amplitudes and BBM-vertices, at the baryon level have a Lorentz and Dirac structure [57], which is independent of the internal structure of the baryons and mesons. At the baryon level, the vertices have in Pauli-spinor space the $1/M_B$-expansion

$$\begin{aligned}\bar{u}(p',s')\Gamma u(p,s) &= \chi'^{\dagger}_{s'}\left\{\Gamma_{bb}+\Gamma_{bs}\frac{\boldsymbol{\sigma}\cdot\mathbf{p}}{E+M}-\frac{\boldsymbol{\sigma}\cdot\mathbf{p}'}{E'+M'}\Gamma_{sb}-\frac{\boldsymbol{\sigma}\cdot\mathbf{p}}{E+M}\Gamma_{ss}\frac{\boldsymbol{\sigma}\cdot\mathbf{p}'}{E'+M'}\Gamma_{sb}\right\}\chi_s \\ &\equiv \sum_l c^{(l)}_{BB}\,\left[\chi'^{\dagger}_{s'}O_l(\mathbf{p}',\mathbf{p})\,\chi_s\right]\,(\sqrt{M'M})^{\alpha_l}\;\;(l=bb,bs,sb,ss). \qquad \text{(J.1)}\end{aligned}$$

As emphasized above, this expansion is general and does not depend on the internal structure of the baryon. A similar expansion can be made on the quark level, but now with quark masses m_Q and coefficients $c^{(l)}_{QQ}$. It appears that in the CQM, i.e. $m_Q = M_B/3$, the QQM-vertices can be chosen such that the ratios $c^{(l)}_{QQ}/c^{(l)}_{BB}$ are constant for each type of meson [9]. Then, by scaling the couplings, these coefficients can be made equal. Ipso facto, this defines a meson-exchange quark-quark interaction. This shows that the use of the QPC model is consistent with the 1/M-expansion.

Appendix K. Exchange Forces

The proper treatment of the flavor-exchange forces for the $S = -2$ channels is a little more subtle than for the $S = 0, -1, -3, -4$-channels. The extra complication is the occurrence of couplings between channels with identical particles and channels with non-identical particles. In order to understand the several $\sqrt{2}$-factors, mentioned in Ref. [36] and treated in a concise form in Ref. [13], a systematic treatment of the flavor-exchange potentials is given. The method followed is using a multi-channel framework, which starts by ordering the two-particle states by assigning A_i and B_i for the channel labeled with the index i, like in Eqn. (2.1). The particles A_i and B_i have the center-of-mass (c.m.) momenta p_i and $-p_i$, spin components $s_{A,i}$ and $s_{B,i}$. The two-baryon states $|A_iB_i\rangle$ and $|B_iA_i\rangle$ are considered to be distinct, leading to distinct two-baryon channels. The 'direct' and the 'exchange' T-matrices are given by the following T-matrix elements

$$(A_jB_j|T_d|A_iB_i),\;\;(B_jA_j|T_e|A_iB_i), \qquad \text{(K.1)}$$

and similarly for the direct and flavor-exchange potentials V_d and V_e. It is obvious from rotation invariance that

$$(A_jB_j|T_d|A_iB_i) = (B_jA_j|T_d|B_iA_i),\;\;(B_jA_j|T_e|A_iB_i) = (A_jB_j|T_e|B_iA_i). \qquad \text{(K.2)}$$

A similar definition (K.1) and relation (K.2) apply for the direct and flavor-exchange potentials V_d and V_e. Notice that in interchanging A and B, there is no exchange of momenta or spin-components, see Fig. K.50. This is necessary for the application of Lippmann-Schwinger type of integral equations, which can produce only one type of the Mandelstam double spectral functions [109], *e.g.* $\rho(s,t)$ or $\rho(s,u)$. (The third double spectral function $\rho(t,u)$ can only be included approximately in potential scattering.) So, the momentum transfer for V_d and for V_e is the same. Viewed from the coupled-channel scheme, this is the standard situation.

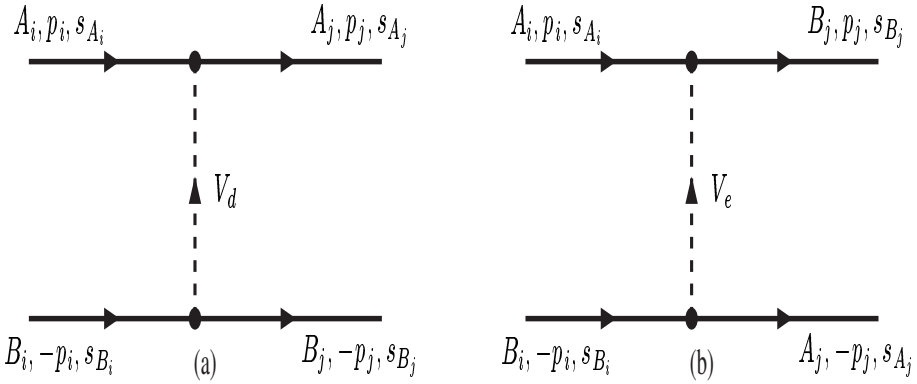

Figure K.50: V_d (a) and V_e (b) in the c.m. system.

The integral equations with two-baryon unitarity, *e.g.* the Thompson-, Lippmann-Schwinger-equation etc., read for the T_d- and T_e-operator

$$\begin{aligned}(A_jB_j|T_d|A_iB_i) &= (A_jB_j|V_d|A_iB_i) + \sum_k \Big[(A_jB_j|V_d|A_kB_k)\, G_k\, (A_kB_k|T_d|A_iB_i) \\ &\quad +(A_jB_j|V_e|B_kA_k)\, G_k\, (B_kA_k|T_e|A_iB_i)\Big]\,, \qquad \text{(K.3a)} \\ (B_jA_j|T_e|A_iB_i) &= (B_jA_j|V_e|A_iB_i) + \sum_k \Big[(B_jA_j|V_d|B_kA_k)\, G_k\, (B_kA_k|T_e|A_iB_i) \\ &\quad +(B_jA_j|V_e|A_kB_k)\, G_k\, (A_kB_k|T_d|A_iB_i)\Big]. \qquad \text{(K.3b)}\end{aligned}$$

These coupled equations can be diagonalized by introducing the $T^{\pm}$- and $V^{\pm}$-operators

$$T^{\pm} = T_d \pm T_e\,, \quad V^{\pm} = V_d \pm V_e. \qquad \text{(K.4)}$$

which, as follows from (K.3), satisfy separate integral equations

$$(A_jB_j|T^{\pm}|A_iB_i) = (A_jB_j|V^{\pm}|A_iB_i) + \sum_k (A_jB_j|V^{\pm}|A_kB_k)\, G_k\, (A_kB_k|T^{\pm}|A_iB_i). \qquad \text{(K.5)}$$

Notice that on the basis of states with definite flavor symmetry

$$|A_iB_i\rangle_{\pm} = \frac{1}{\sqrt{2}}\left[|A_iB_i\rangle \pm |B_iA_i\rangle\right]\,, \qquad \text{(K.6)}$$

the $T^{\pm}$ and $V^{\pm}$ matrix elements are also given by

$$T^{\pm}_{ij} =_{\pm}(A_iB_i|T|A_jB_j)_{\pm}\,, \quad V^{\pm}_{ij} =_{\pm}(A_iB_i|V|A_jB_j)_{\pm}. \qquad \text{(K.7)}$$

Appendix K.1. Identical Particles

So far, considered is the general case where $A_i \neq B_i$ for all channels. In the case that $A_i = B_i$ for some i, one has $\langle B_iA_i|V_e|A_iB_i\rangle = 0$, because there is no distinct physical state corresponding to the 'flavor exchange-state'. For example for a flavor single channel like pp one deduces from (K.3) that then also $T_e = 0$, and one has in this case the integral equation

$$(A_jB_j|T_d|A_iB_i) = (A_jB_j|V_d|A_iB_i) + \sum_k (A_jB_j|V_d|A_kB_k)\, G_k\, (A_kB_k|T_d|A_iB_i), \qquad \text{(K.8)}$$

where the labels i and j now denote *e.g.* the spin-components.

Appendix K.2. Coupled ΛΛ and ΞN system

This multi-channel system represents the case where there is a mixture of channels with identical and with non-identical particles. The three states distinguished are $|\Lambda\Lambda\rangle, |\Xi N\rangle$, and $|N\Xi\rangle$. Choosing the same ordering, the potential written as a 3×3-matrix reads, see Eqn. (3.18),

$$V = \begin{pmatrix} (\Lambda\Lambda|V|\Lambda\Lambda) & (\Lambda\Lambda|V|\Xi N) & (\Lambda\Lambda|V|N\Xi) \\ (\Xi N|V|\Lambda\Lambda) & (\Xi N|V|\Xi N) & (\Xi N|V|N\Xi) \\ (N\Xi|V|\Lambda\Lambda) & (N\Xi|V|\Xi N) & (N\Xi|V|N\Xi) \end{pmatrix}. \tag{K.9}$$

and a similar notation for the T-matrix. The Lippmann-Schwinger equation can be written compactly as a 3×3-matrix equation:

$$T = V + V\,G\,T\ , \text{ with } G_{ij} = G_i\,\delta_{ij}. \tag{K.10}$$

Next, transforming to states, which are either symmetric or antisymmetric for particle interchange. Then, according to (K.7), one can separate them in the Lippmann-Schwinger equation. This is achieved by the transformation

$$\begin{pmatrix} \Lambda\Lambda \\ \Xi N \\ N\Xi \end{pmatrix} \Rightarrow \begin{pmatrix} \Lambda\Lambda \\ (\Xi N + N\Xi)/\sqrt{2} \\ (\Xi N - N\Xi)/\sqrt{2} \end{pmatrix} \tag{K.11}$$

where a standard multi-channel notation is used for the states. This yields in the transformed basis the potential

$$UVU^{-1} = \begin{pmatrix} V_{\Lambda\Lambda;\Lambda\Lambda} & (V_{\Lambda\Lambda;\Xi N} + V_{\Lambda\Lambda;N\Xi})/\sqrt{2} & (V_{\Lambda\Lambda;\Xi N} - V_{\Lambda\Lambda;N\Xi})/\sqrt{2} \\ (V_{\Xi N;\Lambda\Lambda} + V_{N\Xi;\Lambda\Lambda})/\sqrt{2} & (V_{\Xi N;\Xi N} + V_{\Xi N;N\Xi}) & 0 \\ (V_{\Xi N;\Lambda\Lambda} - V_{N\Xi;\Lambda\Lambda})/\sqrt{2} & 0 & (V_{\Xi N;\Xi N} - V_{\Xi N;N\Xi}) \end{pmatrix}, \tag{K.12}$$

and of course, a similar form is obtained for the T-matrix on the transformed basis. Now, obviously $V_{\Lambda\Lambda;\Xi N} = V_{\Lambda\Lambda;N\Xi}$ and $V_{\Xi N;\Lambda\Lambda} = V_{N\Xi;\Lambda\Lambda}$. Therefore, one sees that the even and odd states under particle exchange are decoupled in (K.12). Also $(V_{\Xi N;\Lambda\Lambda} + V_{N\Xi;\Lambda\Lambda})/\sqrt{2} = \sqrt{2}V_{\Xi N;\Lambda\Lambda}$, etc. showing the appearance of the $\sqrt{2}$-factors, mentioned before. Indeed, they appear in a systematic way using the multi-channel framework. In Ref. [13] the details are worked out for K-, η-, and π-exchange potentials for the $\Lambda\Lambda, \Xi N, \Sigma\Lambda$ etc. channels. The results are summarized in Table 3.

Appendix L. Diquark-exchange Quark-Nucleon Interaction

The diquark exchange potential $V_{DQE}^{(qN)}$ is derived from a description of the confinement-deconfinement process at high baryon densities via the (density dependent) nucleon-triquark coupling

$$\mathcal{L}_{int}^{(1)} = -\lambda_3[\bar{\psi}(x)\eta_N(x) + \bar{\eta}_N(x)\psi(x)] \tag{L.1}$$

with [164]

$$\eta_N(x) = \left[\widetilde{q}^a(x)C\gamma^\mu q^b(x)\right]\gamma_5\gamma_\mu q^c(x)f^{abc}, \tag{L.2}$$

where C is the charge conjugation operator, and momentarily left out are the isospin labels.
The interaction Lagrangian in (L.1) with the triquark field $\eta_N(x)$ is rewritten using diquark fields for two reasons: (i) the functional form of the partition function is difficult to handle, and (ii) diquarks are meaningful physical entities. In terms of the (bosonic) diquark fields $\chi_\mu^a(x)$

$$\eta_N(x) = (\hbar c)^2\gamma_5\gamma^\mu q^a(x)\cdot\chi_\mu^a(x), \tag{L.3a}$$

$$\chi_\mu^a(x) \equiv f^{abc}\widetilde{q}^b(x)C\gamma_\mu q^c(x)/(\hbar c)^2. \tag{L.3b}$$

The interaction (L.1) becomes

$$\mathcal{L}_{int}^{(1)} = -\lambda_3(\hbar c)^2[(\bar{\psi}(x)\gamma_5\gamma^\mu q^a(x))\chi_\mu^a(x) + h.c.] \tag{L.4}$$

As the proton and neutron presentation [164] shows, the diquark field has isospin one. So, $\chi^a_\mu(x)$ is an isovector axial-vector field. Therefore, introduce are the fields

$$\mathbf{D}^a_\mu(x) \equiv \boldsymbol{\chi}^a_\mu(x) = \varepsilon^{abc}\tilde{Q}^b(x)C\gamma_\mu\boldsymbol{\tau}Q^c(x)/(\hbar c)^2, \tag{L.5}$$

where $Q = (u, d)$ is the isospin-spinor $SU_I(2)$ doublet and a $SU_C(3)$ triplet. Similarly for the diquark $\mathbf{D}^a_\mu$. The diquark NQ-vertex is given by the interaction Lagrangian

$$\mathcal{L}^{(1)}_{int} = -\lambda_3\{(\bar{\psi}(x)\gamma_5\gamma^\mu\boldsymbol{\tau}q^a)\cdot\mathbf{D}^a_\mu(x) + h.c.\}, \tag{L.6}$$

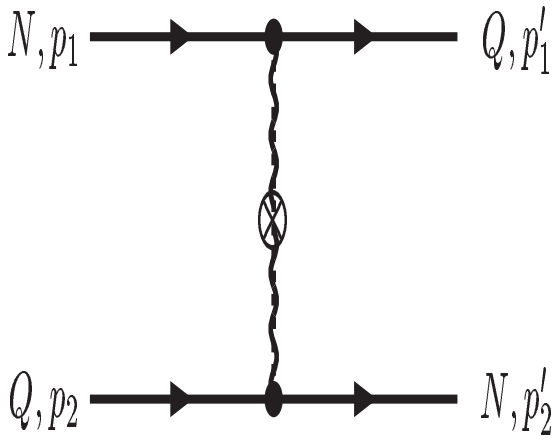

Figure L.51: Diquark-exchange for $NQ \to QN$ reaction.

The derivation of the diquark Feynman propagator is given in [166, 167], where it is pointed out that QQ-exchange differs from Q$\bar{Q}$-exchange as follows from the Wick-expansion.
The Feynman propagator for the $\eta_{\mu\nu}$-term can be written as

$$i(\widetilde{\Delta_F})^{ab}_{\mu\nu}(\boldsymbol{\Delta}) = -i\delta_{ab}\widetilde{D}(\boldsymbol{\Delta}^2)\left(\eta_{\mu\nu} - \frac{\boldsymbol{\Delta}_\mu\boldsymbol{\Delta}_\nu}{m^2_\chi}\right), \;\; \widetilde{D}(\boldsymbol{\Delta}^2) > 0, \tag{L.7}$$

where $\Delta = p'_1 - p_1 = p'_2 - p_2$. In the Gaussian approximation

$$\widetilde{D}(\boldsymbol{\Delta}^2) \approx exp\left[-\boldsymbol{\Delta}^2/\Lambda^2\right]/\mathcal{M}^2. \tag{L.8}$$

The second-order amplitude for Fig. L.51 using the interaction (L.6) can be described (effectively) by

$$M^{(2)}(p'_1, s'_1, p'_2, s'_2; p_1, s_1, p_2, s_2) = -\frac{\lambda_3^2}{2!}\left[\bar{u}_Q(p'_1, s'_1)\gamma_5\gamma^\mu\boldsymbol{\tau}u_N(p_1, s_1)\right]\cdot\left[\bar{u}_N(p'_2, s'_2)\gamma_5\gamma_\mu\boldsymbol{\tau}u_Q(p_2, s_2)\right]\widetilde{D}(\boldsymbol{\Delta}^2), \tag{L.9}$$

where $\Delta = p'_1 - p_1 = p'_2 - p_2$. In the low momentum transfer region, the approximation $\widetilde{D} \approx \exp\left[-\boldsymbol{\Delta}^2/\Lambda^2\right]/\mathcal{M}^2$ leads to a Gaussian contact interaction.

$$V(p'_1, s'_1, p'_2, s'_2; p_1, s_1, p_2, s_2) = -(\lambda_3^2/2)\left[\bar{u}_Q(p'_1, s'_1)\gamma_5\gamma^\mu\boldsymbol{\tau}u_N(p_1, s_1)\right]\cdot\left[\bar{u}_N(p'_2, s'_2)\gamma_5\gamma_\mu\boldsymbol{\tau}u_Q(p_2, s_2)\right]\widetilde{D}(\boldsymbol{\Delta}^2) \tag{L.10}$$

Using Pauli-spinor matrix elements

$$\bar{u}(\mathbf{p}'\gamma_5\gamma_0 u(\mathbf{p}) = -\sqrt{\frac{\mathcal{E}'\mathcal{E}}{4M'M}}\left[\frac{\boldsymbol{\sigma}\cdot\mathbf{p}'}{\mathcal{E}'} + \frac{\boldsymbol{\sigma}\cdot\mathbf{p}}{\mathcal{E}}\right], \tag{L.11}$$

$$\bar{u}(\mathbf{p}')\gamma_5\boldsymbol{\gamma}u(\mathbf{p}) = -\sqrt{\frac{\mathcal{E}'\mathcal{E}}{4M'M}}\left[\boldsymbol{\sigma} + \frac{(\boldsymbol{\sigma}\cdot\mathbf{p}')\,\boldsymbol{\sigma}\,(\boldsymbol{\sigma}\cdot\mathbf{p})}{\mathcal{E}'\mathcal{E}}\right] \approx -\boldsymbol{\sigma}, \tag{L.12}$$

where M',M denote the quark or the nucleon mass, and $\mathcal{E} = E_p + M$. Note that the leading term from the vertex factors [....][....] in (L.10) has $-(\boldsymbol{\sigma}_1 \cdot \boldsymbol{\sigma}_2)$. In momentum space, using the notation $\widetilde{V}_{QN} \equiv \widetilde{V}^{(a)}_{QN} + \widetilde{V}^{(b)}_{QN}$, where (a) is similar to the axial-exchange in NN-potentials, and (b) represents terms emphasizing the nucleon and quark mass, and obtain

$$\begin{aligned}
\widetilde{V}^{(a)}_{QN} &= +2\lambda_3^2\Big[\Big(1 - \frac{2\mathbf{k}^2}{3M_QM_N} + \frac{3(\mathbf{q}^2+\mathbf{k}^2/4)}{2M_QM_N}\Big)\,\boldsymbol{\sigma}_1\cdot\boldsymbol{\sigma}_2 + \frac{1}{4M_QM_N}\Big((\boldsymbol{\sigma}_1\cdot\mathbf{k})(\boldsymbol{\sigma}_2\cdot\mathbf{k}) - \frac{1}{3}\mathbf{k}^2\boldsymbol{\sigma}_1\cdot\boldsymbol{\sigma}_2\Big) \\
&\quad + \frac{i}{4M_QM_N}(\boldsymbol{\sigma}_1+\boldsymbol{\sigma}_2)\cdot\mathbf{q}\times\mathbf{k}\Big]\cdot\widetilde{g}(\mathbf{k}^2), \qquad \text{(L.13a)} \\
\widetilde{V}^{(b)}_{QN} &= -2\lambda_3^2\Big[\frac{(M_N-M_Q)^2}{4M_N^2M_Q^2}\{\big(\mathbf{q}^2+\mathbf{k}^2/4\big) - \mathbf{k}^2/2\}\,\boldsymbol{\sigma}_1\cdot\boldsymbol{\sigma}_2 \\
&\quad - \frac{i}{4}\Big(\frac{M_N^2-M_Q^2}{8M_N^2M_Q^2}\Big)\,(1+\boldsymbol{\sigma}_1\cdot\boldsymbol{\sigma}_2)\,(\boldsymbol{\sigma}_1-\boldsymbol{\sigma}_2)\cdot\mathbf{n}\Big]\cdot\widetilde{g}(\mathbf{k}^2), \qquad \text{(L.13b)}
\end{aligned}$$

where $\widetilde{g}(\mathbf{k}^2) = \exp\left(-\mathbf{k}^2/\Lambda^2\right)/\mathcal{M}^2$. Here, the Gaussian cut-off and a scale parameter $\mathcal{M}$ has been added.

Note: $V^{(a)}_{QN}$ is similar to axial-vector exchange in NN and YN. $V^{(b)}_{QN}$ is the "extra term" proportional to the $M_N - M_Q$ mass difference, which is not small in the QN-potential.

In configuration space, taking into account the exchange character of the potential, there is a factor P_fP_σ. Since the physical states satisfy $P_fP_\sigma P_x = -1$, this leads to a factor $-P_x$ and a sign-change in the anti-symmetric spin-orbit. Then, one obtains for the central, spin-spin, tensor, and spin-orbit-potentials, see *e.g.* Ref. [4],

$$\begin{aligned}
V^{(a)}_{QN}(r) &= -2\lambda_3^2\,\frac{\Lambda}{8\pi}\Big[\Big(\phi^0_C(r) - \frac{\Lambda^2}{6M_NM_Q}\phi^1_C(r)\Big)(\boldsymbol{\sigma}_1\cdot\boldsymbol{\sigma}_2) - \frac{3}{4M_QM_N}\Big(\boldsymbol{\nabla}^2\phi^0_C(r) + \phi^0_C(r)\boldsymbol{\nabla}^2\Big)(\boldsymbol{\sigma}_1\cdot\boldsymbol{\sigma}_2) \\
&\quad - \frac{\Lambda^2}{16M_NM_Q}\,\phi^0_T(r)\,S_{12} + \frac{\Lambda^2}{8M_NM_Q}\phi^0_{SO}(r)\,\mathbf{L}\cdot\mathbf{S}\Big]\,(\boldsymbol{\tau}_1\cdot\boldsymbol{\tau}_2)\,P_x, \qquad \text{(L.14a)} \\
V^{(b)}_{QN}(r) &= -2\lambda_3^2\,\frac{\Lambda}{8\pi}\Big[\frac{(M_N-M_Q)^2}{4M_NM_Q}\Big\{+\frac{\Lambda^2}{8M_NM_Q}\phi^1_C(r) + \frac{1}{2M_NM_Q}\Big(\boldsymbol{\nabla}^2\phi^0_C(r) + \phi^0_C(r)\boldsymbol{\nabla}^2\Big)\Big\}\cdot \\
&\quad \times(\boldsymbol{\sigma}_1\cdot\boldsymbol{\sigma}_2) - \frac{\Lambda^2}{4M_NM_Q}\frac{(M_N^2-M_Q^2)}{4M_NM_Q}\phi^0_{SO}(r)\cdot\frac{1}{2}(\boldsymbol{\sigma}_1-\boldsymbol{\sigma}_2)\cdot\mathbf{L}\Big]\,(\boldsymbol{\tau}_1\cdot\boldsymbol{\tau}_2)\,P_x, \qquad \text{(L.14b)}
\end{aligned}$$

where

$$\begin{aligned}
\phi^0_C(r) &= \frac{1}{\sqrt{\pi}}\frac{\Lambda^2}{\mathcal{M}^2}\,\exp\Big[-\frac{1}{4}\Lambda^2r^2\Big], \qquad \text{(L.15a)} \\
\phi^1_C(r) &= \frac{2}{\sqrt{\pi}}\frac{\Lambda^2}{\mathcal{M}^2}\,\big(3-\Lambda^2r^2/2\big)\exp\Big[-\frac{1}{4}\Lambda^2r^2\Big], \qquad \text{(L.15b)} \\
\phi^0_T(r) &= \frac{1}{6\sqrt{\pi}}\frac{\Lambda^2}{\mathcal{M}^2}\,(\Lambda r)^2\exp\Big[-\frac{1}{4}\Lambda^2r^2\Big], \qquad \text{(L.15c)} \\
\phi^0_{SO}(r) &= \frac{2}{\sqrt{\pi}}\frac{\Lambda^2}{\mathcal{M}^2}\,\exp\Big[-\frac{1}{4}\Lambda^2r^2\Big]. \qquad \text{(L.15d)}
\end{aligned}$$

As a last step, a Gaussian cut-off is introduced with the parameter Λ. This parameter is a free parameter and can be used to tune the diquark exchange potential, which is also the case with λ_3. The non-local potential is

$$V^{(n.l.)}(r) = -\Big[\boldsymbol{\nabla}^2\frac{\phi(r)}{2M_{red}} + \frac{\phi(r)}{2M_{red}}\boldsymbol{\nabla}^2\Big]P_x, \text{ with } \phi(\mathrm{r}) = -\frac{\lambda_3^2}{4\pi}\frac{3\Lambda}{4\mathrm{M_Q}\mathrm{M_N}}\phi^0_{\mathrm{C}}(\mathrm{r})\,(\boldsymbol{\sigma}_1\cdot\boldsymbol{\sigma}_2)\,(\boldsymbol{\tau}_1\cdot\boldsymbol{\tau}_2). \qquad \text{(L.16)}$$

For the statistical average S-wave potential one obtains from Eq. (L.14)

$$\bar{V}(CQM) = \frac{1}{4}V(^1S_0) + \frac{3}{4}V(^3S_1) = +\frac{3\lambda_3^2}{4\pi}\,\Lambda\Big(\phi^0_C(r) - \frac{\Lambda^2}{6M_NM_Q}\Big\{1 - \frac{3(M_N-M_Q)^2}{16M_NM_Q}\Big\}\phi^1_C(r)\Big) \qquad \text{(L.17)}$$

which result comes from $(\boldsymbol{\sigma}_1 \cdot \boldsymbol{\sigma}_2)(\boldsymbol{\tau}_1 \cdot \boldsymbol{\tau}_2) = -3$ for both ${}^1S_0$ and ${}^3S_1$.

The confinement-deconfinement transition can be parametrized as $\lambda_3 \rightarrow \gamma_D \lambda_3$ with *e.g.*

$$\gamma_D(\rho_N, \rho_D) \quad = \quad [\exp\{+\gamma_3\,(\rho_N/\rho_D - 1)\} - 1]\ \theta(\rho_N - \rho_D), \tag{L.18}$$

where ρ_D is the deconfinement threshold. In [10, 11, 12] a similar form is used for the density dependence of the constituent quark mass.
Notes: *1. The S-wave quark-nucleon potential (L.17) is repulsive and becomes strong for high densities. 2. The* ${}^1P_1$*-wave has* $\boldsymbol{\sigma}_1 \cdot \boldsymbol{\sigma}_2 \boldsymbol{\tau}_1 \cdot \boldsymbol{\tau}_2 P_x = -9$ *giving strong repulsion. For* ${}^3P_J (J = 0, 1, 2)$ *the spin-isospin and the exchange operator give a factor -1, giving again a (weaker) repulsion. 3. The diquark exchange potential gives a repulsive wall for the nucleons between the nucleon- and quark-phase.*

Appendix M. Acronyms and Abbreviations

Term	Meaning	Term	Meaning
$M_{8,1}$	Octet- and Singlet-meson	J^{PC}	J= ang.mom., P=parity, C=charge-conj. parity
B_8	Octet-baryon	I,S	Isospin, strangeness
BB	Baryon-baryon	SU(3)	Unitary (flavor) symmetry
NN	Nucleon-nucleon	CQM	Constituent Quark-model
YN	Hyperon-nucleon	BBM	Baryon-baryon-meson
YY	Hyperon-hyperon	QPC	Quark-pair creation
BQ	Baryon-quark	PWA	Partial wave analysis
QQ	Quark-quark	QQM	Quark-quark-meson
OBE	One-boson-exchange	GMO	Gell-Mann-Okubo mass-mixing
OPE	One-pion-exchange	CSB	Charge-symmetry breaking
TPS	Two-pseudoscalar-exchange	CS	Chiral-symmetry
TME	Two-meson-exchange	SCSB	Spontaneous-chiral-symmetry breaking
MPE	Meson-pair-exchange	OPT	Old-fashioned Perturbation Theory
BW	Bruckner-Watson TPS 1953	TMO	Taketani-Machida-Ohnuma TPS 1952
NSC	Nijmegen soft-core model	QCE	Quark-core-effect
ESC	Extended soft-core model	OGE	One-gluon-exchange
KFT	Kadyshevsky Field Theory	RQFT	Relativistic Quantum Field Theory
s.p.	Single-particle	n.l.	Non-local
G-matrix	In-medium interaction	CON	continuos choice
TNR	Three-nucleon Repulsion	TNA	Three-nucleon Attraction
TBA	Three-baryon Attraction	MPP	Multi-Pomeron Potential
WS	Wood-Saxon	ADA	Average density approximation
$ESC16^{+}$	ESC16 + MPP+TBA	$ESC16^{(\star)}$	ESC16 + SU(3) contact interactions
NS	Neutron star	EoS	Equation-of-State
BHF	Bruckner-Hartree-Fock	MR	Mass-radius relation
NUCM	Nucleonic matter	BRYM	Baryonic matter
NQM	Nucleon-quark mixed matter	BQM	Baryon-quark mixed matter
QHT	Quark-hadron transition model	DQE	Diquark-exchange

Table M.40: List of acronyms and abbreviations used in the text

References

[1] Th.A. Rijken, in *Proceedings of the XIVth European Conference on Few-Body Problems in Physics*, Amsterdam 1993, edited by B. Bakker and R. van Dantzig, Few-Body Systems, Suppl. **7**, 1 (1994).
[2] Th. A. Rijken, Phys. Rev. **C 73** (2006) 044007.
[3] Th. A. Rijken and Y. Yamamoto, Phys. Rev. **C 73** (2006) 044008.
[4] Th. A. Rijken, M.M. Nagels, and Y. Yamamoto, Progress of Theoretical Physics, Suppl. No. **185**, 14 (2010).
[5] M.M. Nagels, Th. A. Rijken, and Y. Yamamoto, Phys. Rev. **C 99** (2019) 044002.
[6] M.M. Nagels, Th. A. Rijken, and Y. Yamamoto, Phys. Rev. **C 99** (2019) 044003.
[7] M.M. Nagels, Th. A. Rijken, and Y. Yamamoto, Phys. Rev. **C 102** (2020) 054003.
[8] M.M. Nagels, Th. A. Rijken, and Y. Yamamoto, Phys. Rev. **C 108** (2023) 024003.
[9] Th.A. Rijken, *Nucleon-Nucleon Interactions*, talk at KITPC workshop on Present Status Nuclear Interaction Theory, Beijin August 2014.
[10] Y. Yamamoto, N. Yasutake, and Th.A. Rijken, Phys. Rev. **C 105** (2022) 015804.
[11] Y. Yamamoto, N. Yasutake, and Th.A. Rijken, Phys. Rev. **C 108** (2023) 035811.
[12] Y. Yamamoto, N. Yasutake, and Th.A. Rijken, Phys. Rev. **C 110** (2024) 025805.
[13] Th.A. Rijken, M.M. Nagels, and Y. Yamamoto, Progr. Theor. Phys. Suppl. **185** (2010) 14.
[14] V. G. Kadyshevsky, Sov. Phys. JETP, **19** (1964) 443.
[15] V. G. Kadyshevsky, Nucl. Phys. **B6** 125 (1967);

[16] V. G. Kadyshevsky and N. D. Mattev, Nuov. Cim. **55A**, 275 (1968).
[17] C. Itzykson, V. G. Kadyshevsky, I. T. Todorov, Phys. Rev. **D1**, 2823 (1970).
[18] J.W. Wagenaar and Th.A. Rijken, Phys. Rev. **C 80** (2009) 055204; *ibid* 055205; J.W. Wagenaar, *Pion-Nucleon Scattering in Kadyshevsky Formalism and Higher Spin Field Quantization*, Ph.D.-thesis Radboud Universityi, Nijmegen, The Netherlands 2009.
[19] R.P. Feynman, Phys. Rev. **76**, 769 (1949).
[20] J. Schwinger, Proc. Nat. Acad. of Sciences (USA) **37**, 452 (1951).
[21] E. Salpeter and H.A. Bethe, Phys. Rev. **84**, 1232 (1951).
[22] B.A. Lippmann and J. Schwinger, Phys. Rev. **79**, 469 (1950).
[23] R.H. Thompson, Phys. Rev. **D1**, 110 (1970).
[24] A. Klein, Phys. Rev. **90**, 1101 (1952); W. Macke, Z. Naturforsch. **89**, 599 (1953); **89**, 615 (1953).
[25] A. Klein and T-S. H. Lee, Phys. Rev. **D12**, 4308 (1974).
[26] Th. A. Rijken, Ann. Phys. (N.Y.) **208**, 253 (1991); THEF-NIJM 90.07, http://nn-online.org/eprints 2002.
[27] F. Rohrlich, Phys. Rev. **80**, 666 (1950).
[28] C. Itzykson and J-B Zuber, *Quantum Field Theory*, McGraw-Hill Inc. 1980.
[29] Th. A. Rijken and V.G.J. Stoks, Phys. Rev. **C 54** (1996) 2851.
[30] Th. A. Rijken and V.G.J. Stoks, Phys. Rev. **C 54** (1996) 2869.
[31] L. Fabietti *et al.*, ALICE-collaboration, CERN-LHC, arXiv:1910.14407 [hep-ex] 25 Oct. 2019.
[32] M. Isshiki, EPJ Web of Conferences **259** 11015 (2022).
[33] M.M. Nagels, T.A. Rijken, and J.J. de Swart, Phys. Rev. D**17**, 768 (1978).
[34] P.M. Maessen, T.A. Rijken, and J.J. de Swart, Phys. Rev. C**40**, 2226 (1989).
[35] Th.A. Rijken, V.G.J. Stoks, and Y. Yamamoto, Phys. Rev. C 59 (1999) 21.
[36] V.G.J. Stoks and Th.A. Rijken, Phys. Rev. C **59**, 3009 (1999).
[37] J.J. de Swart, Rev. Mod. Phys. **35** (1963) 916; *ibid* **37** (1965) 326(E).
[38] J. Schwinger, Phys. Rev. Lett. **18**, 923 (1967); Phys. Rev. **167**, 1432 (1968); *Particles and Sources*, Gordon and breach, Science publishers, Inc., New York, 1969.
[39] S. Weinberg, Phys. Phys. 166 (1968) 1568; Phys. Phys. 177 (1969) 2604.
[40] V. De Alfaro, S. Fubini, G. Furlan, and C. Rosetti, *Currents in Hadron Physics* Ch. 5, North-Holland Pulishing Company, Amsterdam 1973.
[41] M. Gell-Mann, Phys. Rev. **125**, 1067 (1962); S. Okubo, Progr. Theor. Phys. **27** 949 (1962); ibid **28** 24 (1962).
[42] C. Patrignani et al (Particle Data Group), Chin. Phys. **C 40**, 100001 (2016).
[43] V.G.J. Stoks and Th.A. Rijken, Nucl. Phys. **A 613** (1997) 311.
[44] M. Ablikim et al, Phys. Lett. **B 645** (2007) 19. In this analysis of the $J/\psi \to \omega\pi^+\pi^-$ data the ε-pole is at $E(\varepsilon) = (552 - i\,232)$ MeV, which corresponds to $m_\varepsilon = 620$ MeV, $\Gamma_\varepsilon = 464$ MeV.
[45] L. Micu, Nucl. Phys. **B10** (1969) 521; R. Carlitz and M. Kislinger, Phys. Rev. D **2** (1970) 336.
[46] A. Le Yaouanc, L. Oliver, O. Péne, and J.-C. Raynal, Phys. Rev. D **8** (1973) 2223; Phys. Rev. D **11** (1975) 1272.
[47] F.E. Low, Phys. Rev. **D 12** (1975) 163.
[48] S. Nussinov, Phys. Rev. Lett. **34** (1975) 1286.
[49] J.J. de Swart, Th. A. Rijken, P.M. Maessen, and R.G.E. Timmermans, Nuovo Cimento **102A**, 203 (1989).
[50] S. Otsuki, R. Tamagaki, and W. Wada, Progr. Theor. Phys. **32** (1964) 320; S. Otsuki, R. Tamagaki, and M. Yasuno, Progr. Theor. Phys. Suppl. Extra number (1965), 578.
[51] M. Oka, K. Shimizu, and K. Yazaki, Progr. Theor. Phys. Suppl. **137**, 1 (2000).
[52] Y. Fujiwara, Y. Suzuki, and C. Nakamoto, Progr. in Part. and Nuclear physics, **58** (2007) 439.
[53] Th.A. Rijken, M.M. Nagels, and Y. Yamamoto, Nucl. Phys. **A 835** (2010) 160.
[54] M.M. Nagels, T.A. Rijken, and J.J. de Swart, *N-N Potentials from Regge-Pole Theory*, in Few body Systems and Nuclear Forces I, Proceedings Graz 1978, Edited by H.Zingl, M. Haftel, and H. Zankel. Springer-Verlag, Berlin Heidelberg New york.
[55] Followed are the conventions of J.D. Bjorken and S.D. Drell, *Relativistic Quantum Mechanics* and *Relativistic Quantum Fields* (McGraw-Hill Inc., New York; 1965).
[56] A. Gersten, P.A. Verhoeven, and J.J. de Swart, Nuovo Cimento, Vol. **26 A**, 385 (1975); P.A. Verhoeven, *Off-Shell Baryon-Baryon Scattering*, Ph.D. University of Nijmegen, 1976.
[57] J.J. de Swart, M.M. Nagels, Th. A. Rijken, and P.A. Verhoeven, *Springer Tracts in Modern Physics*, Vol. **60**, 138 (1971).
[58] T.A. Rijken, Ann. Phys. (NY) **164**, 1 and 23 (1985).
[59] K.A. Brueckner and K.M. Watson, Phys. Rev. **92**, 1023 (1953), hereafter referred to as BW.
[60] M. Taketani, S. Machida, and S. Ohnuma, Progr. Theor. Phys. (Kyoto) **7**, 45 (1952), hereafter referred to as TMO.
[61] V.G.J. Stoks, R.A.M. Klomp, M.C.M. Rentmeester, and J.J. de Swart, Phys. Rev. C 48 (1993) 792.
[62] R.A.M. Klomp, private communication (unpublished).
[63] V.G.J. Stoks, R.A.M. Klomp, C.P.F. Terheggen, and J.J. de Swart, Phys. Rev. C**49** (1994) 2950.
[64] Y. Yamamoto, T. Motoba, and Th.A. Rijken, *G-matrix approach to Hyperon-Nucleus systems*, Progr. Theor. Phys. Suppl. **185** (2010) 72.
[65] R.A. Bryan and A. Gersten, Phys. Rev. D **6** (1972) 341.
[66] D.V. Bugg and R.A. Bryan, Nucl. Phys. **A540** (1992) 449.
[67] M.M. Nagels, Th.A. Rijken, J.J. de Swart, G.C. Oades, J.L. Petersen, A.C. Irving, C. Jarlskog, W. Pfeil, H. Pilkuhn, and H.P. Jacob, Nucl. Phys. **B 147** (1979) 189-276.
[68] D.E. Gonzales Trotter et al, Phys. Rev. Lett. **83** (1999) 3788.
[69] V. Huhn et al, Phys. Rev. Lett. **85** (2000) 1190.
[70] G.A. Miller, B.M.K. Nefkens, and I. Šlaus, Phys. Rep. **194**, 1-116 (1990)
[71] G. Alexander, U. Karshon, A. Shapira, G. Yekutieli, R. Engelmann, H. Filthuth, and W. Lughofer, Phys. Rev. **173**, 1452 (1968).
[72] B. Sechi-Zorn, B. Kehoe, J. Twitty, and R.A. Burnstein, Phys. Rev. **175**, 1735 (1968).

[73] F. Eisele, H. Filthuth, W. Fölisch, V. Hepp, E. Leitner, and G. Zech, Phys. Lett. **37B**, 204 (1971).
[74] R. Engelmann, H. Filthuth, V. Hepp, and E. Kluge, Phys. Lett. **21**, 587 (1966).
[75] V. Hepp and M. Schleich, Z. Phys. **214**, 71 (1968).
[76] D. Stephen, Ph.D. thesis, University of Massachusetts, 1970. Z. Phys. **214**, 71 (1968).
[77] J.K. Ahn *et al*, Nucl. Phys. A 761 (2005) 41.
[78] J.A. Kadyk, G. Alexander, J.H. Chan, P. Gaposchkin and G.H. Trilling, Nucl. Phys. B27 (1971) 13.
[79] Y. Kondo *et al*, Nucl. Phys. A 676 (2000) 371.
[80] T. Takahashi *et al*, Phys. Rev. Lett. 87 (2001) 212502.
[81] M.M. Nagels, T.A. Rijken, and J.J. de Swart, Phys. Rev. **D15** (1977) 2547.
[82] J. Haidenbauer, U-G. Meissner, and A. Nogga, Few Body Syst. **62** (2021) 4, 105.
[83] T. Inoue *et al*, Nucl. Phys. **A 881** (2012) 28.
[84] Y.Yamamoto and H.Bandō, Prog. Theor. Phys. Suppl. **No.81** (1985), 9.
[85] Y.Yamamoto, T.Motoba, H.Himeno, K.Ikeda and S.Nagata, Prog. Theor. Phys. Suppl. **No.117** (1994), 361.
[86] Y. Yamamoto, T. Furumoto, N. Yasutake, and Th.A. Rijken, Phys. Rev. **C 88**, 022801(R) (2013).
[87] Y. Yamamoto, T. Furumoto, N. Yasutake, and Th.A. Rijken, Phys. Rev. **C 90**, 045805 (2014).
[88] Y. Yamamoto, T. Furumoto, N. Yasutake, and Th.A. Rijken, Eur. Phys. J. **A52** (2016) 19.
[89] Y. Yamamoto, H. Togashi, T. Tamagawa, T. Furumoto, N. Yasutake, and Th.A. Rijken, Phys. Rev. **C 96**, 065804 (2017).
[90] J.P. Jeukenne, A. Lejeune, and C. Mahaux, Phys. Rev. **C 16** (1977) 80.
[91] R.R. Scheerbaum, Nucl. Phys. **A257** (1976), 77.
[92] O. Hashimoto and H. Tamura, Prog. Part. Nucl. Phys. **57** (2006), 564.
[93] T. Gogami *et al*, Phys. Rev. **C93** (1995), 034314.
[94] D.J. Millener, C.B. Dover, and A. Gal, Phys. Rev. **C38** (1988) 2700.
[95] A. Gal, Prog. Theor. Phys. Suppl. **No.186** (2010), 270.
[96] H. Noumi et al, Phys. Rev. Lett. 89 (2002) 072301.
[97] T. Harada and Y. Hirabayashi, Nucl. Phys. A759, 143 (2005).
[98] M. Kohno, Y. Fujiwara, Y. Watanabe, K. Ogata and M. Kawai Phys. Rev. **C74** (2006), 064613.
[99] M.M. Nagels, T.A. Rijken, and J.J. de Swart, Phys. Rev. **D20** (1979), 1633.
[100] Y.C. Tang and B.C. Herndon, Phys. Rev. **138**, B637 (1965).
[101] A.R. Bodmer and S. Ali, Phys. Rev. **138**, B644 (1965).
[102] R.H. Dalitz, D.H. Davis, P.H. Fowler, A. Montwill, J. Pniewski, and J.A. Zakrewski, Proc. Roy. Soc. (London) **A426**, 1 (1989).
[103] A. Ohnishi, K. Morita, K. Miyahara, and T. Hyodo, Nucl. Phys. **A 954**, 294 (2016), arXiv:1603.05761 [nucl-th].
[104] Th.A. Rijken and Y. Yamamoto, *Extended-soft-core Baryon-Baryon Model. III, Hyperon-Nucleon Interactions*, arXiv:nucl-th/06087 (2006).
[105] S. Aoki *et al.*, Prog. Theor. Phys. **89** (1993), 493.
[106] S. Aoki *et al.*, Phys. Lett. **B355** (1995), 45.
[107] K. Nakazawa, private communication.
[108] T. Fukuda *et al.*, Phys. Rev.**C58** (1998), 1306.
P. Khaustov *et al.*, Phys. Rev. **C61** (2000), 054603.
[109] S. Mandelstam, Phys. Rev. **112**, 1344 (1958).
[110] J.J. De Swart, Nuovo Cimento, Vol. **31**, 420-426 (1964).
[111] M. Gell-Mann, California Institute of Technology Laboratory, Report CTSL-20 (1961), reprinted in *The Eightfold Way*, Benjamin Inc. 1964.
[112] Th.A. Rijken and V.G.J. Stoks, Phys. Rev. C **54**, 2869 (1996).
[113] K. Nakazawa *et al.*, Prog. Theor. Exp. Phys. **2015**, 033D02.
[114] K. Sasaki, HAL-QCD Collaboration, Nucl. Phys. A **998** (2020), 121737.
[115] M. Kohno, Phys. Rev. **C100** (2019) 024313.
[116] M.M. Nagels, T.A. Rijken, and J.J. de Swart, Ann. Phys. (N.Y.) **79**, 338 (1973).
[117] H.P. Stapp, T. Ypsilantis, and N. Metropolis, Phys. Rev. **105**,302 (1957).
[118] R.A. Bryan, Phys. Rev. C **24**, 2659 (1981); **30** 305 (1984).
[119] S. Klarsfeld, Phys. Lett. **B126**, 148 (1983).
[120] D.W.L. Sprung, Phys. Rev. C **32**, 699 (1985).
[121] A. Kabir and M.W. Kermode, J.Phys.G:Nucl.Phys. **13** (1987) 501.
[122] T. Doi *et al*, arXiv:1702.01600v2 [hep-lat].
[123] S.L. Shapiro and S.A. Teukolsky, *Black Holes, Whiter Dwarfs, and Neutron Stars*, John Wiley & Sons, New York 1983.
[124] H.-J. Schulze and Th.A. Rijken, Phys. Rev. C **84**, 035801 (2011).
[125] P.B. Demorest, T. Pennucci, S.M. Ransom, M.S.E. Roberts, and J.W. Hessels, Nature (London) **467**, 1081 (2010).
[126] J. Antoniadis *et al.*, Science **340**, 6131 (2013).
[127] H.T. Cromartie *et al.*, Nat. Astron. **4** (2020) 72.
[128] R.W. Romani *et al*, Astrophysical J. Lett. 934: L17 (2022)
[129] A. Drago, A. Lavagno, G. Pagliara, and D. Pigato, Phys. Rev. C **90** 065809 (2014)
[130] D.B. Kaplan, A.E. Nelson, Phys, Lett. B **175**, 57 (1986); **179**, 409 (1986).
[131] G.E. Brown, C.-Lee, M. Rho, and V. Thorsson, Nucl. Phys. A **567**, 937 (1994).
[132] V. Thorsson, M. Prakash, and J.M. Lattimer, Nucl. Phys. A **572**, 693 (1994).
[133] C.-H. Lee, Phys. Rep. **275**, 255 (1996).
[134] N.K. Glendenning and J. Schaffner-Bielich, Phys. Rev. Lett. **81**, 4564 (1998).
[135] M.Baldo, G.F. Burgio, and H-J. Schulze, *Superdense QCD Matter and Compact stars (NATO Science Series 2: Mathematics, Physics and Chemistry vol.197)* (2006) ed D.Blaschke and D. Sedrakian.

[136] F. Özel, D. Psaltis, S. Ransom, P. Demorest, and M. Alford, Astrophys. J. Lett. **740**, L14 (2011).
[137] S. Weissenborn, D. Chatterjee, and J. Schaffner-Bielich, Nucl. Phys. A**881**, 62 (2012).
[138] T. Kähn, D. Blaschke, and D. Lastowiecky, Phys. Rev. D**88**, 085001 (2013).
[139] L. Bonanno and A. Sedrakian, Astrophys. J. j**539**, 416 (2012).
[140] R. Lastowiecki, D. Blaschke, H. Grigorian, and S. Typel, Acta Phys. Pol. **B5** (2012) 535.
[141] M. Shahrbaf, D. Blaschke, A. Grunfeld, and H. Moshfegh, Phys. Rev. **C101** (2020) 025807.
[142] M. Shahrbaf, D. Blaschke, and S. Khanmohamadi, J. Phys. G: Nucl. Part. Phys. **47** (2020) 115201.
[143] K. Otto, M. Oertel, and B-J Schaefer, arXiv:1910.11929 (2020)
[144] T. Kojo, G. Baym, and T. Hatsuda, Astrophys. J. **934**, 46 (2022), arXiv:2111.11919 (2022).
[145] T. Salmi *et al*, arXiv:2406..14466 [astro-ph.HE]
[146] S. Nishizaki, Y. Yamamoto, and T. Takatsuka, Prog. Theor. Phys. **105**, 607 (2001); **108**, 703 (2002).
[147] I. Vidaña, D. Logoteta, C. Provodencia, A. Polls, and I. Bombaci, Eur. Phys. Lett. **94**, 1002 (2011).
[148] D. Lonardoni, A. Lovato, S. Gandolfi, and F. Pederiva, Phys. Rev. Lett. **114**, 092301 (2015).
[149] D. Logoteta, I. Vidaña, I. Bombaci, Eur. Phys. J. bf A55 207 (2019).
[150] D. Cerstung, N. Kaiser, and W. Weise, Eur. Phys. J. **A56**, 175 (2020).
[151] L. McLerran and H.D. Pisarski, Nucl. Phys. A**796**, 83 (2007).
[152] Y. Hidaka, L. McLerran, and H.D. Pisarski, Nucl. Phys. A**808**, 117 (2008).
[153] L. McLerran and S. Reddy, Phys. Rev. Lett. **122**, 122701 (2019).
[154] S. Han, M.A.A. Manum, S. Lalit, C. Constantinou, and M. Prakash, Phys. Rev. D**100**, 103022 (2019).
[155] D.C. Duarte, S. Hernandes-Ortiz, and K.S. Jeong, Phys. Rev. C**102**, 025203 (2020), 065202 (2020).
[156] T. Zhao and J.M. Lattimer, Phys. Rev. **D102**, 023021 (2020).
[157] J. Margeron, H. Hansen, P. Proust, and G. Chanfray, Phys. Rev. **C104**, 055803 92021.
[158] G. Cao, Phys. Rev. **D105**, 114020 (2022).
[159] A. Akmal, V.R. Pandharipande, and D.G. Ravenhall, Phys. Rev. C**58**, 1804 (1998).
[160] H. Togashi and M. Takano, Nucl. Phys. A**902**, 53 (2013).
[161] Th.A. Rijken and Y. Yamamoto, *Quark-Quark and Quark-Nucleon potential model. ESC Meson-exchange Interactions*, THEF-NIJM 24.02, http://nn-online.org/eprints 2024.
[162] M. Hutter, "Interaction in QCD, Theory and Application of the Instanton Liquid Model", Ph.D.-thesis, University of Munich, 1995.
[163] N.K. Glendenning, Phys. Rev. **D46**, 1274 (1902).
[164] B. L. Ioffe, Nucl. Phys. B **188**, 317 (1981).
[165] Th. A. Rijken, *Quark-Nucleon Di-Quark-exchange Potentials*, THEF-NIJM 24.03, http//nn-online.org/eprints 2024.
[166] Th. A. Rijken, *Diquark Feynman Propagator in Mixed Nuclear-Quark Matter, Nucleon-Quark Diquark-exchange Interaction*, THEF-Nijm 25.01, http//nn-online.org/eprints 2025.
[167] Th. A. Rijken, *Nucleon-Quark Diquark-exchange Interaction*, arXiv:2506.22079v1 [nucl-th] 27 June 2025.
[168] L.J. Reinders, H.R. Rubinstein, and S. Yazaki, *QCD Sum Rules*, Physics Reports 1985.
[169] Th. A. Rijken, *Quark-Baryon Di-Quark-exchange Potentials*, THEF-NIJM 25.02, http//nn-online.org/eprints 2025.
[170] G. Baym, A. Bethe, and C. Pethick, Nucl. Phys. A**175**, 225 (1971).
[171] G. Baym, C.J. Pethick, and P. Sutherland, Astrophys. J.**170**, 299 (1971).
[172] A. Manohar and H. Georgi, Nucl. Phys. **B 234** (1984) 189.
[173] G.A. Miller, Phys. Rev. **C 39** (1989) 1563.
[174] P.V. Landshoff and O. Nachtmann, Z. f. Physik, **C 35** (1987) 405.
[175] K. Huang, *Quarks Leptons & Gauge Fields*, World Scientific Publishing Co Pte Ltd, 1982.
[176] J. Polchinsky, Nucl. Phys. **B231** (1984) 269.
[177] D.I. Diakonov and V.Yu. Petrov, Phys. Lett. **147B** (1984) 351.
[178] D.I. Diakonov and V.Yu. Petrov, Nucl. Phys. **B245** (1984) 259-292.
[179] D.I. Diakonov and V.Yu. Petrov, Nucl. Phys. **B272** (1986) 457-489.
[180] A.A. Belavin, A.M. Polyakov, A.S. Schwarz, and Yu.S. Tyupkin, Phys. Lett. **59B** (1975) 85.
[181] E.V. Shuryak, Phys. Rep. **C115** (1984) 152.
[182] M.A. Shiffman, A.I. Vainshtein, and V.I. Zakharov, Nucl. Phys. **B147** (1979) 385, 448.
[183] E.V. Shuryak, Nucl. Phys. **B203** (1982) 93-115.
[184] L.Ya. Glozman and D.O. Riska, Physics Reports, **268** (1996) 263-303.
[185] O.W. Greenberg, Phys. Rev. Lett. **13** (1964) 598; J.J.J. Kokkedee, *The quark model*, W.A. Benjamin, New York, 1969.
[186] Th. A. Rijken, *Constituent Quark-model for Baryons, Harmonic confinement and Meson-exchange Potentials*, THEF-NIJM 20.05, http//nn-online.org/eprints 2000.
[187] G. 't Hooft, Phys. Rev. **D14** (1976) 3432.
[188] L.Ya. Glozman, W. Plessas, and K. Varga, Nucl. Phys. **A 666 & 667** (2000) 29c-32c.
[189] L.Ya. Glozman, e-print nucl-th/9909021 (1999).
[190] Y. Nambu, Phys. Rev. Lett. **4**, 380 (1960); *Proc. Int. Conf. on High Energy Physics*, Tokyo, p. 971 (1978);
Y. Nambu and G. Jona-Lasinio, Phys. Rev. **122**, 345 (1961) and *ibid* **124**, 246 (1961).
[191] D. Diakonov, in "Selected Topics in Non-perturbative QCD", Proceedings of the Enrico Fermi School, Course CXXX, edited by A. DiGiacomo and D. Diakonov, Bologna (1996); arXiv:hep-ph-9602375.
[192] L.Ya. Glozman and K. Varga, Phys. Rev. **D61**, 074008 (2000).
[193] Th.A. Rijken, *Momentum-space Lippmann-Schwinger-Equation, Fourier-transform with Gauss-Expansion Method*, arXiv:1409.5593 [nucl-th] (2014).
[194] A. Andronic, P. Braun-Munzinger, and J. Stachel, Physics Letters B 673 (2009) 142.

[195] R. Kokoski and N. Isgur, Phys. Rev. **D 35** (1987) 907.
[196] S. Kumano and V.R. Pandharipande, Phys. Rev. **D 38** (1988) 146.
[197] R. Navarro Perez, J.E. Amaro, and E. Riu Arriola, Phys. Rev. **C 88** (2013) 024002.
[198] B. von Przewoski *et al*, Phys. Rev. **C 58** (1998) 1897.
[199] C.E. Allgower *et al*, Phys. Rev. **C 62** (2000) 064001.
[200] E. Hiyama, M. Kamimura, T. Motoba, T. Yamada, and Y. Yamamoto, Phys. Rev. Lett. 85 (2000) 270.
[201] C.J. Batty, E. Friedman, and A. Gal, Prog. Theor. Phys. Suppl. No.117 (1994) 227.
[202] J. Dabrowski, Phys. Rev. C 60 (1999) 025205.
[203] M. Kohno, Y. Fujiwara, Y. Watanabe, K. Ogata, and M. Kawai, Prog. Theor. Phys. 112 (2004) 895.
[204] S. Nishizaki, Y. Yamamoto, and T. Takatsuka, Progr. Theor. Phys. **105**, 607 (2001); **108**, 703 (2002).
[205] Th.A. Rijken, *GESC18 Two- and Three-body YNN Potentials,* $\Lambda N, \Sigma N, \Xi N$ *G-matrix Application.*, THEF-NIJM 20.03, http://nn-online.org/eprints, 2020.
[206] I.E. Lagaris and V.R. Pandharipande, Nucl. Phys. bf A 359 (1981) 349.
[207] M. Baldo, G.F. Burgio and H.-J. Schulze, Phys. Rev. **C61** (2000), 055801.
[208] I. Vidana, A. Polls, A. Ramos, L. Engvik and M. Hjorth-Jensen, Phys. Rev. **C62** (2000), 035801.
[209] A.B.Kaidalov and K.A. Ter-Martirosian, Nucl. Phys. B75 (1974), 471.
[210] J.B. Bronzan and R.L. Sugar, Phys. Rev. D16 (1977), 466.
[211] Th.A. Rijken, *Multi-Pomeron Exchange and the Universal Repulsion in Nuclear/Hyperonic Matter*, THEF-NIJM 20.02, http//nn-online.org/eprints 2020.
[212] P.S. Signell and R.E. Marshak, Phys. Rev. **109**, 1229 (1958); P.S. Signell, R. Zinn, and R.E. Marshak, Phys. Rev. Lett. **1** (1958) 416.
[213] N. Hoshizaki, S. Otsuki, W. Watari, M. Yonezawa, Progr. Theor. Phys.(Kyoto), **27**, 1199 (1962); Y. Kishi, S. Sawada, and W. Watari, Progr. Theor. Phys. **38**, 892 (1967).
[214] R. Bryan and B.L. Scott, Phys. Rev. **177**, 1435 (1969).
[215] W.N. Cottingham, M. Lacombe, B. Loiseau, J.M. Richard, and R. Vinh Mau, Phys. Rev. **D 8**, 800 (1973); M. Lacombe et al, Phys. Rev. **C 21**, 861 (1980).
[216] R. Machleidt, K. Holinde, and C. Elster, Phys. Rep. **149**, 1 (1987); R. Machleidt, *The high-precision, charge-dependent Bonn NN-potential (CD-Bonn)*, arXiv.nucl-th/0006014.
[217] C. Ordóñez, L. Ray, and U. van Kolck, Phys./ Rev. Lett. **72**(1994) 1982; Phys. Rev. **C 53**, 2086 (1996).
[218] E. Epelbaum, W. Gloeckle, and U.-G. Meissner, Nucl. Phys. A **637**, 107 (1998)
[219] J. Haidenbauer and Ulf-G. Meissner, Phys. Rev. **C 72** 044005 (2005).
[220] Y. Fujiwara, Y. Suzuki, and C. Nakamoto, Progress in Particle and Nuclear Physics **58** (2007) 439-520.
[221] N. Ishii, *et al*, arXiv:1702.03495v1 [hep-lat].
[222] J. Rowley *et al*, Phys. Rev. Lett. **127**, 272303 (2021).
[223] K. Miwa *et al*, Phys. Rev. C, **104** (2021) 4, 04520.
[224] K. Miwa *et al*, Phys. Rev. Lett. **128** (2022) 7, 072501.
[225] T. Nanamura *et al*, Progr. Theor. Exp. Phys. **2022** 093D01.
[226] W.S. Jung *et al*, arXiv:2503.17614 [nucl-ex] (2025)
[227] M. Ablikim *et al*, Phys. Rev. Lett. **130**,251902 (2023); arXiv:2512.04702 [hep-ex] (2025).
[228] N. Nakanishi and I. Ojima, *Covariant Operator Formalism of Gauge Theories and quantum Gravity*, section 2.4.2, World Scientific Lecture Notes in Physics, Vol. 27, World Scientific Pub. Co 1990.
[229] A. Le Yaouanc, L. Oliver, O. Péne, and J.-C. Raynal, Phys. Rev. D **12** (1975) 2137; ibid **18**, 1591 (1978).
[230] R. van Royen and V.F. Weisskopf, Nuovo Cimento A **50**, 617 (1967).
[231] E. Leader and E. Predazzi, *An introduction to gauge theories and modern particle physics*, Vol. I, chapter 12, Cambridge Monographs on Particle Physics, Nuclear Physics and Cosmology, Editors T. Ericson and P.V. Landshoff, Cambridge University Press 1996.
[232] M. Chaichian and R. Kögerler,Ann. Phys. **124**, 61 (1980).
[233] *Review of Particle Physics*, Particle Data Group, Phys. Rev. **D 66** 010001-1 (2002).
[234] Th. A. Rijken, *Baryon-baryon Couplings in the* $^3P_0$ *and* $^3S_1$ *QPC-models*, Notes University of Nijmegen, Nijmegen, The Netherlands, *NN-online, THEF 12.01*.
[235] L.B. Okun, *Leptons and Quarks*, chapter 29, North-Holland Publishing Company 1984.
[236] A. De Rújula, H. Georgi, and S.L. Glashow, Phys. Rev. **D 12**, 147 (1975).
[237] E.M. Henley and Z.-Y. Zhang, Nucl. Phys. **A472**, 759 (1987).
[238] R. Van Royen and V.F. Weisskopf, Nuovo Cimento **50 A**, 617 (1967).
[239] M. Gell-Mann and F. Low, Phys. Rev. **51**, 350 (1951).